Doctoral theses at NTNU, 2022:333

Nikolina Stanic

Bubble Phenomena and Bubble Properties for Different Carbon Anodes in Cryolite Melt

Doctoral thesis

NTNU
Norwegian University of Science and Technology
Thesis for the Degree of
Philosophiae Doctor
Faculty of Natural Sciences
Department of Materials Science and Engineering

NTNU
Norwegian University of
Science and Technology

Nikolina Stanic

Bubble Phenomena and Bubble Properties for Different Carbon Anodes in Cryolite Melt

Thesis for the Degree of Philosophiae Doctor

Trondheim, November 2022

Norwegian University of Science and Technology
Faculty of Natural Sciences
Department of Materials Science and Engineering

NTNU
Norwegian University of
Science and Technology

NTNU
Norwegian University of Science and Technology

Thesis for the Degree of Philosophiae Doctor

Faculty of Natural Sciences
Department of Materials Science and Engineering

ISBN 978-82-326-5921-0 (printed ver.)
ISBN 978-82-326-6148-0 (electronic ver.)
ISSN 1503-8181 (printed ver.)
ISSN 2703-8084 (online ver.)

Doctoral theses at NTNU, 2022:333

Printed by NTNU Grafisk senter

... to my family
in love and gratitude

Preface

This thesis has been submitted to the Faculty of Natural Sciences, Norwegian University of Science and Technology (NTNU) in partial fulfilment for the degree of Philosophiae Doctor (PhD). This thesis contains the results of the research carried out at the Department of Materials Science and Engineering at the Norwegian University of Science and Technology (NTNU) from 2015 to 2022 with two longer breaks because of maternity leave. The presented research was performed under supervision of Espen Sandnes (Associate Professor, NTNU) as main supervisor and Ana Maria Martinez (Senior Scientist, SINTEF) as co-supervisor.

The thesis is written as a collection of articles, with three already published articles, one in the process of publishing and two manuscripts intended for publication at a later stage.

All the individual chapters present the people who has been involved in the author list. Generally, all writing has been done by the first author with input from the co-authors.

All experimental work and data processing was conducted by the first author except for the FFT analysis of the potential-time data included in Chapter 4, gas measurements of the hollow gas anode in Chapter 5 and CT measurements in Chapter 7. The FFT analysis in relation to Chapter 4 was done by Ivana Jevremovic (in that time Postdoctoral fellow, Department of material science and engineering, NTNU). The gas measurements for the hollow gas anode in relation to Chapter 5 were done by Embla T. Bø (in that time Master Student, Department of Material Science and Engineering, NTNU). CT scanning of the samples in relation to Chapter 6 were performed by engineers in MANULAB, NTNU Gjøvik.

Main supervisor Espen Sandnes and co-supervisor Ana Maria Martinez as well as Kristian Etienne Einarsrud all contributed to the discussion of the results.

Trondheim, 3rd of June 2022
Nikolina Stanic

Acknowledgements

I would like to express my deep and sincere gratitude to my supervisor, Espen Sandnes, for giving me the opportunity to do research and providing invaluable guidance throughout this research. I have enjoyed our discussions and I really appreciate that you have always shown interest in my work.

I wish to thank my co-supervisor Ana Maria Martinez for her support, advice, and fruitful discussions.

I would like to give a special thanks to Kristian Etienne Einarsrud for his insightful comments, suggestions, and constructive criticisms.

I am also grateful to Henrik Gudbrandsen (SINTEF Industry) for all his help while working in the Chemistry Hall.

I wish to thank Embla T. Bø (then NTNU) for her extensive work performed with the hollow gas anode.

PhD fellow candidate Viviann Hole Pedersen (NTNU) has been essential when it comes to help with the XRD measurements: XRD training and processing of the data. Many thanks for that!

I also greatly appreciated all help from PhD fellow candidate Luis Carlos Izaguirre Bracamonte while working with the see-through furnace.

I wish to thank my office mate and fellow Postdoc candidate Siri Marie Skaftun for many great, mostly off-topic discussions.

I want to thank the staff engineers, present and former, Pei Na Kui, Anita Storsve, Agnes Christina Digranes and Magnus Bentzen Følstad, at the Department of Materials Science and Engineering, for the support during this PhD study.

I would like to give a special thanks to Aksel Alstad (Mechanical Workshop, NTNU) and Sebastian Bete (Glassblowing Workshop, NTNU) for all the hours spent in manufacturing all the parts needed for my research.

I am grateful to staff engineers in Department of Manufacturing and Civil Engineering NTNU for their help in performing CT analysis of my carbon samples and their advice.

I am also very grateful to Orakel Support Services for fast response and help every time when I had a problem.

Furthermore, I am thankful to all the colleagues and friends at the department of Materials Science and Engineering, NTNU, both former and present.

To all my friends, extended family, and former professors, thank you all for being in my life.

Finally, I express my deepest gratitude to my beloved family. To my parents and sister, without their support and dedication I could not have come this far. To my loving, and supportive husband, Alberto who has stood by me through all. Your patience, help and encouragement are very much appreciated. Without your tremendous understanding and encouragement in the past few years, it would be impossible for me to complete my study. To my children Jan and Dora, my greatest gifts, who made me stronger, better and who I am today.

Summary

This doctoral work is an experimental laboratory scale study of the effect of anode geometry, anode orientation and carbon anode material on bubble behavior and bubble properties in cryolite melt. The increased knowledge of the bubbles is useful for further studies, especially in laboratory-scale studies which typically applies similar anode designs. The anodes used in this work are frequently used to study reaction kinetics and mass transport, anode effect, current efficiency, anode quality properties, *etc*. It is therefore interesting to study bubble dynamics of these anodes in more detail because bubbles are relevant for all the above-mentioned phenomena.

The anode potential has been shown to be highly dependent on anode geometry and orientation. For this study four different anode designs were made: horizontal (downward-facing), inverted horizontal (upward-facing), vertical, rod (with both vertical and horizontal surface). All anodes were through experimental work redesigned, though retaining its original orientation, in order to improve its performance. From polarization curves it was found that the vertical anode and the inverted horizontal anode operated at lowest potentials. Above 1 A cm^{-2} the vertical anode showed the lowest potential. As the current increases the transition towards smaller noise is pronounced for the horizontal anode and to some degree for the vertical anode and inverted horizontal anode. Only random bubble noise was found for the vertical and the inverted horizontal anode and is probably due to more effective and random bubbles detachment from these surfaces in comparison with the rod and the horizontal anode.

This work aims to study the CO-CO_2 gas composition at low potentials and low current densities in cryolite melt with relatively low alumina content (≤ 2 wt%). There is a scarcity of data in the literature in the low current density region and also for bath low in alumina. The experimental setup was constructed to minimize the back reaction as well as the Boudouard reaction. For potentials up to 1.55 V and corresponding current densities up to 0.07 A cm^{-2} it was found that CO is dominant product. Between 1.55 V and 1.65 V (corresponding current density region 0.07 A cm^{-2} to 0.2 A cm^{-2}) CO_2 becomes the dominant gas product. These potential values are probably slightly large due to suspected Boudouard reaction between CO_2 and carbon particles in the melt formed by

disintegration of the graphite anode. The results are discussed in the relation with the literature data and thermodynamic calculations.

Gas bubble behavior on a carbon anode in a cryolite melt have been studied using a see-through cell. The phenomena studied have been growth, coalescence, detachment and wetting during electrolysis. The surface orientation affects the bubble behavior. Therefore, two different anode designs were tested, an anode with a horizontal facing-downwards surface and an anode with a vertical surface. At the horizontal anode it was found that one large bubble was formed by growth and coalescence of smaller bubbles and finally the large bubble detached periodically. For the vertical anode surface the detaching bubbles were smaller and most of them had been going through a coalescence process prior to detachment. The bubbles detached randomly. The coalescence process from the initiation to the final bubble shape at the vertical surface took about 16-24 ms. The current density did not affect the duration of the coalescence. The bubble diameter was decreasing with increasing current density for both anodes. The values were in the range 7.2 mm to 5.7 mm for the horizontal anode in the current density interval 0.2-1.0 A cm^{-2} and in the range 3.7 mm to 1.5 mm for the vertical anode in the current density interval 0.1-2.0 A cm^{-2}. The wetting contact angle for the vertical anode stayed more or less constant with an increase in current density which likely can be attributed to the decreasing bubble size rather than an increase in polarization. In addition to the bubble phenomena described and bubble properties found the impact of the results for better design of laboratory scale studies is discussed.

Anode gas bubble behavior and anode effect on graphite and industrial carbon rod-shaped anode in a cryolite melt have been studied using a see-through furnace. The different carbon materials have different properties which can affect bubble behavior and electrochemical properties. Industrial carbon is more inhomogeneous with respect to structure, pores, aggregates, and impurities in comparison to the graphite. More bubbles were nucleated on the industrial carbon than on the graphite for the same current density. The time related to the coalescence process for both anodes was found to be in the interval 16-24 ms and independent of the current density. Bubbles detached from the horizontal surface of the anode have similar average diameter value for both anodes for current densities < 1.0 A cm^{-2}, while for current densities > 1.0 A cm^{-2}, the average diameter is lower for the industrial carbon anode. The onset of the anode effect occurred faster on the graphite than on the industrial anode. The

PFC-containing gas layer appeared to be thicker and more stable on the graphite anode than on the industrial carbon anode.

To investigate the effect of different anode size regarding bubble behavior, anodes with 10 mm and 20 mm diameter with a downward-facing horizontal surface were made. It was found that the bubble diameter was decreasing with increasing current density for both anodes. Bubbles detached from the 20 mm anode are larger in size than bubbles detached from the 10 mm anode for the same current density. The thickness of the bubble just before it starts to slide towards edge to be detached from the anode surface, was found to be around 4.6 mm for the 10 mm anode while for the 20 mm anode it was 3.9 mm. At the moment of the anode effect initiation the bubble formation and bubble detachment stopped and the gas layer, a mixture of CO, CO_2 and PFC gases, was formed at the surface completely covering the surface thus preventing contact between surface and electrolyte.

Bubble behavior and dynamics on an upward-facing horizontal carbon anode was studied in order to get more detailed understanding of the regular electrolysis and anode effect in the Hall-Héroult process. The presence of weak saw-tooth features for this anode at low current densities was explained by bubble retention time long enough for coalescence into a larger bubble to take place. Different stages of bubble growth were observed: hemispherical spreading, cylindrical spreading, cylindrical growth, and necking. Coalescence was observed only in the hemispherical spreading stage. The evolution of the anode effect depends on the possibility of the gas bubbles and gas layer to be detached from the anode surface. If the gas is trapped the gas layer is covering the anode surface, disabling contact between anode and electrolyte and further gas production is strongly hindered. The anode surface of the inverted horizontal anode after anode effect was found to be still electrochemically active. The gas was not trapped and the gas evolution could continue. Results from this doctoral work supported and also gave new information to the anode effect mechanism regarding formation of surface compounds and/or gas layer insulating the anode surface. It was found that the PFC-containing gas layer only can cover the whole anode surface if the gas is not able to leave the anode. As long as produced gas can escape there is no gas layer completely covering the anode surface. With the existence of a (C – F) surface compound on the anode, the anode seems to be electrochemically active towards both CO/CO_2 and PFC formation.

Table of contents

Chapter 1

Introduction

1.1 Motivation

Aluminium is produced by the Hall-Héroult process which is an electrolytic process. Alumina (Al_2O_3) is dissolved in molten cryolite ($3NaF\text{-}AlF_3$), a reduction is taking place at the cathode forming liquid aluminium and an oxidation is taking place at the anode forming CO_2. The anode process gives a significant contribution to the energy-intensive process of electrolysis. Understanding the anode process is important in a future effort for energy saving, process control, and for reduction of greenhouse gas emissions (CO_2, PFC).

During the aluminium electrolysis process, small spherical gas bubbles are initially generated on the anode bottom surface. They grow to a certain size before expanding horizontally. When bubbles come into contact with each other they can coalesce into larger individual bubbles and cover larger surface area upon which large bubbles move along the surface because of the bath flow and inclination of the anode. When the bubble reaches the anode edge, it rises rapidly because of buoyancy and escapes up the side of the anode [1, 2]. Gas present at the anode surface causes an additional voltage drop, so called a bubble overvoltage. Since bubbles are covering the anode, they can be responsible for as much as 10% of the total cell voltage [3]. The extra voltage drop to bubbles is about 0.15-0.35 V out of a typical total cell voltage of ~4.5 [4]. In the lab-scale studies it was found that the additional voltage loss due to bubbles has been shown to be highly dependent on anode geometry and orientation [2, 5, 6].

1.2 Aim of the work

The aim of this work was to study bubble phenomena and bubble properties such as nucleation, growth and size, coalescence, detachment and wetting during electrolysis for different current densities on different laboratory scale anode designs. Different carbon materials have different surface properties which can affect bubble behavior and electrochemical properties. One anode material was pure graphite and the other was industrial carbon. Graphite and industrial carbon show differences in composition (*e.g.,* impurities content), heterogeneity, porosity, surface roughness, *etc.*, that all have effect on bubble behavior (bubble life cycle, bubble size, wetting properties, *etc.*). An additional aspect of the study was on anode effect and how different materials affect it, prior to, during and after anode effect. The lab-scale anodes used in this paper are typically used to study reaction kinetics and mass transport, anode effect phenomena, current efficiency, anode quality properties, *etc*. It was therefore interesting to study bubble dynamics of these anodes in more detail because bubble dynamics are relevant for all the above-mentioned features. Since anode design and surface orientation affects bubble behavior, four main anode designs were made: horizontal anode with a downward-facing surface, vertical anode, rod anode with both a vertical and horizontal surface and inverted horizontal anode with an upward-facing surface. The first three anode designs have been reported in earlier papers [7, 8]. The inverted horizontal anode, not previously reported in the literature w.r.t. aluminium electrolysis, was constructed to have a horizontal surface which has faster bubble release in comparison to a downward-facing horizontal anode where bubbles cannot be released easily due to the buoyancy alone. During this doctoral work some anode designs were slightly modified in order to improve the quality and output of the experiments, but the orientation was kept the same.

Electrochemical methods such us linear sweep voltammetry, impedance spectroscopy, chronopotentiometry, chronoamperometry were used to study electrochemical characteristics (current oscillation, potential oscillation, polarization curves, *etc.*) of the bubble evolution during anode reaction in laboratory scale cell. Gas measurements were performed to get an indication of the CO_2-CO composition. This was especially interesting regarding gas bubbles formed at low current densities as more CO is then

formed. At the beginning of the work a closed furnace was used, but later was switch to a see-through furnace with high-speed camera. Gas bubble behavior during electrolysis was recorded and analyzed. The bubble phenomena such as nucleation, growth, coalescence, detachment of the bubbles was studied in detail as well as wetting properties and anode effect.

Results obtained in this doctoral work cannot be directly applied to an industrial setting but increased knowledge of the bubble behavior is especially useful for further laboratory scale studies applying similar anode designs.

1.3 Structure of thesis

Chapter 2 gives a brief introduction in the field of aluminium production and anode process.

Chapter 3 introduces the experimental setup and methodology together with some pre-tests.

Chapter 4, 5, 6 and 7 include work published or in the process of publishing in peer-reviewed journals. Chapters are written in the same chronological order as the work was done and published. Chapter 4 contains the electrochemical study of bubble behavior, effect of anode design and orientation on the bubble behavior. Chapter 5 deals with a study of CO_2-CO gas composition at low anode potentials and low current densities with a low alumina content. In Chapter 6 the bubble behavior on graphite anode and phenomena like bubble growth, coalescence, detachment and wetting during electrolysis are studied using a see-through cell. In Chapter 7 the see-through cell was again used to study bubble behavior on the anode made of different anode materials (graphite and industrial carbon). The study also focused on anode effects and how different materials affect it.

Chapter 8 and 9 contain results which contribute to better understating of phenomena from earlier Chapters 4-7. In Chapter 8 bubble behavior on a horizontal anode with different diameters, 10 mm and 20 mm, was studied to check the anode size dependency. Chapter 9 presents a study of a horizontal anode facing upwards design with an emphasis on the

anode effect mechanism. Chapter 8 and 9 are written in a form of an article structure for future publishing.

At the end the overall conclusion from the work is presented and suggestions for further work are given.

The thesis is written as collection of articles and some repetition is inevitable.

References

1. Fortin, S., M. Gerhardt, and A.J. Gesing, *Physical Modeling of Bubble Behavior and Gas-release from Aluminium Reduction Cell Anodes*, in *Light metals 1984*, J.P. McGeer, Editor. 1984, Metallurgical Society of AIME: Warrendale. p. 721-741.
2. Cassayre, L., T. Utigard, and S. Bouvet, *Visualizing gas evolution on graphite and oxygen-evolving anodes.* JOM (USA), 2002. **54**(5): p. 41-45.
3. Einarsrud, K.E., S.T. Johansen, and I. Eick, *Anodic Bubble Behavior in Hall-Héroult Cells*, in *Light Metals 2012*, C.E. Suarez, Editor. 2012, John Wiley & Sons, Inc.: Hoboken, NJ. p. 875-880.
4. Zhao, Z., Z. Wang, B. Gao, Y. Feng, Z. Shi, and X. Hu, *Observation of Anodic Bubble Behavior Using Laboratory Scale Transparent Aluminium Electrolysis Cells*, in *Light Metals 2015*, M. Hyland, Editor. 2015, Springer: Cham. p. 801-806.
5. Leistra, J., P. Sides, and J. Leistra, *Hyperpolarization at Gas Evolving Electrodes. II. Hall/Heroult Electrolysis.* Electrochim. Acta, 1988. **33**(12): p. 1761-1766.
6. Cassayre, L., G. Plascencia, T. Marin, S. Fan, and T. Utigard, *Gas Evolution on Graphite and Oxygen-Evolving Anodes During Aluminium Electrolysis*, in *Light Metals 2006*, T.J. Galloway, Editor. 2006, TMS: Warrendale. p. 379-383.
7. Thorne, R.J., C. Sommerseth, A.P. Ratvik, S. Rorvik, E. Sandnes, L.P. Lossius, H. Linga, and A. Svensson, *Bubble Evolution and Anode Surface Properties in Aluminium Electrolysis.* J. Electrochem. Soc., 2015. **162**(8): p. E104-E114.
8. Thorne, R.J., C. Sommerseth, A.M. Svensson, E. Sandnes, L.P. Lossius, H. Linga, and A.P. Ratvik, *Understanding Anode Overpotential*, in *Light Metals 2014*, J. Grandfield, Editor. 2014, John Wiley & Sons, Inc.: Hoboken, NJ. p. 1213-1217.

Chapter 2

A brief introduction to aluminium electrolysis

This chapter contains a brief introduction to aluminium electrolysis with focus on areas investigated in this doctoral work. More theory and literature references for specific topics are included in the Introduction and Discussion part of the articles.

2.1 The Hall-Héroult process

The Hall–Héroult process has been applied in the production of aluminium for more than hundred years. It is named after its inventors the French Paul Héroult and the American Charles Martin Hall who independently in 1886 developed and patented electrolytic reduction of aluminium oxide (alumina, Al_2O_3) dissolved in molten cryolite ($3NaF\text{-}AlF_3$) with consumable carbon anodes [1]. Today the industrial electrolysis is following the same principle, but substantial technical improvements has been made.

In the cell carbon anodes are immersed into the bath. The alumina is dissolved and oxygen contain species are oxidized at the anode forming among other gaseous CO_2. Under the bath is a pool of liquid aluminium. Aluminum is formed at the bath/metal interface which acts as a cathode. A sketch of an aluminium reduction cell with the prebaked anodes is shown in the Figure 2.1. The overall chemical reaction can be written:

$$\frac{1}{2}Al_2O_3(\text{diss.}) + \frac{3}{4}C(s) = Al(l) + \frac{3}{4}CO_2(g) \quad (2.1)$$

The bath temperature is usually in the range 950-980 °C. A common bath in modern cells may contain in addition to cryolite as the main component: 6-13 wt% aluminium fluoride (AlF_3), 4-6 wt% calcium fluoride (CaF_2), 2-4 wt% alumina (Al_2O_3) [2]. All additives to the bath reduce its melting point and the cell operating temperature but they also reduce the alumina solubility. Two anode designs, the prebaked anodes and the Søderberg anodes are used. Since the anodes are consumable the prebaked anodes have to be changed in regular intervals, usually after 22-30 days [1]. The leftover anodes are called butts and after the cleaning process they are reused as a raw material for new anodes. Søderberg anodes are continuous and self-baking. These anodes need anode paste addition and stud pullings. Compared with prebaked, Søderberg cells are less efficient and have higher production costs, they are more difficult to automate and have bigger environmental and health challenges. The Søderberg cells have more frequent anode effects because of less efficient alumina feeding control. Modern cell designs have special automatic alumina point feeders. The alumina concentration in the bath is typically in the range 2-4 wt%. Higher alumina content may lead to formation of an undissolved alumina sludge. A low alumina content may lead to an anode effect which disrupts normal electrolysis. The bath surface is covered with a crust consisting of alumina and frozen bath. On top of the crust a layer of alumina is deposited to maintain good heat insulation. Some plants apply a mixture of alumina and crushed bath in this layer. The removal of liquid aluminium from the cell (metal tapping) is done approx. every second day. A steel tube is lowered into the metal pad and the metal is sucked out with an air-ejector system. The Hall-Héroult process has two major weaknesses, high energy consumption and small units giving high operational and capital costs. There have been many attempts to develop alternative processes, but the Hall-Héroult process is still the only method by which aluminium is produced industrially today.

The current efficiency with respect to aluminium can be as high as 96 % in modern cells running at ~ 300 kA or higher [3]. The pot room current efficiency is determined by the dividing the actually produced aluminium by the theoretical Al value in the same time period. Because the aluminum production depends on the magnitude of the electrical current, there has been a steady increase in amperage and size of industrial aluminum cells from 40 kA cells (7 m length) in the 1940s to 200-250 kA cells (9 m length) in the 1980s and 350-400 kA cells (20 m length) in the

2000s. Industrial aluminum cells prior to the 1970s operated from 85% to 88% current efficiency, while modern cells now can operate 95-96% current efficiency [4].

The current efficiency can also be estimated by measuring the off-gas. For example, Thonstad reported in 1964 [5] that the industrial anode off-gas consist of CO_2 together with 30-50% of CO. Kimmerle and Noël observed in 1997 [6] 82% CO_2 and 17% CO in industrial anode off-gas. Aarhaug et al. reported in 2016 [7] 7700 ppm of CO_2 and 764 ppm CO in off-gas from primary aluminium production, that would correspond to around 9 % of CO and 91 % of CO_2.

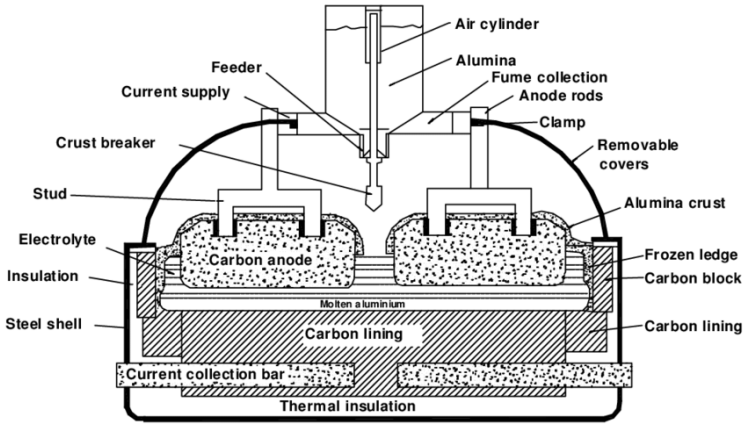

Figure 2.1. Industrial Hall-Héroult cell with the prebaked anodes. Adapted from [2, 8].

2.2 Anode reaction and mechanism

The overall reaction can be one or both of the following:

$$2Al_2O_3(l) + 3C(s) \rightarrow 4Al(l) + 3CO_2(g) \qquad E^0 = -1.16\ V \tag{2.2}$$

$$Al_2O_3(l) + 3C \rightarrow 2Al(l) + 3CO(g) \qquad E^0 = -1.02\ V \tag{2.3}$$

The cathode product is liquid aluminum, and the anode product is a CO_2/CO gas mixture. As a result, carbon anodes are consumed. The main primary anode product is CO_2 (g), but some CO can be formed at low current densities, 0.05-0.1 A cm^{-2} [9].

Several mechanisms are proposed for the anode reaction. Each mechanism in general contains electrochemical adsorption of the oxide anion followed by desorption of CO_2.

Picard *et al.* [10] studied anode reaction using electrochemical impedance and proposed the following three-step mechanism at low current densities and low overpotentials:

1. Diffusion of the oxyfluoroaluminate species from the bulk of the melt to the surface of the graphite anode:

$$AlOF_x^{1-x}\ (\text{bath}) \rightarrow AlOF_x^{1-x}\ (\text{electrode})$$

2. Dissociation of the oxyfluoroaluminate species and adsorption of the oxide ions, followed by their discharge and the formation of the adsorbed carbon-oxygen species:

$$AlOF_x^{1-x} + C \rightarrow CO_{ads} + AlF_x^{3-x} + 2e^-$$

3. Dissociation of the oxyfluoroaluminate species and the adsorption of the oxide ions, their discharge in the presence of the CO_{ads} and the desorption of gaseous carbon dioxide CO_2:

$$AlFO_x^{1-x} + CO_{ads} \rightarrow CO_{2\,(g)} + AlF_x^{3-x} + 2e^-$$

Thonstad [9] also proposed an electrochemical adsorption followed by a thermal desorption step involving a combination of two CO_{ads} species :

1. Discharge of oxygen: $O^{2-}_{(\text{in complex})} \rightarrow O + 2e^-$
2. Chemisorption of oxygen: $O + C \rightarrow C_xO$
3. Conversion of C_xO: $2C_xO \rightarrow CO_{2(\text{ads.})} + C$
4. Desorption of CO_2: $CO_{2(\text{ads.})} \rightarrow CO_{2(g)}$

Kisza *et al.* [11] studied the anodic reaction and found that a total electrode reaction can be interpreted by a two-step two-electron charge-transfer process with an intermediate adsorption. Adopting that in alumina-rich bath the predominant species is $Al_2O_2F_6^{4-}$, a similar mechanism with the electrochemical desorption step was proposed:

1. Charge transfer step with an intermediate adsorption:

$$Al_2O_2F_6^{4-} + C \rightleftarrows Al_2OF_6^{2-} + "CO_{ads}" + 2e^-$$

2. Electrochemical desorption

$$Al_2O_2F_6^{4-} + "CO_{ads}" \rightleftarrows CO_2 + Al_2O_2F_6^{2-} + 2e^-$$

2.3 Anode gas products

The electrochemical anode gas product in aluminium electrolysis is CO_2, but also some CO is produced, according to reactions (2.2) and (2.3). The CO content in the anode off gas can arise from the electrochemical reaction directly, and from chemical reactions where CO_2 is converted to CO.

The most unwanted reaction responsible for the loss in current efficiency in the aluminum electrolysis is the back reaction between dissolved CO_2 and dissolved Al and Na in the melt. The sodium is created through the reaction between aluminium and sodium fluoride at the cathode/electrolyte interface. The back reaction can be written [2, 5]:

$$2Al(diss.) + 3CO_2(diss.) \rightarrow Al_2O_3(diss.) + 3CO(g) \quad (2.4)$$

Another possibility for CO formation is through the Boudouard reaction where CO_2 gas is reacting with solid carbon forming CO gas according to:

$$CO_2 + C = 2CO \quad (2.5)$$

The carbon reacting in reaction (2.5) may be anode carbon or carbon particles floating in the bath formed by disintegration (dusting) of the carbon anodes during electrolysis.

Another source of CO could be reaction of aluminium carbide and CO_2, forming also carbon dust [12]:

$$Al_4C_3 + 6CO_2(g) \rightarrow 2Al_2O_3 + 3C + 6CO(g) \quad (2.6)$$

Alumnium carbide can be formed either chemically or electrochemically at the cathode and transported away from the cathode by dissolution into the bath.

CO can also be formed by air burn.

2.4 Anode gas bubbles

Gas present at the anode surface contributes to an increase cell voltage as the current lines between the anode and cathode become prolonged. This is also in the literature sometimes referred to as a bubble overpotential. In addition, charge transfer and concentration overpotential contribute to total cell voltage. The bubbles can be responsible for as much as 10 % of the total cell voltage [13]. Reducing energy consumption in aluminium electrolysis is of major importance for production cost savings and for reduction of greenhouse gas emissions.

Hyperpolarization can be defined as a potential component at gas evolving electrodes due to the masking of the electrode by bubbles, *i.e.,* active surface area is reduced by a bubble covering part of the electrode surface. This causes areas with higher local current density than the calculated current density based on the geometric area. The increased current density causes increased charge transfer overpotential related to an electrode reaction. Hyperpolarization causes also an increase in concentration overpotential [14]. The extra voltage due to bubbles is about 0.15-0.35 V out of a typical total cell voltage of ~ 4.5 V [15]. The additional potential increase due to bubbles has been shown to be highly dependent on anode geometry and orientation.

2.5 Anode effect

An anode effect is a phenomenon in molten salts electrolysis. In aluminium electrolysis the anode effect is caused by depletion of alumina underneath the anodes and causes the resistance and thereby the voltage to increase dramatically. In the industrial cell the voltage can increase from around 4 V to as much as 40 V. During anode effect the bottom operating surface of the anode seems to be covered by a film of gas. This covers the

surface of the anode and pushes the bath away, producing the so-called non-wetting of the anode. The anode effect causes low energy-efficiency and reduces the current efficiency. It also induces the formation of PFCs (CF_4 and C_2F_6) and increases formation of CO [16]. Thonstad *et al.* [17-19] studied anode effect on graphite anodes in cryolite-alumina melts prior to and during the occurrence of the anode effect by potential sweep and galvanostatic measurements. When a carbon anode in a molten salt is exposed to an increasing anode potential the current will eventually reach a so called critical current density (ccd) and then abruptly drop towards zero at onset of anode effect. The onset for anode effect seems to be a depletion of oxygen-containing ions which is followed by co-deposition of fluorine that leads to anode effect. The anode surface is covered by insulating gas film that inhibits charge transfer. The insulating gas film contains (C – F) bond [16]. The film becomes thicker once the anode effect is established. Haverkamp [20] studied fluorination of carbon anode using XPS and SEM and discovered fluorocarbon on the anode surface resulting from anode effect. The author concluded that a (C – F) film exist. During anode effect the fluorine reacts with the carbon forming PFC gases, CF_4 and C_2F_6. PFC formation happens according to reactions [21]:

$$Na_3AlF_6 + \frac{3}{4}\,C = Al + \frac{3}{4}\,CF_4 + 3NaF \qquad E^0 = -\,2.42\ V \tag{2.7}$$

$$Na_3AlF_6 + C = Al + \frac{1}{2}\,C_2F_6 + 3NaF \qquad E^0 = -\,2.68\ V \tag{2.8}$$

Tabereaux *et al.* [22] measured the change in the anode gas composition during anode effects in industrial cell and found that the gas mixture consists primarily of CO, 60-70 %, and CO_2, 20-30 %; CF_4 content from both prebaked and Søderberg cells was in the range 16-20 %, and the C_2F_6 content was small, 0.0-0.05 %.

References

1. Thonstad, J., P. Fellner, G.M. Haarberg, J. Híveš, H. Kvande, and Å. Sterten, *Aluminium electrolysis : fundamentals of the Hall-Héroult process*. 3rd ed. 2001, Düsseldorf: Aluminium-Verlag. 359.

2. Grjotheim, K. and H. Kvande, *Introduction to aluminium electrolysis : understanding the Hall-Héroult process*. 2nd ed. 1993, Düsseldorf: Aluminium-Verlag.
3. Haarberg, G.M. *The Current Efficiency for Aluminium Deposition from Molten Fluoride Electrolytes with Dissolved Alumina*. in *Advances in Molten Slags, Fluxes, and Salts: Proceedings of the 10th International Conference on Molten Slags, Fluxes and Salts 2016*. 2016. Cham: Springer International Publishing.
4. Tabereaux, A.T. and R.D. Peterson, *Chapter 2.5 - Aluminum Production*, in *Treatise on Process Metallurgy*, S. Seetharaman, Editor. 2014, Elsevier: Boston. p. 839-917.
5. Thonstad, J., *On the Anode Gas Reactions in Aluminum Electrolysis.* J. Electrochem. Soc., 1965. **111**(8): p. 955-959.
6. Kimmerle, F.M. and L. Noël, *COS, CS_2 and SO_2 Emissions from Prebaked Hall Héroult Cells*, in *Light metals 1997* R. Huglen, et al., Editors. 1997, Minerals, Metals & Materials Society: Warrendale, Pa. p. 153-158.
7. Aarhaug, T.A., A. Ferber, O. Kjos, and G. H., *Online Monitoring of Aluminium Primary Production Gas Composition by use of Fourier-Transform Infrared Spectroscopy*, in *Light Metals 2014*, J. Grandfield, Editor. 2016, Springer International Publishing : Imprint: Springer: Cham. p. 647-652.
8. Prasad, S., *Studies on the Hall-Heroult aluminum electrowinning process.* Journal of the Brazilian Chemical Society, 2000. **11**(3): p. 245-251.
9. Thonstad, J., *On the Anode Gas Reactions in Aluminum Electrolysis, II.* J. Electrochem. Soc., 1965. **111**(8): p. 959-965.
10. Picard, G.S., E.C. Prat, Y.J. Bertaud, and M.J. Leroy, *Evidencing the Electrochemical Mechanism at Carbon/Bath Interface by Means od Impedance Measurement: An Improved Approach to the Aluminium Reduction Process*, in *Light metals 1987* R.D. Zabreznik, Editor. 1987, Metallurgical Society: Warrendale. p. 507-517.
11. Kisza, A., J. Thonstad, and T. Eidet, *An impedance study of the kinetics and mechanism of the anodic reaction on graphite anodes in saturated cryolite-alumina melts.* J. Electrochem. Soc., 1996. **143**(6): p. 1840-1847.
12. Novak, B., A.P. Ratvik, Z. Wang, and T. Grande, *Formation of Aluminium Carbide in Hall-Héroult Electrolysis Cell Environments*, in *Light Metals 2018*, O. Martin, Editor. 2018, Springer International Publishing: Cham. p. 1215-1222.
13. Einarsrud, K.E., S.T. Johansen, and I. Eick, *Anodic Bubble Behavior in Hall-Héroult Cells*, in *Light Metals 2012*, C.E. Suarez, Editor. 2012, John Wiley & Sons, Inc.: Hoboken, NJ. p. 875-880.
14. Thorne, R.J., C. Sommerseth, A.P. Ratvik, S. Rorvik, E. Sandnes, L.P. Lossius, H. Linga, and A. Svensson, *Bubble Evolution and Anode Surface Properties in Aluminium Electrolysis.* J. Electrochem. Soc., 2015. **162**(8): p. E104-E114.
15. Zhao, Z., Z. Wang, B. Gao, Y. Feng, Z. Shi, and X. Hu, *Observation of Anodic Bubble Behavior Using Laboratory Scale Transparent Aluminium Electrolysis Cells*, in *Light Metals 2015*, M. Hyland, Editor. 2015, Springer: Cham. p. 801-806.
16. Tabereaux, A., *Anode Effects, PFCs, Global Warming, and the Aluminium Industry.* JOM, 1994. **46**: p. 30-34.
17. Thonstad, J., F. Nordmo, and K. Vee, *On the anode effect in cryolite-alumina melts—I.* Electrochimica Acta, 1973. **18**(1): p. 27-32.

18. Thonstad, J., F. Nordmo, and J.K. Rødseth, *On the anode effect in cryolite-alumina melts—II the initiation of the anode effect.* Electrochimica acta, 1974. **19**(11): p. 761-769.
19. Nordmo, F. and J. Thonstad, *On the anode effect in cryolite—alumina Melts—III. Current—voltage behaviour during anode effect.* Electrochimica acta, 1984. **29**(9): p. 1257-1262.
20. Haverkamp, R.G., *An XPS study of the fluorination of carbon anodes in molten NaF–AlF3–CaF2.* Journal of Materials Science, 2012. **47**(3): p. 1262-1267.
21. Thonstad, J., S. Rolseth, and R. Keller, *On the Mechanism Behind Low Voltage PFC Emissions*, in *Light Metals 2013*, B.A. Sadler, Editor. 2016, Springer International Publishing: Cham. p. 883-885.
22. Tabereaux, A.T., N.E. Richards, and C.E. Satchel, *Composition of reduction cell anode gas during normal conditions and anode effects*, in *Light Metals 1995*, J.W. Evans, Editor. 1995, TMS: Warrendale, Pennsylvania. p. 325-333.

Chapter 3

Experimental part

Chapter 3 introduces different electrode designs used in this work, furnace setups, and cell designs each briefly explained. Methodology and some additional tests done prior to experiments are also described. This chapter describes all experimental parts for the doctoral work.

3.1 Electrodes

Each electrode was fabricated "in house". Two different types of carbon material were used, a purified graphite material (Schunk Tokai Scandinavia, AB, Sweden) and a sample from industrial carbon anode. A high purity boron nitride BN (BN5000) material was used for anode shielding. The calcium borate binder in BN5000 makes this the most versatile of all the BN grades due to the reduced susceptibility to moisture pick-up. BN5000 can be used in a variety of higher temperature applications where lower thermal expansion and higher thermal shock resistance are required.

3.1.1 Working electrodes

As working electrode different designs were used in different setups: rod anode, horizontal anode, vertical anode and inverted horizontal anode. In Figure 3.1 and Figure 3.2 are shown principal drawings with dimensions of the anodes.

The horizontal anode was made as described in [1]. The graphite rod (Ø 10 mm) and stainless steel rod (Ø 3 mm) were threaded together and the graphite was shielded using boron nitride (BN) in order to expose

only 10 mm diameter horizontal base when the anode is immersed in the melt, Figure 3.1(a). The active anode area is 0.785 cm^2. The BN edges were chamfered by an angle of 45 degrees in order to improve bubble release avoiding thick shielding around graphite surface. Still less than 1 mm of the BN shielding is present around horizontal anode surface.

The vertical anode design had a defined surface area of 1.57 cm^2 by using boron nitride shielding and it was made as described in [2]. Two boron nitride rods (Ø 10 mm) and graphite rod (Ø 10 mm) were threaded together on the graphite rod (Ø 3 mm), which was attached via the stainless-steel connector to a stainless-steel rod, Figure 3.1(b). For the see-through experiments the bigger vertical anode was used giving then active surface area of 3.14 cm^2, Figure 3.2(d).

The rod anode has mixed geometry, *i.e.,* horizontal and vertical surfaces. It was made as described in [3]. The graphite rod (Ø 10 mm) and stainless-steel rod (Ø 3 mm) were threaded together, Figure 3.1(c). First, the rod anode was not shielded and did not have a well-defined area that was exposed to the melt. When the anode is immersed 1 cm in the melt for, it has approximated active surface area of 3.9 cm^2. Because of the uncertainty in the immersion depth of the rod anode the current density also became uncertain. For later experiments the rod anode was shielded in order to have define surface area of 3.9 cm^2, Figure 3.2(b).

The inverted horizontal design is a horizontal anode facing upwards design that has not been previously reported. Boron nitride rod (Ø 25 mm) was cut and assembled as shown in Figure 3.1(d) and Figure 3.2(e). Holes for the graphite and the stainless-steel rod were drilled in the boron nitride. Electrical contact between graphite and stainless steel was obtained by making threaded connection. The electrical contact was further improved by adding graphite dust in the threads. A horizontal cut of the graphite rod was made which gave the anode surface area the shape of a horizontal ellipse with an area of 0.69 cm^2.

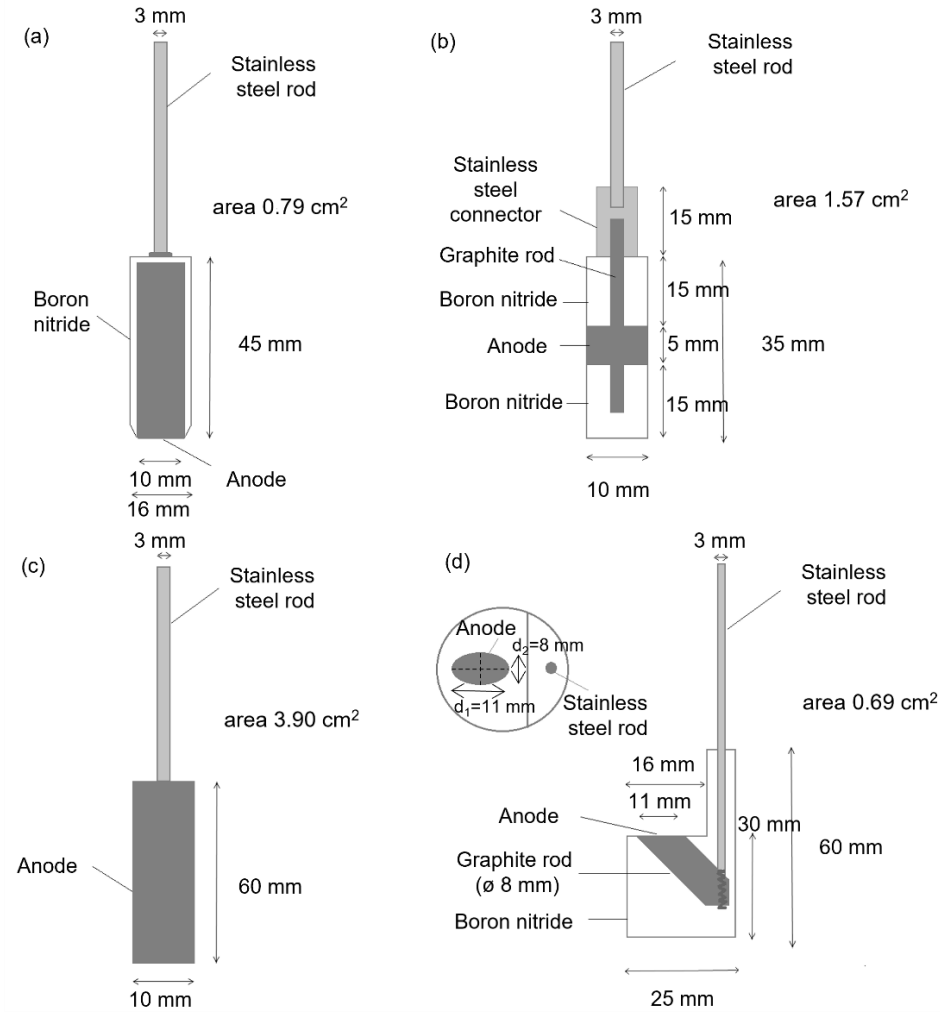

Figure 3.1. Different anode designs: (a) horizontal anode, (b) vertical anode, (c) rod anode, (d) inverted horizontal anode (inset shows electrode seen from above).

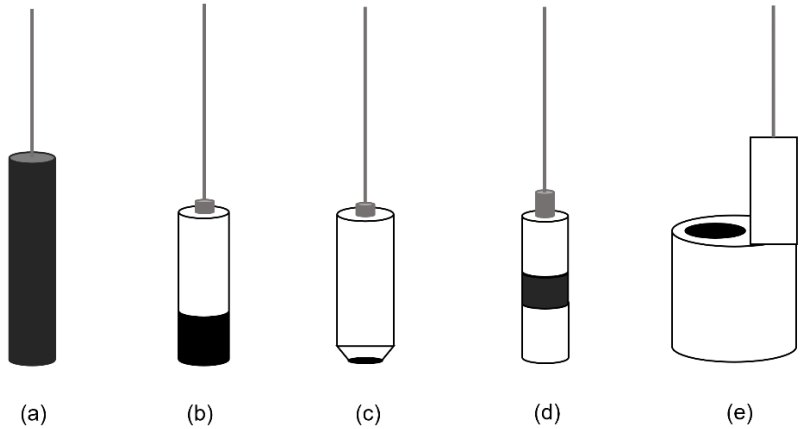

Figure 3.2. The outer body of different anode designs: (a) rod anode when immersed 10 mm in melt gives a geometric surface area of approx. 3.9 cm^2, (b) shielded rod anode with the defined surface area of 3.9 cm^2, (c) horizontal anode with the anode surface area of 0.79 cm^2, (d) vertical anode with the anode surface area of 1.57 cm^2, (e) inverted horizontal anode which gave the anode surface area the shape of a horizontal ellipse with an area of 0.69 cm^2.

One other anode design was used for gas measurements (in Chapter 5), so called a hollow gas anode. The hollow gas anode had the shape of an inverted funnel and was designed as shown in Figure 3.3.

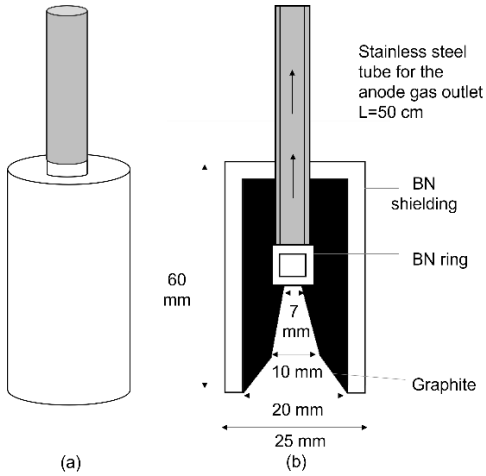

Figure 3.3. The hollow gas anode; (a) the outer body of the hollow gas anode, (b) cross section of the hollow anode design with the inverted funnel shape, anode surface area approx. 10.8 cm^2.

One of the bubbles properties that was studied in detail for different anode designs in the see-through furnace was the bubble size (diameter), Chapters 6-9. In addition to the horizontal anode facing downwards with 10 mm diameter a larger horizontal anode with 20 mm diameter was constructed, Figure 3.4. The purpose was to study the effect of the anode size on the bubble behavior and bubble size. As can be seen in Figure 3.4, the horizontal anode with 20 mm diameter besides horizontal active anode surface has also a small vertical active anode surface. Vertical surface comes from the graphite sticking out of the BN shielding avoiding any BN shielding around graphite surface. Any BN shielding could make it harder for bubble to be released.

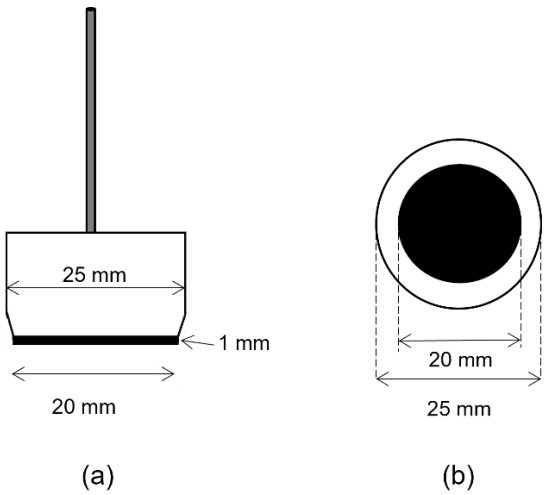

Figure 3.4. (a) The outer body of the horizontal anode with 20 mm diameter and 1 mm of graphite sticking out of the BN shielding giving the surface area of the vertical part 0.63 cm^2 and of the horizontal part 3.14 cm^2. BN edges chamfered 45 degrees and (b) the horizontal anode shown from below.

In order to study bubble behavior on the inverted horizontal anode in the see-through furnace the existing design was not suitable. Two main problems were a relatively big size of the anode in comparison to the size of the quartz crucible and a great number of bubbles resting at the boron nitride. It was difficult to see the anode surface because of the bubbles resting on the BN surface. After trial and error, a new design was found which worked properly and electrode is shown in Figure 3.5. As can be seen in BN edges were 45 degrees angle chamfered and 2 mm of graphite

was sticking out of the BN shielding. In first attempts BN edges were not chamfered and graphite was not sticking out of the BN shielding.

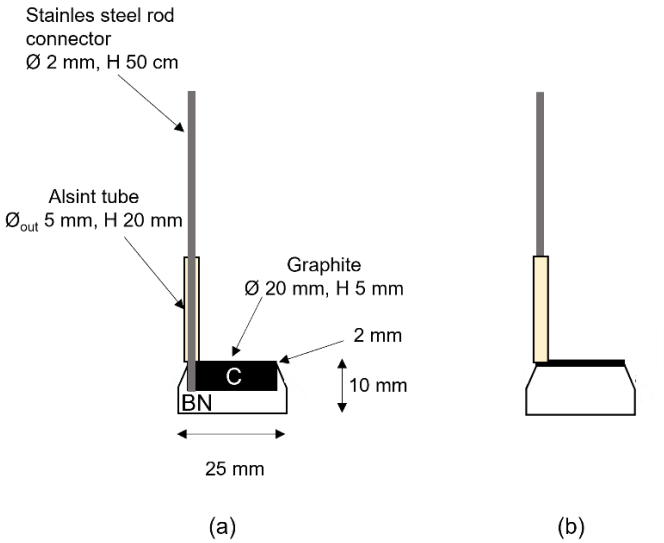

Figure 3.5. The new anode design with horizontal surface facing upwards: (a) cross-section with the surface area of the vertical part 1.26 cm^2 and of the horizontal part 3.14 cm^2, (b) the outer body of the inverted horizontal anode.

3.1.2 Counter electrodes

In the electrochemical and gas measurements (Chapter 4 and 5) a shielded graphite rod was used as a counter electrode. The graphite rod (Ø 10 mm) and stainless-steel rod (Ø 3 mm) were threaded together and graphite sides were shielded using boron nitride, as shown in Figure 3.6. The graphite crucible was used as a counter electrode during gas measurements with the hollow gas anode.

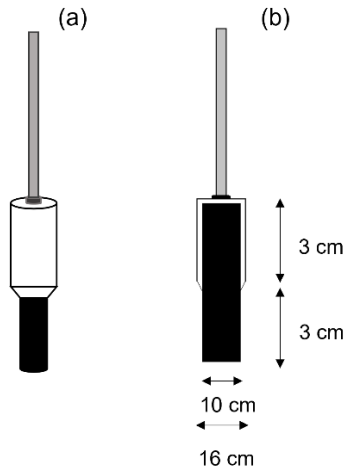

Figure 3.6. (a) The outer body of the shielded rod-shaped counter electrode with the surface area of 10.2 cm^2 and (b) its cross sections.

In the see-through furnace (Chapters 6-9) a stainless-steel (SS) rod was used as a counter electrode. Since the see-through furnace is kind of the open furnace, it was difficult to use graphite rod as a counter electrode since the exposed graphite completely burned. Due to smaller size of the cell and the light inside the cell the graphite rod shielded with the BN it was desirable to be avoided. Due to this the SS rod with 5 mm diameter was constructed. The SS rod was immersed 4 cm into the melt. The approx. area was 6.5 cm^2.

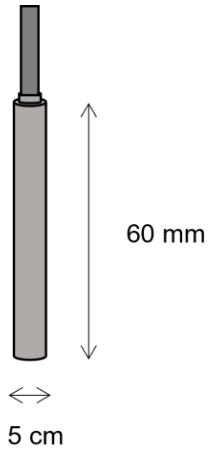

Figure 3.7. The stainless-steel rod as the counter electrode.

3.1.3 Aluminium reference electrode

A commonly used reference electrode in laboratory scale experiments in fluoride melts is the aluminium reference electrode. The aluminium reference electrode is produced in-house, and a new reference was made for each experiment. In Figure 3.8 is shown design of the aluminium reference electrode. It was fabricated based on [4, 5]. The reference electrode was made of a stainless-steel tube threaded to the boron nitride tube closed at one end ($Ø_{inner}$ = 5 mm, $Ø_{outer}$ = 10 mm). A hole (Ø = 1.5 mm) was drilled approximately 2.5 cm above the inner bottom of the BN tube. The purpose of the hole was to allowed electrolyte to enter the reference electrode. Around 0.6 g pure aluminium was placed in the BN tube, giving a melted pool of aluminium at the bottom of the tube with a height of approx. 12 mm. A tungsten wire was placed into an aluminium oxide (Alsint) tube (1.5 x 3 x 600 mm) and placed inside the steel tube. The unshielded tungsten wire was lowered into the pool of aluminium and was used for electrical contact.

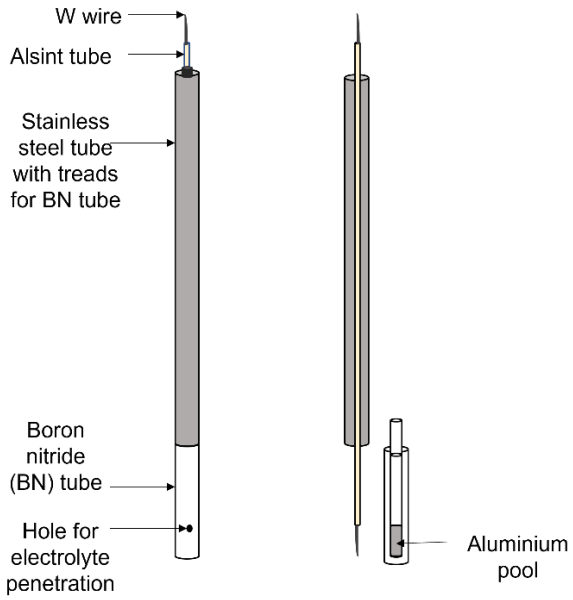

Figure 3.8. The aluminium reference electrode.

3.2 Electrolyte composition

Bath composition in aluminium industry can be divided into[6]:

1. Traditional baths, 3-7% AlF_3
2. Modified baths, 2-4% AlF_3, LiF, MgF_2
3. Low-ratio baths, 8-14% AlF_3.

Common bath composition is 1.5-6 % Al_2O_3, 4-8% CaF_2, 8-13% AlF_3. The rest is cryolite. The bath temperature is usually 950-980 °C. The bath density is 2.05 g/ cm^2 and depends on temperature and composition. The density of the metal at 950 °C is approx. 2.3 g/cm^2 [7]. It is not recommended to add too much of the CaF_2 because it could increase the density of the bath. All additives (except KF) lower the solubility of alumina.

The following empirical equation could be used for the calculation of the liquidus temperature [8]:

$$\begin{aligned} t = {} & 1011 + 0.14(\text{mas\%}AlF_3) - 0.071(\text{mass}AlF_3)^{2.5} + 0.0051(AlF_3)^3 \\ & - 10(\text{mass\%}LiF_3) + 0.736(\text{mass\%LiF})^{1.3} \\ & + 0.063((\text{mass\%}AlF_3)(\text{massLiF}))^{1.1} - 3.19(\text{mass\%}CaF_2) \\ & + 0.03(\text{mass\%}CaF_2)^2 + 0.27((\text{mass}AlF_3)(\text{mass}CaF_2))^{0.7} \\ & - 12.2(\text{mass\%}Al_2O_3) + 4.75(\text{mass}Al_2O_3)^{1.2} \end{aligned} \quad (3.1)$$

For the typical additions of the additives, the equation (3.1) agrees reasonably with the literature data [9]. Typically, the bath temperature is 5-15 °C above the liquidus temperature.

Bath composition used in present work can not fit in above mentioned classification. For the electrochemical and gas measurements (Chapter 4 and 5) the bath was synthetic cryolite (purity ≥ 97%) with addition of Al_2O_3 to obtain concentration of 2 wt% for general understanding of the pure cryolite melt. No other additives were used. Cryolite ratio was 3. According to equation (3.1), the calculated liquidus temperature is 997.5 °C. The actual working temperatures were 1005°C (in Chapter 4) and 1010 °C (in Chapter 5) making theoretical superheat around 7 °C.

For the experiments in the see-through cell (Chapter 6-9) it was crucial to reduce the liquidus temperature and with it to increase the service time of the quartz crucible. With the pure synthetic cryolite

(liquidus temperature 1005 °C), the service time of the quartz crucible was short that it was not practical to perform experiments. Additives AlF_3 and CaF_2 were introduced together with the LiF. In addition of reducing temperature, it was observed that LiF also helped to reduce the fumes inside the furnace and, with that, improved total visibility. The bath composition was synthetic cryolite with excess of AlF_3 equal to 24 wt% and Al_2O_3 concentration of 3 wt% with additions of 15 wt% LiF and 5 wt% CaF_2. Cryolite ratio was 1.85. The calculated liquidus temperature was 838 °C. Experiments were performed at a temperature of 890 ± 10 °C. The crucible lifetime was maximum 5-6 hours including the heating process which took minimum 2 hours. The quartz crucible normally broke down due to formation of holes in the quartz wall at the bath meniscus. A superheat of ~ 50 °C was on purpose kept this large in order to avoid bath freeze due to frequent openings of the furnace side lids.
The bath was contained in the graphite crucible (Schunk Tokai Scandinavia AB, Sweden) for the electrochemical measurements in Chapter 4, in the silicon-nitride crucible (Morgan Advanced Material, Technical Ceramics, UK) for the electrochemical and gas measurements in Chapter 5, and in the quartz crucible (fabricated "in-house", Glass Workshop NTNU) for the experiments in Chapter 6-9. These experimental setups are the next to be introduced.

3.3 Furnace setups and cell designs

3.3.1 Furnace setup with graphite crucible

In Figure 3.9 is shown picture of the furnace and a drawing of the experimental setup inside the furnace. The cryolite bath was contained in the graphite crucible. Alumina discs made of Alsint were used for the bottom and top construction as thermal radiation shield. Furnace was flushed all the time from heating till cooling with N_2 to obtain inert atmosphere. The working temperature was around 1005 °C. This setup was used to perform electrochemical measurements to study bubbles on different anode designs (Chapter 4). The thermocouple type S was used to measure the temperature during the experiment. Type S thermocouple is made of one Pt wire and one Pt 90%/Rh 10% wire. Thermocouple type S

was produced “in house” and is shown in Figure 3.10. Pt and Pt 90%-Rh 10% wires were threaded into Alsint two-bore tube and the wires were joined at one end by welding. This was placed in Alsint tube closed end. The two-bore tube made wires not coming in contact with each other. The thermocouple has two ends; one end is attached to the voltmeter (multimeter) which is cold junctions and other end is placed at exact position where temperature is to be measured, hot junction. Thermocouple was connected to Isotech Trio 885 that compensates for the reference temperature and Keithley 2000 Multimeter. The monitored temperature values were displayed in the main window of the software.

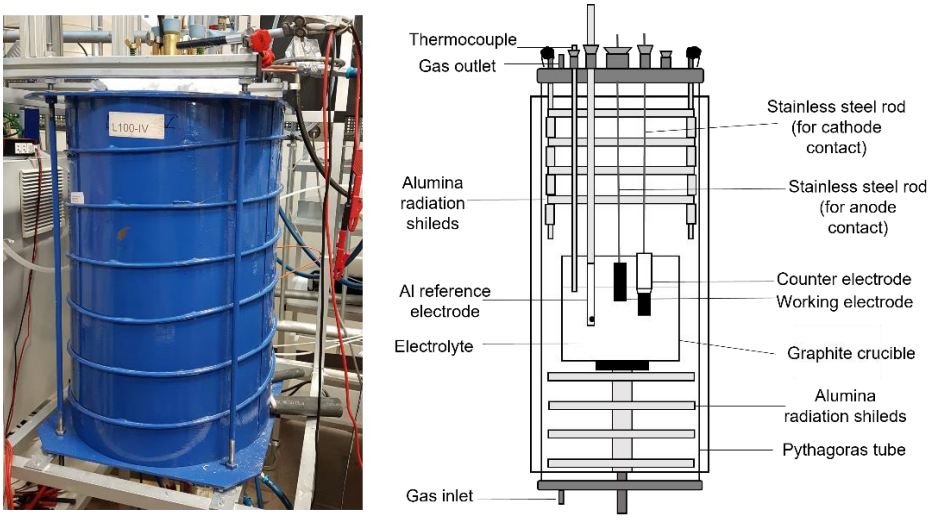

Figure 3.9. Furnace setup with graphite crucible.

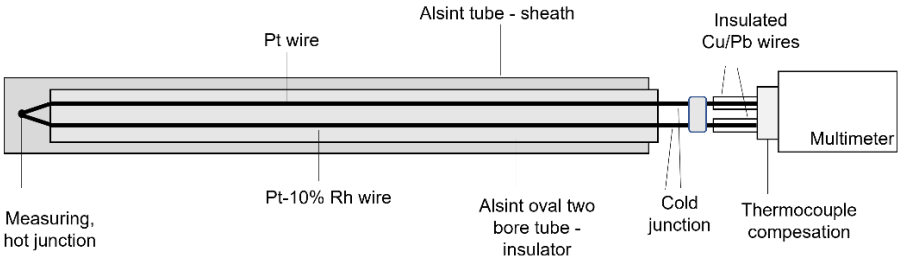

Figure 3.10. Thermocouple type-S.

3.3.2 Furnace setups for gas measurements

In Figure 3.11 is shown the furnace setup used for the gas measurements in Chapter 5. This setup was similar to the previous setup with a difference that all carbon parts were replaced with the non-carbon parts (except the electrodes). The setup was designed to minimize reaction between CO_2 and the carbon. Instead of the graphite crucible, non-graphite crucible made of high-temperature ceramic materials, silicon nitride Si_3N_4 (Morgan Advanced Materials), was used. The anode and cathode were physically separated in order to prevent anodic and cathodic products to react (back reaction). Hence, the smaller silicon-nitride crucible was placed into the big crucible as a cathode compartment preventing the transport of dissolved aluminium metal to the anode. Three holes were drilled above the immersed graphite part to make a contact. The lid with holes was placed at the top of the crucible and the gas was collected above the bath surface near the anode. Thermocouple type S was placed inside to measure the temperature during the experiment. Working temperature was around 1010 °C.

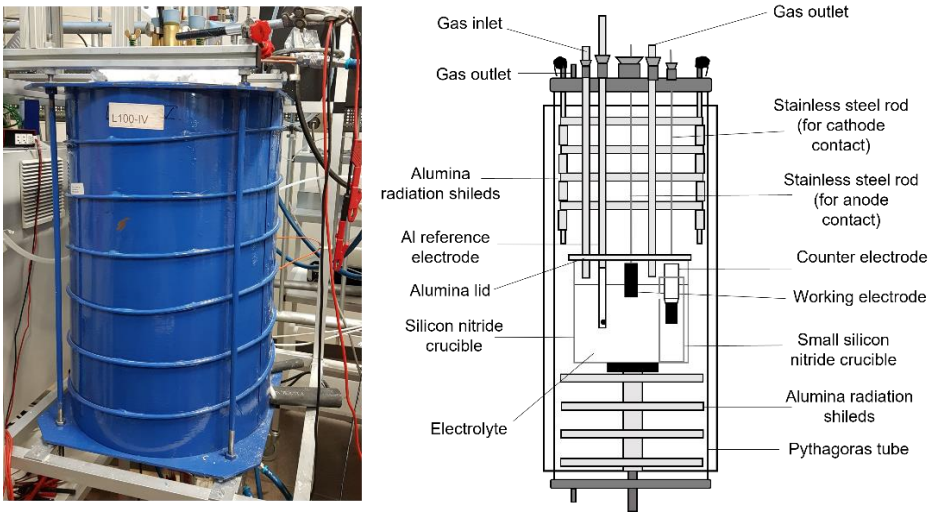

Figure 3.11. Furnace and cell setup for gas measurements.

In Figure 3.12 is shown setup for the gas measurements using the hollow gas anode. The graphite crucible was used as a counter electrode. The nitrogen was flushed through the cell from the bottom to ensure that the furnace is kept under an inert atmosphere. The nitrogen gas was not in

the contact with the anode gas. The force for driving the anode gas out of the cell was the overpressure made by the produced gas, *i.e.,* no carrier gas was used. Thermocouple type S was used to measure the temperature during the experiment. Working temperature was around 1005 °C.

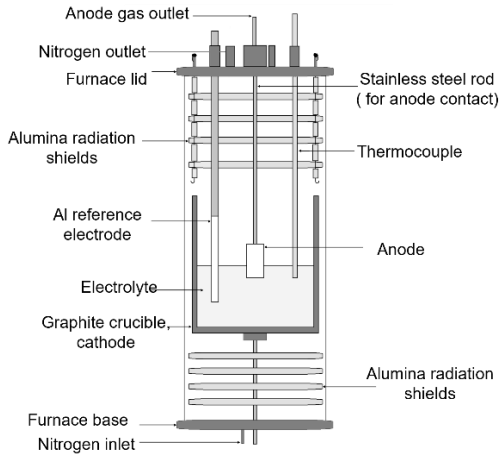

Figure 3.12. Setup for gas measurements using hollow gas anode.

3.3.3 See-through furnace and cell design

The see-through furnace is shown in Figure 3.13(a). In Figure 3.13(b) is shown a principal sketch of the experimental setup. Video recording was performed from the side. The furnace has two side openings which are closed with lids. The lids are removed and replaced with quartz windows only during video recording in order to reduce heat loss. The quartz crucible was resting at an alumina tower construction which was used to adjust the height level of the crucible. The alumina tower was placed in a ceramic crucible whose function was to catch the bath in case of crucible breakage during the experiment. Experiments were performed in a cryolite bath at a temperature of 890 ± 10 °C. The superheat was ~ 50 °C and on purpose kept large in order to avoid bath freeze due to frequent openings of the furnace side lids and to prolong the video recording time. The bath was contained in the quartz crucible with a wall thickness of 2 mm. The crucible lifetime was maximum of 5-6 h, including the heating process, which took minimum of 2 h. The quartz crucible normally broke down due to formation of holes in the quartz wall at the bath meniscus.

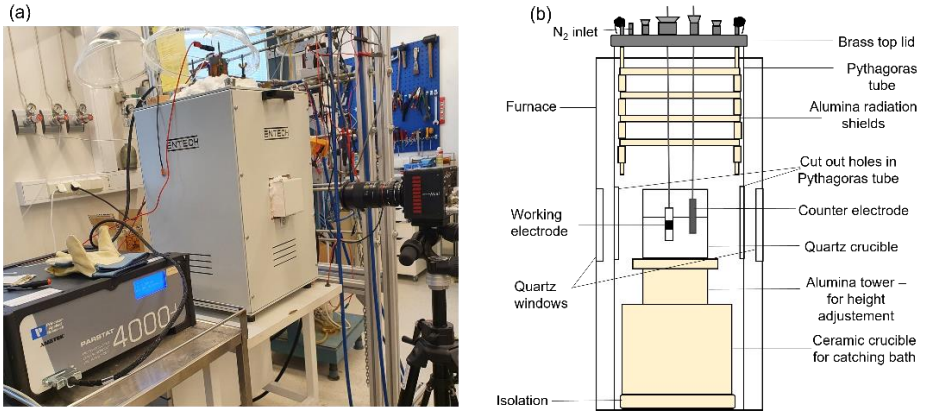

Figure 3.13. (a) See-through furnace and experimental cell setup, (b) principal sketch of the interior of the furnace.

3.4 Methodology

3.4.1 Electrochemical cell principle

Three-electrode cell consists of a working electrode (WE), a counter electrode (CE) and a reference electrode (RE), Figure 3.14. The WE is the electrode to be study. The CE is the other electrode where current passes but it only serves to complete the electrical circuit. The RE is an electrode with stable and known electrochemical potential. The purpose of three-electrode cell is to be able to measure or control the potential of the working electrode. In present work the three-electrode cell was used during the first electrochemical characterization of bubble evolution (Chapter 4) and for gas measurements (Chapter 5). The potentiostat besides WE, CE and RE has working sense electrode (WSE) which was connected to a WE. The WSE measures the potential at the working electrode without any current flowing meaning no-IR drop occurs in the WSE. In Figure 3.15 is shown principal sketch of the three-electrode cell

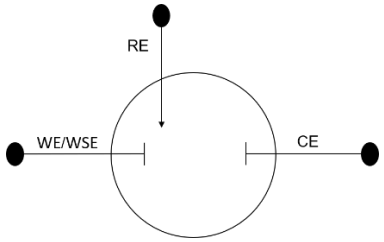

Figure 3.14. Principle diagram of the three-electrode cell.

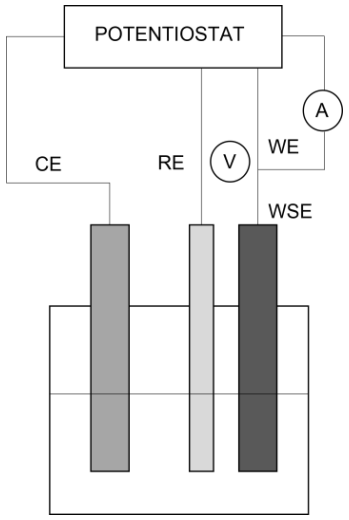

Figure 3.15. Principal sketch of the three-electrode cell.

For the experiments in the see-through cell (Chapters 6-9) to get better visibility of the bubbles a two-electrode cell was used. It was chosen not to use the RE due to several reasons: taking up the space, causing excess reflections and existence of the non-electrochemical bubbles on the BN surface. The principal sketch of the two-electrode cell is shown in Figure 3.16.

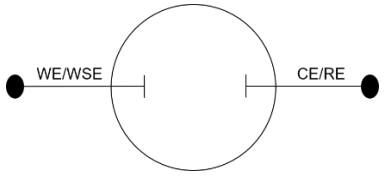

Figure 3.16. Principal diagram of the two-electrode cell.

3.4.2 Linear sweep voltammetry and polarization curves

Linear sweep voltammetry (LSV) is a method in which the current at a working electrode is measured while the potential between the working electrode and a reference electrode is swept linearly with time. The scan rate is defined as the rate of change of potential as a function of time. Linear sweep voltammetry in this work was used to obtained polarization curves and to provoke anode effect.

Polarization curves can be obtained in different ways [10]: (a) constant resistance discharge, measured by connecting different resistors and determining the resulting currents and potentials; (b) potentiodynamic polarization, in which current is measured at a slow potential scan rate; (c) galvanostatic discharge, in which current is maintained constant and the resulting potentials are measured; and (d) potentiostatic discharge, in which the potential is maintained constant and the resulting currents are measured.

The polarization curves in electrochemical measurements in Chapter 4 were obtained with potentiodynamic polarization by using the linear voltammetry method at a low scan rate of 5 mV s^{-1}. In Figure 3.17 is shown comparison of the linear sweep voltammogram at 5 mV s^{-1} and polarization curves points obtained potentiostatically. It can be seen that the voltammogram followed E-I relation as the polarization curve, except the bubble noise visible in the voltammogram. For the horizontal and vertical anodes, it can be seen deviation at the higher current densities. This could be explained by anode consummation that affected the bubbles retention time (explained in gas measurements in Chapter 5). It can be stated that the sweep rate of 5 mV s^{-1} was sufficiently low to obtain polarization curve.

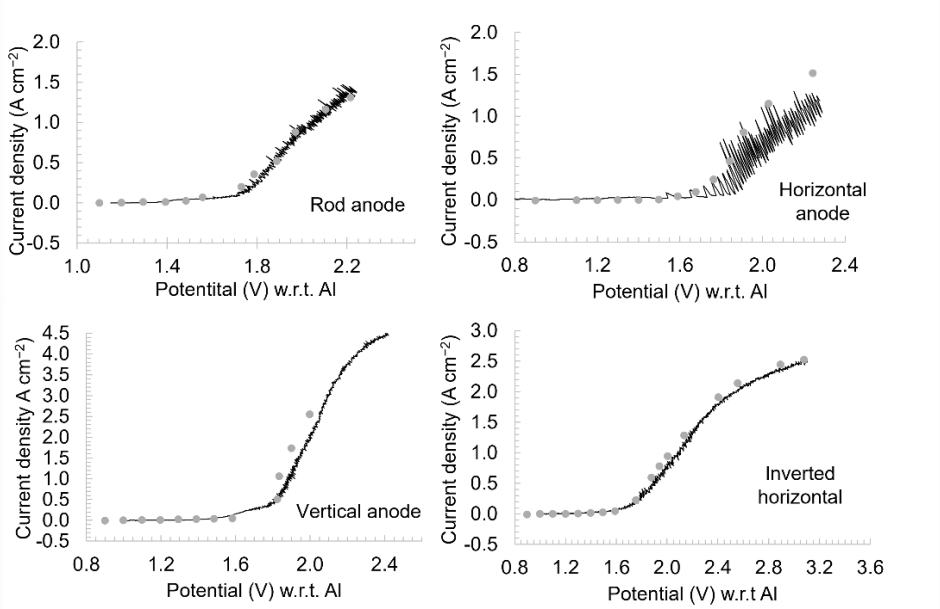

Figure 3.17. Comparison of the data of linear sweep voltammetry at 5 mV s^{-1} (black line) and polarization curves points obtained potentiostatically (gray points) for different anode designs.

3.4.3 Constant current and constant voltage measurements

Constant current and constant voltage measurements were conducted by applying the chronopotentiometry and chronoamperometry procedures in VersaStudio, respectively. VersaStudio is the software used to control the PARSTAT 4000+ potentiostat. Chronopotentiometry and chronoamperometry techniques were generally not used in this work to obtain current/potential gradients which together with the proper analysis (*e.g.* Cottrell equation) would give kinetic data. They were used as general-purpose techniques to run electrochemical measurements. Constant current measurements were most used. Constant voltage measurements were used when voltage overloading of the instrument (compliance voltage) occurred due to bubble blockage of especially the small horizontal anode surface.

Fast Fourier Transform (FFT) spectrum analysis of potential-time and current-time was done using "Sigview v4.3-spectrum and signal

analysis" software and gave a dominant frequency which was discussed in a term of bubble release frequency.

3.4.4 Electrochemical impedance spectroscopy

Electrochemical impedance spectroscopy (EIS) is a highly sensitive characterization technique used to establish the electrical response of chemical systems.

The impedance is a complex number and can be expressed.

$$Z = \frac{E(t)}{I(t)} = \frac{|E|\ \sin(\omega t)}{|I|\sin(\omega t\ +\ \emptyset)} =\ |Z|\frac{\sin(\omega t)}{\sin(\omega t\ +\ \emptyset)} =\ |Z|(\cos\emptyset\ +\ i\ \sin\emptyset) \tag{3.2}$$

The expression (3.2) may be separated into a real part, $Z_{Re}=|Z|\cos\emptyset$ and imaginary part, $Z_{Im}=|Z|i\sin\emptyset$. The data can be presented in a variety of ways, *e.g.* real and imaginary impedance components are plotted against one another in Nyquist plots, charge transfer resistances and Warburg impedance as well as time constants, whereas in Bode plots, the impedance and phase angle is plotted against frequency which can be helpful to find capacitive or inductive effects of electrochemical systems [11].

Electrochemical impedance spectroscopy in present work was used to determine the ohmic resistance at open circuit potential (OCP) between the working and reference electrode.

A current passing through electrolyte will always induce potential drop (IR). The potential drop will depend on the applied current and the resistance of the electrolyte between the electrodes. IR distortion could be reduced when RE is placed close to the WE. The IR-compensation of the measured potential is [12]:

$$\Delta E = \Delta V\ -\ IR_{el} \tag{3.3}$$

EIS was used to find the ohmic drop at open circuit potential (OCP), between the working and the reference electrode, including the electrode itself and the connections.

In Figure 3.18 is shown an illustration of a Nyquist plot, where $-Z_{Im}$ versus Z_{Re} is plotted for a simple charge transfer reaction. The Nyquist Plot for a simplified Randles cell is always a semicircle. The electrolyte

resistance, R_{el}, can be extracted from the real axis value at the high frequency intercept as illustrated.

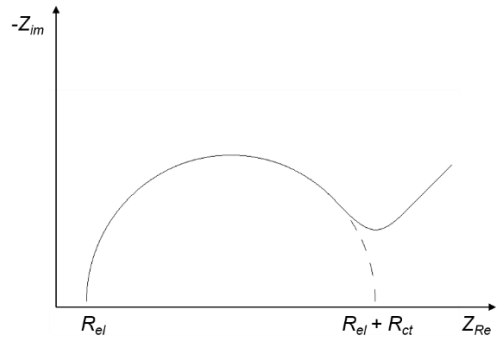

Figure 3.18. Nyquist plot (Z_{im} against Z_{re}) illustrating how the ohmic resistance, R_{el}, is determent by EIS.

In Figure 3.19 is shown a Nyquist plot ($-Z_{Im}$ as a function of Z_{Re}) from the electrochemical impedance spectroscopy measurements from the electrochemical measurements in Chapter 4 for the rod anode, horizontal, vertical, and inverted horizontal anode at open circuit potential. The indicated intersection with the real Z_{Re}-axis gives the electrolytic resistance R_{el}, used to IR-compensate the measured potential. The R_{el} obtained this way is a rough estimation that might cause some errors. Any voltage drop due to resistance introduced by bubbles and overvoltage has not been compensated. The IR compensation was deliberate partial since the main focus in this work was on the voltage drop due to the resistance introduced by bubbles produced during electrolysis.

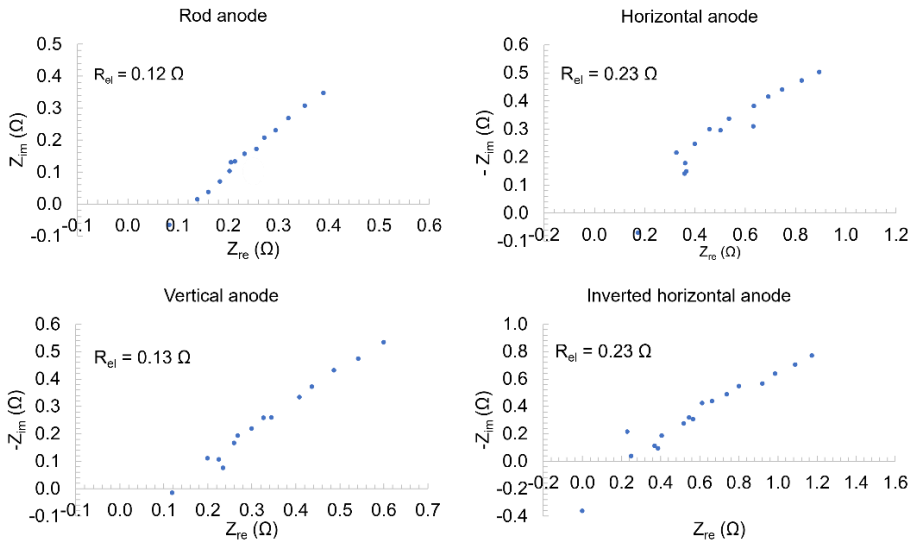

Figure 3.19. Nyquist plot at open circuit potential (OCP) with the determined R_{el} for different anode designs.

3.5 Instrumentation

3.5.1 Potentiostat

All electrochemical experiments were performed using PARSTAT 4000+ potentiostat, Figure 3.20(a). The potentiostat was connected to a KEPCO bipolar operational power supply amplifier with a current limit 20 A, shown in Figure 3.20(b). It was used for all experiments due to current normally exceeding the limit of the potentiostat.

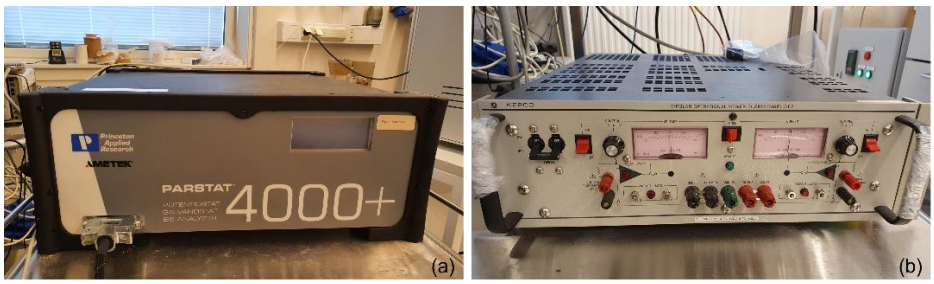

Figure 3.20. (a) PARSTAT 4000+ potentiostat and (b) KEPCO current booster.

3.5.2 Gas analyzer and calibration

Gas analysis of the off-gas was performed with Servomex Xendos 2550 Multicomponent Infrared, Figure 3.21, which reported potential values proportional to the concentration, vol%, of CO and CO_2. The analyzer also contained a display giving real time values of the concentration of CO and CO_2 in vol%.

Figure 3.21. Servomex Xendos 2550-gas analyzer.

The gas analyzer was calibrated before each experiment with N_2 gas for zero calibration and with 10%CO-20%CO_2/N_2 gas for span calibration. Nitrogen was flushed through the instrument for 20-30 minutes before zero calibration, to make sure that only nitrogen is present in the system. Zero calibration of the analyzer was then performed. After zero calibration, the gas mixture 10%CO-20%CO_2/N_2 was flushed through the instrument till the values at the display is stabilized, around 15 min, and span calibration was performed. From this data, calibration curves were constructed for each of the gas species (CO and CO_2), giving the relation between the output voltage and the gas concentration given in vol% percent. In Figure 3.22 is shown one of examples of CO_2 and CO calibration curves obtained for gas measurements (Chapter 5). The calibration curve obtained was later used to calculate the actual concentration during the gas measurements. The instrument gave a voltage reading every 5 s.

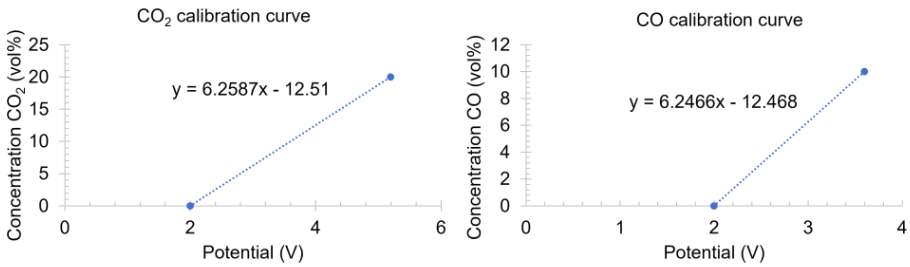

Figure 3.22. Example of CO_2 and CO calibration curve.

3.5.3 Video recording in the see-through cell

The Photron FASTCAM Mini AX50 is an advanced high-speed camera that delivers 1-megapixel image resolution (1024 x 1024 pixels) at frame rates up to 2 000 fps. The camera was used for a video recording and observation of different processes Figure 3.23(a). The camera was positioned 40 cm of the right side of the furnace opening, Figure 3.23(b). A camera lens of 20 mm was used. A circular polarizer filter was used to reduce reflections and glare by filtering out light that became polarized from a non-metallic surface, to benefit desirable imagery.
Photron Fastcam Viewer 4 (PFV4) software was used for controlling the Photron high-speed camera, for data saving, and for image processing.

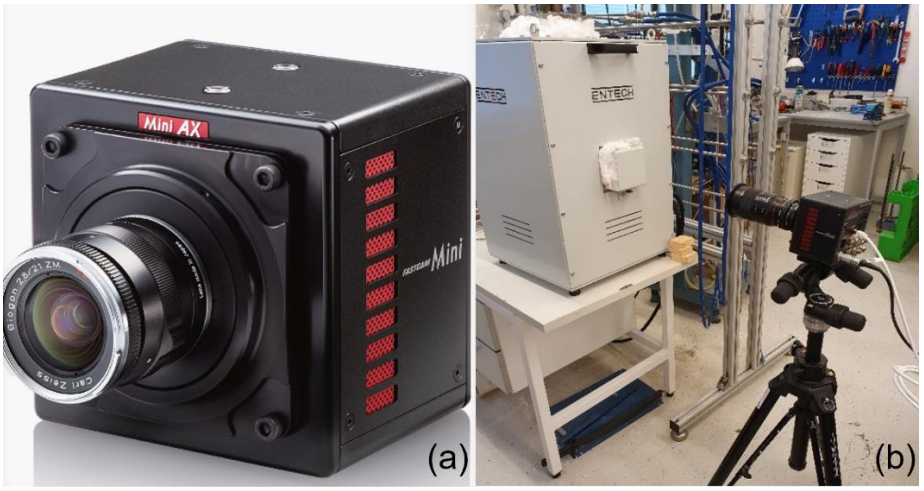

Figure 3.23 (a) Fastcam Mini AX camera used for recording. The picture was adapted from the Photron official Web Page [13], (b) camera position during experiment.

3.5.4 X-ray diffraction (XRD)

X-ray diffraction is a very useful techniques to nondestructively study carbon materials. It is employed to study the phase composition of samples, to analyze the qualitative and quantitative composition of specific phases, and to assess the structural characteristics of carbon materials. Samples are pulverized to homogeneous powder prior to XRD analysis. The individual crystalline phases are then identified with help of the International Centre for Diffraction Data (ICDD) database.

X-ray diffraction analysis was performed using a D8 A25 DaVinci X-ray Diffractometer with CuKα radiation at room temperature, Figure 3.24. To perform analysis, graphite and industrial carbon were grounded to powder (< 250 μm) and the powder was poured into a sample holder (5 mm deep, and 40 mm diameter). The scans were recorded in the 2θ range between 5°-90° with a scanning step of 0.02° and accumulation time of 2 s. X-ray diffraction pattern of graphite and industrial carbon was obtained and results were discussed in Chapter 7.

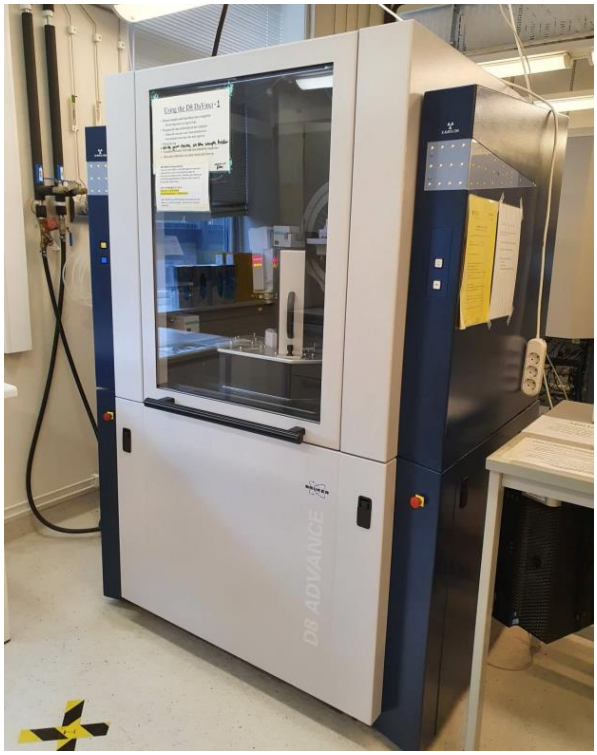

Figure 3.24. Bruker D8 A25 DaVinci X-ray Diffractometer with CuKα radiation.

3.5.5 Micro X-ray computed tomography (CT)

Micro-CT is a non-destructive 3D imaging technique utilizing X-rays revealing the internal structure of material, slice by slice. CT was used to investigate the structure and heterogeneity of the carbon materials. CT technique can represent the information visually at high resolution. Scanners capture a series of 2D planar X-ray images and reconstruct the data into 2D cross-sectional slices which further can be processed into 3D models. X-rays are generated in an X-ray source, transmitted through the sample, and recorded by the X-ray detector as a 2D projection image. The sample is then rotated and another X-ray projection image is taken. This step is repeated through a 180-degree or 360-degree turn. The series of X-ray projection images is then computed into cross-sectional images through the computational process called "reconstruction". Micro-CT resolution is of one micron.

CT was performed with a model Zeiss Metrotom 1500. For the scan, the X-ray tube was set for 90 kV and 200 μA. The number of projection (Np) was 2050 (0.176 ° per projection). Around ~ 20 mm of the length of the sample was scanned. The basic unit in the CT image is the volume element, voxel (volumetric pixel). The CT image is composed of many voxels, depending on resolution and properties of the scanner, which are displayed as a 2D image array of picture elements (pixels).

References

1. Thorne, R.J., C. Sommerseth, A.P. Ratvik, S. Rorvik, E. Sandnes, L.P. Lossius, H. Linga, and A. Svensson, *Bubble Evolution and Anode Surface Properties in Aluminium Electrolysis.* J. Electrochem. Soc., 2015. **162**(8): p. E104-E114.
2. Thorne, R.J., C. Sommerseth, A.M. Svensson, E. Sandnes, L.P. Lossius, H. Linga, and A.P. Ratvik, *Understanding Anode Overpotential*, in *Light Metals 2014*, J. Grandfield, Editor. 2014, John Wiley & Sons, Inc.: Hoboken, NJ. p. 1213-1217.
3. Thorne, R.J., C. Sommerseth, E. Sandnes, O. Kjos, T.A. Aarhaug, L.P. Lossius, H. Linga, and A.P. Ratvik, *Electrochemical Characterization of Carbon Anode Perfomance*, in *Light Metals 2013*, B. Sadler, Editor. 2013, Springer. p. 1207-1211.
4. Kjos, O.S., T.A. Aarhaug, E. Skybakmoen, A. Solheim, and H. Gudbrandsen. *Fundamental Studies of Perfluorocarbon Formation*. in *10th Australasian Aluminium Smelting Technology Conference*. 2011. Launceston, Tasmania.
5. Sommerseth, C., *The effect of production parameters on the performance of carbon anodes for aluminium production*. 2016, Norwegian University of

Science and Technology, Department of Materials Science and Engineering: Trondheim.
6. Grjotheim, K., H. Kvande, and B.J. Welch, *Low-melting Baths in Aluminium Electrolysis*, in *Light metals 1986*, W.S. Peterson and R.E. Miller, Editors. 1986, Metallurgical Society: Warrendale, Pa. p. 417-423.
7. Leitner, M., T. Leitner, A. Schmon, K. Aziz, and G. Pottlacher, *Thermophysical Properties of Liquid Aluminum.* Metallurgical and Materials Transactions A, 2017. **48**(6): p. 3036-3045.
8. Grjotheim, K. and H. Kvande, *Introduction to aluminium electrolysis : understanding the Hall-Héroult process*. 2nd ed. 1993, Düsseldorf: Aluminium-Verlag.
9. Haupin, W., *The Liquidus Enigma*, in *Light metals 1992* E.R. Cutshall, Editor. 1991, Minerals, Metals & Materials Society: Warrendale, Pa. p. 477-480.
10. Webb, C. and M.R. Kosseva, *Food Industry Wastes: Assessment and Recuperation of Commodities*. 2013, US: Academic Press: US. p. 242-243.
11. Randviir, E.P. and C.E. Banks, *Electrochemical impedance spectroscopy: an overview of bioanalytical applications.* Analytical Methods, 2013. **5**(5): p. 1098-1115.
12. Pletcher, D., *A first course in electrode processes*. 2nd ed. 2009, Cambridge: RSC Publ.
13. Photron. *Photron - Ultra High-Speed Cameras*. Available from: https://photron.com/fastcam-mini-ax/.

Chapter 4

Bubble evolution on different carbon anode designs in cryolite melt

Nikolina Stanic [1], Ana Maria Martinez [2] and Espen Sandnes [3]
[1, 3] Department of Materials Science and Engineering, Norwegian University of Science and Technology NTNU, NO-7491 Trondheim, Norway;
[2] SINTEF Industry, 7034 Trondheim, Norway

Results were presented at *7th Baltic Electrochemistry Conference: Finding New Inspiration* (BEChem 2018), November 4-7, 2018, Tartu, Estonia.
This paper has been published in Metallurgical and Materials Transactions B 2020 [1]. Some minor corrections have been made to this paper post-publication for spelling/typos and to improve clarity.

Abstract
The anode potential has been shown to be highly dependent on anode geometry and orientation in the Hall–Héroult process. This work is an experimental laboratory scale study of the effect of anode geometry and orientation on bubble formation and detachment for four different anode designs: horizontal (surface facing downwards), inverted horizontal (surface facing upwards), vertical, rod (with both vertical and horizontal surface). From polarization curves, it was found that the vertical anode and the inverted horizontal anode operated at lowest potentials. Above 1 A cm^{-2}, the vertical anode showed the lowest potential. As the current increases, the transition towards smaller noise is pronounced for the horizontal anode and to some degree for the vertical anode and inverted horizontal anode. Fast Fourier Transform (FFT) analysis of the chronoamperometric data gave a dominant frequency only for the

horizontal anode and the rod anode. The bubble release time corresponded well with the dominant frequency for the rod anode for all current densities and for the horizontal anode at lower current densities. Only random bubble noise was found for the vertical and the inverted horizontal anode and is probably due to a bubble-induced convection effectively removing the bubbles.

Keywords: aluminium electrolysis, cryolite, graphite anodes, carbon consumption.

4.1 Introduction

The anode reaction in the Hall–Héroult process is complicated because it involves discharge of oxide present in oxyfluoride complex ions, among others $Al_2OF_6^{2-}$ and $Al_2O_2F_4^{2-}$, presumably adsorption of oxygen at the carbon anode and a following thermal or electrochemical desorption [2, 3]. The electrolysis takes place in cryolite melt ($3NaF\text{-}AlF_3$) with dissolved alumina but discharge of fluoride ions does not take place during normal electrolysis since this potential is higher than the discharge potential of the oxyfluoride complexes. The overall reaction can be one or both of the following:

$$2Al_2O_3(l) + 3C(s) \rightarrow 4Al(l) + 3CO_2(g) \qquad E^0 = -1.16\ V \tag{4.1}$$

$$Al_2O_3(l) + 3C \rightarrow 2Al(l) + 3CO(g) \qquad E^0 = -1.02\ V \tag{4.2}$$

The cathode product is liquid aluminum, and the anode product is a CO_2/CO gas mixture. As a result, carbon anodes are consumed. The main primary anode product is CO_2 (g), but some CO can be formed at low current densities 0.05-0.1 A cm^{-2} [4].

Several mechanisms are proposed for the anode reaction. Picard *et al.* [5] studied reaction (4.1) using electrochemical impedance and proposed the following three-step mechanism at low current densities and low overpotentials:

1. Diffusion of the oxyfluoroaluminate species from the bulk of the melt to the surface of the graphite anode:

$$AlOF_x^{1-x}\ (\text{bath}) \rightarrow\ AlOF_x^{1-x}\ (\text{electrode})$$

2. Dissociation of the oxyfluoroaluminate species and adsorption of the oxide ions, followed by their discharge and the formation of the adsorbed carbon-oxygen species:

$$AlOF_x^{1-x} + C\ \rightarrow\ CO_{ads} +\ AlF_x^{3-x} +\ 2e^-$$

3. Dissociation of the oxyfluoroaluminate species and the adsorption of the oxide ions, their discharge in the presence of the CO_{ads} and the desorption of the gaseous carbon dioxide CO_2:

$$AlFO_x^{1-x} +\ CO_{ads}\ \rightarrow\ CO_{2\,(g)}\ +\ AlF_x^{3-x} +\ 2e^-$$

A similar mechanism with the electrochemical desorption step was also proposed by Kisza *et al.* [6]. Thonstad [4] also proposed an electrochemical adsorption followed by a thermal desorption step involving a combination of two CO_{ads} species.

The most important reaction responsible for the loss in current efficiency in the aluminum electrolysis is the back reaction between dissolved CO_2 and dissolved Al and Na in the melt. The sodium is created through the reaction between aluminium and sodium fluoride at cathode/electrolyte interface. The back reaction can be written [7, 8]:

$$2Al(\text{diss.}) +\ 3CO_2(\text{diss.})\ \rightarrow\ Al_2O_3(\text{diss.}) +\ 3CO(g) \tag{4.3}$$

The CO content in the anode off gas can arise from the electrochemical reaction directly, from the back reaction and also from the Boudouard reaction:

$$CO_2\ +\ C\ =\ CO \tag{4.4}$$

The carbon can come from the anode itself or carbon dust in the melt. At 950-1000 °C, the equilibrium is displaced far to the right.

Spherical gas bubbles have been found in laboratory experiments to initially be generated on the downward facing anode surface and released in a cyclic pattern [9]. Zhao *et al.* [10] studied anodic bubble behavior in a

laboratory scale transparent aluminum electrolysis cell using a cylindrical anode shielded by an alumina tube giving only a horizontal downward facing active area. Individual bubbles were observed which grew to a certain size and coalesced to form larger bubbles. The bubbles expanded and almost covered the full bottom surface. The bubbles then slid towards the edge of the anode and were released from the anode bottom. Cassayre *et al.* [11] also studied bubble formation in a transparent cell and found that periodic gas bubble release occurred. Bubble nucleation occurred at specific spots. On the downward facing horizontal part of the anode, bubbles come into contact with each other and coalesce first into large individual bubbles and then further coalesce into a single bubble covering a bigger area. When the bubble layer reaches the anode edge, the gas bubble rises rapidly because of buoyancy. Bubble coalescence was also observed on vertical anode surface.

Gas present at the anode surface contributes to an increase cell voltage as the current lines between the anode and cathode become prolonged. This is also in the literature referred to as a bubble overvoltage. In addition, charge transfer and concentration overvoltage contribute to total cell voltage. The bubbles can be responsible for as much as 10 % of the total cell voltage, which gives a significant contribution to the energy consumption [12]. Reducing energy consumption in aluminum electrolysis is of major importance for production cost savings and for reduction of greenhouse gas emissions.

Hyperpolarization is by definition a voltage component at gas evolving electrodes due to the masking of the electrode by bubbles, *i.e.,* active surface area is reduced by a bubble covering part of the electrode surface. This causes areas with higher local current density than the calculated current density based on the geometric area. The increased current density causes increased charge transfer overvoltage. Hyperpolarization causes increase in concentration overvoltage [13]. The extra voltage drop due to bubbles is about 0.15-0.35 V out of a typical total cell voltage of ~ 4.5 V [10]. The additional voltage increase due to bubbles has been shown to be highly dependent on anode geometry and orientation.

The aim of the present work was to study bubble behavior of different laboratory scale anode designs. The anodes used in this paper are typically used to study reaction kinetics and mass transport, anode effect phenomena, current efficiency, anode quality properties, *etc*. It is therefore

interesting to study bubble dynamics of these anodes in more detail because bubble dynamics are relevant for all the above-mentioned features. Four anode designs were made: horizontal anode (with a downward-facing surface), vertical anode, rod anode (having both a vertical and horizontal surface) and inverted horizontal anode (with an upward-facing surface). The first three anode designs have been reported in earlier papers [13, 14]. The inverted horizontal anode, not previously reported, was constructed to have a horizontal surface which has faster bubble release in comparison to a downward facing horizontal anode where bubbles cannot be released easily due to the buoyancy alone. The measurements included bubble induced current and potential oscillations.

4.2 Experimental part

4.2.1 Anode design and furnace setup

Four electrode designs were used to investigate the impact of electrode geometry and orientation on anode reaction in aluminum electrolysis. The electrodes were constructed as shown in Figure 4.1. As a counter electrode was used a graphite rod shielded with the boron nitride which gave a surface area of 10.2 cm^2. The carbon crucible could have been used as a counter electrode but the shielded rod design was needed for later gas measurements in the same experimental setup. Risking having an uneven current distribution on the anode the bubble behavior and polarization curves of the horizontal and the vertical anodes were compared with the work of Thorne *et al*. [13, 14]. The comparison showed very similar bubble behavior and potential-current values for the polarization curves. It was therefore concluded that the chosen electrode configuration could be used. A purified graphite material (Schunk Tokai Scandinavia AB, Sweden) was the active electrode material. In Figure 4.1(a) is shown the horizontal anode design. A graphite rod and a stainless-steel rod were threaded together and the sides of the graphite were shielded using boron nitride in order to expose only the horizontal surface when anode is immersed in the melt. The horizontal anode was made as described in [13] with the differences that boron nitride edges were cut off by an angle of 45 degrees in order to provide easier bubble detachment. The rod anode in Figure 4.1(b) has mixed geometry, *i.e.,* horizontal and

vertical surfaces. The rod anode was made as described in [15]. The anode was immersed 10 mm in the melt, which gave it a geometric surface area of approx. 3.9 cm^2. The vertical anode design in Figure 4.1(c) had a defined surface area by using boron nitride shielding and it was made as described in [14]. The inverted horizontal design in Figure 4.1(d) is an anode design that has not been previously reported. Holes for the graphite and the stainless-steel rod were drilled in the boron nitride. Electrical contact between graphite and stainless steel was obtained by making threaded connection. The electrical contact was further improved by adding graphite dust in the threads. A horizontal cut of the graphite rod was made which gave the anode surface area the shape of a horizontal ellipse with an area of 0.69 cm^2.

There are large differences in the area between the anode designs. However, more important for comparison of bubble behavior of each anode design is the dimensional length of the electrode, *e.g.,* the diameter of the horizontal anode and rod anode was 10 mm, the immersion dept of the rod was 10 mm and the diameters for the inverted horizontal anode were d_1 = 11 mm and d_2 = 8 mm. The height for the vertical anode was only 5 mm but still considered to be comparable to the other anodes as the bubbles on the vertical surface have been reported to be relatively small and this design was earlier successfully used [14, 16]. Experiments were performed under inert N_2-atmosphere in a cryolite melt. The cryolite was supplied from Sigma Aldrich (purity ≥ 97%, cryolite ratio = 3). The alumina concentration was 2 wt% (Merck). The temperature was 1005 °C. The melt was contained in a graphite crucible (Schunk Tokai Scandinavia AB, Sweden). The aluminum reference electrode was fabricated according to [17]. The schematic setup of the cell is shown in Figure 4.2.

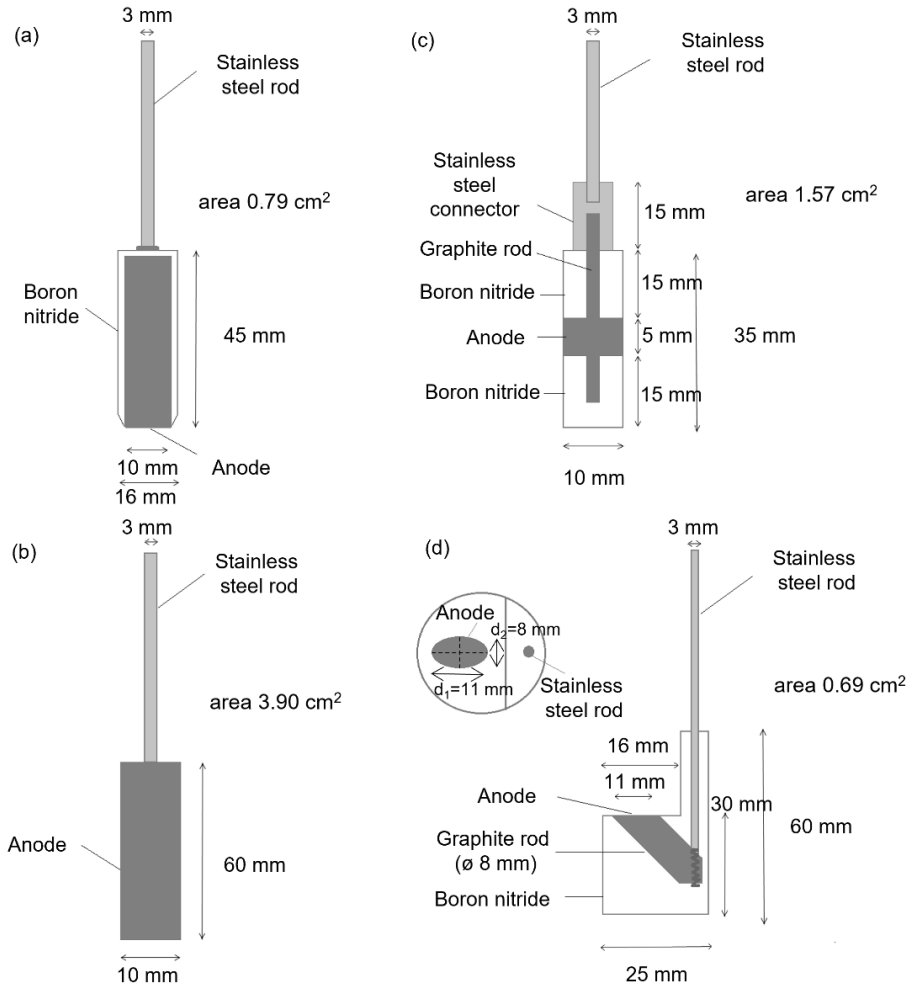

Figure 4.1. Different anode designs: (a) horizontal anode, (b) rod anode, (c) vertical anode, (d) inverted horizontal anode (inset shows electrode seen from above).

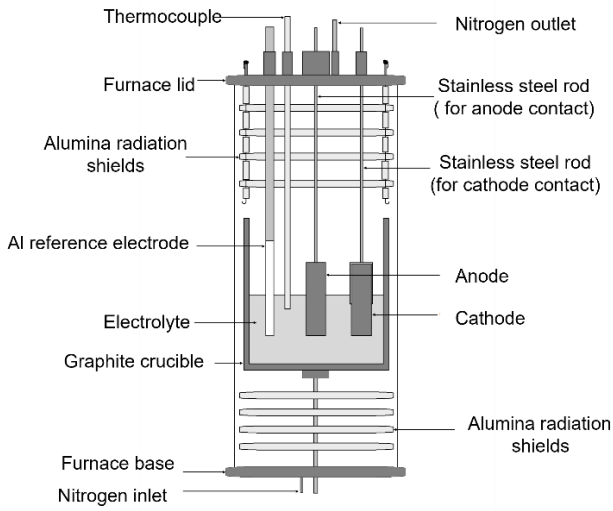

Figure 4.2. The cell setup.

4.2.2 Experimental methods

Electrochemical Impedance Spectroscopy (EIS) was used to determine the ohmic resistance at Open Circuit Potential (OCP). This value was used to IR compensate all electrochemical measurements. This means that any voltage drop due to resistance introduced by bubbles and overvoltage has not been compensated. This partial IR compensation is deliberate because the intention was to study the effect of anode design on bubbles. The potential of the working electrode (anode) was measured with respect to an aluminum reference electrode. Linear Sweep Voltammetry (LSV) was performed sweeping from OCP and up to 2.6 V at a sweep rate of 5 mV s^{-1}. The effect of anode geometry on bubble behavior was also studied by using chronopotentiometric measurements with current densities in the range 0.1-1.0 A cm^{-2}. Potential *vs.* time measurements were transformed into frequency spectra by using a Fast Fourier Transform algorithm in Matlab. The signals were transformed into the frequency domain to evaluate how the power of the signal is distributed over a range of frequencies. The frequency spectrum is a simple way of showing the total amplitude at each frequency. The highest frequency that can be represented is one-half the sampling frequency, called the Nyquist

frequency. The sampling rate (Fs) was 5 Hz when applied current density was lower than 0.5 A cm^{-2}, and 10 Hz for applied current density > 0.5 A cm^{-2}, consequently the spectrum has a frequency range from zero to Fs/2, 0-2.5 Hz and 0-5 Hz respectively. Dominant frequency is considered the frequency where FFT peak with the maximum magnitude of the signal is observed. All electrochemical measurements were carried out using a PARSTAT (Princeton Applied Research) potentiostat and a 20 A booster (KEPCO).

4.3 Results and discussion

In Figure 4.3 polarization curves for different anode designs are presented. The polarization curves are actually obtained by using the LSV method. It was checked that a sweep rate of 5 mV s^{-1} was sufficiently low to permit steady state, meaning the voltammogram followed the same E-I relation as a stationary polarization curve, except the bubble noise visible in the voltammogram. Thorne *et al.* [14] presented voltammograms which were recorded at even higher sweep rate, 100 mV s^{-1}, and claimed these curves to also give steady state. Starting from OCP the first increase in current in Figure 4.3 is observed at 1.4 V for all anode designs. The current increase was due to CO_2/CO gas evolution [15]. After initiation of gas evolution, the current for the different anode designs started to differ. The curves in Figure 4.3 all show varying degree of current oscillations. These oscillations arise from growth, coalescence and detachment of bubbles and are also referred to as bubble noise. The polarization curve for the horizontal anode is shown separately in Figure 4.3(b). Due to the large amount of bubble noise for this anode the polarization curve shown in Figure 4.3(a) has been smoothed for easier comparison. Bubble behavior is influenced by wetting of the anode by the melt. Good wetting (*i.e.,* small wetting angle) implies low coverage and easier movement of the bubbles on the anode surface. The wetting angle is decreasing with increasing polarization/current density until anode effect occurs and varies in level somehow with the carbon anode material [18]. Since the same graphite material is used for all anodes in the present work it is assumed that comparison of the anode performance at similar potential/current density values is meaningful.

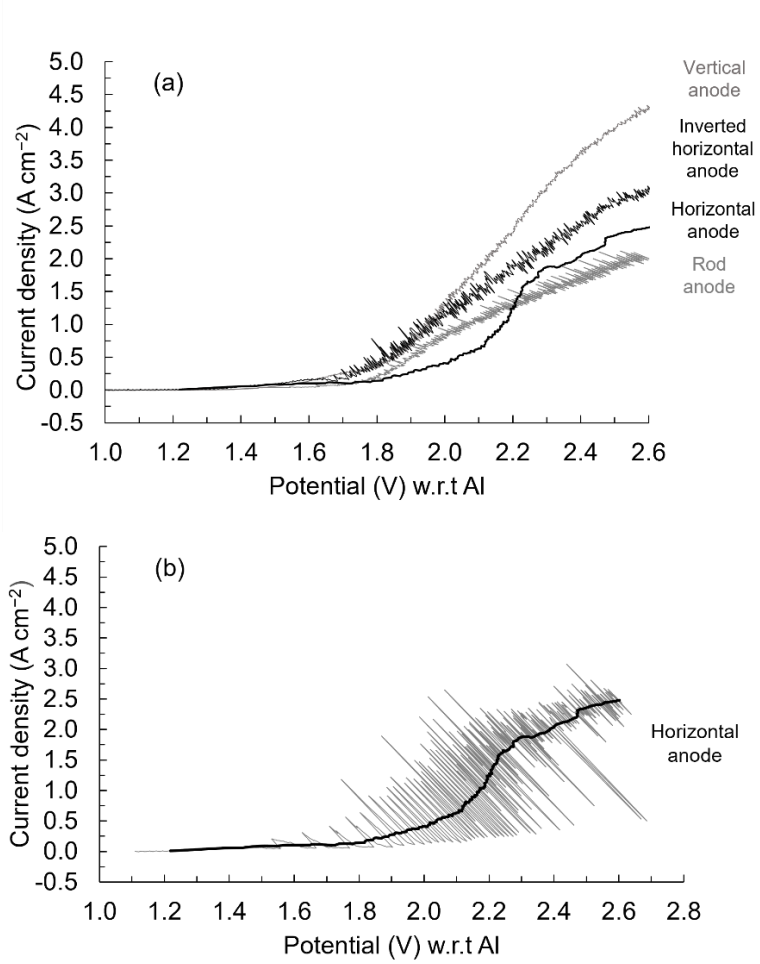

Figure 4.3. Polarization curves for rod, vertical, inverted horizontal and horizontal anode. Polarization curves are IR-compensated with the values of ohmic resistance at OCP. (a) All anode designs plotted together for comparison. The polarization curve of the horizontal anode is smoothed using the moving average method (100 points) for easier comparison. (b) The actual polarization curve together with the smoothed curve.

The current oscillation for the horizontal anode is the largest among the anodes, while the current oscillation for the vertical anode is the smallest. Figure 4.4 shows current oscillations for the polarization curves in Figure 4.3 normalized around the smoothed average for easier comparison of the noise. At lower potentials the current density of the horizontal anode is low, meaning the bubbles are forming slowly. As the bubble detaches there is a sudden increase in the current. This periodic

behavior causes the characteristic saw-tooth shape of the polarization curve. The saw tooth shape is visible up to 2.1 V. Above 2.3 V more stochastic behavior is pronounced rather than periodic indicating nucleation and growth on more sites. Between 2.1 V and 2.3 V a transition from periodic behavior to stochastic behavior occurs. This transition is caused by bubble induced convection promoting easier bubble release resulting in a decrease in the bubble noise. In the same potential range, it is also observed a faster increase in current. This improvement in the performance of the horizontal anode is also linked to the improved bubble induced convection.

The polarization curve of the vertical anode (Figure 4.3 and Figure 4.4) shows a similar noise trend compared to the horizontal polarization curve, meaning there is an increase in the noise up to around 2.1 V followed by a small decrease in the noise. The bubble noise is significantly smaller than for the horizontal anode. This could be due to the evolution of smaller bubbles from the vertical surface, caused both by the buoyancy force making a detachment easier as well as the induced convection regime being more efficient for bubble detachment compared to the horizontal anode.

The mixed geometry of the rod anode suggests the polarization curve to follow the same noise trend as the combination of the horizontal and the vertical anode. However, the polarization curve gets noisier with increasing potential without going through a transition towards smaller noise. The polarization curve in Figure 4.3 shows that at similar potential the current density is 2-3 times higher for the vertical than for the horizontal anode. This indicates that the current density of the vertical part and the horizontal part of the rod anode has a similar relation. The rod was immersed 10 mm giving a ratio between the vertical and the horizontal area of the rod of approx. 4. There is an uncertainty regarding current density of the rod anode arising from the uncertainty in immersion depth of the rod. However, within reasonable error, the major fraction of the current is taken up by the vertical surface. This should make the bubble noise of the rod anode to more resemble the noise of the vertical anode than the horizontal anode. However, at the same time the bubble noise contribution from the horizontal part is expected to be large based on the noise seen for the horizontal anode. The bubble noise for the rod anode is slightly larger compared to the vertical and considerably smaller compared to the horizontal anode. The clear transition seen for the horizontal anode is not observed for the rod anode as the current density of the horizontal

part of the rod anode never reaches a current density as high as the current density for where the transition for the horizontal anode was observed. It was unexpected that the rod anode operated at the higher potentials than the horizontal anode as most of the current is taken up by the vertical part. As the rod anode is positioned at the melt surface, the bubble induced convection at higher current density is less efficient since bubbles escape the electrode at the melt surface into the furnace atmosphere. This escape does not contribute to any bubble induced convection. Thonstad reported critical current densities on graphite anodes for different alumina concentrations [19]. Comparing the current densities obtained in the present work with Thonstad's work it seems that the current densities for all anodes are approaching the limiting current densities at the highest potential. The flattening out of all polarization curves at the highest potentials is caused by increased reaction overpotential in generals and increased gas coverage with hyperpolarization as a consequence. On the other hand, the better gas bubble induced convection is diminishing this effect by more effective transport of reactants towards the surface and reduced Nernst diffusion layer.

The polarization curve for the inverted horizontal anode has a high noise already from lower potentials (Figure 4.3 and Figure 4.4). The noise stays practically unchanged up to 2.3 V where it decreases slightly, but the transition to lower noise seen for the horizontal anode and the vertical anode is much less pronounced. The bubble noise is slightly larger than for the vertical anode. The current density at higher potentials is lower than compared to the vertical anode. The difference in bubble noise and current density is related to the ability of these two anodes to create bubble induced convection as discussed in relation to Figure 4.7

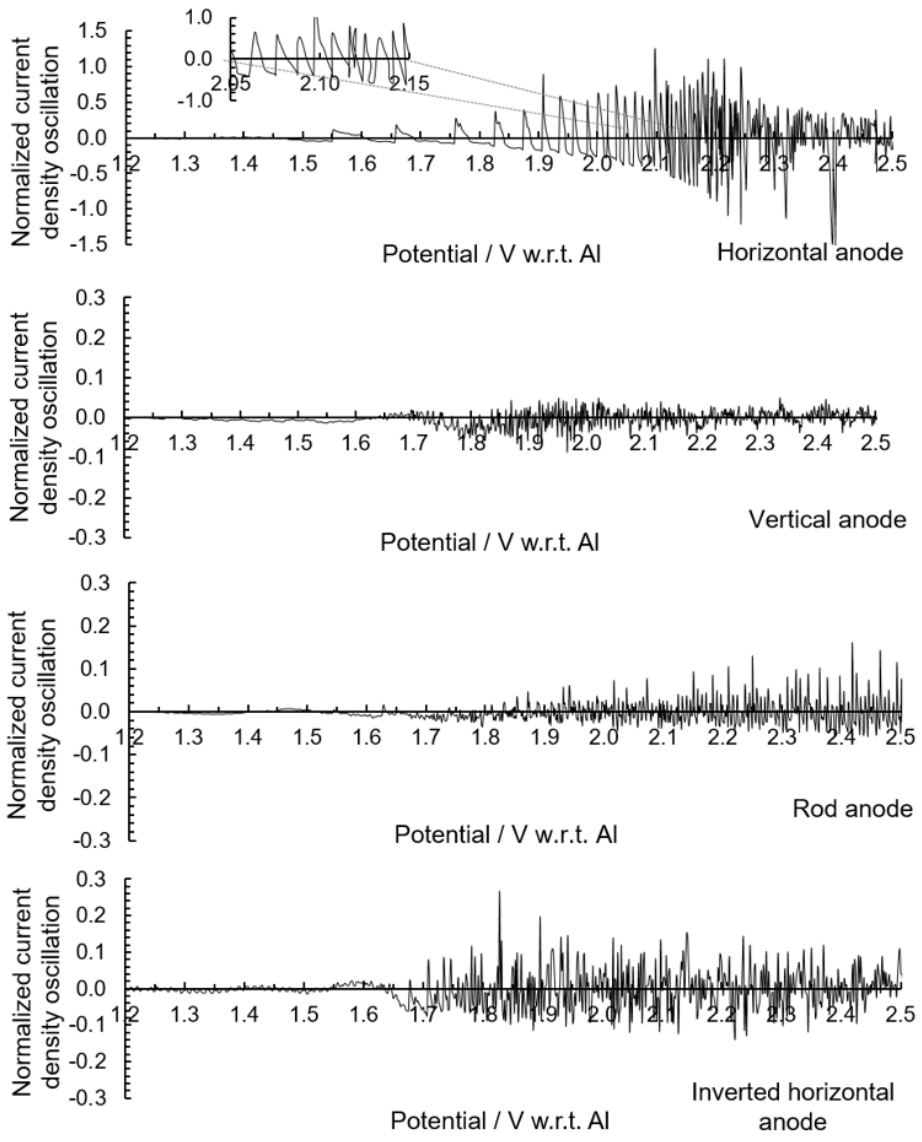

Figure 4.4. Data of current density oscillation for rod, vertical and inverted horizontal and horizontal anode, normalized around smoothed average. Data are IR-compensated with the value of the ohmic resistance at OCP.

Figure 4.5 represents potential-time characteristics of the different anode designs for constant geometric current densities. Potential oscillation is a function of applied current, the bubble size and the bubble coverage among others, all of which are interdependent. As a bubble grows

it covers more and more of the anode surface causing the potential to increase as the local current density increases. When the bubble detaches, the local current density decreases and consequently the potential decreases [20]. Zhang *et al.* [21] have combined use of physical and numerical modelling and have found that the bubble size influences the bubble-induced potential drop and local current distribution. The bubble-induced resistance increases as the bubble size increases. For large bubbles, the current needs to travel longer distance to bypass the bubbles leading to higher potential drop. In addition, hyperpolarization increases with increasing bubble surface coverage. As bubbles are formed, the potential increased due to combination of increase in ohmic resistance and hyperpolarization due to a decrease in effective surface area [13]. The current oscillation for different anode designs has been qualitatively described in relation to the data in Figure 4.3. Much of the same reasoning can be applied to the potential-time characteristics shown in Figure 4.5.

Figure 4.6 shows the potential oscillations under galvanostatic control (at 0.5 A cm^{-2}) for the horizontal anode. The figure is included to show the details of the characteristic saw-tooth curve. The bubble growth is characterized by an almost linear growth in potential and the sharp potential drop is due to bubble detachment. The linear growth is a superposition including potential oscillations also from smaller bubbles being formed, coalesced or detached during the development of the larger bubble. Xue and Øye [22] designed a transparent electrolysis cell to allow a single bubble to be formed underneath a horizontal anode and detached from the anode surface so that its life cycle could be observed. They concluded that the frequency with the largest amplitude is coupled with the detachment of the bubble. This process, *i.e.* bubble nucleation-growth-detachment, is pseudo-periodical [22].

The saw-tooth shape of the potential oscillation is by far most pronounced for the horizontal anode which keeps this feature up to 1 A cm^{-2}, Figure 4.5. The vertical anode shows stochastic and small potential oscillation without forming saw-tooth curve at higher current density, but at lower current densities (0.1 and 0.3 A cm^{-2}) saw-tooth features can be observed. The vertical anode has smallest bubble retention time in comparison to the horizontal anode. Thorne *et al.* [15, 16] reported similar trends. The inverted horizontal anode has similar behavior to the vertical anode at current densities > 0.5 A cm^{-2}, *i.e.,* random potential oscillation, and at lower current densities (0.1-0.3 A cm^{-2} for vertical and 0.1-0.5 A cm^{-2}

for inverted horizontal anode) saw-tooth features are present. However, inverted horizontal anode has larger noise as discussed below. Cassayre *et al.* observed [11, 23] that at higher current densities coalescence takes place to a smaller degree than at low current densities and the bubbles escape before covering the whole anode. The same authors also found that with increasing current density smaller bubbles formed and detached more frequently.

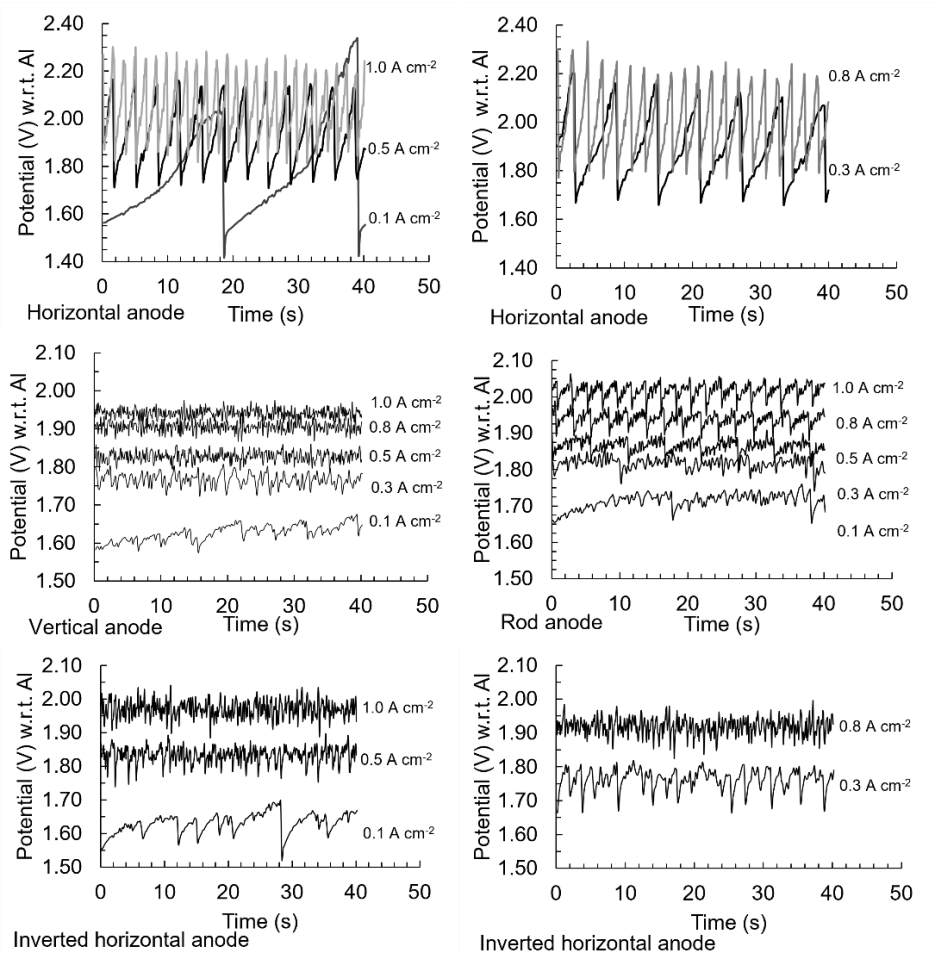

Figure 4.5. Measured anode potential *vs.* time during electrolysis at different current densities.

Zhao *et al*. [24] studied anodic bubble behavior in a laboratory scale transparent aluminum electrolysis cell and found that faster gas generation

rate at high current density causes more turbulence which may play significant role for the quick release of the bubbles from the surface. In the current work the lack of bubble coalescence due to faster bubble detachment could explain disappearance of the saw-tooth shaped potential oscillation for vertical and inverted horizontal anode with increasing current density. The presence of weak saw-tooth features for these anodes at low current densities can then be explained by bubble retention time large enough to allow some degree of coalescence and bubble growth. Saw-tooth features exist up to 0.5 A cm^{-2} for the inverted horizontal but not for the vertical anode.

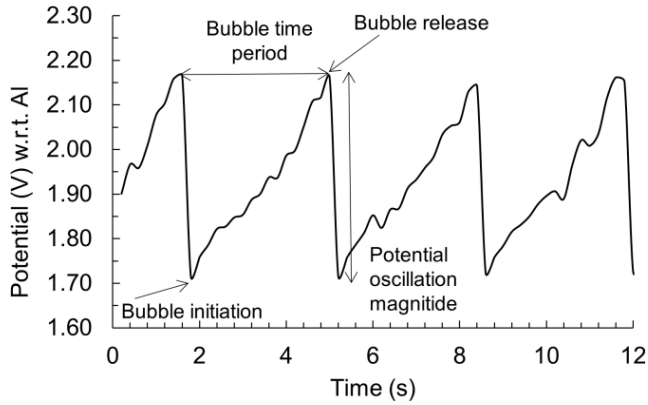

Figure 4.6. Details of the saw-tooth shaped potential *vs.* time curve for the horizontal anode at 0.5 A cm^{-2}.

Anode geometry plays a role as bubbles can be argued to be released more easily form a vertical than from a horizontal facing upward surface. In the case of the vertical anode there is a replacement of the bubble volume by bath coming from the side and from below, illustrated in Figure 4.7(a). Zhang *et al.* [25] established a Zn electrowinning model based on the Nernst-Plank equation and electrode gas evolution reaction kinetics. This model-calculated fluid flow field is comparable to the vertical anode in the present work. The model shows an upward fluid flow with the anode surface due to bubble induced convection arising from formation of oxygen bubbles. The flow direction is parallel to the anode surface and a large vortex is formed at the upper part of the cell. As bubbles rise to higher position the flow velocity typically increases because of bubble coalescence approaching the maximum value at the top of the cell. The anode height

was 15.5 cm. The 0.5 cm height of the vertical anode in the present work is small compared to Zhang *et al.* which indicates that difference in flow rate at the bottom and top of the vertical anode is insignificant. In the case of the inverted horizontal anode the bath flow parallel to the surface is likely to be smaller than for the vertical anode as the bubble volume is replaced by bath coming from the whole periphery of the electrode causing a decrease in the flow as the center of the electrode is reached, illustrated in Figure 4.7(b). In addition, the flow lines will have a vertical component. The upward flow along the vertical anode makes bubble detachment efficient after a certain bubble production rate has been obtained. This effect seemed to be pronounced at current densities larger than 0.3 A cm^{-2} as seen in Figure 4.5.

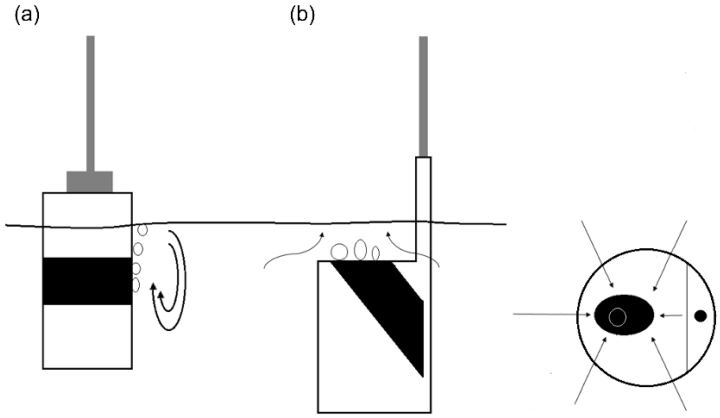

Figure 4.7. Bubble induced bath flow patterns close to electrode surface, (a) vertical design, (b) inverted horizontal design.

The rod anode exhibited potential oscillation magnitude between the horizontal and the vertical anode, something also observed by Thorne *et al.* [13]. Xue and Øye [22] also applied a rod anode but with an immersion dept of only 1 mm compared to 10 mm in the present work. This gave a saw-tooth shape not as pronounced as the horizontal anode but certainly more pronounced than the vertical anode. The relatively small noise of the rod anode suggests that the current density on the vertical part of the surface of the rod anode is higher than on the horizontal part of the surface.

Fast Fourier transform analysis (FFT) of the potential *vs.* time measurements for all anode design at different current densities is shown in Figure 4.8. A dominant FFT frequency was only observed for the

horizontal and the rod anode, for the rod anode in the frequency range 0.05-0.5 Hz and for the horizontal anode in the frequency range 0.05-1.3 Hz. This indicates a clear periodicity of the potential-time data in the case of the horizontal anode and the rod anode. The rod anode shows dominant frequencies due to the larger bubbles detaching from the horizontal part. The FFT dominant frequency corresponded well with bubble detachment time for the rod anode for all current densities (Table 4.1). For the horizontal anode the FFT dominant frequency corresponded well except at higher current densities, 0.8 and 1.0 A cm^{-2}, *i.e.* the dominant frequency became higher than expected based on the bubble detachment time. Einarsrud *et al.* [26] found a discrepancy between bubble detachment times and dominant FFT frequencies and attributed this to a lack of periodicity in the bubble noise signal, possibly due to overlapping bubbles. Looking at the potential-time curve for the horizontal anode (Figure 4.6) there is a small noise in the linear part of the saw-tooth curve which might be caused by coalescence and/or overlapping of the bubbles. Good correlation between FFT dominant frequency and bubble detachment time was also obtained by Thorne *et al.* [13] for a horizontal 8 mm diameter graphite anode. In the frequency spectrum for the vertical and inverted horizontal anode (Figure 4.8) there are several peaks, but none of them can be characterized as dominant. These peaks are related to smaller potential oscillations that can be due to the existence of many bubbles of different size, the growth and coalescence of bubbles or moving bubbles and their interaction on the surface [13, 27]. There is a lack of periodicity in the bubble noise signal and bubbles are probably detaching randomly from these surfaces in comparison with the rod and the horizontal anode.

In a laboratory cell where only, a few bubbles can exist simultaneously, the high frequency and the low amplitude in potential oscillations are associated with the nucleation of the individual bubbles, while the lower frequency and high amplitude are caused by detachment of the big, coalesced bubbles. This was also reported by Kiss *et al.* [27]. In Figure 4.8 it can be observed that the dominant peak for the horizontal anode occurs at lower frequency, $< \sim 1.0$ Hz, while some relative larger peak(s) for vertical and inverted horizontal anode occurs at higher frequency, > 1 Hz. It can also be seen that the vertical and the inverted horizontal anode in general give broader distribution of frequencies and lower amplitude meaning that smaller individual bubbles are released from the surface in comparison with the horizontal anode. Einarsrud *et al.* [26]

also found that higher frequencies are related to smaller amplitudes in potential oscillation in a laboratory cell.

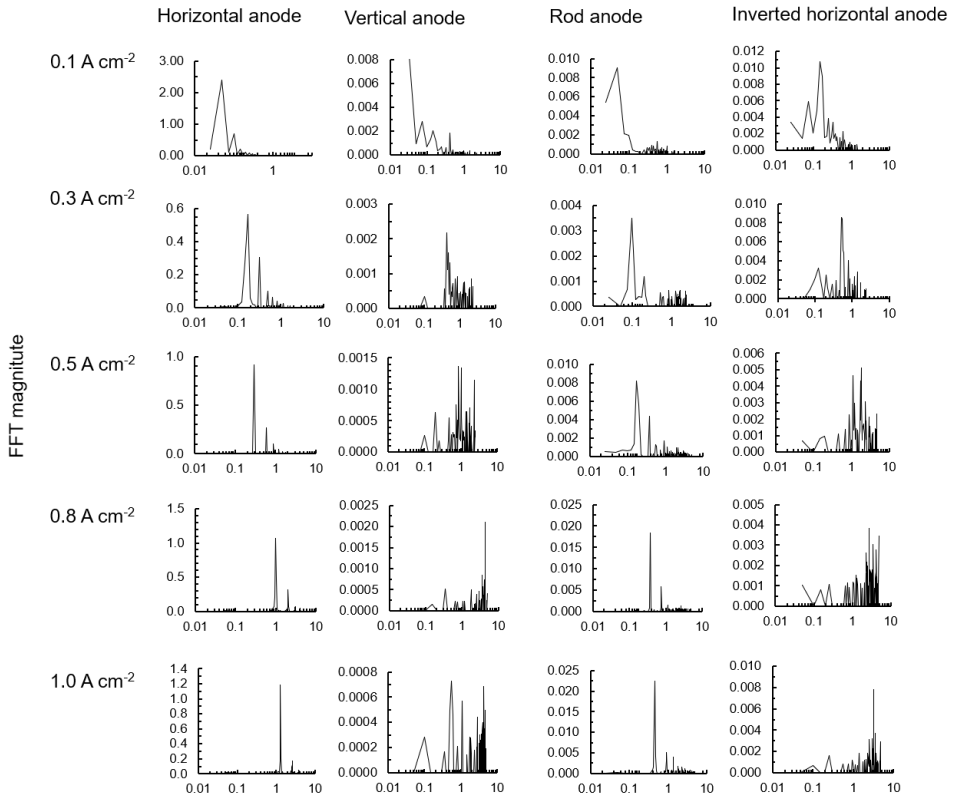

Figure 4.8. FFT spectra of the potential oscillations for rod, horizontal, vertical and inverted horizontal anode for different current densities.

Table 4.1. Bubble detachment time and dominant frequency for the rod and horizontal anode.

Rod anode				Horizontal anode			
Current density (A cm^{-2})	Bubble detachment time (s)	Expected frequency based on the bubble detachment time (Hz)	Dominant frequency (Hz)	Current density, (A cm^{-2})	Bubble detachment time (s)	Expected frequency based on the bubble detachment time (Hz)	Dominant frequency (Hz)
0.1	20	0.05	0.05	0.1	20	0.05	0.05
0.3	9.4	0.11	0.10	0.3	6.2	0.16	0.17
0.5	5.4	0.18	0.17	0.5	3.4	0.29	0.3
0.8	2.7	0.37	0.37	0.8	1.9	0.53	1.00
1.0	2.3	0.44	0.45	1.0	1.5	0.67	1.29

In Figure 4.9 are presented dominant frequency and amplitude for different current densities for the horizontal and the rod anode based on the FFT spectrum. The frequency and the amplitude of the potential oscillation are correlated with the nucleation, coalescence, growth and detachment of the bubbles. In general, both increased with increasing current density. Cooksey *et al.* [28] observed that this effect changed with increasing current density during experiment, *i.e.* frequency became more dependent on current density and amplitude became less dependent. No explanation for this change was suggested. In Figure 4.9 it can be observed that the dominant frequency increases with the increasing current density for both anodes, likely owning to bubbles being smaller at the time of detachment. The FFT magnitude for the horizontal and the rod anode decreases going from 0.1 A cm^{-2} to 0.3 A cm^{-2}, and after 0.3 A cm^{-2} slightly increases with the increasing current density. High value of the FFT magnitude at low current density can be explained by the large bubble retention time during which bubbles have enough time to coalesce and grow large. The long bubble retention time is also a result of a small bubble driven convection and not only low current density. With increasing current density, the bubble formation rate increases and consequently the bubble driven convection is enhanced. The FFT magnitude of the rod anode is significantly smaller than compared to the horizontal anode. This is due to the major fraction of the total current taken up by the vertical surface with the formation of smaller bubbles as discussed in relation to Figure 4.3 and Figure 4.4.

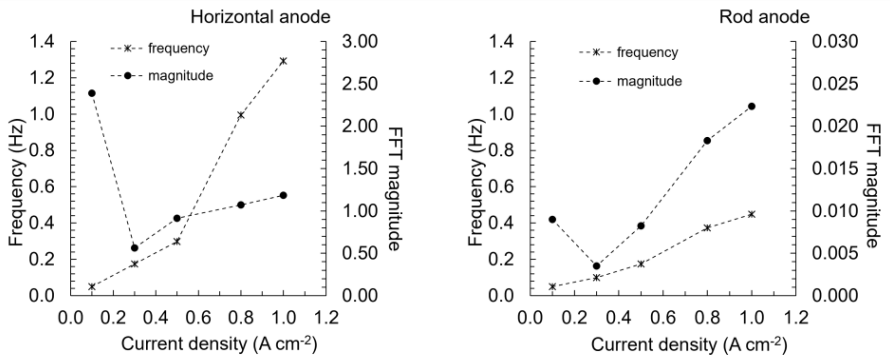

Figure 4.9. Dominant frequency and amplitude for the horizontal and the rod anode at different current densities: 0.1, 0.3, 0.5, 0.8 and 1.0 A cm^{-2}.

4.4 Conclusions

From the polarization curves of the four anode designs (horizontal, vertical, rod and inverted horizontal) the vertical anode and the inverted horizontal operated at lowest potentials. Above 1 A cm^{-2} the vertical anode showed the lowest potential, a result related to an easier bubble release from the vertical anode arising from a more effective bubble induced convection. As the current increases the transition towards smaller noise is pronounced for the horizontal anode and to some degree for the vertical anode and inverted horizontal anode. This transition is caused by increased bubble induced convection effectively removing the bubbles, the effect being relatively largest for the horizontal anode with a large increase in current, 0.5 A cm^{-2}-1.5 A cm^{-2}, going from 2.1 V-2.3 V, respectively. The improved performance of the horizontal anode in this current density range can be important considering current increase in industrial cells which today operate at approx. 0.9 A cm^{-2}, although the dimensions and geometry of the laboratory and industrial scale anodes are not directly comparable. FFT analysis of the chronopotentiometric data gave a dominant frequency only for the horizontal anode and the rod anode. The absence of a dominant frequency for the vertical and inverted horizontal anode indicates random bubble noise caused by effective bubble release. The bubble release time corresponded well with the dominant frequency for the rod anode for all current densities and for the horizontal anode at lower current densities.

References

1. Stanic, N., I. Jevremovic, A.M. Martinez, and E. Sandnes, *Bubble Evolution on Different Carbon Anode Designs in Cryolite Melt.* Metallurgical and Materials Transactions B, 2020. **51**(3): p. 1243-1253.
2. Lacassagne, V., C. Bessada, P. Florian, S. Bouvet, B. Ollivier, J.-P. Coutures, and D. Massiot, *Structure of high-temperature NaF-AlF (sub)3 -Al (sub)2 O (sub)3 melts: a multinuclear NMR study.* J. Phys. Chem. B, 2002. **106**(8): p. 1862.
3. Thonstad, J., P. Fellner, G.M. Haarberg, J. Híveš, H. Kvande, and Å. Sterten, *Aluminium electrolysis : fundamentals of the Hall-Héroult process*. 3rd ed. 2001, Düsseldorf: Aluminium-Verlag. 359.
4. Thonstad, J., *On the Anode Gas Reactions in Aluminum Electrolysis, II.* J. Electrochem. Soc., 1965. **111**(8): p. 959-965.

5. Picard, G.S., E.C. Prat, Y.J. Bertaud, and M.J. Leroy, *Evidencing the Electrochemical Mechanism at Carbon/Bath Interface by Means od Impedance Measurement: An Improved Approach to the Aluminium Reduction Process*, in *Light metals 1987* R.D. Zabreznik, Editor. 1987, Metallurgical Society: Warrendale. p. 507-517.
6. Kisza, A., J. Thonstad, and T. Eidet, *An impedance study of the kinetics and mechanism of the anodic reaction on graphite anodes in saturated cryolite-alumina melts.* J. Electrochem. Soc., 1996. **143**(6): p. 1840-1847.
7. Grjotheim, K. and H. Kvande, *Introduction to aluminium electrolysis : understanding the Hall-Héroult process*. 2nd ed. 1993, Düsseldorf: Aluminium-Verlag.
8. Thonstad, J., *On the Anode Gas Reactions in Aluminum Electrolysis.* J. Electrochem. Soc., 1965. **111**(8): p. 955-959.
9. Fortin, S., M. Gerhardt, and A.J. Gesing, *Physical Modeling of Bubble Behavior and Gas-release from Aluminium Reduction Cell Anodes*, in *Light metals 1984*, J.P. McGeer, Editor. 1984, Metallurgical Society of AIME: Warrendale. p. 721-741.
10. Zhao, Z., Z. Wang, B. Gao, Y. Feng, Z. Shi, and X. Hu, *Observation of Anodic Bubble Behavior Using Laboratory Scale Transparent Aluminium Electrolysis Cells*, in *Light Metals 2015*, M. Hyland, Editor. 2015, Springer: Cham. p. 801-806.
11. Cassayre, L., T. Utigard, and S. Bouvet, *Visualizing gas evolution on graphite and oxygen-evolving anodes.* JOM (USA), 2002. **54**(5): p. 41-45.
12. Einarsrud, K.E., S.T. Johansen, and I. Eick, *Anodic Bubble Behavior in Hall-Héroult Cells*, in *Light Metals 2012*, C.E. Suarez, Editor. 2012, John Wiley & Sons, Inc.: Hoboken, NJ. p. 875-880.
13. Thorne, R.J., C. Sommerseth, A.P. Ratvik, S. Rorvik, E. Sandnes, L.P. Lossius, H. Linga, and A. Svensson, *Bubble Evolution and Anode Surface Properties in Aluminium Electrolysis.* J. Electrochem. Soc., 2015. **162**(8): p. E104-E114.
14. Thorne, R.J., C. Sommerseth, A.M. Svensson, E. Sandnes, L.P. Lossius, H. Linga, and A.P. Ratvik, *Understanding Anode Overpotential*, in *Light Metals 2014*, J. Grandfield, Editor. 2014, John Wiley & Sons, Inc.: Hoboken, NJ. p. 1213-1217.
15. Thorne, R.J., C. Sommerseth, E. Sandnes, O. Kjos, T.A. Aarhaug, L.P. Lossius, H. Linga, and A.P. Ratvik, *Electrochemical Characterization of Carbon Anode Perfomance*, in *Light Metals 2013*, B. Sadler, Editor. 2013, Springer. p. 1207-1211.
16. Thorne, R.J., C. Sommerseth, A.P. Ratvik, S. Rorvik, E. Sandnes, L. Lossius, H. Linga, and A. Svensson, *Correlation between Coke Type, Microstructure and Anodic Reaction Overpotential in Aluminium Electrolysis.* J. Electrochem. Soc., 2015. **162**(12): p. E296-E306.
17. Kjos, O.S., T.A. Aarhaug, E. Skybakmoen, A. Solheim, and H. Gudbrandsen. *Fundamental Studies of Perfluorocarbon Formation*. in *10th Australasian Aluminium Smelting Technology Conference*. 2011. Launceston, Tasmania.
18. Eidsvaag, I.A., E. Sandnes, and H. Åsheim, *The Influence of Polarization on the Wetting of Anodes in the Hall-Héroult Process*. 2016, NTNU.
19. Thonstad, J., *Critical current densities in cryolite-alumina melts.* Electrochimica Acta, 1967. **12**(9): p. 1219-1226.

20. Einarsrud, K.E. and S.T. Johansen, *Modelling of bubble behavior in aluminium reduction cells.* Prog. Comput. Fluid Dyn., 2012. **12**(2-3): p. 119-130.
21. Zhang, K., Y. Feng, P. Witt, W. Yang, M. Cooksey, Z. Wang, and M. Schwarz, *A numerical assessment of bubble-induced electric resistance in aluminium electrolytic cells.* J. Appl. Electrochem., 2014. **44**(10): p. 1081-1092.
22. Xue, J. and H.A. Øye, *Bubble behaviour : cell voltage oscillation during aluminium electrolysis and the effects of sound and ultrasound*, in *Light Metals 1995*, J. Evans, Editor. 1995, TMS: Warrendale. p. 265-271.
23. Cassayre, L., G. Plascencia, T. Marin, S. Fan, and T. Utigard, *Gas Evolution on Graphite and Oxygen-Evolving Anodes During Aluminium Electrolysis*, in *Light Metals 2006*, T.J. Galloway, Editor. 2006, TMS: Warrendale. p. 379-383.
24. Zhao, Z., Z. Wang, B. Gao, Y. Feng, Z. Shi, and X. Hu, *Anodic Bubble Behavior and Voltage Drop in a Laboratory Transparent Aluminum Electrolytic Cell.* Metall. Mater. Trans. B, 2016. **47**(3): p. 1962-1975.
25. Zhang, Z., J.M. Werner, and M.L. Free, *Modeling zinc electrowinning for current efficiency prediction based on nernst-plank equation and electrode gas evolution reaction kinetics.* Journal of the Electrochemical Society, 2018. **165**(15): p. J3246-J3252.
26. Einarsrud, K.E. and E. Sandnes, *Anodic Voltage Oscillations in Hall-Heroult Cells*, in *Light Metals 2011*, S.J. Lindsay, Editor. 2011, Springer. p. 555-560.
27. Kiss, L.I. and S. Poncsak, *Effect of the Bubble growth Mechanism on the Spectrum of Voltage Fluctuations in the Reduction Cell*, in *Light metals 2002*, W.A. Schneider, Editor. 2002, TMS: Warrendale. p. 217-223.
28. Cooksey, M., M. Taylor, and J. Chen, *Resistance due to gas bubbles in aluminum reduction cells.* JOM (TMS), 2008. **60**(2): p. 51-57.

Chapter 5

CO and CO_2 anode gas concentration at lower current densities in a cryolite melt

Nikolina Stanic [1], Embla Tharaldsen Bø [2] and Espen Sandnes [3]
[1, 3] Department of Materials Science and Engineering, Norwegian University of Science and Technology NTNU, NO-7491 Trondheim, Norway;
[2] SINTEF Helgeland AS, 8622 Mo I Rana, Norway

This paper has been published in Metals MDPI 2020 [1]. Some minor corrections have been made to this paper post-publication for spelling/typos and to improve clarity.

Abstract
This work aims to study the CO-CO_2 gas composition at low potentials and low current densities in cryolite melt with relatively low alumina content (≤ 2 wt%). There is a scarcity of data in the literature in the low current density region and also for bath low in alumina. The experimental setup was constructed to minimize the back reaction as well as the Boudouard reaction. For potentials up to 1.55 V and corresponding current densities up to 0.07 A cm^{-2} it was found that CO is dominant product. Between 1.55 V and 1.65 V (corresponding current density region 0.07 A cm^{-2} to 0.2 A cm^{-2}) CO_2 becomes the dominant gas product. These potential values are probably slightly large due to suspected Boudouard reaction between CO_2 and carbon particles in the melt formed by disintegration of the graphite

anode. The results are discussed in the relation with the literature data and thermodynamic calculations.

Keywords: aluminium electrolysis, graphite anodes, CO-CO_2 gas analysis, carbon consumption.

5.1 Introduction

The electrochemical anode gas product in industrial aluminium electrolysis is CO_2, but also some CO is produced electrochemically. The amount of the electrochemically produced CO is difficult to determine since there are several chemical reactions where CO_2 is converted to CO. The electrochemically produced compounds are termed as primary products and chemically produced compounds are termed as secondary products.

The anode gas from the industrial cells contains considerable amount of CO where most of the CO is formed by back reaction between dissolved anodic and cathodic products, CO_2 (diss.) and Al (diss.), respectively. Aluminium mainly dissolves in the bath through reaction with sodium fluoride forming dissolved sodium, Na (diss.), and aluminium fluoride. The nature of the dissolved aluminium is still not completely resolved and in the industrial electrolyte composition sodium containing species are dominant. Sodium dissolves in the electrolyte in the form of free Na while dissolved aluminium is probably present as the monovalent species AlF_2^- which by anodic oxidation becomes AlF_4^-. A suggested back reaction takes the form [2]:

$$2\mathrm{Na(diss.)} + 3\mathrm{CO_2} + 2\mathrm{AlF_4^-} \rightarrow 2\mathrm{Na^+} + 3\mathrm{CO} + \mathrm{Al_2O_3} + 4\mathrm{F^-} \quad (5.1)$$

The current efficiency in the industry has improved over the years. For example, in terms of gas measurements, Thonstad reported in 1964 [3] that the industrial anode off-gas consist of CO_2 together with 30-50% of CO. Kimmerle and Noël observed in 1997 [4] 82% CO_2 and 17% CO in industrial anode off-gas. Aarhaug *et al.* reported in 2016 [5] 7700 ppm of CO_2 and 764 ppm CO in off-gas from primary aluminium production, that would correspond to around 9 % of CO and 91 % of CO_2.

Another possibility for forming CO is through the Boudouard reaction:

$$CO_2 + C = 2CO \tag{5.2}$$

CO_2 gas is reacting with solid carbon forming CO gas. In Figure 5.1 is shown equilibrium pressures of CO and CO_2 at a total pressure of 1 atm for reaction (5.2). Above 950 °C CO is the dominant product.

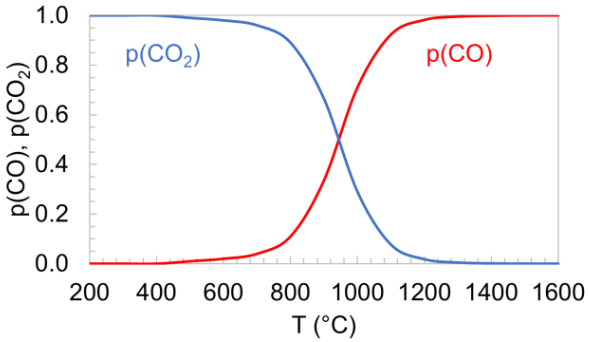

Figure 5.1. Temperature dependent equilibrium of the Boudouard reaction.

The carbon reacting in reaction (5.2) may be anode carbon or carbon particles floating in the bath formed by disintegration (dusting) of the carbon anodes during electrolysis. Reaction (5.2) most likely occurs on the melt surface where carbon particles are concentrated. Thonstad [6] studied the anode process during aluminium electrolysis in the laboratory scale cell. In that study reaction between CO_2 and carbon particles was studied by addition of carbon particles to the melt using a non-disintegrating anode. It was observed that CO_2 reacted with the carbon particles to form CO, reaction (5.2). The non-disintegrating anode, *i.e.,* a carbon anode made with some addition of chemicals that make the carbon anode less reactive, was used in order to test if CO_2 can react with the anode itself. For this experiment CO_2 was bubbled under the anode. It was found that CO_2 cannot react with the anode at normal current densities. It was concluded that the positive surface charge of the anode which is in contact with the bath is the reason for its non-reactivity to CO_2. Barrillon [7] found that the outer surface layer is more porous than the interior layer of the anode. Carbon atoms within such pores are non-polarized as they are not in contact with the bath. Although Thonstad found that CO_2 cannot react with the anode

itself, gas might penetrate into cracks and pores in the anode and Boudouard reaction can take place there.

Ouzilleau *et al.* [8] proposed an electrothermodynamic model for the carbon anode consumption of the prebaked carbon anodes in the aluminium electrolysis process for the prediction of CO_2-CO emission ratios. Their model predicts trends of some operating parameters on the CO_2-CO ratio in primary anode gas; increase in anodic interface potential E increases the CO_2-CO ratio, increase in carbon anode baking temperature increases the CO_2-CO ratio, increase in operating electrolysis temperature decreases CO_2-CO ratio. The model predicts that polarized coke crystallites preferentially form CO_2 during electrolysis and dispersed, non-polarized, carbon particles would rather react with CO_2 to form CO, reaction (5.2). Another secondary reaction is formation of CO by the reaction of the primary anode gas and non-polarized carbon atoms within pores in the interior of the carbon anode following penetration of CO_2 in the non-polarized structure as mentioned above.

Another source of CO could be anodic oxidation of aluminium carbide where carbon dust is also formed [9]:

$$Al_4C_3 + 6CO_2(g) \rightarrow 2Al_2O_3 + 3C + 6CO(g) \quad (5.3)$$

In the present work the laboratory cell setup was constructed in a such way that anodic and cathodic area were physically separated in order to limit reaction between anodic and cathodic products. Thus, reaction (5.1) and reaction (5.3) can be considered to contribute negligible to the CO_2 conversion. CO can also be formed by air burn. Since nitrogen is flushed through the furnace air burn in the laboratory scale cell could also be neglected.

Thorne *et al.* [10] used GC MS to measure CO and CO_2 based on an adapted method from Kjos et al. [11] who used anodes with a hole in the center for the gas collections. Thorne *et al.* found that the main product was CO_2 but substantial amounts of CO was also detected. The CO was proposed to originate mostly from the back reaction, but CO was also proposed to partially be a primary anode product or formed via the Boudouard reaction. Grjotheim *et al.* [12] measured the anode gas composition as a function of the anodic current density and found close to 100% of CO_2 in the current range 0.32-1.34 A cm^{-2}. The hollow anode applied was designed to effectively collect the gases after being formed without coming into

contact with the outer bath surface. A hole was made through the center of the anode for gas collection. For graphite it was found that the anode consumption was much higher (in the range 135-150 %) than the theoretical value. For analysis of anode gas during electrolysis in a bath with low alumina concentration (< 0.6 wt%) Zhu and Sadoway [13] used tubular anode where the outer vertical surface was insulated with boron nitride to avoid contact with the electrolyte. It was found that over the entire potential range CO was the main component of the anode gas. Brun *et al.* [14] studied the Boudouard equilibrium in a laboratory scale aluminium cell and found that carbon particles probably formed by disintegration of the anode could react with the CO_2 causing its reduction to CO.

Most of the experiments for studying CO-CO_2 composition are performed at higher current densities [10, 12, 15]. Clearly CO_2 seems to be the primary anodic off-gas. However, there is a scarcity of studies at lower current densities where also CO could be primary off-gas. This work aims to study more closely the CO-CO_2 composition at low potentials and the corresponding low current densities and to thoroughly discuss the obtained results in relation to the few literature references that exist. Drossbach [16], Thonstad [6] and Silny and Utigard [17] have reported gas composition data for the low current densities but also as well for higher current densities. Only in the work by Thonstad CO was found to be dominant product at a potential close to reversible potential for CO evolution. The present work aims to contribute to the fundamental understanding of CO-CO_2 gas composition at lower potentials and current densities. The study was done in a laboratory cell where also different anode designs were used. The different designs were introduced because they could potentially give different gas composition. Four different anode designs were used: horizontal anode (with a downward-facing surface), vertical anode, rod anode (having both a vertical and horizontal surface) and an inverted horizontal anode (with an upward-facing surface). The carbon material used was graphite. The bubble behavior of these electrodes has been reported in an earlier paper [18]. A hollow anode design made from the same graphite material was also tested.

5.2 Experimental part

5.2.1 Anode design and furnace setup

Experiments were performed in a cryolite melt (cryolite ratio = 3) under N_2-atmosphere at the temperature 1005 °C. Nitrogen also had the role as carrier gas. Synthetic cryolite (purity ≥ 97.0 %, Sigma Aldrich) was used. Alumina (Merck) was added to the cryolite to make a start concentration of 2 wt% of alumina. The different anodes designs are shown in Figure 5.2. The graphite rod anode was made as described in [10], the vertical anode, horizontal anode and inverted horizontal anode together with the counter electrode (CE) were made as described in [18]. As a counter electrode (CE) a graphite rod shielded with boron nitride was used. The surface area was 10.2 cm^2. The purpose of shielding the CE was to minimize exposed carbon above the melt. The CE was physically separated from the anode by placing it in a smaller silicon-nitride crucible thus preventing cathodic and anodic product to react. The hollow gas anode had the shape of an inverted funnel and was designed as shown in Figure 5.3. The force for driving the anode gas out of the cell was the overpressure made by the produced gas, i.e., no carrier gas was used. When the hollow anode was used as working electrode the graphite crucible had the role as counter electrode. A purified graphite material (Schunk Tokai Scandinavia AB, Sweden) was the active electrode material for all electrodes. The aluminum reference electrode was constructed according to [11].

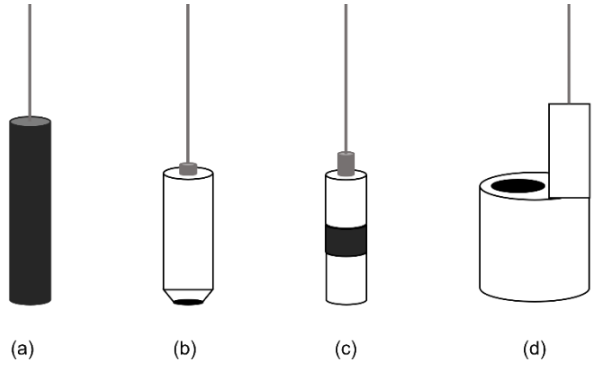

Figure 5.2. Different anode designs: (a) rod anode, when immersed 10 mm in melt gives a geometric surface area of approx. 3.9 cm^2, (b) horizontal anode, anode surface area 0.79 cm^2, (c) vertical anode, anode surface area 1.57 cm^2, (d) inverted horizontal anode, anode surface area 0.69 cm^2.

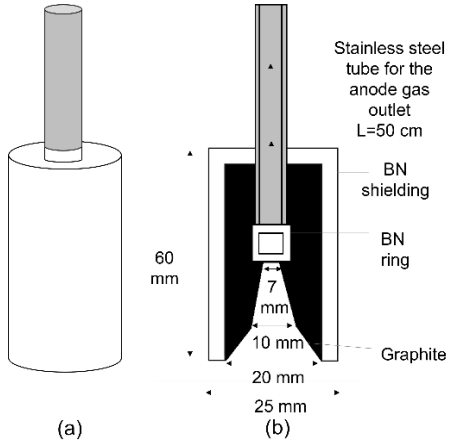

Figure 5.3. The hollow gas anode; (a) the outer body of the hollow gas anode, (b) cross section of the hollow anode design with the inverted funnel shape, anode surface area approx. 10.8 cm^2.

Three cell setups were used in this work, Figure 5.4. In order to study the CO_2 to CO conversion through Boudouard reaction for Setup 1 and Setup 2, a known concentration (1% and 2%) of CO and CO_2 was introduced for a certain amount of time without electrolysis at working temperature of 1005 °C while analyzing the composition of the out gas. Setup 1 was expected to have a high degree of conversion due to the graphite crucible and therefore Setup 2 with a silicon nitride (Si_3N_4) crucible was introduced to minimize any reaction between CO_2 and carbon. The anode and cathode were physically separated in order to prevent anodic and cathodic products to react, reaction (5.1). The counter electrode was placed inside a smaller silicon-nitride crucible. This should minimize the back reaction by preventing the transport of dissolved aluminium metal from the cathode compartment to the anode compartment. Three holes (Ø 5 mm) were drilled in the small Si_3N_4 crucible to ensure ionic contact between the compartments. The gas was collected by a hollow steel tube above the bath surface near the anode. The Setup 2 was used to study the gas composition of the four anode designs shown in Figure 5.2. It was also tested for CO_2 to CO conversion in the same way as Setup 1. The degree of conversion was relatively small and considerably smaller than for Setup 1. Obtained results were used for correction of measured gas concentration values for the four different anodes tested using Setup 2. Setup 3 shown in Figure 5.4(c) was used for the gas measurements with the hollow gas anode, Figure 5.3. The BN ring shown in Figure 5.3(b) was inserted to

prevent the stainless-steel tube to come into direct contact with the melt. The graphite crucible was used as a counter electrode.

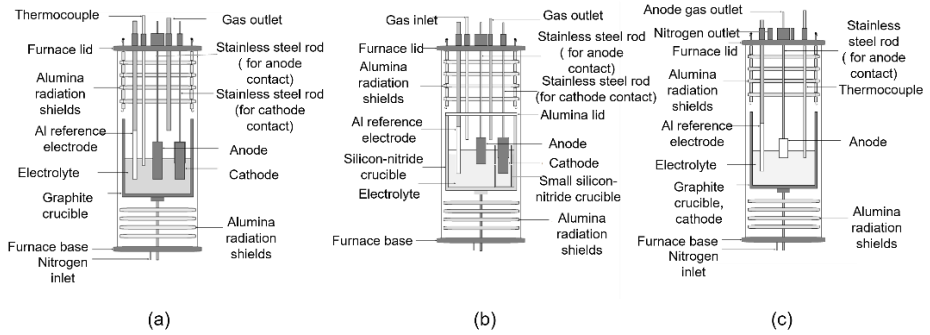

Figure 5.4. The three different setups; (a) Setup 1, (b) Setup 2, (c) Setup 3.

5.2.2 Experimental methods

Electrochemical Impedance Spectroscopy (EIS) was used to determine the ohmic resistance at Open Circuit Potential (OCP). This value was used to IR compensate all electrochemical measurements. This means that any voltage drop due to resistance introduced by bubbles and overvoltage has not been compensated. Chronoamperometry was used for a potential control of the working electrode. The potential of the working electrode was kept constant for > 300 seconds and the resulting current was monitored for several potentials. The current density was corrected for the change in the anode surface area due to carbon consumption (this only applies to the rod and vertical anode, Figure 5.12). The corresponding gas concentration was measured continuously. A time of minimum of 300 s was needed for the gas concentration to stabilize. For the hollow gas anode chronopotentiometry was used. All electrochemical measurements were performed using a PARSTAT (Princeton Applied Research) potentiostat and a 20 A booster (KEPCO).

A gas analyzer (Servomex Xendox 2550 Multicomponent Infrared) was used to analyze the concentration of the CO and CO_2. The gas analyzer gave out potential values proportional to the gas concentration in vol%. A calibration was done before each experiment and calibration curves were constructed for both CO and CO_2 giving the relation between output potential and gas concentration in vol%. For the gas measurements the gas

flow was kept constant at 400 ml/min and the flow was controlled with a flow meter (Bronkhorst mass flow meter/controller).

5.3 Results and Discussion

5.3.1 Testing of Setup 1 and Setup 2 for CO_2 and CO conversion

Setup 1 and Setup 2 were studied for CO_2 to CO conversion and the results were used for correcting the gas measurements values obtained for the anode testing. Results are shown in Figure 5.5 and Figure 5.6 for Setup 1 and Setup 2, respectively. For Setup 1 the CO(1%)/CO_2(2%)/N_2(balance) gas mixture was introduced at the bottom of the furnace and past on the outside of the graphite crucible on its way through the furnace.

Figure 5.5 shows considerable decrease in CO_2 and increase in CO concentration indicating significant CO_2 conversion to CO. When the gas mixture is flushed directly through the analyzer the actual concentration of the CO and CO_2 in the gas mixture was measured. Pure nitrogen gas was flushed through the analyzer and the furnace before and after introduction of the gas mixture. When nitrogen was flushed through the furnace considerable CO concentration was obtained while CO_2 was reaching zero value. This CO excess could be caused by traces of O_2 in N_2 gas reacting with carbonaceous material in the furnace. However, the purity of the N_2 gas was 99.999 % and could not cause those high values of CO. The cause of the high CO value is not understood, but this phenomenon was not observed for Setup 2. The gas mixture was then introduced to the furnace with an arbitrary sequence of flow rate and the CO and CO_2 concentrations were measured.

There was an increase of CO concentration in the whole flow rate range compared against the inlet gas mixture. It was assumed that the Boudouard reaction is responsible for the CO_2 to CO conversion. At temperatures above 950 °C, CO is much more stable than CO_2. The carbon crucible, rod anode and carbon plate in bottom construction in Setup 1 are the sources of carbon. The CO concentration is decreasing with increasing gas flow while CO_2 gas concentration is increasing. This is most likely due to the increased time for reaction. If only the Boudouard reaction is responsible for the loss of CO_2 and corresponding CO concentration, it

would give a CO concentration of 3.34 vol% at the lowest flow rate. The measured concentration as shown in Figure 5.5 was 4.37 vol% CO. This excess of CO could indicate other reactions happening besides the Boudouard reaction as discussed below in relation to Figure 5.7.

The same CO(1%)/CO_2(2%)/N_2(balance) gas mixture was used for Setup 2 and the results are shown in Figure 5.6. When nitrogen was flushed through the analyzer and the furnace, the CO_2 concentration reached 0.00 vol% as expected but the CO concentration reached -0.10 %. A separate test was done where nitrogen was flushed through the analyzer for 20 min and it was found that the CO_2 concentration remained stable (0.00 vol%) while the CO concentration reached -0.10 vol% and remained stable. This value was used later for the baseline correction. When the gas mixture was introduced, it was again obtained a decrease in CO_2 and an increase in CO concentration demonstrating some CO_2 to CO conversion but not to the same degree as for Setup 1. This is due to the absence of the graphite crucible as carbon source. The only carbon source in Setup 2 was the rod anode. The gas flow rate affected the gas composition in the same principal way as for Setup 1. At the highest flow rate, the CO_2 to CO conversion goes towards zero. If it was assumed that all CO_2 loss was due to the Boudouard reaction, the calculated CO concentration becomes higher than the actually measured concentration at the lowest flow rate. The loss of the CO_2 could also be due to thermal decomposition taking place simultaneously as the Boudouard reaction.

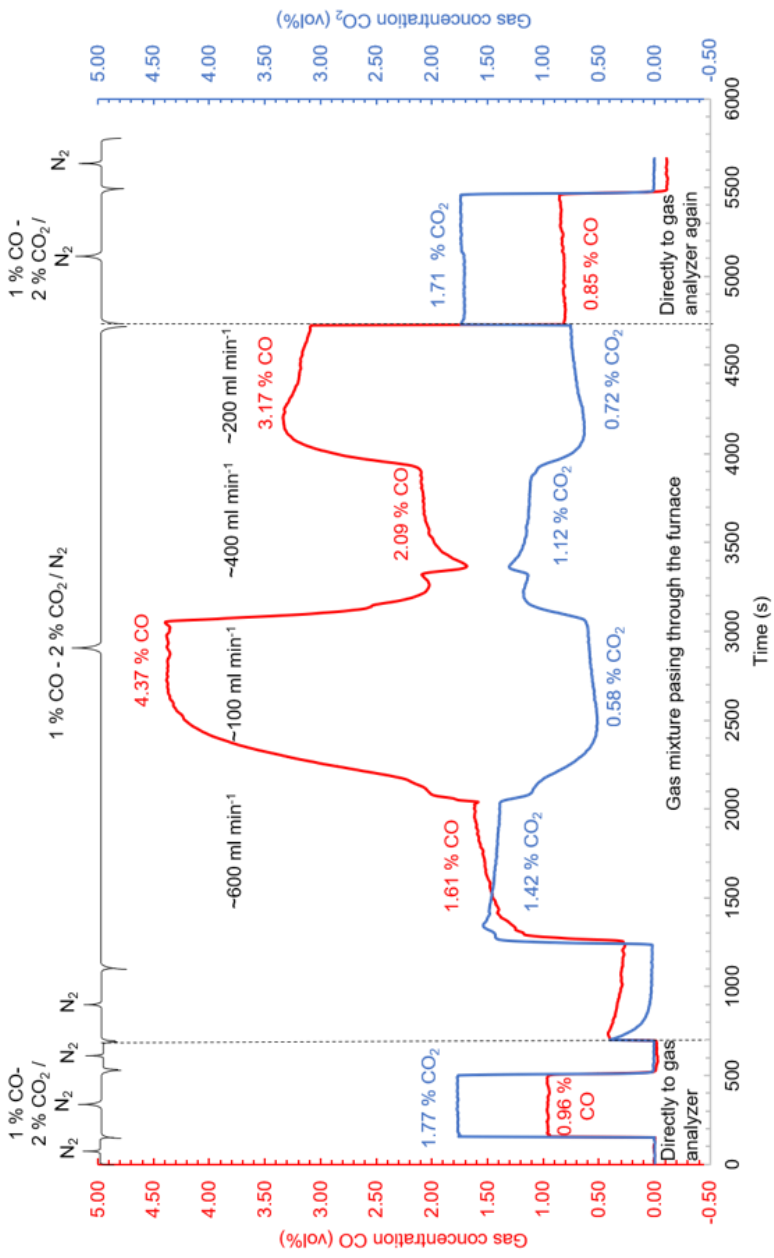

Figure 5.5. CO-CO_2 gas concentration in Setup 1.

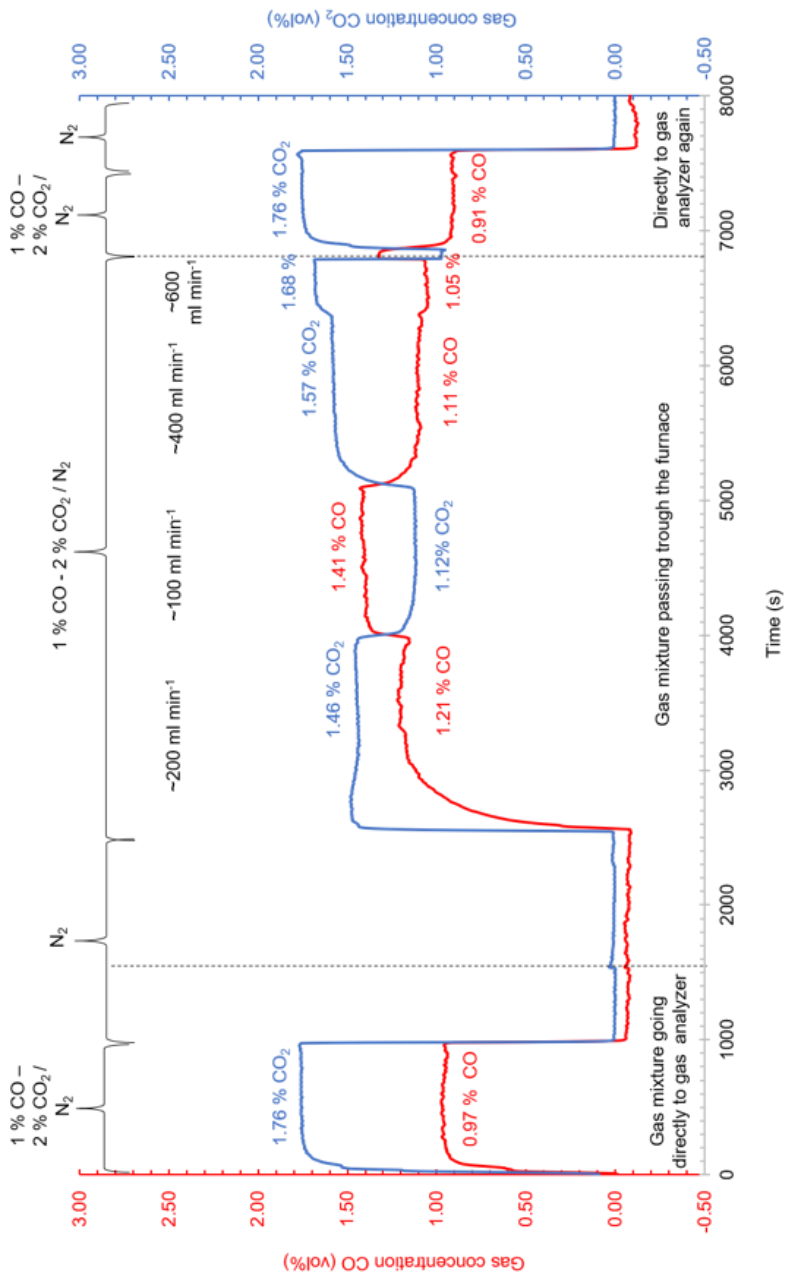

Figure 5.6. CO-CO_2 gas concentration in Setup 2.

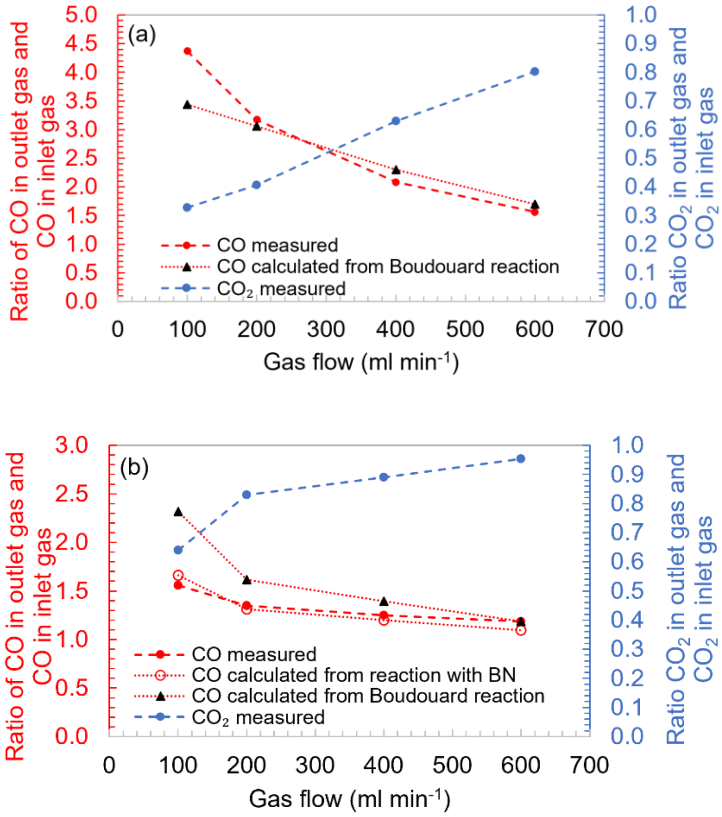

Figure 5.7. The ratio of concentration in outlet gas and inlet gas for both CO and CO_2; (a) Setup 1 and (b) Setup 2. For both setups data for red and blue solid circle marker represents measured CO and CO_2 concentration, respectively. Black triangle marker represents calculated CO concentration in outlet gas if CO_2 loss was only due Boudoard reaction. Non-filled red circle marker in (b) represents calculated CO concentration if CO_2 loss was only due to its reaction with BN.

Silny and Utigard [17] studied some factors which influence the CO/CO_2 ratio in primary gas composition and found that most of CO was generated by CO_2 reacting with carbon particles arising from disintegration of the carbon anode. They also found that CO_2 reacting with parts of boron nitride (BN) was a source for CO and did some tests of the BN reactivity. They observed that CO_2 did not react with the BN in the absence of the bath but when BN was immersed in the bath, CO_2 reacted with the BN, resulting in 17% CO in the outlet gas for that specific setup. Grjotheim *et al.* [19] also observed excess of CO. In their gas measurements helium was the carrier gas and it was found that the outlet gas always contained nitrogen. They

estimated that boron nitride (which was used as construction material in the cell) probably reacted with CO_2 according to the reaction:

$$2BN + 3CO_2 \rightarrow B_2O_3 + 3CO + N_2 \quad (5.4)$$

If it is assumed that in Setup 2 all CO_2 to CO conversion is due to reaction (5.4), the calculated concentration of CO is more in agreement with the obtained results in the test (Figure 5.7), meaning that in Setup 2 the boron nitride could be responsible for the conversion together with the Boudouard reaction. Sun *et al.* [20] found that CO_2 molecules form weak interactions with uncharged BN nanomaterials and are weakly adsorbed. When the BN is negatively charged CO_2, molecules become tightly bound and strongly adsorbed. Once the electrons are removed from the BN, CO_2 molecules spontaneously desorb. From Figure 5.8 it can be seen that reaction between BN and CO_2 is more thermodynamically favorable then the Boudouard reaction. Reaction between Si_3N_4 and CO_2 could also be a source for CO, but it is not occurring at the working temperature of 1005 °C. Data are taken from SI Chemical Data [21].

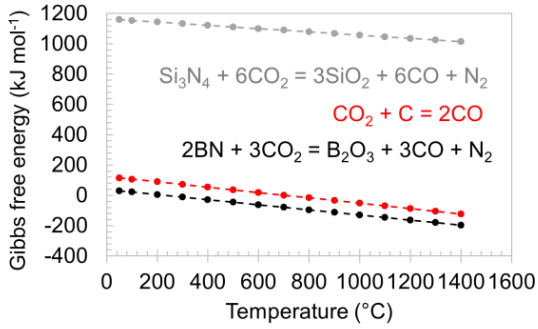

Figure 5.8. Gibbs free energy for the Boudouard reaction, CO_2 reacting with the BN and Si_3N_4 at various temperature.

Brun *et al.* [14] introduced a CO-CO_2 mixture of known amount and composition through a furnace in such a way that the gas mixture flowed past a graphite crucible which contained an alumina saturated cryolite bath (12 wt% alumina) at an operating temperature 1000 °C and no electrolysis took place. It was found that the amount of CO_2 leaving the furnace was only about 5% of the entering amount. They concluded that the Boudouard reaction proceeded rather rapidly. As seen in Figure 5.5 and Figure 5.6, the gas flow affects the gas concentration. Figure 5.7 shows the ratio of

concentrations in outlet gas and inlet gas for both CO and CO_2 for both setups. Assuming that all loss in CO_2 was due to the Boudouard reaction, the corresponding CO concentration was calculated and shown Figure 5.7. For Setup 1, Figure 5.7a), the ratio agrees reasonably well with the calculated ratio except the lowest. The excess was approx. 1% CO. If humidity from the bath reacted with carbon according to reaction 4.5, the produced CO could explain the excess of CO in the outlet gas at the lowest flow rate.

$$C + H_2O = CO + H_2 \tag{5.5}$$

If the excess was caused by reaction (5.5), it was calculated that the required mass of H_2O should be ~ 0.2 g corresponding to only 0.03 wt% of the total amount of cryolite in the crucible. Since the used cryolite has purity of the ≥ 97 %, it could be possible that reaction (5.5) could affect the CO concentration.

For Setup 2, Figure 5.7(b), there is a deficit in CO assumed the Boudouard reaction is the only conversion reaction for CO_2. This means that there must be another conversion reaction for CO_2 taking place. However, the ratios approach each other towards higher flow rates. The only carbon source in Setup 2 is the rod anode. For Setup 2 it was also assumed another extreme case, *i.e.,* all loss of CO_2 was due to reaction with BN. The ratio fits fairly well with the calculated ratios for all flow rates.

In the study of gas concentration obtained from the different anode designs, Setup 2 was used due to the smallest conversion of CO_2. Although the conversion of CO_2 was lowest for the highest flow rate (600 ml min^{-1}) the flow rate of 400 ml min^{-1} was chosen as the dilution of the gas concentration was too large for the highest flow rate. At the flow rate of 400 ml min^{-1} the results from the test with Setup 2 gave that the actual CO_2 concentration is around 10% higher and the actual CO concentration is 20% lower than measured. The measured concentrations were corrected for these values.

5.3.2 Gas measurements during electrolysis

In Figure 5.9 are shown (a) current response and (b) CO and CO_2 concentration for the rod anode at potential-controlled electrolysis. A plot

is shown for the whole potential range but also examples for two specific potentials (1.56 V and 1.67 V) with corresponding current densities (0.07 A cm^{-2} and 0.2 A cm^{-2}). Figure 5.10 and Figure 5.11 summarize the results of many such experiments at different potentials obtained by plotting the anode potential and relative gas concentration as a function of the average current densities for the rod anode and inverted horizontal anode (Figure 5.10) and the horizontal anode and vertical anode (Figure 5.11). Some points for the gas measurements at very low potentials were not included if no significant change in gas concentration compared to open circuit condition could be measured. It can be seen that both the horizontal and vertical anode showed very high CO concentration in the whole potential range. This unlikely high CO concentration indicates that something failed during the experiment. An explanation for the results for these two electrodes is proposed.

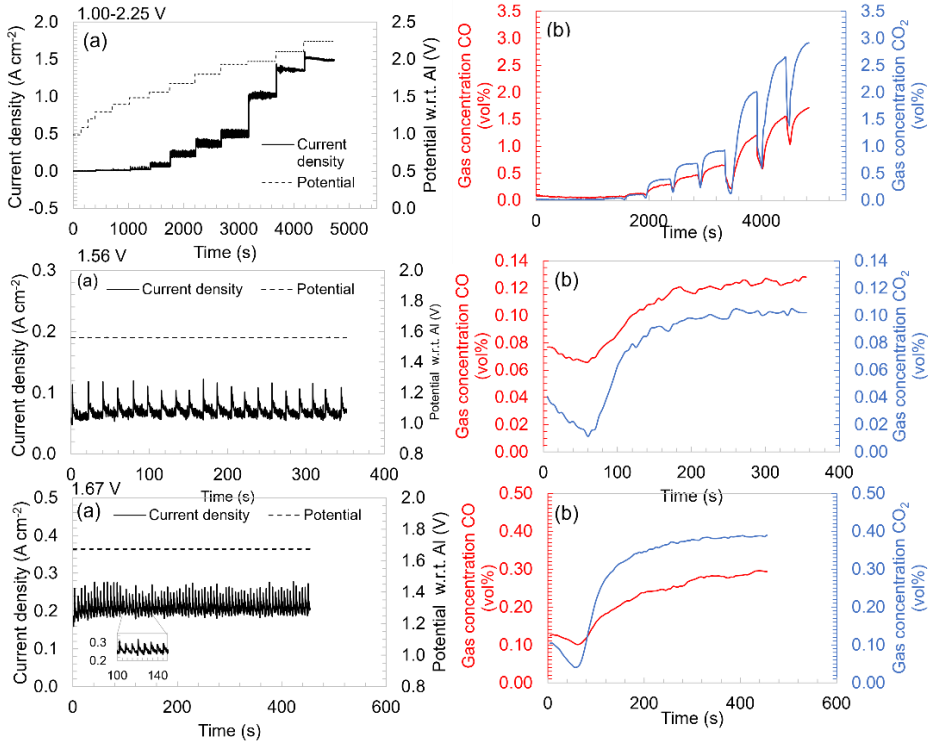

Figure 5.9. Current response and CO-CO_2 concentration for the rod anode at potential-controlled electrolysis in the potential range 1.00-2.25 V (upper plots), at constant potential of 1.56 V (middle plots) and 1.67 V (lower plots), with (a) potential and current response together with (b) CO and CO_2 concentration.

In Figure 5.10 and Figure 5.11 it can be seen that at the potentials and current densities the main anode gas is CO_2 which was also found by Thonstad [6]. Although the main constituent of the primary gas at higher current density should be CO_2, it was also obtained considerable amount of CO. Due to the construction of the cell it was assumed that the back reaction could not be the main source for formed CO at higher current densities. The main source for CO could be Boudouard reaction between CO_2 and carbon particles in the melt. For high current densities, with the electrolysis going on for some time, the anode can disintegrate enabling the Boudouard reaction. Dusting was observed as shown in Figure 5.16. The results from the rod anode are believed to be most trustable because the rod anode was the first electrode tested. After testing the rod electrode, the inverted horizontal anode was tested in the same bath. The bath might have contained carbon particles detached from the rod anode thus converting through Boudouard reaction the CO_2 produced from the inverted horizontal anode.

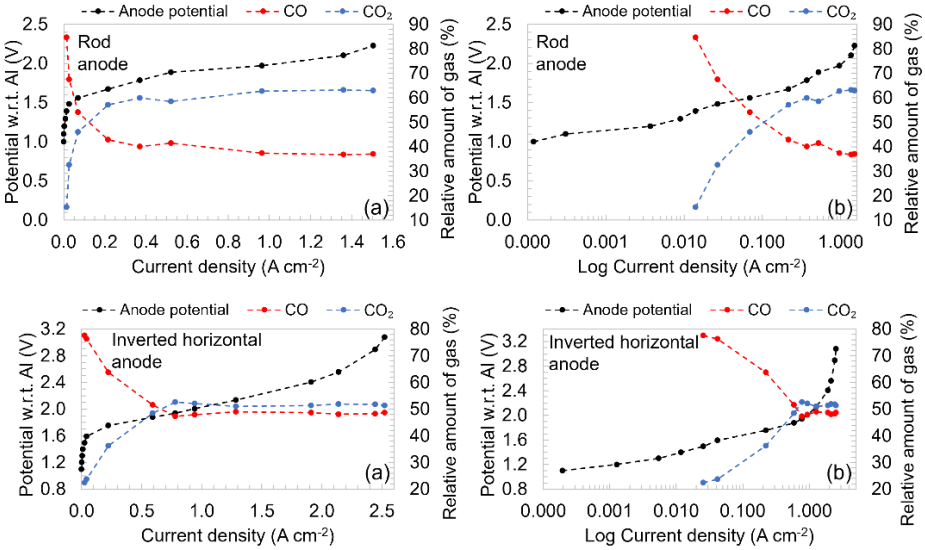

Figure 5.10. Anode potential and relative amount of the CO and CO_2 gas for the rod anode and inverted horizontal anode versus (a) current density (linear scale) and (b) current density (logarithmic scale).

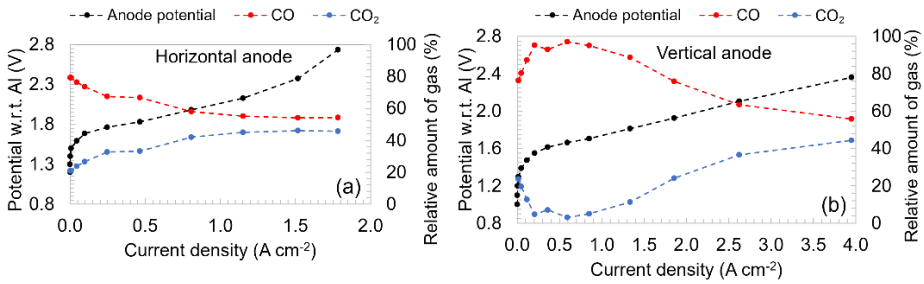

Figure 5.11. Anode potential and relative amount of the CO and CO_2 gas for the (a) horizontal anode and (b) vertical anode versus current density.

Figure 5.12 shows pictures of the anodes after the experiment. Due to the long duration of the experiment the anodes were considerably consumed and have changed from their initial design.

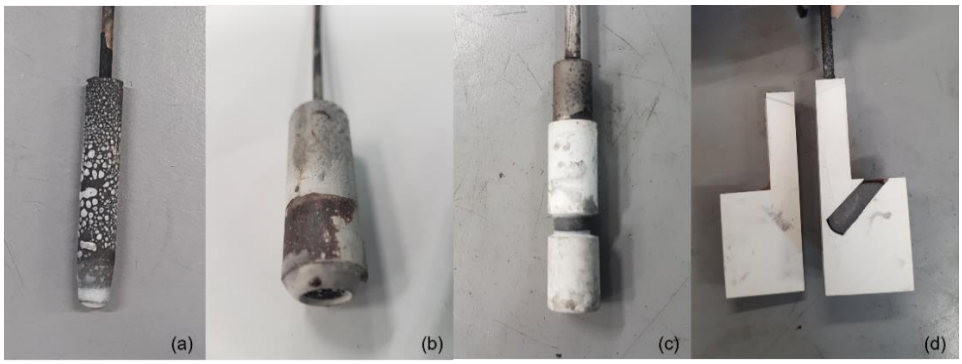

Figure 5.12. Pictures of the anodes after the experiment; (a) rod anode, (b) horizontal anode, (c) vertical anode and (d) inverted horizontal anode (cross-sectioned).

Figure 5.13. Picture of anodes after experiment; (a) horizontal anode and b) vertical anode.

Silny and Utigard [17] and Grjotheim [19] reported that the BN could play a significant role in CO_2 to CO conversion (reaction (5.4). In

Figure 5.13 can be seen that the edges of the BN shielding are still sharp. It is therefore concluded that the BN did not react with the CO_2 as the edges than should be rather rounded. The reaction between CO_2 and BN is therefore not a source for CO in the off gas. Davies and Phennah [22] studied reactions of boron-containing materials with CO_2 and found that of all boron compounds only BN showed a high degree of oxidation resistance in the temperature range 600-750 °C.

As seen in Figure 5.11 high CO concentration is obtained for the horizontal and vertical anode at all current densities. At higher current densities graphite is considerably consumed (Figure 5.13) and the BN shielding hinders bubbles leaving the anode surface easily. Bubbles then will be stuck increasing the contact time at the anode surface thereby promoting CO_2 to CO conversion. For the vertical anode at lower current densities the behavior of the CO curve does not follow the decreasing trend observed for the other anodes (Figure 5.10 and Figure 5.11). This could be explained by the wetting properties of graphite and BN by cryolite bath. Åsheim *et al.* [23] found that BN is better wetted by the cryolite in comparison to the graphite. For the vertical anode produced gas can therefore get entrapped at the boundary between the graphite and the upper BN phase as shown in Figure 5.14.

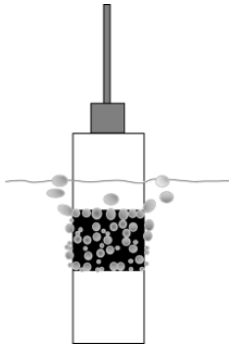

Figure 5.14. Illustration of entrapment of bubbles at the boundary between graphite and BN.

Chronoamperometric data for the horizontal anode were transformed to the frequency spectrum. FFT spectrum analysis was done using Sigview software. The FFT spectrum obtained for different current densities is shown in Figure 5.20 in the Appendix 5.5. The dominant frequency most likely represents bubble release frequency for the horizontal anode. In Figure 5.15 is shown dominant frequency and how it

changes with current density. After longer electrolysis time the graphite anode is considerably consumed and bubbles get trapped in the cavity increasing the bubble retention time. In Figure 5.15 is also shown dominant frequencies for horizontal anode where electrolysis time was much shorter, *i.e.* there was no cavity formation. The dominant frequency for both anodes is increasing with increasing current density. From approx. at 0.5 A cm^{-2} there is a deviation for the anode having long electrolysis time, meaning that from this current density and upwards the cavity formation severely affects the bubble retention time. Increased bubble retention time could have led to the generally high CO values at higher current densities.

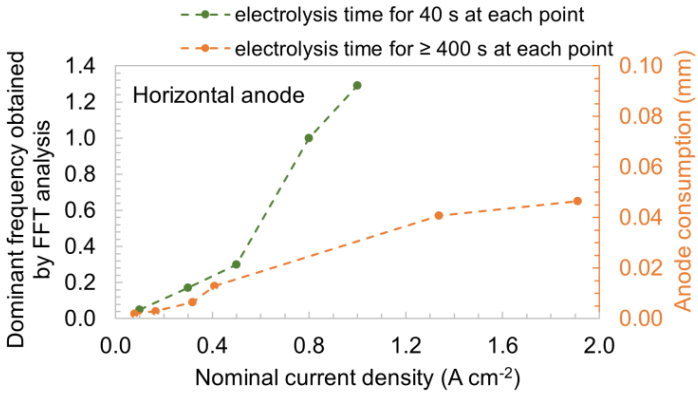

Figure 5.15. Dominant frequency obtained from FFT spectrum for the horizontal anode. Data for electrolysis time of 40 s are obtained from Stanic *et al.* [18].

The carbon consumption for the rod, horizontal, vertical and inverted horizontal anode was calculated based on the measured volumetric consumption of the graphite and the results are shown in Table 5.1. The carbon consumption for the different anodes is comparable. If it was assumed that all CO for current densities above 0.1 A cm^{-2} was coming from the Boudouard reaction the corresponding calculated carbon consumption is in agreement with the carbon consumptions shown in Table 1 except for the rod anode. For the rod anode it was found that only 50 % of the consumed carbon had undergone Boudourd reaction. The remainder of the carbon remained in the melt as a carbon particles. These carbon particles were also observed visually as shown in Figure 5.16. The figure shows the bath surface in the silicon nitride crucible after the experiment. The density of the molten bath is around 2.05 g cm^{-3} and

density of the graphite is 1.8 g cm^{-3} meaning that all carbon particles are found at the surface of the melt.

Table 5.1. Carbon consumption for the different anode designs.

	Rod anode	Horizontal anode	Vertical anode	Inverted horizontal anode
Carbon consumption %	126	130	134	117

Figure 5.16. Picture of the surface of the frozen bath in the silicon nitride crucible at room temperature after the experiment with the rod anode and inverted horizontal anode.

In Figure 5.17 are shown CO-CO_2 gas measurements results for the hollow gas anode from Figure 5.3. The experiments were done in the current range 0.10 A cm^{-2} to 0.85 A cm^{-2}. The retention time (*i.e.,* time until stabilization of gas concentrations) varied widely, for more than two hours at 0.10 A cm^{-2} till three minutes at 0.85 A cm^{-2}. The obtained CO concentration was higher than expected at higher current densities and could be explained by Boudouard reaction taking place between produced CO_2 and carbon particles (formed by anode disintegration). The intersection of the CO and CO_2 curve could therefore be expected at lower current densities than obtained. Despite the long retention time at lower current densities the hollow anode design preformed reasonably well. Use of an inert carrier gas could lower the retention time, however causing

some challenges to get the product gas out regarding overpressure in the cell.

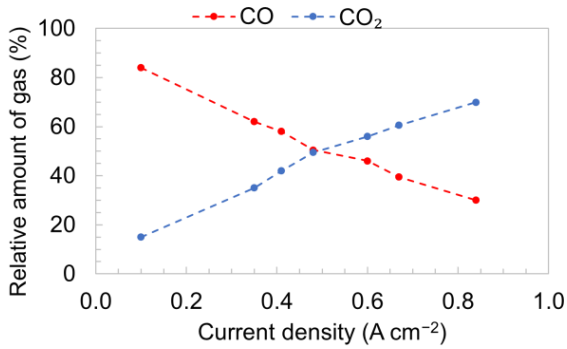

Figure 5.17. Relative amount of CO and CO_2 versus current density for the hollow gas anode.

In general, the construction materials of the furnace were materials (stainless steel, pythagoras, sintered alumina, silicon-nitride) that could by a very little degree react with the primary gases. Experimental conditions such as temperature and alumina concentration also can affect the primary gas concentration. Silny *et al.* [24] reported that increasing working temperature during electrolysis promotes the generation of CO relative to CO_2. CO is always expected to be present at the temperature of the experiment due to the Boudouard reaction (reaction 4.2) [13]. Ouzilleau *et al.* [8] found that the larger the crystallite diameter, L_a value, of the coke crystallites the higher the CO_2 fraction becomes. A single crystal of graphite would have infinite large L_a value. The graphite used in this work was not a single crystal but has seen much higher heat treatment than industrial anode. In this way it should give according to Ouzilleau *et al.* more primary CO_2. The mentioned disintegration and following Boudouard reaction can have covered this effect. It has been reported by several researchers, although not documented quantitatively, that graphite disintegrates more than the industrial carbon anodes. Grjotheim *et al.* [12] observed significant amount of carbon particles in the crucible after experiment using graphite anode. Thonstad [6] also reported that graphite anodes disintegrate more than industrial carbon anode during electrolysis, inducing noticeable generation of CO by the reaction of carbon particles with CO_2.

CO_2 generated at the electrolytic surface of operating anodes permeates the porous anode structure and reacts to form carbon monoxide [25]. This gasification increases anode porosity and generates a reaction

porosity profile. Far-Wharton *et al.* [26] studied gaseous reactions between CO_2 and C at the electrode-electrolyte interface which occurs in the pore structure giving rise to CO formation. The porosity of carbon sample immediately behind the electrode-electrolyte interface was studied. An increasing proportion of CO evolution during electrolysis was associated with a greater amount of reactive carbon which has a larger surface area and less developed crystallites. There is an increase in the number of macro-pores at high current density. The porosity of the anode surface at low current density (0.06 A cm^{-2}) increased while the porosity behind the electrode-electrolyte interface increased at higher current density. Putri *et al.* [27] used porosity measurements techniques to understand the relation between gas diffusion and anode properties. Two industrial anode samples and an anode made form graphite were tested. The graphite pore distribution was associated with a higher intrusion volume than the industrial anodes. According to these findings it is reasonable to believe that any prolonged contact between CO_2 and the anode itself, giving enough time for CO_2 to penetrate the anode, would promote CO. After the reversible potential for CO_2 formation is reached, this effect can influence the primary CO_2 especially when bubble retention time is extended due to *e.g.,* anode design like in the case of the horizontal anode.

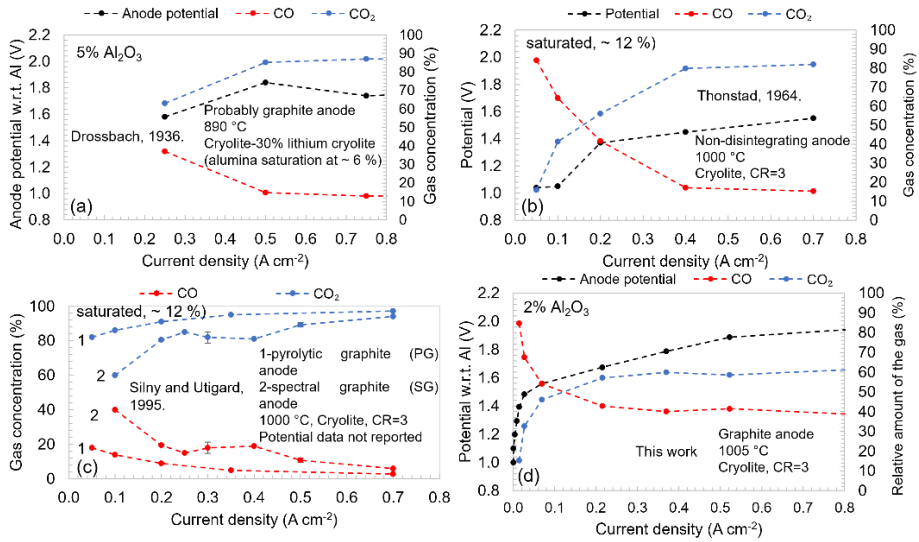

Figure 5.18. Anode potential and CO and CO_2 amounts versus current density. (a) Data extracted from Thonstad [6], (b) Data extracted from Drossbach [16], (c) Data extracted from Silny and Utigard [17], (d) Data from this work (rod anode).

As written above, the anodic current density, anode material, temperature and alumina content determine the CO-CO_2 gas concentration. In Figure 5.18 are shown anode potentials and CO-CO_2 gas amounts as a function of current density from previously reported works. The results from the current work obtained with the rod anode are also included. At potentials below 1.2 V (*i.e.*, approx. the reversible potential for CO_2 evolution) CO is the expected primary product. As seen in Figure 5.18(b) Thonstad reported primary gas composition data from 1.05 V showing that the dominant primary off gas was CO up to 1.2 V and 0.15 A cm^{-2}. Thonstad used a so-called non-disintegrating industrial anode which was supposed to give small dust amounts during electrolysis. Thonstad used a bath saturated with alumina. Alumina saturation is also used in several other works for simplicity regarding cell construction. Silny and Utigard [17] have also reported results for non-saturated bath and found that decreasing alumina content promotes the evolution of CO. Two explanations were proposed for these observations. First, low alumina content results in higher overpotential for the anode process where CO_2 is formed. It was not specified if this was related to concentration or reaction overpotential. Second, the interfacial tension increases with decreasing alumina content which leads to lower wettability of the anode. This leads to larger gas bubbles and larger gas/anode interface area which itself can promote Boudoard reaction. However, this will also increase the local current density which again can result in a higher dusting rate. Another explanation which can also account for the higher CO values at lower alumina concentration can be found in the structure of the oxyfluoro-species. Sterten [28] developed an ionic structure model for NaF-AlF_3 melts containing alumina. There are two major species containing oxygen, $Al_2OF_6^{2-}$ and $Al_2O_2F_4^{2-}$. At low alumina concentration the dominant ion containing oxygen is $Al_2OF_6^{2-}$. Thus, steric effects could influence the reaction mechanism and thereby reaction rate and primary product. For the low oxygen containing species ($Al_2OF_6^{2-}$), the accessibility of oxygen for the surface carbon atoms is lower than for the high oxygen containing species ($Al_2O_2F_4^{2-}$). The oxyfluoro complex containing two oxygen atoms could likewise promote primary CO_2 formation. The relatively low alumina concentration (2 wt%) used in the current work could have given a slightly more primary CO than if the bath was saturated.

Drossbach measured the CO-CO_2 concentrations in a cryolite-lithium cryolite melt at 890 °C, Figure 5.18(a). The starting point was at 0.25 A cm^{-2} where CO_2 was already the dominant product. Values for lower current densities were not reported and CO was never found to be the dominant product as Thonstad later found. At higher currents and potentials CO_2 is the dominant primary anode product even though CO theoretically can be produced. The current perception is that reaction kinetics favors CO_2 formation [6]. However, Drossbach showed that the thermodynamics actually can explain CO_2 being the dominant primary gas product. Drossbach considered the equilibrium (reaction (5.6) and calculated gas composition (CO_2, CO, O_2) for various potentials at 890 °C.

$$2CO_2 = 2CO + O_2 \tag{5.6}$$

In Figure 5.19 is plotted the calculated CO-CO_2 gas concentrations as a function of anode potential. The thermodynamics predict CO to be the dominant gas species at low anode potentials with an intersection somewhere in the interval 1.2 V to 1.4 V.

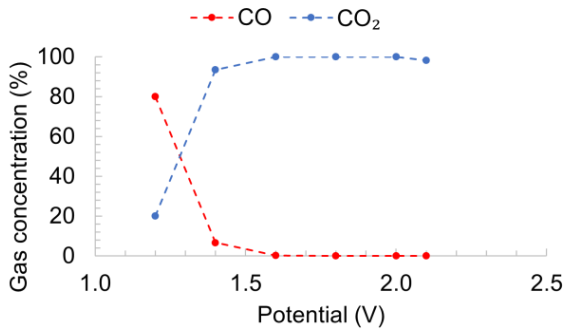

Figure 5.19. Drossbach's tabulated data plotted [16].

Silny and Utigard (Figure 5.18(d)) found the CO_2 to be dominant in the whole current density range. Two different types of anode materials were used, spectral graphite (SG) and pyrolytic graphite (PG). Higher CO_2 concentration was obtained for the PG anode. The SG anode tended to disintegrate and led to higher CO content than the PG anode because CO_2 reacting with the carbon particles from anode disintegration. PG has relatively few defects in its graphitic structure compared to the SG.

Although this finding is not directly transferable to industrial anodes, Jentoftsen *et al*. [29] found that higher baking temperature probably leads to anodes dusting less. The used graphite material in the current work is probably closer in properties to the SG than the PG used by Silny and Utigard and partly can explain the observed disintegration.

In the current work the rod anode was the anode that gave lowest the CO concentration especially at low potentials and low current densities but also at higher applied potentials in comparison to other anodes. The lowest applied anodic potential was 1.0 V which gave a current density 0.1 mA cm^{-2} but the first significant change in gas composition compared that at open circuit condition took place at 1.4 V and 0.015 A cm^{-2}. The dominant gas product was CO. Calculated theoretical value for the reversible potential of CO formation at this working temperature and alumina concentration (2 wt%) is approx. 1.1 V. Thonstad reported gas concentrations from 1.05 V and 0.05 A cm^{-2}. That is close to the reversible potential for CO formation at alumina saturation. Substantial amount of CO_2 (approx. 15 %) was reported for this potential even though the potential probably was below the reversible potential for CO_2 formation. In the current work CO_2 becomes the dominant gas product approx. at 1.6 V and 0.12 A cm^{-2} which is the intersection of CO and CO_2 curve. The carbon particles found on the melt surface after the experiment indicates that anode carbon disintegration took place. This implies that the mentioned intersection could occur at an even lower current density than 0.12 A cm^{-2}.

5.4 Conclusions

In the lower current density region 0.015 A cm^{-2} to 0.07 A cm^{-2} CO is found to be dominant anode gas product. Above 1.6 V and 0.12 A cm^{-2} the dominant gas became CO_2. Data extracted from Thonstads work showed a lower potential but slightly higher current density. However, Thonstad used a saturated bath making the results not directly comparable. Based on thermodynamic calculations presented by Drossbach CO_2 starts to be the dominant gas product is in the potential range 1.2 V to 1.4 V. The relatively low alumina concentration of 2 wt% could have promoted higher primary CO content than in saturated bath, explained by favorable kinetics for CO formation through steric effects of the different oxyfluoro-anion species

that exist for different alumina concentration. The carbon particles found on the melt surface after the experiment indicates that anode disintegration took place. The relatively high CO concentration at higher potentials and current densities was probably caused by Boudouard reaction between CO_2 and carbon particles. The boron nitride used in construction of the electrodes could from a thermodynamic point of view have reacted with CO_2 to form CO and boron oxide. Although stated by other authors to influence the CO-CO_2 gas concentration, this reaction seemed to have occurred to a very small degree because no wear of construction parts made of boron nitride was observed.

5.5 Appendix

Current density *vs.* time measurements were transformed into frequency spectra by using a Fast Fourier Transform algorithm in Sigview software-spectrum and signal analysis, Figure 5.20. The signals were transformed into the frequency domain to evaluate how the power of the signal is distributed over a range of frequencies to determine dominant frequency for the horizontal anode. The dominant frequency most likely represents bubble release frequency for the horizontal anode. The frequency spectrum is a simple way of showing the total amplitude at each frequency. The highest frequency that can be represented is one-half the sampling frequency, called the Nyquist frequency. The sampling rate (Fs) was 5 Hz, consequently the spectrum has a frequency range from zero to Fs/2, 0-2.5 Hz.

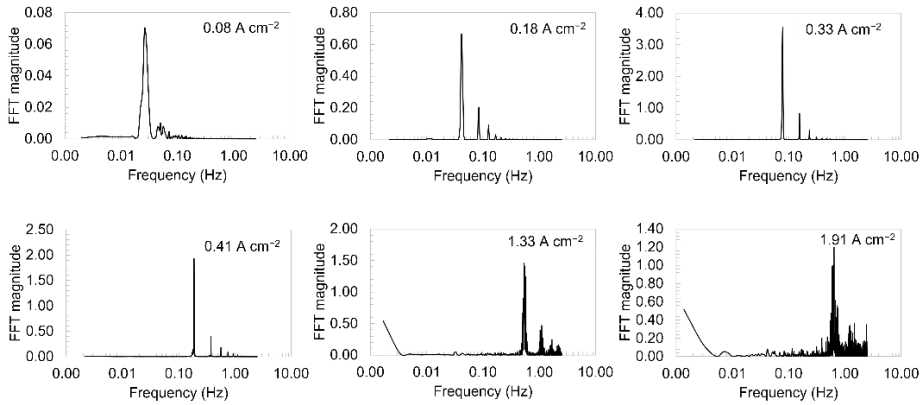

Figure 5.20. FFT spectrum of the current density – time data for the horizontal anode at different applied potentials. The current densities in the figure are the current densities measured in the moment the bubble has detached from the anode surface (*i.e.*, the current obtained for the bubble-free surface).

References

1. Stanic, N., E.T. Bø, and E. Sandnes, *CO and CO_2 Anode Gas Concentration at Lower Current Densities in Cryolite Melt.* Metals, 2020. **10**(12): p. 1694.
2. Thonstad, J., P. Fellner, G.M. Haarberg, J. Híveš, H. Kvande, and Å. Sterten, *Aluminium electrolysis : fundamentals of the Hall-Héroult process*. 3rd ed. 2001, Düsseldorf: Aluminium-Verlag. 359.
3. Thonstad, J., *On the Anode Gas Reactions in Aluminum Electrolysis.* J. Electrochem. Soc., 1965. **111**(8): p. 955-959.
4. Kimmerle, F.M. and L. Noël, *COS, CS_2 and SO_2 Emissions from Prebaked Hall Héroult Cells*, in *Light metals 1997* R. Huglen, et al., Editors. 1997, Minerals, Metals & Materials Society: Warrendale, Pa. p. 153-158.
5. Aarhaug, T.A., A. Ferber, O. Kjos, and G. H., *Online Monitoring of Aluminium Primary Production Gas Composition by use of Fourier-Transform Infrared Spectroscopy*, in *Light Metals 2014*, J. Grandfield, Editor. 2016, Springer International Publishing : Imprint: Springer: Cham. p. 647-652.
6. Thonstad, J., *On the Anode Gas Reactions in Aluminum Electrolysis, II.* J. Electrochem. Soc., 1965. **111**(8): p. 959-965.
7. Barrillon, E. *Les Facteurs de la Consommation de Carbone Anodique dans les Cuves Destinees a la Production Electrolytique de l'Aluminium*. in *Travaux ICSOBA 3rd Int. Conf.* . 1973. Nice.
8. Ouzilleau, P., A.E. Gheribi, and P. Chartrand, *Prediction of CO_2/CO formation from the (primary) anode process in aluminium electrolysis using an electrothermodynamic model (for coke crystallites).* Electrochimica Acta, 2018. **259**: p. 916-929.

9. Novak, B., A.P. Ratvik, Z. Wang, and T. Grande. *Formation of Aluminium Carbide in Hall-Héroult Electrolysis Cell Environments*. 2018. Cham: Springer International Publishing.
10. Thorne, R.J., C. Sommerseth, E. Sandnes, O. Kjos, T.A. Aarhaug, L.P. Lossius, H. Linga, and A.P. Ratvik, *Electrochemical Characterization of Carbon Anode Perfomance*, in *Light Metals 2013*, B. Sadler, Editor. 2013, Springer. p. 1207-1211.
11. Kjos, O.S., T.A. Aarhaug, E. Skybakmoen, A. Solheim, and H. Gudbrandsen. *Fundamental Studies of Perfluorocarbon Formation*. in *10th Australasian Aluminium Smelting Technology Conference*. 2011. Launceston, Tasmania.
12. Grjotheim, K., F. Nai Xiang, B. Haugsdal, and H. Kvande, *Current Efficiency Measurements in Laboratory Aluminium Cells—XI. Anode Gas Composition and Anode Consumption.* Canadian Metallurgical Quarterly, 1987. **26**(3): p. 181-184.
13. Zhu, H. and D. Sadoway, *An electroanalytical study of electrode reactions on carbon anodes during electrolytic production of aluminum*, in *Light Metals: Proceedings of Sessions,*. 2000, TMS: Warrendale, Pa. p. 257-263.
14. Brun, M., J. Thonstad, K. Grjotheim, and D. Bratland, *A study of the effect of cell geometry, bath convection, and the boudouard equilibrium on the operation of laboratory aluminum cells : preliminary report*. 1979, The Metallurgical Society of ASME: Warrendale, Pa.
15. Sjøen, R.V., *Anode gas measurement during aluminium electrolysis*, in *Institutt for materialteknologi*. 2019, NTNU.
16. Droßbach, P., *Zur Elektrometallurgie des Aluminiums.* Zeitschrift für Elektrochemie und angewandte physikalische Chemie, 1936. **42**(2): p. 65-70.
17. Silny, A. and T.A. Utigard, *Determination of the factors which control the CO/CO_2 ratio of the anode gas.*, in *Light metals 1995* J.W. Evans, et al., Editors. 1995, Minerals, Metals & Materials Society: Warrendale, Pa. p. 205–211.
18. Stanic, N., I. Jevremovic, A.M. Martinez, and E. Sandnes, *Bubble Evolution on Different Carbon Anode Designs in Cryolite Melt.* Metallurgical and Materials Transactions B, 2020. **51**(3): p. 1243-1253.
19. Grjotheim, K., M. Malinovsky, K. Matiašovsky, A. Silny, and J. Thonstad, *Current efficiency measurements laboratory aluminum cells II. Influence of alumina content.* Canadian Metallurgical Quarterly, 1972. **11**(2): p. 295-298.
20. Sun, Q., Z. Li, D.J. Searles, Y. Chen, G. Lu, and A. Du, *Charge-Controlled Switchable CO_2 Capture on Boron Nitride Nanomaterials.* Journal of the American Chemical Society, 2013. **135**(22): p. 8246-8253.
21. Aylward, G.H. and T.J.V. Findlay, *SI chemical data*. 5th ed. 2002, Milton: Wiley.
22. Davies, M. and P. Phennah, *Reactions of Boron Carbide and Other Boron Compounds with Carbon Dioxide.* Journal of Applied Chemistry, 1959. **9**: p. 213-219.
23. Åsheim, H., I.A. Eidsvaag, A. Solheim, H. Gudbrandsen, G.M. Haarberg, and E. Sandnes. *The Influence of Polarisation on the Wetting of Graphite in Cryolite-Alumina Melts*. in *Light Metals 2020*. 2020. Cham: Springer International Publishing.
24. Silny, A., M. Korenko, V. Daneck, and M. Chrenkova, *Carbon Consumption during Laboratory Aluminium Electrolysis.* Canadian Metallurgical Quarterly, 2006. **45**(3): p. 275-282.

25. Sadler, B. and S. Algie, *A Porosimetric Study of Sub-Surface Carboxy Oxidation in Anodes*, in *Essential readings in Light Metals*, J.A. Johnson and A. Tomsett, Editors. 2013. p. 594-605.
26. Farr-Wharton, R., B.J. Welch, R.C. Hannah, R. Dorin, and H.J. Gardner, *Chemical and electrochemical oxidation of heterogeneous carbon anodes.* Electrochimica Acta, 1980. **25**(2): p. 217-221.
27. Putri, E., G. Brooks, G. Snook, and I. Eick. *Anode characterisation and gas diffusion behaviour in aluminium smelting*. in *AIP Conference Proceedings 1805*. 2016. Bandung, Indonesia: AIP Publishing.
28. Sterten, Å., *Structural entities in NaF • AlF_3 melts containing alumina.* Electrochimica Acta, 1980. **25**(12): p. 1673-1677.
29. Jentoftsen, T.E., H. Linga, Holden I., B.E. Aga, Christensen V.G., and F. Hoff, *Correlation between Anode Properties and Cell Performance*, in *Light metals 2009* G. Bearne, Editor. 2009, Warrendale, Pa. p. 301-304.

Chapter 6

Bubble phenomena and bubble properties for horizontal and vertical carbon anode surfaces in cryolite melt applying a see-through cell

Nikolina Stanic[1], Ana Maria Martinez[2], Kristian Etienne Einarsrud[1] and Espen Sandnes[1]

[1] Department of Materials Science and Engineering, Norwegian University of Science and Technology NTNU, NO-7491 Trondheim, Norway
[2] SINTEF Industry, 7034 Trondheim, Norway

This paper has been published in Metals Special Issue MDPI 2021 [1]. The paper is extended version of Manuscript published in Materials Proceedings [2] presented at *The 1st International Electronic Conference on Metallurgy and Metals (IEC2M 2021)*. Some minor corrections have been made to this paper post-publication for spelling/typos and to improve clarity.

Abstract
Gas bubble behavior on a carbon anode in a cryolite melt has been studied using a see-through cell. The phenomena studied have been growth, coalescence, detachment, and wetting during electrolysis. The surface orientation affects bubble behavior. Therefore, two different anode designs were tested, an anode with a horizontal downward-facing surface and an

anode with a vertical surface. At the horizontal anode, it was found that one large bubble was formed by the growth and coalescence of smaller bubbles, and finally, the large bubble detached periodically. For the vertical anode surface, the detaching bubbles were smaller, and most of them had been going through a coalescence process prior to detachment. The bubbles detached randomly. The coalescence process from the initiation to the final bubble shape at the vertical surface took about 0.016-0.024 s. The current density did not affect the duration of the coalescence. The bubble diameter was decreasing with increasing current density for both anodes. The values were in the range 7.2 to 5.7 mm for the horizontal anode in the current density interval 0.2-1.0 A cm^{-2} and in the range 3.7 mm to 1.5 mm for the vertical anode in the current density interval 0.1-2.0 A cm^{-2}. The wetting contact angle for the vertical anode stayed more or less constant with an increase in current density, which likely can be attributed to the decreasing bubble size rather than an increase in polarization. In addition to the bubble phenomena described and bubble properties found, the impact of the results for better design of laboratory-scale studies is discussed.

Keywords: carbon anode; cryolite melt; bubble behavior; see-through cell; wetting

6.1 Introduction

Industrial production of aluminum is performed by the Hall-Héroult process in which alumina is dissolved in a molten bath consisting mainly of cryolite, which is predominantly used because of its capacity as a solvent for alumina and fairly suitable ionic conductivity. Aluminum-containing bath species are reduced at the aluminum cathode, forming molten aluminum, while CO_2 is formed in the anode reaction with oxygen-containing bath species and the anode carbon as reactants [3-5]. Gas present at the anode surface contributes to an increased cell voltage. The extra voltage drop in an industrial cell due to the presence of bubbles is about 0.15-0.35 V out of a typical total cell voltage of ~ 4.5 V [6]. The presence of gas bubbles under the anode contributes to the overall bath resistance because the gas is non-conducting. Accordingly, models have been developed for calculating the resistance effect based on the average

layer thickness and fractional surface coverage of the surface. An expression for the additional voltage drop caused by gas bubbles that are applied in numerous cell models has been developed by Hyde and Welch [7]. It expresses the voltage drop in terms of the anodic current density, electrolyte conductivity, average bubble layer thickness, and anode fraction covered by bubbles and is given by:

$$V_{bubble} = \frac{i_a}{\kappa} \cdot \left[\frac{d_b}{(1-\phi)} - d_b\right] \tag{6.1}$$

where i_a is the anodic current density in A cm^{-2}, κ is the conductivity in Ω^{-1} cm^{-1}, d_b is the bubble thickness in cm, and Φ is the fraction of anode covered by bubbles.

Haupin [8] verified that the analysis and Equation (6.1) by Hyde and Welch could also be used for calculating the average bubble layer thickness under the anodes by:

$$d_b = \left[\frac{(0.5517 + i_a)}{(1 + 2.167 \cdot i_a)}\right] \tag{6.2}$$

The average data reported for gas coverage under the anodes that are predominantly horizontally orientated are in the range of 40-80 %, the thickness of the gas bubble layer is 0.5-0.7 cm, and the bubble size is 100-120 cm [5]. The rate of release of the bubbles is also dependent on the path they have to travel and also the angle of the surface from the horizontal. To obtain faster gas bubble release, slotted anode designs have been introduced. With the use of slotted anodes, these parameters have therefore changed, and the bubble layer resistance has been reduced.

Anode bubble behavior for different anode designs and materials has been studied industrially and also on a laboratory scale. The present work examines more closely the bubble behavior for lab-scale anodes typically used to study reaction kinetics and mass transport, anode effect phenomena, current efficiency, kinetics for different carbon quality, wetting, *etc*. To study bubble behavior in more detail is of importance because bubble behavior affects all the above-mentioned features. Bubbles studies are very important in order to improve proposed models for electrolytic aluminum metal production, *e.g.*, the work by Einarsrud *et al.*

[9], which ultimately can be used to improve the industrial process. Lab-scale experiments are crucial for better understanding key phenomena.

Several researchers [10-14] studied the bubble life cycle, which includes processes as bubble nucleation, bubble growth, bubble coalescence, and bubble detachment on a downward-facing horizontal carbon anode surface applying a transparent cell capturing images from the side openings combined with the observation from above [10, 11], side openings only [12], and side and bottom openings [13]. Cassayre *et al.* [10, 11] reported that small individual spherical bubbles were formed at the horizontal anode surface (Ø 9 mm). The bubbles grew and coalesced to form larger bubbles, eventually covering the majority of the anode surface. After reaching maximum size, the bubble was sliding toward the edge of the anode, where it was detached and rose vertically. After bubble detachment, the bubble-free part of the anode surface was available for a new bubble cycle of bubble nucleation, grow, coalescence and detachment. Bubble behavior has also been observed on a vertical anode surface only in a few studies. Cassayre *et al.* [10, 11] studied bubble formation on the verticals side of a graphite anode cylinder at lower current densities (0.05-0.2 A cm^{-2}). It was found that bubble nucleation occurs on specific nucleation sites. The number of nucleation sites grew with the increase in current density. Spherical shaped bubbles grew and coalesced until reaching 23 mm in diameter, then detached and escaped vertically. The surface coverage was found to be very high, and the small bubbles appeared stuck to the anode.

Kiss *et al.* [15] studied the detachment of air bubbles from downward-facing horizontal and inclined plates in transparent water tanks. Bubbles are generated at the nucleation sites. They continue to grow there, and after they reach a certain size, they detach from the surface. During bubble growth, an equilibrium exists between the forces that retain the bubble at the nucleation site and the forces that try to remove the bubble. This equilibrium evolves with the increasing volume of the bubble to the point when the detachment forces overcome the retaining forces. For the detachment process, besides the volume of the bubble, the equilibrium depends on geometry and orientation of the surface, flow-induced forces, *etc.* Bubble detachment from the surface and departure from the nucleation site does not coincide for every surface orientation. For the horizontal surface facing upward, the bubble detachment from the nucleation site and

its departure from the surface typically coincides but for the horizontal surface facing downward or for the vertical surface, the bubble detachment and departure do not have to coincide. On these vertical and horizontal downward-facing surfaces, bubbles can move away from the nuclear site (depart by slow, creeping motion), but to finally leave the surface (detachment from the surface) can occur later. The main detachment force is due to the buoyancy effect. The movement of the liquid exerts another important detachment force, a drag force.

In a liquid, bubbles try to maintain a spherical shape. The driving force behind this shape is the surface tension contracting the bubble to the smallest possible area. When a bubble is moving through a liquid, it can lose its spherical shape because the forces pushing on the bubble from the outside change as it moves through a liquid. Bubble deformation occurs under the effect of gravity and drag forces. Haberman and Morton [16] observed three types of bubble shapes: spherical, ellipsoidal, and spherical cap for vertically rising bubbles in different liquids.

Zawala *et al.* [17] studied bubble bouncing at a clean water surface. When a bubble is rising upwards in a liquid and approaches a flat free surface with a large enough velocity, a film of liquid is trapped, creating a pressure build-up in the bubble. The liquid film in time breaks, and the bubble bursts through the free surface, causing small droplets of the liquid phase to be propelled into the air, and smaller bubbles can also form in the liquid phase. This bubble bursting phenomenon occurs faster, whereas bouncing usually takes more time [18].

Interfacial tension is the force of attraction between the molecules at an interface. At the gas/liquid interface, this force is often referred to as surface tension. Surface tensions determine the geometry of the bubble. A contact angle (also referred to as a wetting angle) is defined geometrically as the angle formed by a liquid at the three-phase boundary where a liquid (l), gas (g), and solid (s) intersect (Figure 6.1). The interfacial tensions form the equilibrium contact angle of wetting (θ), which is described by the Young equation:

$$\cos\theta = \frac{(\gamma_{sg} - \gamma_{sl})}{\gamma_{lg}} \tag{6.3}$$

where θ is the contact angle and γ is interfacial tension with the l, s, and g subscript corresponding to liquid, solid, and gas, respectively.

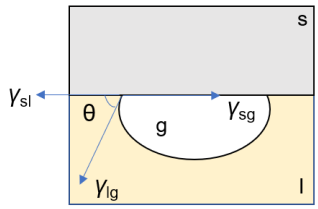

Figure 6.1. Contact angle (θ) and surface tensions (γ) of gas bubble (g) in liquid (l) underneath the solid (s).

Contact angle hysteresis (wetting hysteresis) is a change in contact angle due to movement of the triple line (a line on the surface where solid, liquid, and gas can all coexist in equilibrium) along the solid surface (Figure *6.2*). The advancing contact angle, θ_a (wetting angle), can be defined as the contact angle at the location where the gas phase is displaced by the liquid. The receding angle, θ_r (de-wetting angle), is then defined as the contact angle at the location where the liquid is displaced by the gas. Contact angle hysteresis is the difference between advancing and receding contact angles.

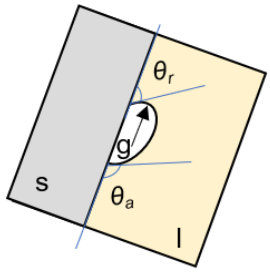

Figure 6.2. Advancing (θ_a) and receding (θ_r) contact angles for a gas bubble at the three-phase boundary where a liquid (l), gas (g), and solid (s) intersect.

The aim of the current work was to study bubble formation and detachment for two typical anode designs used in lab studies, a horizontal (facing downward) electrode surface and a vertical electrode surface. Video recordings during electrolysis were performed in a see-through cell. The results obtained in this work cannot be directly applied to an industrial setting, but the increased knowledge of the bubble behavior is useful for further studies, especially in laboratory-scale studies applying similar anode designs.

6.2 Experimental part

6.2.1 See-through furnace

The experiments were conducted in the see-through furnace shown in Figure 6.3(a). In Figure 6.3(b) is shown a principal sketch of the experimental setup. Video recording was performed from the side. The furnace has two side openings that are closed with lids. The lids are removed and replaced with quartz windows only during video recording in order to reduce heat loss. The quartz crucible was resting at an alumina tower construction that was used to adjust the height level of the crucible. The alumina tower was placed in a ceramic crucible whose function was to catch the bath in case of crucible breakage during the experiment.

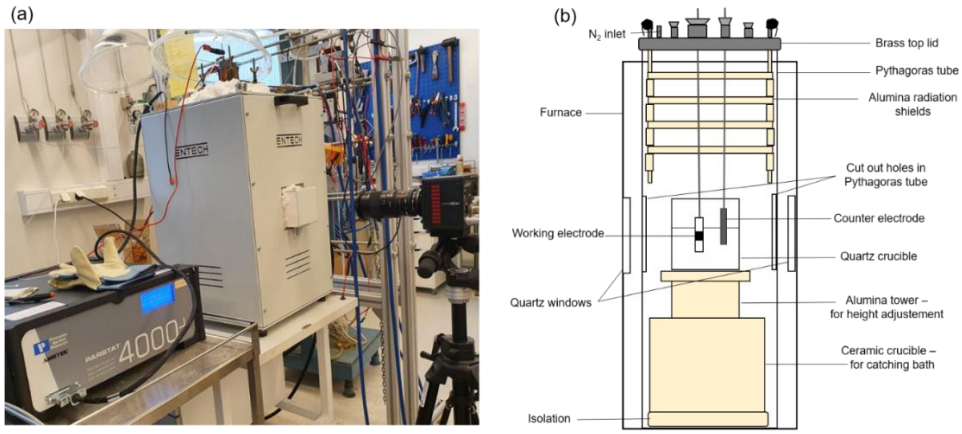

Figure 6.3. (a) The see-through furnace, the potentiostat, and the high-speed camera, (b) principle sketch of the interior of the furnace.

6.2.2 Bath composition and temperature

Experiments were performed in a cryolite bath at a temperature of 890 ± 10 °C. The bath composition used in this study is listed in Table 6.1. The calculated liquidus temperature was 838 °C. The following empirical equation was used for the calculation of the liquidus temperature [3]:

$$t = 1011 + 0.14(\text{mas\%}AlF_3) - 0.071(\text{mass}AlF_3)^{2.5} + 0.0051(AlF_3)^3 - 10(\text{mass\%}LiF_3) + 0.736(\text{mass\%}LiF)^{1.3} + 0.063((\text{mass\%}AlF_3)(\text{mass}LiF))^{1.1} - 3.19(\text{mass\%}CaF_2) + 0.03(\text{mass\%}CaF_2)^2 + 0.27((\text{mass}AlF_3)(\text{mass}CaF_2))^{0.7} - 12.2(\text{mass\%}Al_2O_3) + 4.75(\text{mass}Al_2O_3)^{1.2} \quad (6.4)$$

Equation (6.4) agrees reasonably with the literature data [19].

It was crucial to introduce additives to the cryolite-based bath in order to reduce the liquidus temperature and to increase the service time of the quartz crucible. LiF was added to obtain this low temperature, and in addition, it was observed that LiF helped to reduce the fumes inside the furnace and, with that, improved total visibility. The superheat was on purpose kept this large in order to avoid bath freeze due to frequent openings of the furnace side lids and to prolong the video recording time. The bath was contained in the quartz crucible with a wall thickness of 2 mm. The crucible lifetime was a maximum of 5-6 h, including the heating process, which took a minimum of 2 h. The quartz crucible normally broke down due to a formation of holes in the quartz wall at the bath meniscus. On heating, when a temperature of 890 °C was achieved, the side lids of the furnace were removed and replaced with the quartz windows. After some time (approximately 20-30 min), the bath started to freeze on the quartz walls due to heat loss. This was associated with a reduction in bath temperature. The quartz windows were removed and replaced with the side lids. If necessary, the set point of the furnace power supply was increased by 5-10 °C. After 15 min the side lids were removed, and the quartz crucible and bath were checked for transparency in order to continue the experiment.

Table 6.1. Cryolite bath composition.

-	wt%	Specification	Producer
Al_2O_3	3	γ-alumina	Merck
AlF_3	15	sublimed "in house"	Industrial grade
LiF	15	purum	Riedel-de-Haën
CaF_2	5	precipitated pure	Merck
Cryolite	62	synthetic, purity >97%	Sigma-Aldrich

6.2.3 Anode design

Two anode designs, one horizontal and one with a vertical surface and with the same dimensional length (10 mm), were applied. The horizontal anode and the vertical anode are shown in Figure 6.4. Both anodes were created as described in [20]. A purified graphite material (Schunk Tokai Scandinavia, AB, Trollhättan, Sweden) was the active electrode material. Boron nitride (BN) (BN5000, Kennametal, Newport, UK) was used for anode shielding. The immersion depth of the carbon surface of the anodes was around 3.5 cm. As a counter electrode, a stainless steel (SS) rod with a diameter of 5 mm was used. The SS rod was immersed around 4 cm into the bath, which provided an area of approximately 6.5 cm^2.

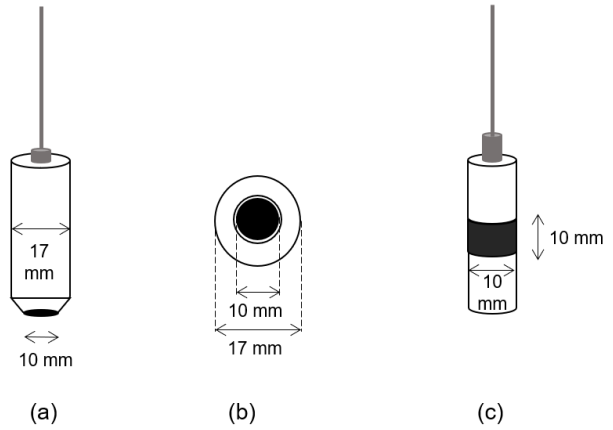

Figure 6.4. Anode designs with the same dimensional length of 10 mm; (a) the horizontal anode with surface area 0.79 cm^2 45 degrees angle chamfered boron nitride edges (with small BN shielding around carbon surface, less than 1 mm), (b) the horizontal anode shown from below and (c) the vertical anode with surface area 3.14 cm^2.

6.2.4 Experimental methods

Electrochemical measurements were performed using a PARSTAT 4000+ (Princeton Applied Research, Oak Ridge, TN, USA) potentiostat and a 20 A booster (KEPCO, Naju, South Korea). A two-electrode system was used. A reference electrode was not applied due to space limitations in the

cell, and the object inside the bath made disturbance to the video image. Electrolysis was performed at constant cell voltage for the horizontal anode (in the interval 1.5-2.5 V) and for both anodes at constant current (in the interval 0.1-0.8 A for the horizontal anode and 0.3-6.3 A for the vertical anode). Current *vs.* time measurements for the horizontal anode were transformed into frequency spectra by using a Fast Fourier Transform (FFT) algorithm in "Sigview v4.3-spectrum and signal analysis" (SignalLab e.K. Pforzheim, Germany) using spectral analysis default settings. The signals were transformed into the frequency domain to evaluate how the power of the signal is distributed over a range of frequencies to determine the dominant frequency. The sampling rate (Fs) was 5 Hz. Consequently, the spectrum has a frequency range from zero to Fs/2, 0-2.5 Hz.

A two-electrode system was used, as shown In Figure 6.5. The working electrode is the electrode where the reaction of interests occurs, and in the present study, it was either the horizontal anode or the vertical anode. The SS rod functioned as the counter electrode. The working (WE) and working sense (WSE) connections from the potentiostat were connected to the anode, while the reference electrode (RE) and counter electrode (CE) connections were connected to a SS rod.

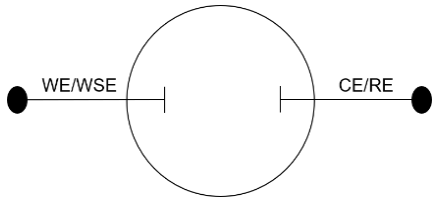

Figure 6.5. The schematics of the two-electrode setup, the working (WE) and working sense (WSE) connected to the anode and the counter (CE) and reference electrode (RE) connected to SS rod.

A PhotronFastcam Mini AX camera (Photron, Tokyo, Japan) was used for the video recording. Three different frame rates were used, 60 fps (frames per second) for the recording of the bubble behavior for both anode designs, and 125 and 250 fps were used in addition for the vertical anode. Recording with the higher rate was used in order to be able to capture fast events such as coalescence. Photron Fastcam Viewer 4 (PFV4) software (Photron, Tokyo, Japan) was used for controlling the Photron high-speed camera, for data saving, and for image processing. An example of the improved image quality is shown in Figure 6.6.

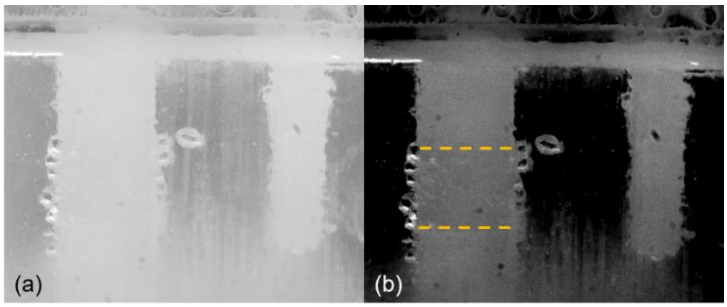

Figure 6.6. The image (a) before and (b) after image processing in PFV4 (Photron Fastcam Viewer 4). The image shows an example of using the vertical anode design. The yellow dashed lines indicate the border between the carbon and boron nitride material. The stainless steel rod is shown on the right in the image. The image was taken during electrolysis at a constant current density of 0.25 A cm^{-2}.

6.3 Results and discussion

6.3.1 Bubble behavior on the horizontal anode

In Figure 6.7 is shown one bubble life cycle, which includes the bubble nucleation, growth, coalescence, and bubble detachment during electrolysis at a constant cell voltage of 1.5 V. The corresponding average current density was 0.4 A cm^{-2}. The beginning of the bubble cycle was defined to be when the anode surface is free of a large bubble, which is the situation right after the bubble from the previous cycle is detached, frame (1). It was found that one cycle lasts 328 frames. Since the video recording was obtained with a speed of 60 fps, the bubble cycle time was found to be 5.47 s. There was no possibility with the current setup to position the camera to observe the bottom of the horizontal anode straight from below. Therefore, the bubble nucleation and coalescence were difficult to observe. Growth of the bubbles and detachment as one big bubble was well observed from the side. The bubbles grew to a size as large or slightly larger than the horizontal carbon surface before it started to slide toward the edge (frame (325)) and was detached (frame (329)) in Figure 6.7.

In Figure 6.8(a), the details of the characteristic saw-tooth curve of the current-time data are shown. When a bubble was detached, a sharp jump in current occurred, and the current obtained its highest value. When

bubbles are nucleating, growing, and coalescing, the current density decreases almost linearly while bubbles are covering more and more of the surface. At the time of detachment of a big bubble, the surface is never totally free of bubbles. As can be seen in Figure 6.7 for frames (1) and (329), the carbon surface is indicated with the yellow dashed line. While one large bubble is sliding toward the edge to be detached, the smaller bubbles are already nucleating and growing at the left part of the anode surface. From frame (329) and to a certain extent frame (1), it can be seen that the bubble layer is thicker on the left side than at the tail of the departing bubble. Bubbles strongly affect the potential components at gas-evolving electrodes. For areas where bubbles almost block the electrode surface, the current density will be close to zero, but for areas where bubbles do not block the electrode surface, the current density is greater than the average [16]. Frame (318) corresponds to the smallest current measured, *i.e.*, when a big bubble almost covers the whole anode surface. Frame (329) corresponds to the highest current value, *i.e.*, the time of detachment of a large bubble. From Figure 6.8(a), the bubble cycle time was found to be around 5.5 s and is very close to 5.47 s found in Figure 6.7.

In Figure 6.8(b) is shown the FFT analysis of current-time data, which provided a dominant frequency of 0.18 Hz corresponding to a bubble cycle time of 5.5 s. This confirms that the dominant frequency equals the bubble release frequency.

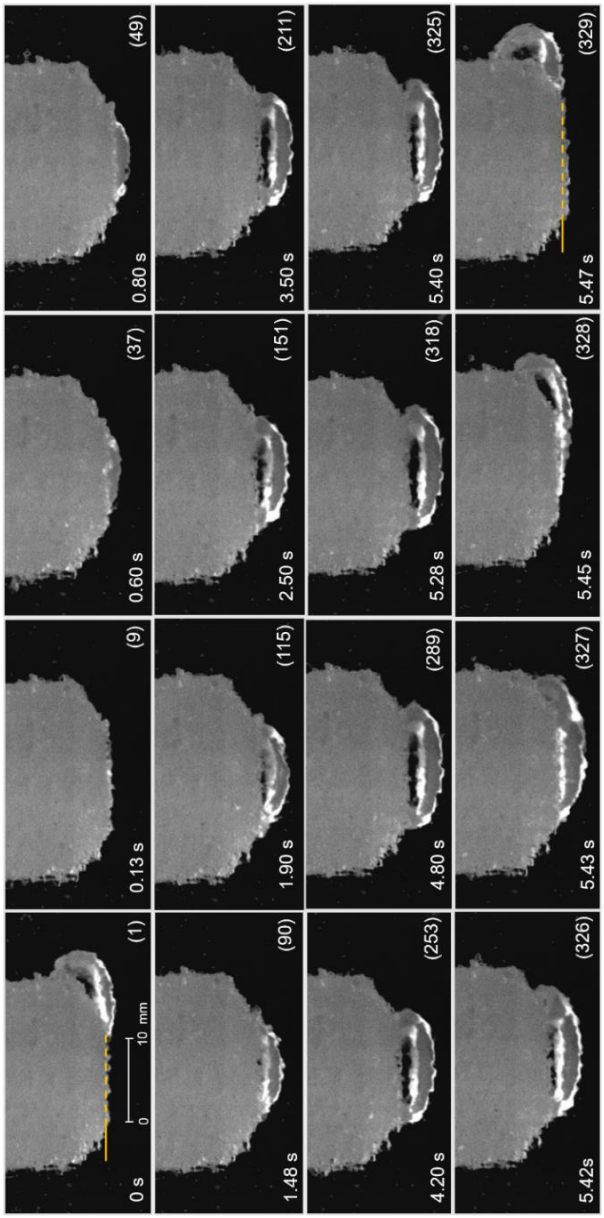

Figure 6.7. Cycle of one bubble at the horizontal surface during electrolysis at a constant cell voltage of 1.5 V with an average current density of 0.4 A cm^{-2}. Each individual image represents one frame with the corresponding number. The frame rate was 60 fps. The frame number is given in the brackets. Frame (1) is defined as 0 s and shows the situation right after a large bubble from the previous bubble cycle is detached from the anode surface. The horizontal yellow line in frames (1) and (329) represents the position of the carbon anode surface. A scale bar is shown in frame (1).

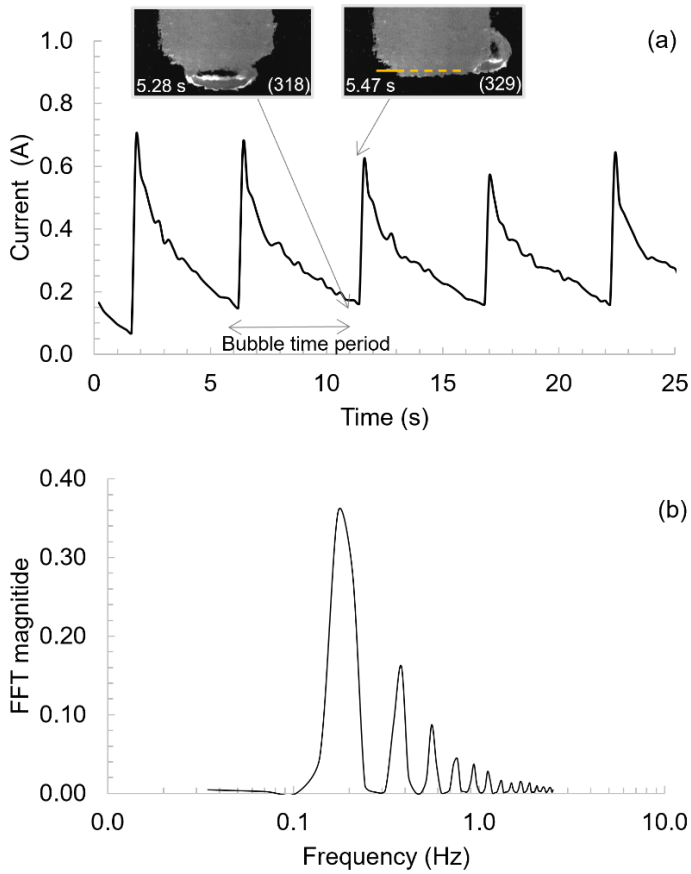

Figure 6.8. The horizontal anode: (a) current *vs.* time at a constant cell voltage of 1.5 V and details of the saw-tooth shaped current density-time curve. Frame (318) corresponds to the smallest current measured, and frame (329) corresponds to the current peak. (b) FFT (Fast Fourier Transform) spectra of current density-time data.

The thickness of the bubble was determined as the vertical distance between the anode surface and the bubble surface just before the bubble started to slide toward the edge of the anode for its detachment. This would correspond to frame (253) in Figure 6.7 for current density 0.1 A cm^{-2}. For the horizontal anode at a current density of 1 A cm^{-2}, the thickness of the bubble was found to be around 4.6 mm. Most studies have suggested that the bubble layer thickness is around 5 mm in laboratory cells [10-12]. Cassayre *et al*. [10] observed that the bubble layer under a graphite anode (Ø 9 mm) was slightly decreasing with current density and its thickness

was in the interval 4.2-5.0 mm for a current range in the interval 0.2-1.6 A cm^{-2}.

In the present study, it was observed that the bubble, after its detachment from the anode surface, was rising vertically up (Figure 6.9) and bounced twice at the bath surface, frame (7) and frame (11), before bursting into many smaller bubbles (frame (16)). Bubble bouncing phenomena due to surface tension have also been observed in a clear water system [17] and in an air/oil/water system [21]. In the present work with cryolite bath, even not observed from the video pictures, there might have been a thin crust that the bubbles have bounced against. The superheat in the experiment was very high, around 50 °C, but also the heat loss from the furnace was largely due to the window openings. Based on this, the existence of a crust cannot be excluded. The observed fog (highlighted at frame (1) in Figure 6.9) around the counter electrode (at the right) forms because the produced aluminum is not being able to dissolve in the electrolyte because the electrolyte is saturated with aluminum around the CE. Metal fog in a see-through cell has been studied by Zhuxian *et al*. [22].

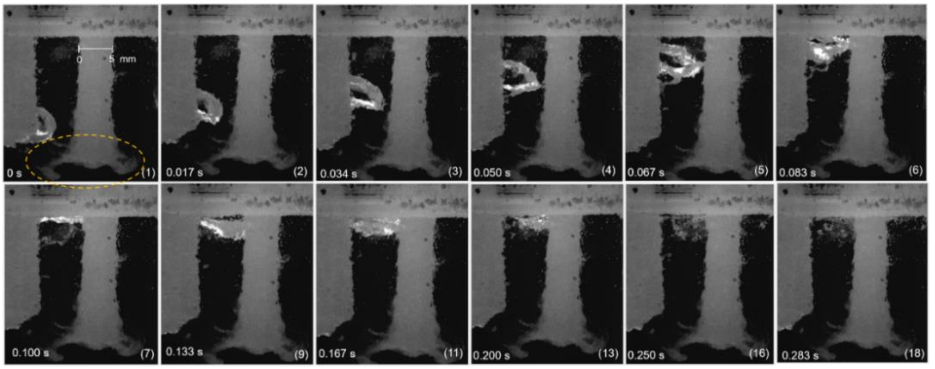

Figure 6.9. A bubble rising after its detachment from the horizontal surface, bouncing and bursting at the bath surface during electrolysis at a constant cell voltage of 1.5 V with the average current density of 0.4 A cm^{-2}. The frame rate was 60 fps. Frame numbers are placed in brackets. Frame (1) is defined as 0 s right after the bubble was detached from the anode surface. A scale bar is shown in frame (1).

For cell voltages above 1.8 V, it was observed that also some small bubbles detached from the surface. The average current density at 1.8 V is 0.6 A cm^{-2}. In Figure 6.10 is shown an example for the cell voltage equals 2.0 V, where a quite clear image was obtained. The bubble is probably

nucleated at the edge of the anode, where the voltage is high when the big bubble is covering the major fraction of the total anode area. The stream of smaller bubbles was also observed in the video, and the stream became more pronounced with increasing current/voltage. At lower cell voltage (1.5 V), this phenomenon was not observed. This was not further investigated.

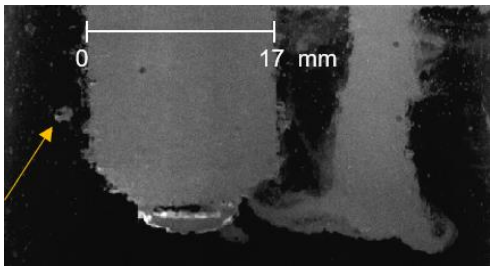

Figure 6.10. One small bubble detaching from the surface (yellow arrow pointing) while one large bubble growing at the surface during electrolysis at a constant cell voltage of 2.0 V. Average current density was 0.7 A cm^{-2}. A scale bar is shown.

The average bubble diameter after bubble detachment from the horizontal surface as a function of current density is presented in Figure 6.11. The bubble diameter was calculated as an average value of 10 bubbles at each current density. Error bars represent a 95% confidence interval assuming a normal distribution. In Appendix 6.6 is described how the bubble diameter was measured (Figure 6.20). The bubble diameter decreases with increasing current density, from around 7 mm at 0.25 A cm^{-2} to around 6 mm at 1 A cm^{-2}. Cassayre *et al.* [10, 11] measured the bubble diameter before its detachment from the surface and also found that the bubble diameter decreased with increasing current density. It was explained by less pronounced coalescence at higher current densities and that bubbles escape before covering the anode and grow to full size. An increase in current density and a corresponding increase in potential lead to an increase in the number of nucleation sites, *i.e.*, meaning a smaller and a higher number of bubbles are formed. These bubbles coalesce into one large bubble, and the bubble cycle time is shorter. It should be added that the bubble-induced convection increases with an increasing current density as more bubbles are released from the surface. The increased convection promotes easier detachment of the bubbles and also contributes to the formation of smaller bubbles [20]. In Figure 6.11 is shown the bubble release frequency as a function of current density. The bubble release

frequency was obtained from analysis of the recorded videos. The error bars show the 95% confidence interval. It was observed that the bubble release frequency variates (mostly increases) with the duration of the polarization, i.e., the bubble release frequency at the beginning of the polarization is lower than toward the end of the polarization. This is most pronounced at the higher current densities, 0.7 and 1.0 A cm^{-2}. This can be explained by the bubble-induced convection regime that establishes during the polarization, and convection increases with an increasing current density as more bubbles are produced and released from the anode surface and promote easier bubble removal. The FFT analysis of voltage-time data was performed by using Sigview software, and dominant frequency was also obtained in Figure 6.11. It can be seen that the dominant frequency coincides with the bubble-released frequency. The bubble release frequency increased with increasing current density. Going from 0.25 to 1.0 A cm^{-2}, the current density has increased by factor 4 while the bubble release frequency has increased from 0.2 to 0.5 Hz corresponding to a factor of 2.5. The difference of the factors suggests that at increasing current densities, a relatively larger number of smaller bubbles is going off from the edge of the anode. This also was observed from the videos. The decrease in bubble diameter with increasing current density magnifies this effect.

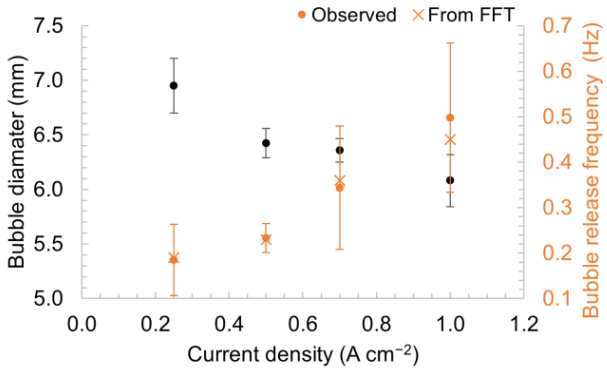

Figure 6.11. Bubble diameter after detachment from the horizontal surface and bubble release frequency as a function of the nominal current density.

Solheim *et al.* [23] and Åsheim *et al.* [24] used an immersion-emersion technique to measure wetting between carbon and cryolite. It was found that the polarization strongly improved wetting for

the melt low in alumina (1 wt% Al_2O_3), and the wetting increased with increased polarization. Xue and Øye [12] measured the contact angle at the horizontal anode (Ø 10 mm) in the coalescence and growth stage to be in the interval 30-45°, which was found to increase with increased bubble size. The contact angle of the bubble just before the bubble left the anode surface was measured to be 110-130°. Cassayre *et al.* [11] used a hot-stage microscope to study the wetting of graphite by the cryolite mixture at 1000 °C. The wetting angle on graphite was measured to be 120-130°. Huang *et al.* [14] used the sessile drop method to study the wettability of the cryolite at 1215 K on graphite and an industrial carbon anode and found that wettability was poor for both anodes.

In the present study, the contact angle of the bubble before it started to slide toward the edge to be detached from the horizontal anode surface was measured for different current densities. In Appendix 6.6 is shown an example of a measurement of contact angle (Figure 6.22). The contact angle was calculated as an average value of 4 bubbles at each current density. Error bars represent a 95 % confidence interval assuming T-distribution. Results are shown in Figure 6.12. It was found for the horizontal anode that the average contact angle values decrease with increasing current density from 120° at 0.25 A cm^{-2} down to 105° at 1.0 A cm^{-2}. However, the error bars more or less overlap, indicating there is not a significant statistical difference. From Figure 6.11, it is seen that the bubble size is decreasing with increasing current density. The anode is shielded with boron nitride (BN), and according to Åsheim *et al.* [24], BN is better wetted by the cryolite in comparison to carbon. The big bubble could be in contact with the BN ring surrounding the anode illustrated in Figure 6.4(b). Hence, the contact angles reported in Figure 6.12 could represent the contact angle in the BN/cryolite/gas system rather than for C/cryolite/gas system or a mix between them. More details on wetting and contact angles are included in the treatment of the results of the vertical anode in 6.3.2.

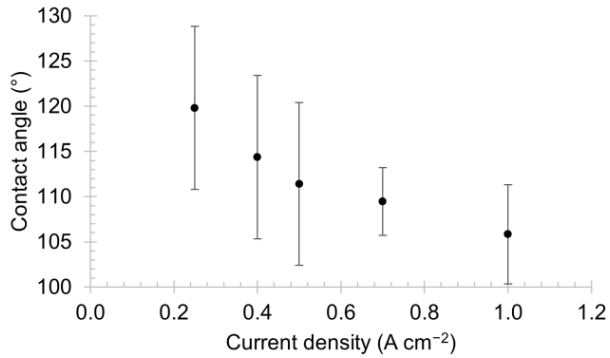

Figure 6.12. The change of contact angle of the bubble at the horizontal anode during electrolysis at different current densities.

6.3.2 Bubble behavior on the vertical anode

The bubble life cycle (nucleation, growth, coalescence, and detachment) at a vertical surface was studied in detail at low current density, 0.1 A cm^{-2}, and with higher frame rates 125 fps and 250 fps, than for the horizontal. At this current density, convection is low in comparison to higher current densities, and the transparency of the melt was at its best due to the small number of dispersed bubbles in the melt. The images are shown in Figure 6.13 and Figure 6.14. It was observed that the bubble formation occurred at specific nucleation sites, which was particularly evident for current densities lower than 0.5 A cm^{-2}. For higher current densities, observation is difficult due to the formation of more and smaller bubbles covering the surface. No periodic pattern in bubble growth and coalescence was found, making the bubble life cycle more of a random process. It was observed that some bubbles formed at the surface were coalescing with other bubbles, either with bubbles positioned nearby or with bubbles sliding upwards along the vertical anode surface. It was also observed that some bubbles were not coalescing, either detaching from the surface immediately or resting at the surface for a random time before detaching. In order for a bubble to leave the surface, it has to grow to a certain size. The measured diameter of detached bubbles for a current density of 0.1 A cm^{-2} was in the range of 3.3 to 3.6 mm (Figure 6.17). If the bubble gets entrapped at the boron nitride/carbon boundary, the resting time is radically increased, as discussed below in relation to Figure 6.14.

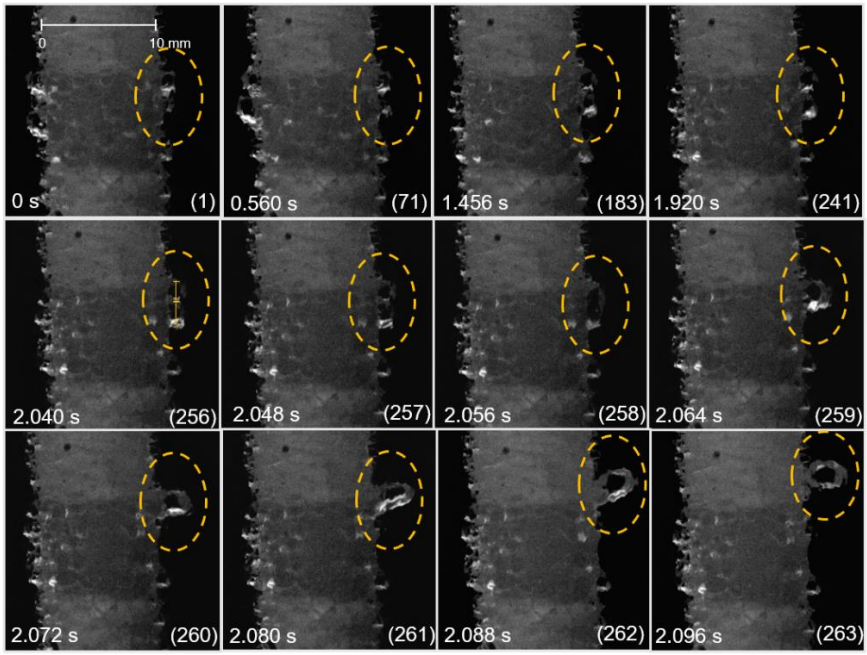

Figure 6.13. Process of coalescence of two bubbles (marked in yellow dashed line) into one bigger bubble and its immediate detachment from the vertical surface during electrolysis at a constant current density of 0.1 A cm^{-2}. The frame rate was 125 fps. The frame number is given in the brackets. Frame (1) is defined as 0 s. A scale bar is shown in frame (1).

In Figure 6.13 is shown the process of coalescence of two bubbles into one bubble and the immediate detachment of that bubble. The upper bubble was growing at the anode surface when a smaller bubble was formed below, in frame (1). Both bubbles were growing, and the lower bubble was approaching the upper bubble. The (apparent) diameter of both bubbles was measured in frame (256) and was found to be 2.0 mm for the upper bubble and 2.5 mm for the lower bubble. The apparent bubble diameter was measured as the maximum diameter when the bubble was sticking to the surface, as shown in frame (256). In frame (257), it can be seen that the lower bubble was approaching the upper bubble. Frame (258) represents the intermediate stage in the coalescence process. In frame (259), the new bubble has obtained its final shape. The coalescence process is fast, taking place in about three frames corresponding to 0.024 s. The apparent bubble diameter after coalescence was 3.3 mm. Immediately after coalescence, the new bubble has gained enough buoyancy to be able to detach from the anode surface. The detachment process starts in frame

(260). The bubble is completely detached in frame (263), and the diameter after detachment was 3.4 mm.

In Figure 6.14 is shown the fast process of coalescence of three bubbles into one bubble. The diameter of the three bubbles was measured to be around 1.5 mm, frame (1). Frame (3) represents the intermediate stage in the coalescence process. In frame (4), the new bubble has obtained its shape and a diameter of 2.7 mm. The coalescence process is fast, taking place in about two frames corresponding to 0.016 s. After coalescence, the bubble was resting and growing at the boundary between boron nitride (BN) and carbon anode (C). The bubble detachment is observed in frame (295), where the bubble is rising. The bubble diameter after detachment was 3.3 mm. The long resting of the bubble at the BN/C boundary could be explained by the work of Åsheim *et al.* [24], who predicted that gas bubbles could be entrapped at the boundary due to better wetting of the BN by the cryolite in comparison to carbon. Probably such a bubble needs extra time to grow to a certain size because it is in contact with the BN. It probably also needs to grow bigger to be able to detach. However, no clear evidence for this was found because the size of the bubbles was in the same size range as bubbles detached from other places on the carbon surface.

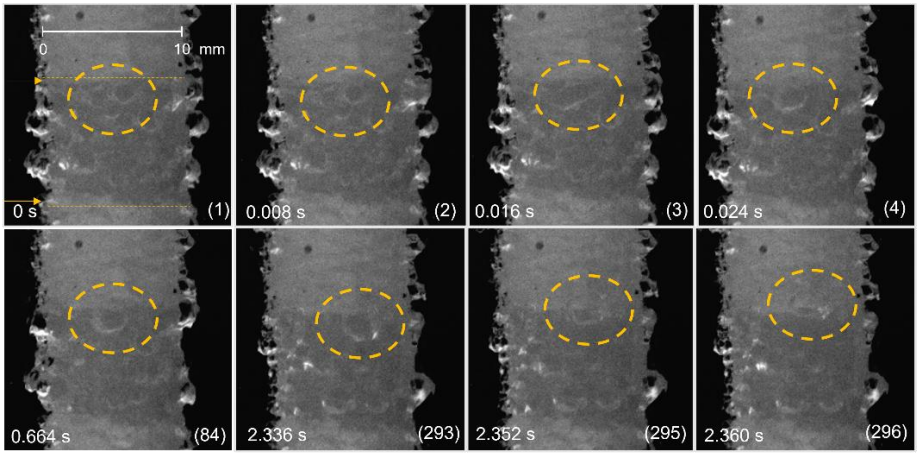

Figure 6.14. Process of coalescence of three bubbles (marked in yellow dashed line) into one larger bubble and its prolonged resting at the upper part of the anode at the boundary between BN and C during electrolysis at a constant current density of 0.1 A cm^{-2}. The frame rate was 125 fps. The frame number is given in the brackets. Frame (1) is defined as 0 s, indicating the start of the coalescence process. A scale bar is shown in frame (1). The yellow arrows in frame (1) indicate the C-BN borders.

The process of coalescence of bubbles at the vertical surface was also studied for three more current densities with different frame rates, 0.2 A cm^{-2} with 125 fps, 0.5 A cm^{-2} with 250 fps, and 1.0 A cm^{-2} with 250 fps. For the current density of 0.2 A cm^{-2}, the coalescence process occurred over 2 to 3 frames corresponding to 0.016-0.024 s. For the current densities of 0.5 A cm^{-2} and 1.0 A cm^{-2}, the coalescence process occurred over 4 to 5 frames corresponding to 0.016-0.020 s. For all applied current densities, 0.1, 0.2, 0.5, and 1.0 A cm^{-2}, the coalescence process took about 0.016 – 0.024 s, meaning the current density and cell voltage did not have a significant influence on the time for the coalescence process.

In Figure 6.15 is shown an example where a bubble was hitting the bath surface three times. After detachment, the bubble is rising and hits the bath surface in frame (4), bounces and hits the bath surface again in frame (8), bounces and hits the bath surface again in frame (11) before bursting in frame (12). As discussed in relation the horizontal anode in 6.3.1., a very thin crust could be responsible for the bubble bouncing at the bath surface.

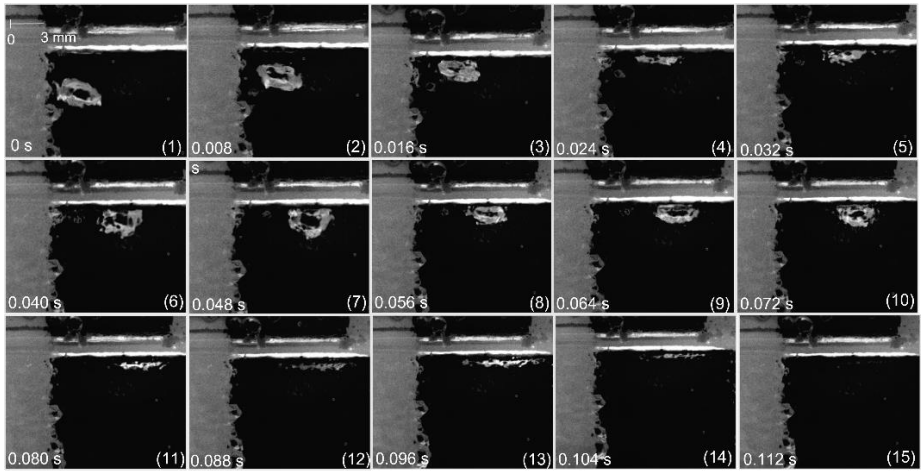

Figure 6.15. Bubble bouncing and bursting at the bath surface after detachment from the vertical anode at 0.1 A cm^{-2}. Upper BN part of the anode is shown. The frame number is given in the brackets. Frame (1) is defined as 0 s, indicating bubble detachment from the carbon surface and rise. A scale bar is shown in frame (1).

During the bubble life cycle, it was found that also some smaller bubbles (Ø ~ 1 mm) were detached from the surface, although not many

bubbles (Figure 6.16). With the increasing current density, this phenomenon became more pronounced. At the stainless-steel rod (to the right) it could be observed a droplet at the rod bottom, which probably is aluminum produced.

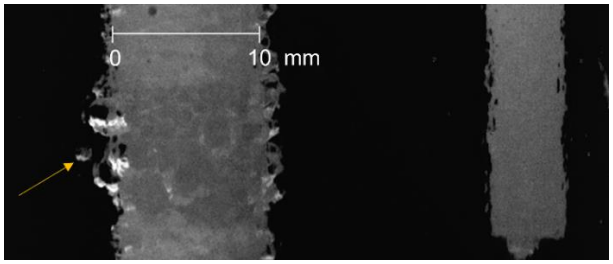

Figure 6.16. One small bubble (yellow arrow pointing) is detaching from the vertical surface (at the left) at a constant current density of 0.1 A cm^{-2}. A scale bar is shown in the figure.

The average bubble diameter after detachment from the vertical surface as a function of current density is presented in Figure 6.17. It was calculated as an average value of 10 bubbles at each current density. Error bars represent a 95% confidence interval assuming a normal distribution. In Appendix 6.6 is described how the bubble diameter was measured (Figure 6.21). The bubble diameter is decreasing with increasing current density, from around 3.4 mm at 0.1 A cm^{-2} to around 1.7 mm at 2.0 A cm^{-2}. The increase in current density and thereby the corresponding increase in potential provide a higher driving force for nucleation of relatively more bubbles. The bubble-induced convection is more efficient for the vertical anode than for the horizontal anode due to the increased number and smaller bubbles formed on the vertical anode. The larger flow makes bubble detachment faster. The buoyancy also favors the vertical anode since for the horizontal anode, the bubbles have to grow to a larger in size before being able to detach.

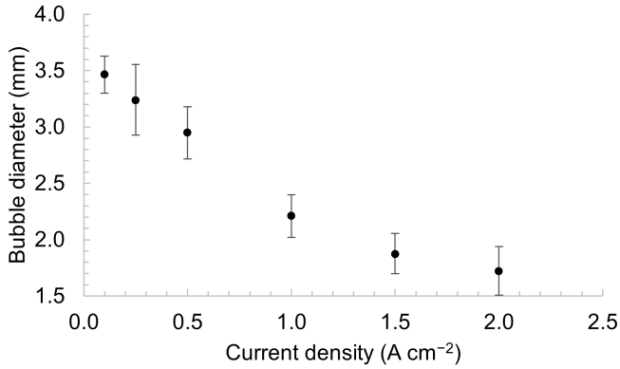

Figure 6.17. Bubble diameter after detachment from the vertical surface as a function of nominal current density.

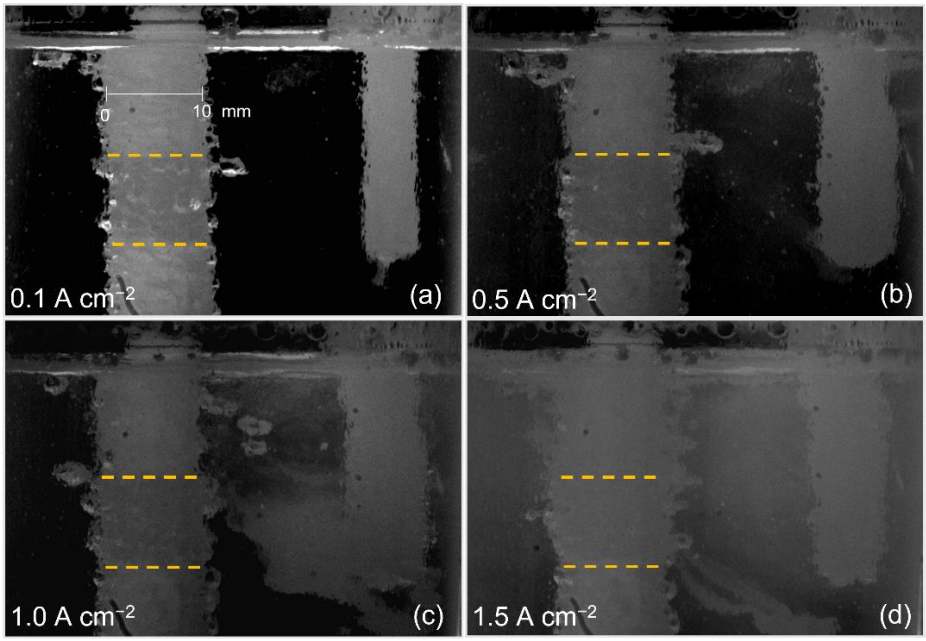

Figure 6.18. Images of bubble evolution at the vertical anode during electrolysis at different current densities: (a) 0.1, (b) 0.5, (c) 1.0, and (d) 1.5 A cm^{-2}. The yellow line indicates the border between the carbon and boron nitride material. The frame rate was 125 fps. A scale bar is shown in (a).

In Figure 6.18 can be seen bubble evolution at different current densities: 0.1, 0.5, 1.0, and 1.5 A cm^{-2}. With increased current density, more and smaller bubbles are released from the anode surface. At 1.5 A cm^{-2}, it is difficult to distinguish the carbon from the BN due to the great amount of

smaller bubbles that hinder visibility. At the counter electrode, aluminum is produced, and in Figure 6.18I for 1.0 A cm^{-2}, it is evident that aluminum fog is approaching the anode. At 1.5 A cm^{-2} in Figure 6.18(d), the melt is less transparent because of more fog produced and more efficient spread from convection in addition to more numerous and smaller bubbles.

In the present work, contact angles of bubbles at the vertical anode were measured for different current densities, 0.1, 0.5, and 1.0 A cm^{-2}. Angles were measured for bubbles in two different stages in the bubble cycle, *i.e.*, in the growth stage before coalescence and after coalescence just before detachment from the surface. An example of how the contact angle was measured is shown in Figure 6.23 in Appendix 6.6. If the bubble was moving very slowly, *i.e.*, sliding upwards along the surface, the advancing and receding contact angles could be measured. The bubbles were, to a small degree, observed sliding up along the carbon surface. The bubbles measured were either resting at the surface or in the detachment process. The measured contact angles were therefore termed as lower and upper rather than advancing and receding contact angles, respectively. The measured contact angles of bubbles and corresponding bubble diameter are shown in Figure 6.19 as a function of current density. Contact angles were calculated as an average value of 4 bubbles at each current density. Error bars are in 95% confidence interval assuming T-distribution. As mentioned earlier, Åsheim *et al.* [24] found that the wetting is improved with the increased polarization, *i.e.*, increased current density. In the present paper, it was not observed a decrease in contact angle with an increase in current density, which would indicate improvement in wetting. Only slight variations in contact angle were observed, which could depend more on bubble size than polarization.

The modified Young equation describes the relationship between the cosine of the contact angle and the base radius of the drop (bubble) [25, 26]:

$$\cos\theta = \cos\theta_{\infty} - \frac{\gamma_{slg}}{r \cdot \gamma_{lg}} \tag{6.5}$$

θ is the contact angle, $\theta\infty$ when $r \rightarrow \infty$, r is the drop (bubble) base radius.

According to the modified Young equation (6.5), a decrease in bubble diameter should increase the wetting angle, i.e., the wetting decreases. Applied to Figure 6.19, this indicates that the increase in wetting

expected from an increase in polarization might be counteracted by a decrease in the bubble size with current density.

For the bubbles resting at the vertical surface in the growth stage just before coalescing with other bubbles, the lower angle was measured to be around 67°, and it seems not to vary significantly with the increased in current density, Figure 6.19(a). The apparent bubble diameter was measured as the maximum diameter when the bubble was sticking to the surface, as shown in Figure 6.13 (frame 256). The upper angle was measured to be around 55°, and it seems to slightly decrease with the increasing current density, Figure 6.19(a). An increase in current density is accompanied by a decrease in bubble size, as shown in Figure 6.17. Hence contact angle slightly increases with the increase in bubble size.

Drelich *et al.* [25, 27] studied advancing and receding contact angle for water and ethylene glycol and the air bubble and water system for a homogenous surface and different heterogeneous surfaces as a function of a drop (bubble) size. For the smooth and homogeneous surface, Drelich observed that both advancing and receding angles remained constant with small variations (~ 3°) for the system with a 1-7 mm drop (bubble) diameter. For rough and heterogeneous surfaces, only a slight variation in the advancing contact angle value occurred while receding contact angles measured with the use of the sessile drop technique decreased with the drop or bubble size for all examined rough surfaces. Drelich concluded that surface roughness and heterogeneity affect the contact angle and drop or bubble size relationship for the system with 1-7 mm drop or bubble diameter. In the present work, the upper angle, which corresponds to the receding angle, seems to slightly, although not significantly, increase with the increasing bubble diameter. The bubble diameter interval is narrow, less than 1 mm, which is probably not large enough to see a bigger picture and to relate Drelich's conclusions with the obtained results.

In the final stage of the bubble cycle, just before its detachment from the anode surface, the lower and upper contact angles also showed little variation with the increase in current density, as shown in Figure 6.19(b). The lower contact angle is measured to be around 120° and the upper around 67°. The values of the upper angles increased from ~ 55° to ~ 67°, from (a) to (b) but values for the lower angle increased significantly: from ~ 67° to ~ 120°. The difference between measured upper and lower contact angles from Figure 6.19(a) and (b) is mainly due to different stages in the bubble life cycle and different bubbles state (static/dynamic).

Bubbles in Figure 6.19(a) are sticking at the surface and are in the growth stage just before coalescence. After coalescence, the bubbles have grown large enough to be detached from the surface Figure 6.19(b). Measured contact angles in Figure 6.19(a) are considered to be static because the bubble is sticking to the surface; the lower contact angle is slightly higher than the upper contact angle due to the buoyancy effect, which acts on the bubble at the vertical surface. For bubbles in Figure 6.19(b), the detachment process has already started as the detachment process started immediately after the coalescence. In general, a contact angle for a bubble in a detachment process is considered to be dynamic [28]. The bubble undergoes deformation, and the apparent symmetrical shape of the bubble was distorted. Hence, the lower contact angle increased significantly in going from (a) to (b).

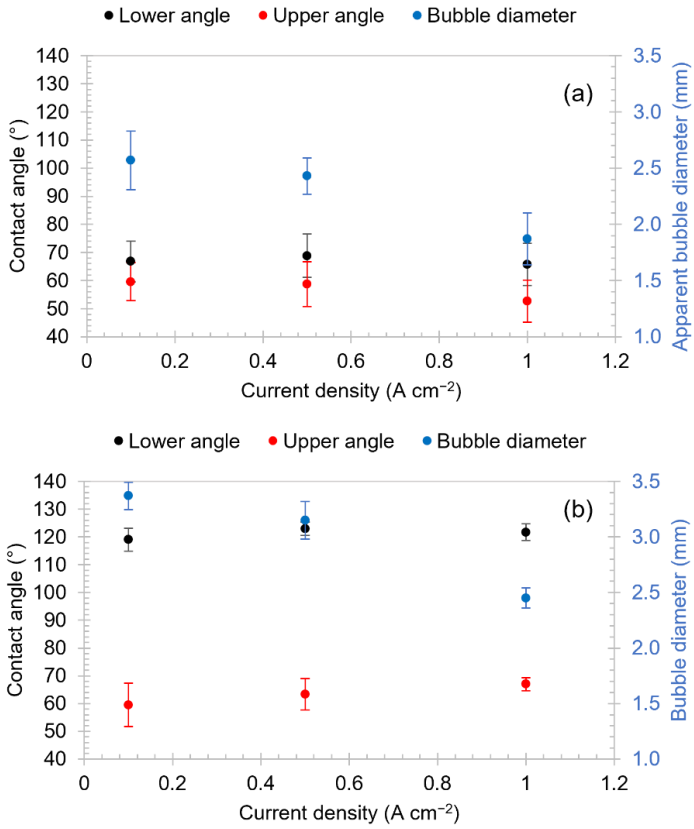

Figure 6.19. Lower and upper contact angle and the bubble diameter as a function of applied current density for the vertical anode, (a) for the bubble resting at the surface in the growth stage just before coalescence (b) for the bubble after coalescence just before detachment.

With the increased polarization, only slight variations in contact angle were observed. According to Åsheim *et al.* [24], wetting is improved with the increased polarization. For the present work, the alumina saturation was around 3.4 wt% at 898 °C according to calculation obtained by Software for Aluminum Smelting [29]. Since the alumina concentration was 3 wt%, the bath is close to saturation. Solheim *et al.* [23] observed in a bath with high alumina concentration (8 wt%) that polarization did not affect wetting significantly since the increase in alumina concentration changed the wetting of carbon by cryolite from non-wetting to good wetting. However, the actual alumina concentration might be as important as the degree of saturation. The alumina concentration of 3 wt% in the present work is probably lower than the concentration needed to make the wetting change from non-wetting to good wetting. Fellner and Lubyova [30] studied the influence of the addition of different additives, among others LiF, on the wetting of graphite by cryolite. It was concluded that in an acidic bath, LiF has no effect on wetting, while in neutral and basic baths, LiF increases contact angle. In the present work, the bath contained 15 wt% LiF, 15 wt% AlF_3, and 5 wt% of CaF_2. The bath could therefore be neutral or slightly basic, and it is difficult to judge the influence of LiF on the actual contact values. However, the trends should be unaffected.

6.4 Impact of results and relation to other works

6.4.1 Small laboratory-scale anodes

One of the aims of the present work was to gain more knowledge for further improvement of the laboratory-scale studies. Based on the obtained results, the following could be stated:

1. Position of the counter electrode (CE): The current distribution across the working electrode (WE) is important. The CE was placed to the right of the WE, meaning the current path to the left side of the WE is longer than for the right side. During all experiments, it was not observed more bubbles forming on the right side of the WE compared to the left side. It can then be assumed that the current distribution for this electrode setup is sufficiently suitable for all practical purposes. This supports the findings in the work of Stanic *et al*. [20].

2. Bubbles resting at the BN surface: During all experiments, bubbles were observed resting at the boron nitride surfaces. The bubbles were formed as soon as the anode was immersed in the melt. The bubbles did not take part in any electrochemical reaction, and the same bubbles rested at the surface during the entire experiment, which typically could last about one hour for one specific electrode. The bubbles are thought to be either moisture or nitrogen arising from the bulk of the BN material.
3. Bubbles resting at the carbon surface: When immersing the anode in the melt, it was observed that bubbles to some degree formed at the carbon surface before any current or voltage was applied. The phenomenon was most pronounced for the horizontal anode where one big bubble was formed at the surface and interfered with the experiment. By gently vibrating the anode, the bubble could be removed but a new bubble formed in less than one minute. In the timeframe before a new bubble formed, the electrochemical measurement could be started. The bubble formation caused voltage overloading of the potentiostat when using the horizontal anode because the large bubble covered almost the whole anode surface.

The origin of the bubbles formed at both carbon and BN surfaces is not identified, although humidity and nitrogen gas are two compounds that are suspected. The anodes were dried at 120 °C for two to three hours before introduced to the cell. Even after having been immersed in the melt at 890 °C for one hour, the bubbles still formed. However, the bubbles are believed not to interfere with the electrochemical experiments because the bubbles on the carbon were easily displaced by the electrochemically formed CO and CO_2. For experiments involving gas coverage and gravimetric measurements, one should pay attention to the existence of these bubbles, *e.g.*, Åsheim *et al.*, where wetting of carbon anodes with and without BN shielding was studied by a gravimetric anode.

4. Presence of metal fog: The presence of fog can influence bubble size, wetting, reaction products. Metal fog can be electrochemically oxidized on the anode, and the CO/CO_2 ratio can be changed by the back reaction. Figure 6.18 shows that more fog is produced at higher current densities. For cathodic current densities up to 0.05 A cm^{-2} (the corresponding anodic current density is then about 0.1 A cm^{-2} as the counter electrode has approximately twice the area of

the vertical anode), the fog does not reach the anode in the time frame of the recording, which lasted about 40 s. For cathodic current densities around 0.25 A cm^{-2}, the fog reached the anode after 20 s. At higher current density, this time decreased. To reduce complications caused by the metal fog, the anode and cathode should be physically separated at least for longer duration experiments. Examples for physical separation can be found in the work by Zhao *et al.* [13], Stanic *et al.* [31], and Silny and Utigard [32]. A pool of aluminum at the bottom of the crucible could help by having a less foggy electrolyte.

6.4.2 Laboratory-scale anodes versus industrial anodes

For the lab anodes, it was found that with increasing current density, more and smaller bubbles formed at the surface as the increase in potential causes the number of nucleation sites to increase. The bubble release frequency was found to slightly increase with the duration of the polarization, and the size of released bubbles was observed to decrease. Overall, the increased number of smaller bubbles screen the anode surface to a higher degree. Kiss *et al.* [33] developed a mathematical model of the bubble layer in an aluminum reduction cell based on microscopic modeling. From simulations, it was found that (when the size of the anode is large enough) big gas bubbles move slowly toward the edge of the anode and sweep away smaller bubbles during their movement. Instead of having many smaller bubbles detaching randomly, the detachment of the gas is more organized with bigger bubbles. A larger bubble gives a higher probability for collision with other bubbles. Wang *et al.* [34] concluded that the anode size has some influence on the bubble size. Horizontal anodes with 20, 30, and 40 mm in diameter were studied. The bubble size was found to decrease with decreasing surface area for the same current density. Einarsrud [35] carried out experiments on an industrial cell and found that with increasing anode age, the voltage oscillation related to bubbles increased in frequency and in magnitude due to the slots worn down toward the end of the anode service time. The disappearing of the slots makes in practice a larger anode and probably reflects the same phenomenon, *i.e.*, larger bubbles with increased anode size both for lab and industrial sized anodes illustrating some similar findings at different scales.

Wang and Taberaux [36] studied gas bubbling using an intermediate size anode (15.2 cm in diameter) and the impact of anode consumption. The electrolysis was conducted at 200 A for over 72 h. For an anode with a large diameter and sharp edges, the bubble volume increased as current density increased till it reached a maximum (at ~0.8 A cm^{-2}) and then decreased with a further increase in current density. For an anode with reduced diameter and rounded edge, an increase in current density increased both bubble frequency and bubble volume, although the bubble size was always smaller than for the anode with sharp edges. In the present paper using a small lab anode (10 mm in diameter), it was observed that the size of the detached bubble decreased with increasing current density, which can be comparable with the results of Wang and Taberaux for the sharp edge anode after a reaching specific current density. The increased current density causes larger bubble-induced convection, which might be the main cause of the observed trends. The bubble size obtained with the rounded edge anode of Wang and Taberaux is probably less influenced by the current induced convection and does not have an initial high bubble size or a maximum bubble size.

6.5 Conclusions

At the horizontal downward-facing surface, the bubbles grew and coalesced to form one large bubble that then grew larger and finally started to slide toward the edge of the anode surface for detachment. Even though the big bubble detached, the surface was never free of bubbles for the studied current density range 0.25-1.0 A cm^{-2}. At the vertical anode surface, the detaching bubbles were smaller, and most of them had been going through a coalescence process prior to detachment. Coalescence of two and three bubbles into one bigger bubble was observed on the vertical anode surface. The coalescence process occurred quite fast, in the interval 0.016-0.024 s from initiation to the final bubble shape was established. Some intermediate stages in the coalescence process were captured. The bubble diameter decreased with the increasing current density for both the horizontal and the vertical anode. Explanations for these observations are the larger number of nuclei formed at higher potential and the more efficient bubble-induced convection. The measured contact angles for the

vertical anode termed as lower and upper contact angles showed little variation with change in current density. It was assumed that the current density had a stronger effect on the contact angle through its effect on the bubble size than the polarization and associated surface roughening. The applied current densities (0.1-1.0 A cm^{-2}) and the obtained bubble diameter interval (~ 1.9-2.6 mm) were probably not large enough to reveal eventual changes in the contact angle.

The obtained results are helpful for easier and better design of laboratory-scale studies investigating, *e.g.*, current distribution, anode bubble evolution, current efficiency, and wetting properties.

6.6 Appendix

Bubble diameter was measured based on the pixel information using PFV4 software. The target bubble was a bubble detached from the carbon surface and had a nearly spherical shape. In Figure 6.20 and Figure 6.21 are shown examples of some nearly spherical-shaped bubbles during electrolysis for the horizontal and the vertical anode, respectively. The diameter was measured as shown in Figure 6.20 and Figure 6.21 and was defined as the distance between two points of the spherical bubble.

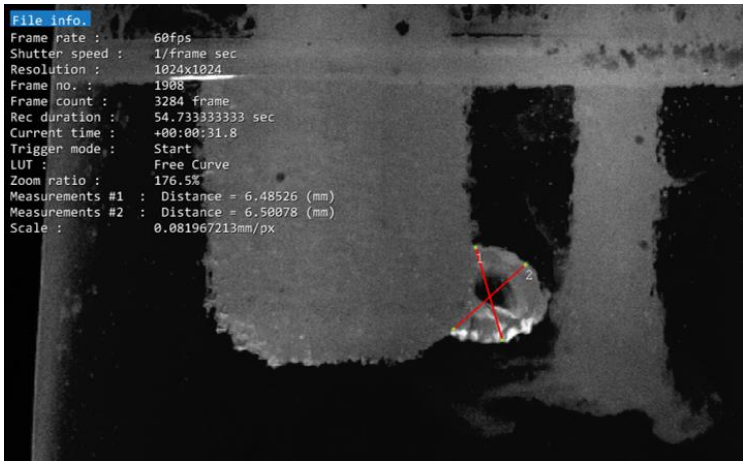

Figure 6.20. An example of measurement of the bubble diameter during electrolysis using the horizontal anode at current density 0.7 A cm^{-2}. The average value was used.

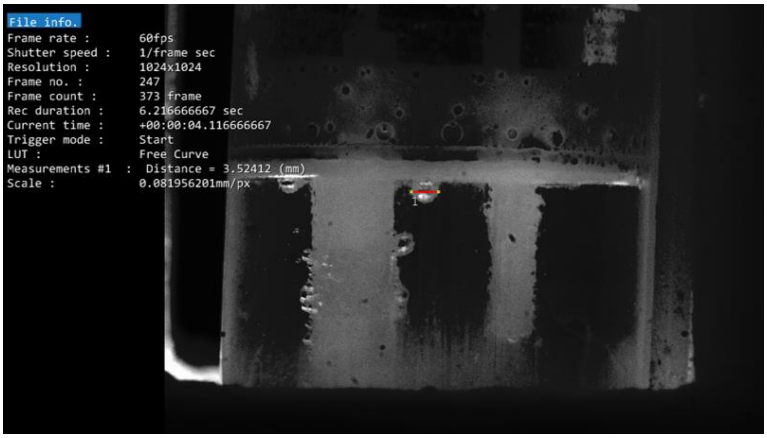

Figure 6.21. An example of measurement of the bubble diameter during electrolysis using the vertical anode at current density 0.25 A cm^{-2}.

The contact angle of the bubble at the horizontal and vertical anode was measured by drawing a tangent to the bubble profile at the point of the three-phase contact on an enlarged image. An example of a measurement of contact angle for the horizontal anode is shown in Figure 6.22, and an example for lower and upper contact angle for the vertical anode just before detachment is shown in Figure 6.23.

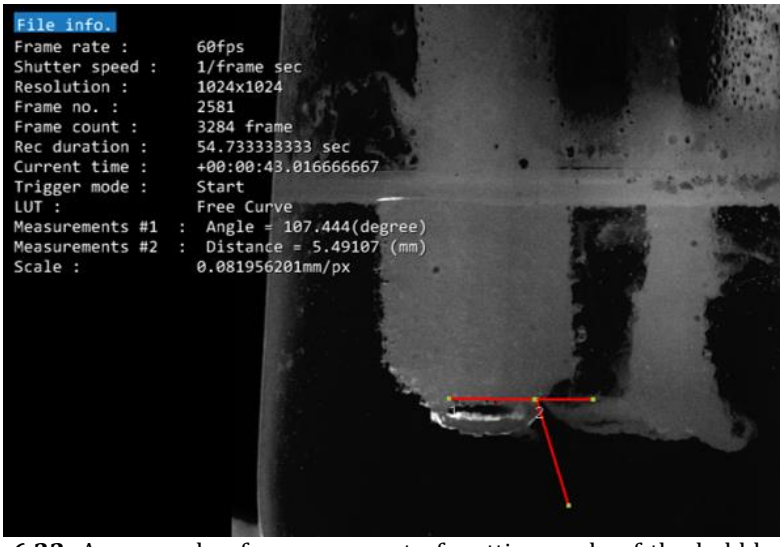

Figure 6.22. An example of measurement of wetting angle of the bubble on the horizontal anode just before it started to slide toward the edge of the anode to be detached during electrolysis at an average current density of 0.7 A cm^{-2}.

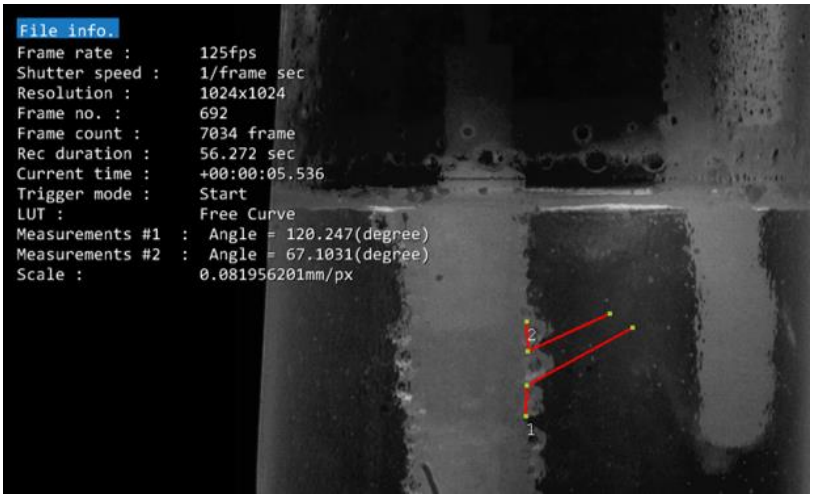

Figure 6.23. An example of measurement of lower and upper contact angle of the bubble just before detachment on the vertical anode during electrolysis at a constant current density of 0.5 A cm^{-2}.

References

1. Stanic, N., A.M. Martinez, K.E. Einarsrud, and E. Sandnes, *Bubble Phenomena and Bubble Properties for Horizontal and Vertical Carbon Anode Surfaces in Cryolite Melt Applying a See-Through Cell.* Metals, 2021. **11**(6): p. 965.
2. Stanic, N. and E. Sandnes, *Bubble Behavior on Horizontal and Vertical Carbon Anode Surfaces in Cryolite Melt Applying a See-Through Cell.* Materials Proceedings, 2021. **3**(1): p. 8.
3. Grjotheim, K. and H. Kvande, *Introduction to aluminium electrolysis : understanding the Hall-Héroult process*. 2nd ed. 1993, Düsseldorf: Aluminium-Verlag.
4. Thonstad, J., P. Fellner, G.M. Haarberg, J. Híveš, H. Kvande, and Å. Sterten, *Aluminium electrolysis : fundamentals of the Hall-Héroult process*. 3rd ed. 2001, Düsseldorf: Aluminium-Verlag. 359.
5. Tabereaux, A.T. and R.D. Peterson, *Chapter 2.5 - Aluminum Production*, in *Treatise on Process Metallurgy*, S. Seetharaman, Editor. 2014, Elsevier: Boston. p. 839-917.
6. Zhao, Z., Z. Wang, B. Gao, Y. Feng, Z. Shi, and X. Hu, *Observation of Anodic Bubble Behavior Using Laboratory Scale Transparent Aluminium Electrolysis Cells*, in *Light Metals 2015*, M. Hyland, Editor. 2015, Springer: Cham. p. 801-806.
7. Hyde, T.M. and B.J. Welch, *The Gas Under Anodes in Aluminium Smelting Cells. Part I: Measuring and Modelling Bubble Resistance under Horizontally Oriented Electrodes*, in *Light Metals The Minerals, Metals & Materials Society (TMS)*. 1997. p. 333.

8. Haupin, W. *Interpreting the components of cell voltage*. in *Light Metals: Proceedings of Sessions, TMS Annual Meeting (Warrendale, Pennsylvania)*. 1998.
9. Einarsrud, K.E., I. Eick, W. Bai, Y. Feng, J. Hua, and P.J. Witt, *Towards a coupled multi-scale, multi-physics simulation framework for aluminium electrolysis.* Applied Mathematical Modelling, 2017. **44**: p. 3-24.
10. Cassayre, L., G. Plascencia, T. Marin, S. Fan, and T. Utigard, *Gas Evolution on Graphite and Oxygen-Evolving Anodes During Aluminium Electrolysis*, in *Light Metals 2006*, T.J. Galloway, Editor. 2006, TMS: Warrendale. p. 379-383.
11. Cassayre, L., T. Utigard, and S. Bouvet, *Visualizing gas evolution on graphite and oxygen-evolving anodes.* JOM (USA), 2002. **54**(5): p. 41-45.
12. Xue, J. and H.A. Øye, *Bubble behaviour : cell voltage oscillation during aluminium electrolysis and the effects of sound and ultrasound*, in *Light Metals 1995*, J. Evans, Editor. 1995, TMS: Warrendale. p. 265-271.
13. Zhao, Z., Z. Wang, B. Gao, Y. Feng, Z. Shi, and X. Hu, *Anodic Bubble Behavior and Voltage Drop in a Laboratory Transparent Aluminum Electrolytic Cell.* Metall. Mater. Trans. B, 2016. **47**(3): p. 1962-1975.
14. Huang, Y., Z. Wang, Y. Yang, B. Gao, Z. Shi, and X. Hu, *Anodic Bubble Behavior in a Laboratory Scale Transparent Electrolytic Cell for Aluminum Electrolysis.* Metals, 2018. **8**: p. 806.
15. Kiss, L., S. Poncsak, D. Toulouse, A. Perron, A. Dröge, and V. Mackowiak. *Detachment of bubbles from their nucleation sites*. in *Multiphase Phenomena and Cfd Modeling and Simulation in Materials Processes*. 2004. Charlotte, North Carolina: Warrendale PA, TMS
16. Haberman, W.L. and R.K. Morton, *An Experimental Investigation of the Drag and Shape of Air Bubbles Rising in Various Liquids*. 1953, Navy Department The David W. Taylor Model Basin: Washington 7 D.C. p. 55.
17. Zawala, J., S. Dorbolo, N. Vandewalle, and K. Malysa, *Bubble bouncing at a clean water surface.* Phys Chem Chem Phys, 2013. **15**(40): p. 17324-17332.
18. Manica, R., E. Klaseboer, and D. Chan, *The impact and bounce of air bubbles at a flat fluid interface.* Soft Matter, 2016. **12**: p. 3271-3282.
19. Haupin, W., *The Liquidus Enigma*, in *Light metals 1992* E.R. Cutshall, Editor. 1991, Minerals, Metals & Materials Society: Warrendale, Pa. p. 477-480.
20. Stanic, N., I. Jevremovic, A.M. Martinez, and E. Sandnes, *Bubble Evolution on Different Carbon Anode Designs in Cryolite Melt.* Metallurgical and Materials Transactions B, 2020. **51**(3): p. 1243-1253.
21. Feng, J., M. Muradoglu, H. Kim, J.T. Ault, and H.A. Stone, *Dynamics of a bubble bouncing at a liquid/liquid/gas interface.* Journal of Fluid Mechanics, 2016. **807**: p. 324-352.
22. Zhuxian, Q., F. Liman, K. Grjotheim, and H. Kvande, *Formation of metal fog during molten salt electrolysis observed in a see-through cell.* Journal of Applied Electrochemistry, 1987. **17**(4): p. 707-714.
23. Solheim, A., H. Gudbrandsen, A.M. Martinez, K.E. Einarsrud, and I. Eick, *Wetting between Carbon and Cryolitic Melts. Part II: Effect of Bath Properties and Polarisation*, in *Light Metals 2015*. 2015, Hoboken, NJ, USA: John Wiley & Sons, Inc: Hoboken, NJ, USA. p. 671-676.
24. Åsheim, H., I.A. Eidsvaag, A. Solheim, H. Gudbrandsen, G.M. Haarberg, and E. Sandnes. *The Influence of Polarisation on the Wetting of Graphite in Cryolite-*

Alumina Melts. in *Light Metals 2020*. 2020. Cham: Springer International Publishing.
25. Drelich, J., *The Effect of Drop (Bubble) Size on Contact Angle at Solid Surfaces.* The Journal of adhesion, 1997. **63**(1-3): p. 31-51.
26. Boruvka, L. and A.W. Neumann, *Generalization of the classical theory of capillarity.* The Journal of Chemical Physics, 1977. **66**(12): p. 5464-5476.
27. Drelich, J., J.D. Miller, and R.J. Good, *The Effect of Drop (Bubble) Size on Advancing and Receding Contact Angles for Heterogeneous and Rough Solid Surfaces as Observed with Sessile-Drop and Captive-Bubble Techniques.* Journal of Colloid and Interface Science, 1996. **179**(1): p. 37-50.
28. Wang, G., D. Feng, A. Nguyen, and G.M. Evans, *The dynamic contact angle of a bubble with an immersed-in-water particle and its implications for bubble–particle detachment.* International journal of mineral processing, 2016. **151**: p. 22-32.
29. *Software for Aluminum Smelting*. 2005
Available from: https://peter-entner.com/E/ElProp-2/ElProp-2.htm.
30. Fellner, P. and Ž. Lubyova, *Influence of LiF, CaF_2, MgF_2 additives and of dissolved aluminium on wetting of graphite by the cryolite-based melt.* Chem. Papers, 1991. **45**(2): p. 201-204.
31. Stanic, N., E.T. Bø, and E. Sandnes, *CO and CO_2 Anode Gas Concentration at Lower Current Densities in Cryolite Melt.* Metals, 2020. **10**(12): p. 1694.
32. Silny, A. and T.A. Utigard, *Determination of the factors which control the CO/CO_2 ratio of the anode gas.*, in *Light metals 1995* J.W. Evans, et al., Editors. 1995, Minerals, Metals & Materials Society: Warrendale, Pa. p. 205–211.
33. Kiss, L.I., S. Poncsak, and J. Antille, *Simulation of the Bubble Layer in Aluminium Electrolysis Cells*, in *Light metals* H. Kvande, Editor. 2005, TMS: Warrendale, Pa. p. 559-564.
34. Wang, Z., B. Gao, H. Li, Z. Shi, X. Lu, and Z. Qiu. *Study on Bubble Behavior on Anode in Aluminum Electrolysis-Part I*. in *Technical Sessions, Minerals, Metals and Materials Society.; Light metals 2006*. 2006. Warrendale, Pa.:, San Antonio, Texas: TMS.
35. Einarsrud, K.E., *A Treatise on Interpolar Transport Phenomena*, in *Energy and Process Engineering*. 2012, Norwegian University of Science and Technology, NTNU: Trondheim, Norway. p. 303.
36. Wang, X. and A.T. Tabereaux. *Anodic Phenomena - Observations of Anode Overvoltage and Gas Bubbling During Aluminium Electrolysis*. in *Sessions, Light metals*. 2000. Nashville, TN: TMS;.

Chapter 7

A study of bubble behavior and anode effect on graphite and industrial carbon anode in a see-through furnace during aluminium electrolysis

Nikolina Stanic[1], Ana Maria Martinez[2], Kristian Etienne Einarsrud[1] and Espen Sandnes[1]

[1] Department of Materials Science and Engineering, Norwegian University of Science and Technology NTNU, NO-7491 Trondheim, Norway
[2] SINTEF Industry, 7034 Trondheim, Norway

The manuscript has been published as Scientific Article in the Journal *Metallurgical and Materials Transactions B* [1]. Some minor corrections have been made to this paper post-publication for spelling/typos and to improve clarity.

Abstract

Anode gas bubble behavior and anode effect on graphite and industrial carbon rod-shaped anode in a cryolite melt have been studied using a see-through furnace. The different carbon materials have different properties which can affect bubble behavior and electrochemical properties. Industrial carbon is more inhomogeneous with respect to structure, pore, aggregates and impurities in comparison to the graphite. More bubbles were nucleated

on the industrial carbon than on the graphite for the same current density. The time related to the coalescence process for both anodes was found to be in interval 16-24 ms and independent of the current densities. Bubbles detached from the horizontal surface of the anode have similar average diameter value for both anodes for current densities < 1.0 A cm^{-2}, while for current densities > 1.0 A cm^{-2}, the average diameter is lower for the industrial carbon anode. The onset of the anode effect occurred faster on the graphite than on the industrial anode. The PFC-containing gas layer appeared to be thicker and more stable on the graphite anode than on the industrial carbon anode.

Keywords: gas bubble, graphite, industrial carbon, cryolite, see-through furnace

7.1 Introduction

During the process of aluminum electrolysis CO_2 gas bubbles are produced and released from the anode. Gas present at the anode surface contributes to an increase in cell voltage by covering the anode surface and reducing the active surface area which increases current density (hyperpolarization). Due to gas present at the surface, the current lines between the anode and cathode become prolonged causing so called bubble overvoltage. The produced gas also causes an increase in ohmic resistance. The presence of bubbles makes an increase in energy consumption, the extra voltage drop due to bubbles is about 0.15 to 0.35 V out of a typical industrial cell voltage of ~ 4.5 V [2]. Thus, increased knowledge about bubble behavior is important. The gas evolution can be divided into three stages: nucleation, growth, and detachment. Bubbles nucleate at electrode surfaces, grow by mass transport of dissolved gas to the bubble surface or by coalescence with other bubbles, and detach from the electrode when forces pulling the bubbles away overcome the surface forces of adhesion. Many phenomena of gas evolution within each of these stages have been theoretically and experimentally investigated, but much remains to be studied in Hall-Héroult process.

Different carbon anode materials and anode surface properties affect bubble behavior. Huang *et al.* [3] studied bubble behavior under the graphite and industrial carbon anode in a transparent lab cell. Authors

found that bubbles on the industrial anode just before release were larger in comparison to bubbles on the graphite anode in the current density interval 0.7-1.1 A cm^{-2}. Gas coverage was found to be lower on industrial in comparison to a graphite anode. Bubble release period was found to be faster on the carbon than the graphite anode. Kasherman and Skyllas-Kazacos [4] studied the differences in the bath resistivity values for different anode materials, two carbon anodes with the same coke and pitch raw materials but with differences in granulation, the first had as authors referred optimum granulometry, while second had 50% fines fraction and was more porous than the first. The graphite was also used as a third material. Different materials can influence the bubble contribution to the effective bath resistivity by affecting the nature of the CO_2 gas bubbles produced during electrolysis. The two most likely causes of this phenomenon are differences in bubble size and differences in wetting behavior of the anode materials. Kasherman and Skyllas-Kazacos results showed that the anode with non-optimized granulometry had a lower gas volume fraction and it would produce a smaller bubble contribution to the bath resistivity than first anode and graphite for bath with CR = 3. No current density data were reported. Thorne *et al.* [5] studied anodes made from differences in coke and a graphite anode. Isotropic cokes had higher level of impurities than anisotropic cokes. Anodes made of isotropic cokes showed slightly lower overpotential. In another study, Thorne *et al.* [6] observed from polarization curves that graphite operated at the higher potential in comparison to coke anodes. It was also found that anodes with lowest metallic and sulfur impurities had highest overpotential [7]. Metallic impurities could act as electrocatalyst, *i.e.*, to catalyze the anode reaction and therewith reduce overpotential.

An anode effect is a phenomenon in molten salts electrolysis, especially in aluminium electrolysis and is not well understood in detail. The anode effect is caused by depletion of alumina underneath the anodes and causes the resistance (and the voltage) to increase dramatically. In industrial cell the voltage can increase from around 4 V to as much as 40 V and even higher. As the anode effect occurs, the bottom operating surface of the anode seems to be entirely surrounded by a film of gas. This covers the surface of the anode and pushes the bath away, producing the so-called non-wetting of the anode. The anode effect causes low energy-efficiency and decreases the aluminium production of the cell. It also induces the formation of PFCs (CF_4 and C_2F_6) and increases formation of CO [8].

Thonstad *et al.* [9-11] studied anode effect on graphite anodes in cryolite-alumina melts prior to and during the occurrence of the anode effect by potential sweep and galvanostatic measurements. The onset for anode effect seems to be a depletion of oxygen-containing ions which is followed by co-deposition of fluorine that leads to anode effect. The anode surface is covered by insulating gas film that inhibits charge transfer. The film becomes thicker once anode effect is established. The insulating gas film contains (C – F) bond [8]. During anode effect the fluorine reacts with the carbon forming PFC gases, CF_4 and C_2F_6. PFC formation happens according to reactions [12]:

$$Na_3AlF_6 + \frac{3}{4}\,C = Al + \frac{3}{4}\,CF_4 + 3\,NaF \qquad E^0 = -\,2.42\ V \tag{7.1}$$

$$Na_3AlF_6 + C = Al + \frac{1}{2}\,C_2F_6 + 3\,NaF \qquad E^0 = -\,2.68\ V \tag{7.2}$$

When a carbon anode in a molten salt is exposed to an increasing anode potential the current will eventually reach a so called critical current density (ccd) and then abruptly dropped towards zero referring to an anode effect. Zhu and Sadoway [13, 14] studied by cyclic voltammetry and chronoamperometry mechanisms of electrode reactions on carbon anodes (microelectrode) and observed that anode effect occurred when the potential exceeds 3.4 V *vs.* Al/Al^{3+} the cell current drops precipitously for bath containing 0.4 wt% Al_2O_3. It was observed that the existence of the resistive film formed on the anode surface was potential dependent which means that the film can be formed and removed at will by regulation of applied potential. The exit gas during anode effect occurs contains a mixture of CO_2, CO (secondary reaction between CO_2 and Al or C) and PFC gases (CF_4 and C_2F_6) [8]. Tabereaux *et al.* [15] measured the change in the anode gas composition during anode effects in industrial cell and found that the gas mixture consists primarily of CO, 60-70%, and CO_2, 20-30%; CF_4 content from both prebaked and Søderberg cells was in the range 16-20 %, and the C_2F_6 generation was small, 0.0-0.05%.

In previous work of Stanic *et al.* [16], the see-through cell was used to study in detail bubble behavior on the horizontal and vertical graphite anode. The aim of the present work was to study bubble behavior on anodes made from different materials. Different carbon materials have

different surface properties which can affect bubble behavior and electrochemical properties. One anode material was pure graphite and the other was industrial carbon. Graphite and industrial carbon show differences in composition (impurities content, *etc*), heterogeneity, porosity, surface roughness, *etc.*, that all have effect on bubble behavior (bubble life cycle, bubble size, wetting properties, *etc*). A shielded rod anode with defined surface area was used. The study goes into the details of bubble nucleation and its relationship with material surface properties. The bubble coalescence and size were studied for different current densities and discussed in detail. An additional focus of the study was on anode effects and how different materials affect it, prior to, during and after anode effect.

7.2 Experimental part

7.2.1 Furnace setup and anode design

The experimental setup was the same as used in [16, 17] and a principle sketch of the interior of the furnace is shown Figure 7.1. The furnace has two side openings which are closed with lids. In previous experiments lids were removed and replaced with quartz windows only during video recording in order to reduce heat loss. In this study when lids were removed, the furnace was left open during short recording times (max 60 seconds) in order to obtain clear images. The quartz crucible was resting at an alumina tower construction which was used to adjust the height level of the crucible. The alumina tower was resting inside and at the bottom of a ceramic crucible whose function was to catch the bath in case of crucible breakage during the experiment. Experiments were performed in a cryolite bath at a temperature of 890 ± 10 °C. The bath composition was synthetic cryolite with excess of AlF_3 equal to 24 wt% and Al_2O_3 concentration of 3 wt% with addition of 15 wt% LiF, 5 wt% CaF_2. The calculated liquidus temperature was 838 °C. Cryolite ratio was 1.85. It was crucial to reduce the liquidus temperature this low to increase the service time of the quartz crucible. With the pure synthetic cryolite, (the liquidus temperature 1005 °C), the service time of the quartz crucible was that short that it was not practical to perform experiments. The superheat of ~ 50 °C

was on purpose kept this large in order to avoid bath freeze due to frequent openings of the furnace side lids. The bath was contained in the quartz crucible with a wall thickness of 2 mm.

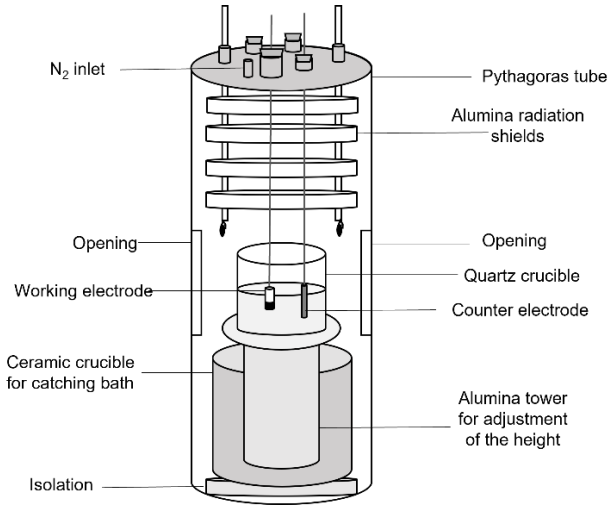

Figure 7.1. Principle sketch of the interior of the furnace.

An anode design used in this study was a shielded rod anode which has mixed geometry, *i.e.*, both horizontal and vertical surfaces, Figure *7.2*. Two different types of carbon material were used, a purified graphite material (Schunk Tokai Scandinavia, AB, Sweden) and a sample from new industrial carbon anode (Hydro Aluminium AS Årdalstangen, Norway). Some physicochemical properties of the graphite and industrial carbon used for anode construction given by supplier are listed in Table 7.1. A stainless steel (SS) rod with a diameter of 5 mm was used as a counter electrode, as in [17]. The rod was immersed around 4 cm into the bath which gave an area of approx. 6.5 cm^2.

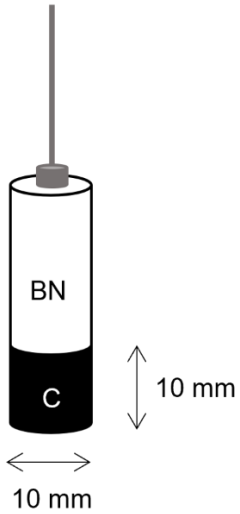

Figure 7.2. The shielded rod anode with surface area 3.9 cm^2.

Table 7.1. Physicochemical properties (from supplier) of the graphite and industrial carbon used for anode construction.

	Graphite anode	Industrial anode
Density, g cm^{-3}	1.80	1.60
Mean aggregate size, μm	76	-
Electrical Resistivity, μΩm	10	52
Compressive Strenght, MPa	68.9	41.6
Ash content, %	< 0.6	0.25
Na, ppm	< 0.05	6
Al, ppm	< 0.08	11
Ca, ppm	< 0.04	42
Ni, ppm	< 0.1	170
Fe, ppm	< 0.04	160
Si, ppm	< 0.1	54
S	15 ppm	1.74 %

7.2.2 Experimental methods

Electrochemical measurements were carried out using a PARSTAT (Princeton Applied Research) potentiostat and a 20 A KEPCO booster. A two-electrode system was used. A reference electrode was not applied due to space limitations in the cell and the object inside the bath made

disturbance to the video image. Electrochemical Impedance Spectroscopy (EIS) was used to determine the ohmic resistance of the cell at the Open Circuit Potential (OCP). OCP is the potential which the electrode obtains when it is not polarized. The electrolyte resistance R at OCP is value was used in the IR compensation of the voltage-time data. IR-compensation is needed as a current passing through the electrolyte will always induce a voltage drop (IR). Electrolysis was performed at constant current (in the interval 0.1-2.0 A cm^{-2}) with a sampling frequency of 50 Hz. A linear sweep technique was used to study an anode effect. The sweep rate was deliberately chosen to be higher (5 V s^{-1}) in order to avoid many disturbances due to evolution of gas and to reduce convection to get clear and visible bath. The potential was swept from open circuit potential (OCP) to 10 V and video of reaction was recorded together with I-E data. Due to furnace/cell and camera limitations this was found to be an only way to obtain and observe an anode effect under the given conditions.

A Photron Fastcam Mini AX camera was used for the video recording. Different frame rates were used: 60, 500 and 1000 fps (frames per second). Photron Fastcam Viewer 4 (PFV4) software was used for controlling the Photron high-speed camera, for data saving, and for image processing. Potential *vs.* time measurements were transformed into frequency spectra by using a Fast Fourier Transform algorithm in "Sigview software-spectrum and signal analysis" using spectral analysis default settings [18]. The signals were transformed into the frequency domain to evaluate how the power of the signal is distributed over a range of frequencies to determine dominant frequency. The sampling rate (Fs) was 50 Hz, consequently the spectrum has a frequency range from zero to Fs/2, 0-25 Hz. Dominant frequency is considered the frequency where FFT peak with the maximum magnitude of the signal is observed.

X-ray diffraction analysis was performed using a D8 A25 DaVinci X-ray Diffractometer with CuKα radiation at room temperature (LynxEye™ SuperSpeed Detector). To perform analysis, anode material was ground to powder (< 250 μm) and the powder was poured into a sample holder (5 mm deep, and 40 mm diameter). The sample holder was placed on the stage with the focusing plane of the X-ray tube. The scans were recording in the 2θ range between 5° - 90° with a scanning step 0.02° and accumulation time of 2 s. Total scanning time for one sample was 2h and 23 min. The indexing of the diffractions peaks was carried out using the powder

database ICDD PDF-4 2021 by means of the card index PDF 00-056-0159C [19].

X-ray computed tomography (CT) was used to investigate the structure and heterogeneity in samples. CT is a non-destructive technique that can represent the information visually at high resolution. One rod shaped sample of graphite (L 300 mm) and one rod shaped sample of industrial carbon (L 45 mm) both with a diameter of 20 mm that were used for an electrode construction, were sent to CT laboratory, MANULAB, NTNU Gjøvik for CT scanning using model Zeiss Metrotom 1500. For the scan, X-Ray tube was set for 90 kV and 200 µA. Number of projection (Np) was 2050 (0.176 ° per projection). According to Villarraga-Gomez and Smith [20] Np above 2000 is preferable for a satisfying accuracy of dimensional information provided by CT measurement. Although the rods are different length only ~ 20 mm of the length of the sample was scanned. The basic unit in the CT image is the volume element, voxel (volumetric pixel). The CT image is composed of many voxels, depending on resolution and properties of the scanner, which are displayed as a 2D image array of picture elements (pixels). The voxel size of graphite material was 13.85 µm x 13.85 µm x 13.85 µm, and voxel size of industrial carbon was 12.83 µm x 12.82 µm x 12.83 µm. Picard *et al.* [21] observed that size of the sample affects the resolution of CT scan images and studied samples with 3 different diameter, 50.8 mm, 152.1 mm and 292.1 mm. Authors observed that aggregates and porosities were clearly visible in the smaller sample while they were not revealed in the larger one. The reason for this was that the voxel volume increases by increasing the sample size resulting in lower resolution. It is believed that size of graphite and industrial carbon rod (20 mm in diameter) used in present work for a CT analysis was sufficient to observe aggregates, impurities, and porosities.

7.3 Results and discussion

7.3.1 Material analysis

X-ray diffraction (XRD) analysis and Micro-computed tomography (micro-CT) of graphite and industrial carbon material were performed in

order to analyze the crystallographic structure and macrostructure, respectively.

X-ray diffraction analysis

Figure 7.3 shows X-ray diffraction patterns of the graphite and industrial carbon sample. The reflexes (002), (004), and (006) are reflections from stacked polyarene layers. Reflexes (004) and (006) are of higher order. The appearance of reflections (002) and its higher order reflections make it possible to calculate the crystallite size, Lc. For the graphite reflections (100) and (101) are less pronounced thus making the determination of La less accurate. Industrial carbon showed a smaller and broadened peak for the (002) reflection. The (100) band is also visible for the industrial carbon but no distinct peaks are visible. The same applies to the (110) band.

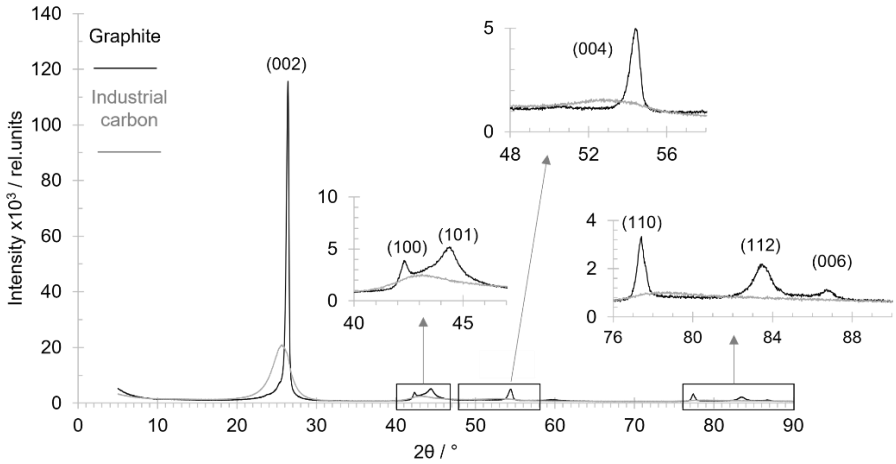

Figure 7.3. X-ray diffraction patterns of graphite and industrial carbon.

The interplane distance (d_{002}), structural components Lc and La, and the corresponding number of polyarene layers (N), packing density of layers (ρ), and degree of graphitization (D.G.), are calculated and results are given in Table 7.2.

The interplanar distance, d_{002}, of the arene/graphene layers in the coherent domain is calculated using Bragg's law:

$$d_{00l} = \frac{\lambda}{2 \sin \theta_{00l}} \tag{7.3}$$

where λ is the radiation wavelength (1.5406 Å) and θ is the refection angle for the reflex 00l (l = 2, 4 or 6).

The stacking height, L_c, is the dimension of the coherent domain perpendicular to the graphene plane. The crystallite size, L_a, is longitudinal dimension of the coherent domain. L_c and L_a are calculated using the Scherrer equation:

$$L = \frac{K\lambda}{\beta_{hkl} \cos \theta_{hkl}} \tag{7.4}$$

where K is equal to ~ 0.9 for C, and is a constant dependent on crystallite shape, β_{hkl} is the full width at half maximum (FWHM) of the reflex, θ is the reflection angle for the reflex (hkl), where hkl are Miller indices ((002) reflex and (100) reflex used for calculating Lc and L_a, respectively).

The number of polyarene layers, N, in the coherent domain is calculated:

$$N = \frac{L_c}{d_{00l}} + 1 \tag{7.5}$$

The packing density, ρ, of the layers in the coherent domain is calculated:

$$\rho = \frac{3.354}{d_{00l}} \cdot 2.26 \tag{7.6}$$

where 3.354 (Å) is the interplanar distance (d_{002}) in an ideal graphite crystal, and 2.26 (g cm^{-3}) is the theoretical density of the ideal graphite.

Porosity, p, could be calculated:

$$p = 1 - \frac{\rho_{bulk}}{\rho_{layer}} \tag{7.7}$$

The degree of graphitization, D.G., can be roughly estimated by using the equation [22]:

$$D.G. = \frac{3.44 - d_{001}}{3.44 - 3.354} \quad (7.8)$$

where 3.440 (Å) is defined the smallest interplanar distance in turbostratic carbon.

The interplanar distance d_{002} for the graphite material of 3.38 Å is well beyond the limit for turbostratic carbon and can definitely be termed a graphite. The industrial carbon has d_{002} of 3.47 Å which makes it a turbostratic carbon, but still a material with graphitic properties. Thus, from a crystallographic point of view the industrial carbon has more defects than graphite material. These findings make sense as the graphitization temperature producing the graphite (above 2000 °C) is much higher than the temperature during calcination of the coke (typically in the interval 1100 – 1300 °C).

Table 7.2. Structural parameters of the graphite and industrial carbon.

Parameter	Graphite	Industrial Carbon
2θ, ° (002)	26.37	25.67
d_{002}, Å	3.38	3.47
FWHM, ° (002)	0.41	2.77
FWHM, ° (100)	0.49	-
L_c, Å	203	31
L_a, Å	174	-
N	61	38
ρ_{bulk}, g cm^{-3}	1.80	1.60
ρ_{layer}, g cm^{-3}	2.24	2.18
p, %	19.64	26.60
D.G., %	70	-

Estimation of the gas composition at low current densities based on XRD results and electrochemical measurements

Ouzilleau *et al.* [23] proposed an electrothermodynamic model for prediction of CO_2/CO ratios. The model predicts that the CO_2/CO ratio increases with the diameter of the coherent domain, L_a, of the coke. In the present work L_a for the graphite was found to be 17.4 nm. The L_a of industrial carbon was not calculated due to absence of the (100) reflex in the diffractogram (Figure 7.3). Due to the higher heat treatment

temperature of the graphite than the industrial carbon it can be assumed that $L_{a\ (ind.\ carbon)} < L_{a\ (graphite)}$. Ouzilleau *et al.* [23] proposed the use of a L_a/L_c ratio of 1.35 for typical industrial carbon. From this ratio and the calculated L_c for the industrial carbon anode (Table 7.2), L_a is estimated to 4.2 nm. The model predicts that the graphite anode should give higher CO_2/CO ratio above the reversible potential for CO_2 evolution.

Ouzilleau *et al.* [23] compared data from the model with CO_2/CO ratios measured by Thonstad [24] and Drossbach [25]. The model was plotted based on conditions used by Drossbach, temperature 890 °C and alumina concentration close to saturation and estimated L_a to be 3 ± 0.5 nm. These conditions are similar to the conditions of the present work concerning the industrial carbon anode. Assuming the cathodic overvoltage is very low at lower current densities (0.1 A cm^{-2}) the cell voltage approx. equals the anode potential which normally would be measured versus aluminium reference electrode. For the current density of 0.1 A cm^{-2}, the cell voltage was 1.02 V when using the graphite anode and 0.9 V when using the industrial carbon. Using these voltages and the model results for 890 °C and alumina saturation, a CO_2/CO ratio less than 1 is found from the model. This means that CO is likely the major product on the anode at this low current density.

For the current density of 0.25 A cm^{-2}, the corresponding voltage at the beginning of electrolysis was found to be around 1.25 V for the industrial carbon. From this the model predicts CO_2/CO ratio to be 4. The ratio increases rapidly with anode potential. Therefore, it could be assumed that in the current work images that show bubbles produced at the current density 0.1 A cm^{-2} mostly represents CO while for the current density ≥ 0.25 A cm^{-2} a major fraction of produced bubbles is CO_2.

The difference in cell voltage of 0.12 V at 0.1 A cm^{-2} when using the graphite and the industrial carbon anode can be explained with the findings of Ouzilleau *et al.* [23] who observed reversible anode potential decreases with decreasing L_a. Ouzilleau *et al.* calculated potential at 1273 K and 1 atm for different coke crystallites. Since the industrial carbon has a lower L_a than the graphite anode, *i.e.*, 4.2 nm < 17.4 nm, it is expected that the reaction on the industrial carbon proceeds at a potential lower than for the graphite.

Micro X-ray computed tomography (CT)

Figure 7.4 and Figure 7.5 show CT images of the cross section of the graphite and industrial carbon material. On the CT images of the graphite (Figure 7.4) it can be seen that the structure is rather homogeneous in comparison to the industrial carbon. No larger pores were observed. White spots, representing regions of high density, were observed to appear and disappear when scanning through sample. Picard *et al.* [21] studied prebaked carbon anode using CT and observed that impurities were represented by white spots on the CT images. The outer edge appears to be even indicating a smooth surface. CT images of the industrial carbon, Figure 7.5, show variety in the structure. The material is made of coke aggregate of different sizes bonded together by the pitch coke formed during baking. The aggregates cannot generally be distinguished, the structure is more sponge coke like, sponge coke being the typical coke preferred by anode producers. The pores are within the sponge coke and between aggregates.

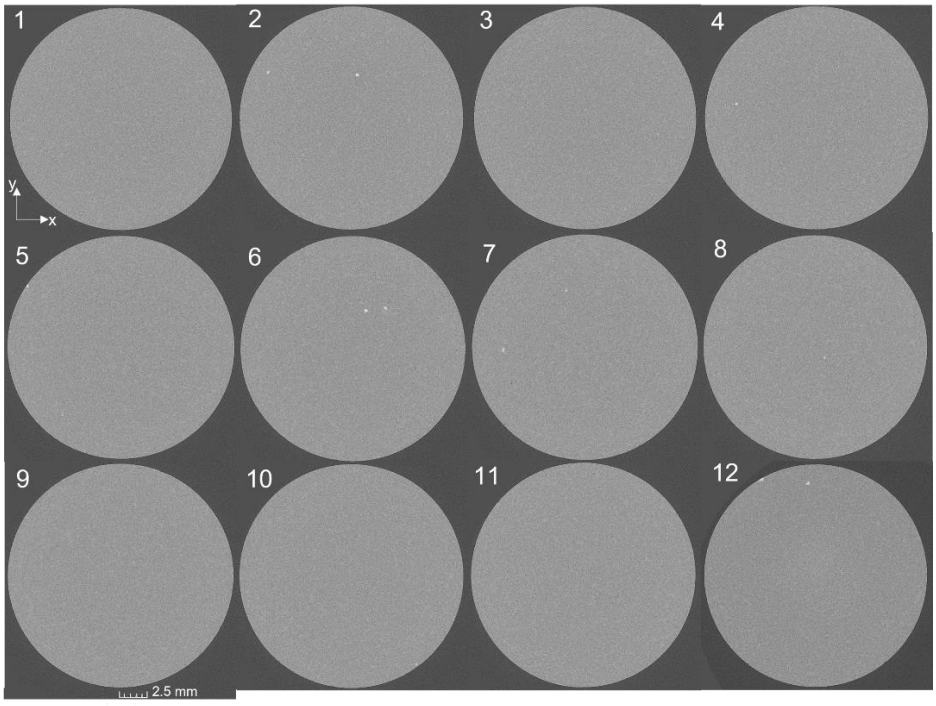

Figure 7.4. CT images of the cross section of the graphite rod sample (Ø 20 mm). The distance between each image is 1.87 mm. The figure therefore shows the graphite rod sample over a length of 20.57 mm. Orientation axis are shown in image 1. Images lie in x-y plane.

The largest aggregate particle was found to have width in x-y direction and height in y-z direction of approx. 5 mm and 3 mm, respectively. The first appears in image 9 in Figure 7.5, while in image 10 it is close to its maximum width. In image 11 it has already disappeared. Similar numbers for the pores were approx. 2 mm width and 3 mm depth. Only one industrial carbon sample was analyzed, thus not necessary represents the situation for the whole industrial anode it was taken from.

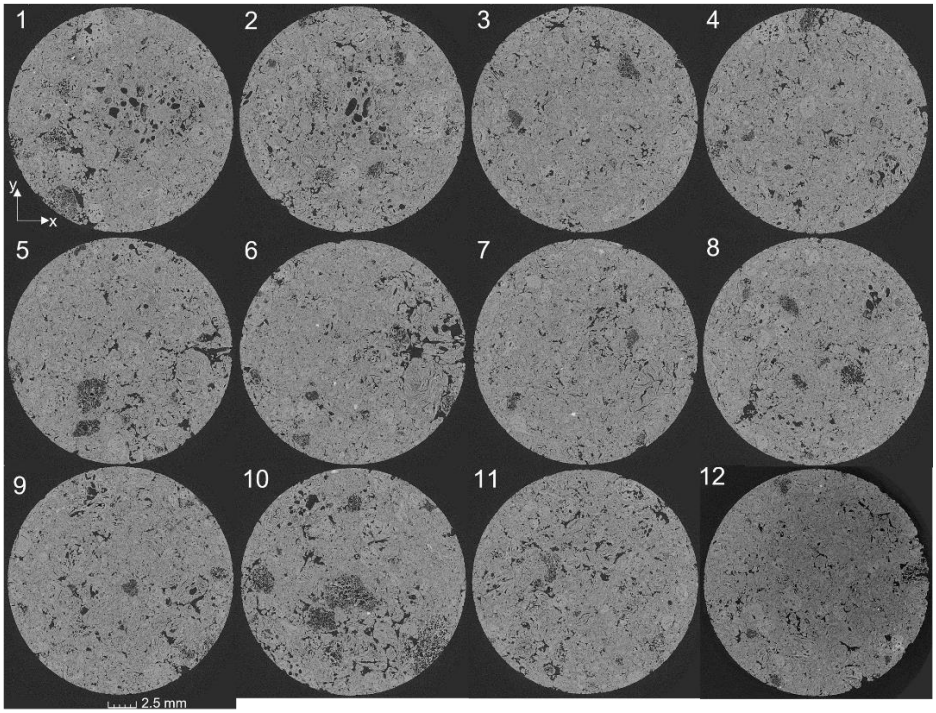

Figure 7.5. CT images of cross section of the industrial carbon rod sample (Ø 20 mm). The distance between each image is 1.99 mm. The figure therefore shows the industrial carbon rod sample over a length of 21.89 mm. Orientation axis are shown in image 1. Images lie in x-y plane.

Figure 7.6 shows enlarged upper part of the CT images for more detailed presentation, image 2 from Figure 7.4 for the graphite and image 2 from Figure 7.5 for the industrial carbon. For the graphite in Figure 6a), aggregates can be observed (lighter in color) with the darker binder phase in between them. Aggregates are different in size, *i.e.*, majority of the aggregates have width less than 100 microns, while a few have width up to

300 microns. The supplier stated an aggregate average value to be 79 microns, Table 7.1. In Figure 7.6(b) on the industrial carbon sample pores, cracks and sponge coke can be easily observed. Coke aggregates lighter in color can be also observed although they are not so distinct, possibly due to similar density as the pitch. As mentioned above white spots for both samples are probably impurities.

It can be observed that the graphite anode has a smoother outer surface without cracks and pores compared to the industrial anode. The effects of the cracks and pores on the bubble behavior (bubble nucleation, bubble layer, *etc.*) are discussed in relation to the images from the see-through cell discussed below.

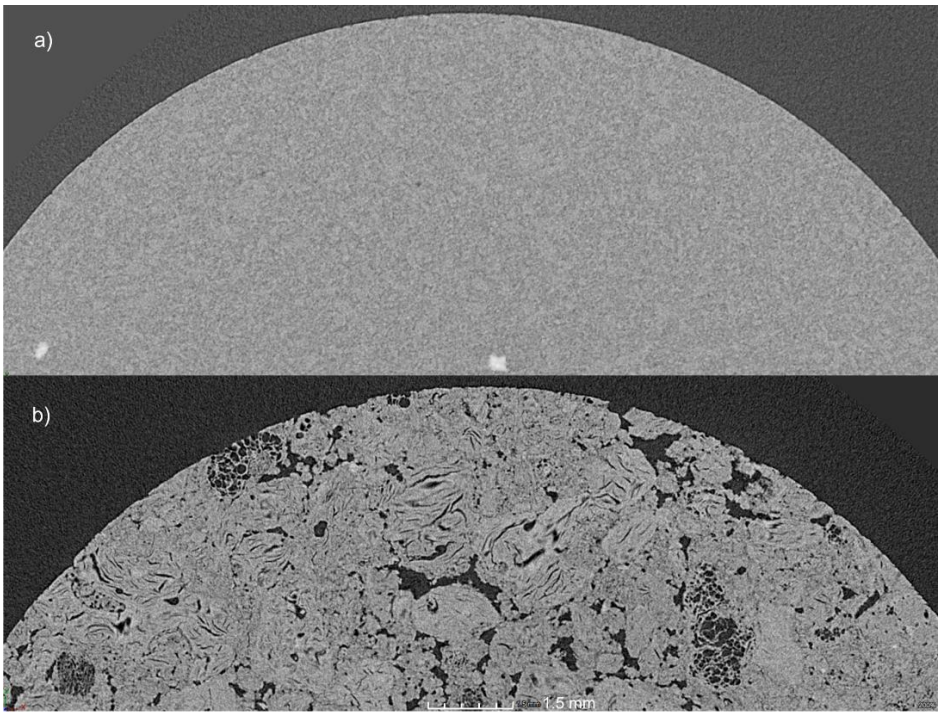

Figure 7.6. Enlarged upper part of the CT images; (a) image 2 from Figure 7.4 (graphite sample), (b) image 2 from Figure 7.5, (industrial carbon sample).

7.3.2 Cell voltage – time data

Figure 7.7(a) shows cell voltage-time data for both graphite and industrial carbon anode at 1.0 A cm^{-2}. Potential oscillation has characteristic saw-tooth shape studied in detail in [26, 27]. As can be seen the saw-tooth curve and voltage drop for the graphite and industrial carbon anode is different although the average bubble size (in 7.3.3) is similar for both anodes for the same applied current. The cell voltage appears to be similar too. The experiment was not designed to study potential difference for anodes made of different material and the cell voltage is not discussed. The saw-tooth curve is representing one big bubble cycle [16, 26, 27]. The voltage drop occurs when bubble detaches. The lowest value of voltage represents a surface free from big bubbles. New smaller bubbles are produced and the voltage is rising. Bubbles are growing and coalescing into one big bubble that will eventually be detach and the voltage drop will occur again. Bubbles from the vertical side does not contribute much to the oscillation since the oscillations are very small [26]. The bubbles responsible for the oscillations at the saw-tooth curves are all events happening at the horizontal surface, *i.e.*, bubbles nucleation, growth, coalescence, sliding, etc. In video recordings it was observed that at the industrial carbon anode for current densities ≥ 1.0 Acm^{-2} in addition to a big bubble detaching from the horizontal part of the anode, smaller bubbles, were also sometimes formed and detached from the horizontal anode edge. The formation and detachment of smaller bubbles at the anode edge increases with increasing current density. These bubbles are larger than bubbles formed and detached at the vertical side of the anode. Since the anode is observed from only one side and horizontal part of the anode is not seen in total from below it is believed that those individual smaller bubbles could exist at all over the edge of the horizontal surface and when the big bubble is sliding towards the anode edge to be detached it withdraws other bubbles on its path and all are together detached. The voltage drop is larger for the industrial carbon anode than for the graphite anode. From the video recording, it was observed that a bubble coverage of the industrial anode is higher than on the graphite anode. The industrial carbon anode has more active surface and the nucleation is more powerful which lowers the voltage additionally. On the graphite anode nucleation is slower and needs more driving force. The rise in the voltage after voltage drop, *i.e.*, bubble detachment, is sharper for the industrial carbon than the

graphite anode. This could also be explained with the nucleation that happens faster at the industrial carbon anode and smaller bubbles coalesced into one big bubble that grow faster and is detached. As discussed below, the number of nucleation sites is larger for the industrial carbon and more bubbles are formed at the same current density in comparison to the graphite anode. On the horizontal side of the anode more bubbles were formed and detached from the industrial carbon anode.

Fast Fourier transform analysis (FFT) of the cell voltage-time data for both anodes at 1.0 A cm^{-2} is shown in Figure 7.7(b). For the graphite and industrial carbon anode a dominant FFT peak is observed at 0.15 Hz, and at 0.27 Hz, respectively. This dominant peak frequency probably corresponds to a bubble detachment time for the bubble from the horizontal part of the anode [16, 26]. The life cycle of one big bubble on the horizontal surface is shorter for the industrial carbon anode in comparison to the graphite anode.

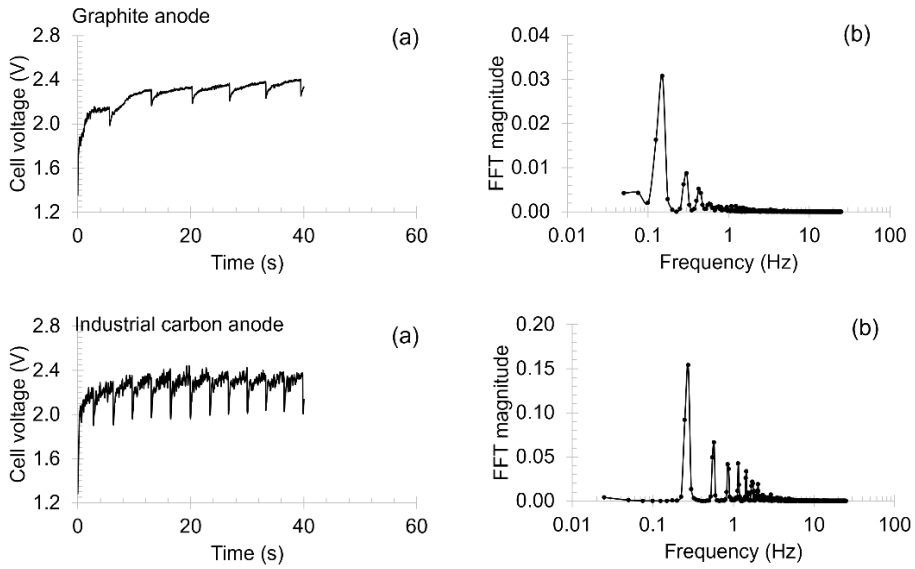

Figure 7.7. (a) Cell voltage-time data for the graphite anode and industrial carbon anode during electrolysis at constant current density of 1.0 A cm^{-2}. Cell voltage data are post-IR-compensated. (b) FFT spectra of cell voltage-time data for the graphite and industrial carbon anode.

7.3.3 Bubble properties and bubble dynamics

Figure 7.8 shows anode surface area of the rod anode for the graphite and industrial carbon anode during electrolysis at constant current of 0.1 A cm^{-2} at different times from the beginning of electrolysis ~ 6 s, ~ 14 s and ~ 21 s. For both anodes it was observed that bubbles were nucleated at certain nucleation sites on the anode surface for the same current density, but nucleation was more pronounced for the industrial carbon than graphite, *i.e.*, relatively more bubbles were formed and detached from the industrial carbon for the same current density. This is due to differences in surface heterogeneity in relation to CT a structure of coke and possible different composition w.r.t. to metallic impurities and sulfur. The quantity of the nucleation sites depends on the structure of the anode. Classical nucleation theory predicts a reduced energy barrier in surface defects [28]. Nucleation takes place on active sites which are defects and pores on the anode surface. As can be seen in the CT images (Figure 7.4 and Figure 7.5) the industrial carbon has larger surface irregularity compared to the graphite anode. In other systems this phenomenon was also found, *e.g.* Westerheide and Westwater [29] studied isothermal growth of hydrogen bubbles during electrolysis at a platinum cathode and reported that nucleation occurred at specific nucleation sites being preferred as pits and scratches which acted as active sites on the electrode.

Bubble evolution over time is shown in Figure 7.8. As discussed in previous work [16], after immersing the anode in the bath, non-electrochemical bubbles are formed and sticking at both boron nitride and graphite/industrial carbon part. After electrolysis started, non-electrochemical bubbles were removed by electrochemical bubbles, *i.e.,* gaseous reaction products. Since it took ~ 5.5 s from the beginning of the electrolysis for all nonelectrochemical bubbles to be removed from the anode surface, the frames in Figure 7.8 shows only gas products. Between 14 s and 21 s a big bubble is detached from the horizontal surface of the industrial carbon anode. At ~ 21 s at the left vertical sides of the industrial carbon anode it seems like bubbles are accumulating at the surface, something like “bubble foam” occurred. Produced bubbles are not big enough to be detached and the effect of the bubble induced convection and current is not enough to promote bubble detachment. In some point bubbles will grow and coalesce and be detached from the surface. In this

specific case accumulation of bubbles didn't occur at the right vertical side of the anode. The reason is that the big bubble from the horizontal side was latterly detached at the right side and while rising up it withdrew some smaller bubbles from the vertical side which otherwise would not yet be detached. The process is shown in Figure 7.9. The occurrence of the "bubble foam" phenomenon was not observed for the graphite anode. It was observed that nucleation points were more or less at the same position for the graphite anode for observed time. For the industrial anode more bubbles are formed with time despite current remaining constant.

Figure 7.9 shows a big bubble sliding along the horizontal surface towards the anode edge, frames (1) and (2), and its detachment, frame (3). While rising up, frame (4), the big bubble entrains smaller bubbles from the vertical surface and making them to detach, leaving the surface free of bubbles, frames (5)-(8). The process was observed for both anodes.

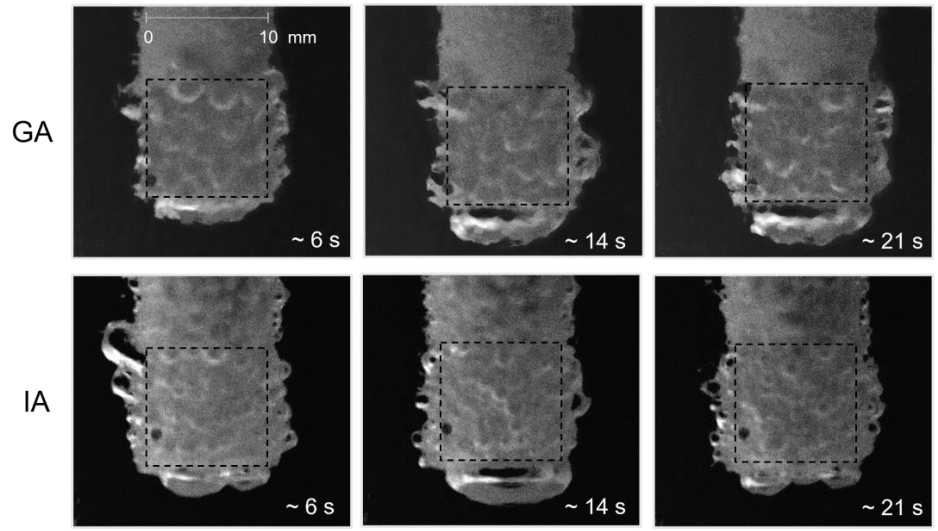

Figure 7.8. Anode surface area (the black dashed line illustrating the border of the anode surface) of shielded rod anode for graphite (GA) and industrial anode (IA) during electrolysis at constant current of 0.1 A cm^{-2}. The time stamps refer to the time after start of electrolysis. The capture frame rate was 500 fps. A scale bar is shown.

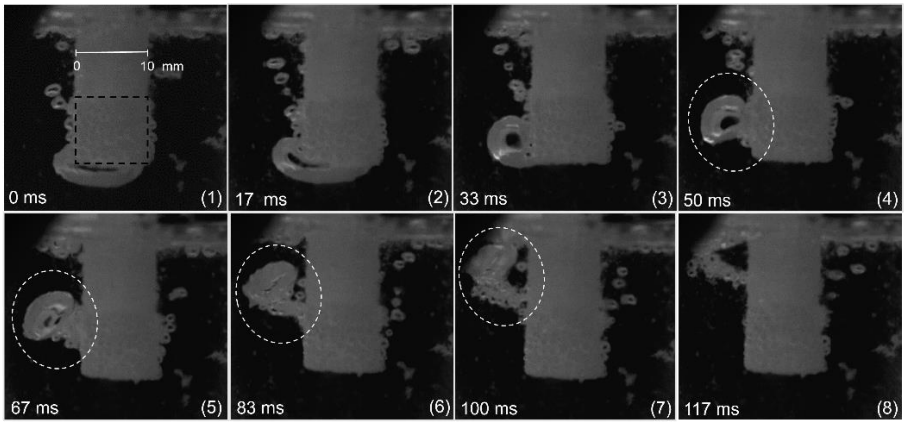

Figure 7.9. Big bubble (highlighted with white dashed line) while detaching from the horizontal surface of the graphite rod anode withdraws smaller bubbles from the vertical surface at 1.0 A cm^{-2}. Border of the anode surface area is highlighted with black dashed line. The frame rate was 60 fps. Frame numbers are given in brackets. Timestamp of 0 ms is added to frame (1), by that, other frames are relative to the first frame. A scale bar is shown in frame (1).

Coalescence was studied for both anodes for different fps and different current densities. High fps was used in to order to capture formation of the intermediate. Bubble coalescence is a process by which two or more gas bubbles in a liquid medium collide and form one larger bubble. Coalescence occurs in three stages: *i.e.*, collision of particles, drainage of the film of liquid during the collision and later film rupture leading to a larger bubble. In previous study of vertical graphite anode [16] it was found that coalescence process occurred in time interval of 16-20 ms and that the current density and electrode potential did not have a significant influence on the time for the coalescence process. In the present study it was also observed at video recorded with 500 fps and 1000 fps that coalescence process for both anodes lie in interval 16-24 ms for current densities 0.1, 0.25 and 0.5 A cm^{-2}. In Figure 7.10 and Figure 7.11 coalescence processes are shown on the vertical surface for both anodes, for current densities where images with the best visibility were obtained. Corresponding videos of the coalescence processes on the graphite and industrial carbon anode are available in Appendix . In Figure 7.12 is shown process of coalescence at the horizontal surface for the graphite anode. The corresponding video is available in Appendix 7.5.

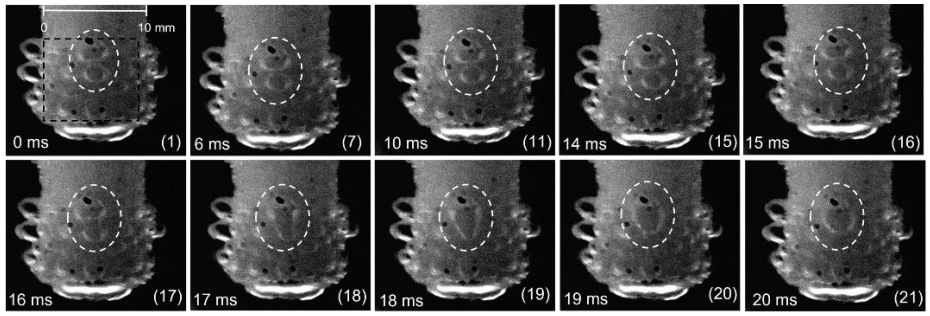

Figure 7.10. The process of coalescence of two bubbles (highlighted with white dashed line) into one bigger bubble at the vertical surface of graphite anode during electrolysis at a constant current density of 0.1 A cm^{-2}. Frame (1) represents the beginning of the coalescence process and is given a 0 ms timestamp, by that, other frames are relative to the first frame. The frame rate was 1000 fps. The anode surface is highlighted with a black dashed line in frame (1) together with a scale bar.

Figure 7.10 shows the coalescence process of two bubbles (highlighted with white dashed line) into one bigger bubble at the vertical surface of graphite anode during electrolysis at a constant current density of 0.1 A cm^{-2}. Frame (1) is believed to be a frame where gas bubbles came in touch and "collision" of gas bubbles and drainage of the film occurred. In frames (17-21) are shown film rupture and formation of one larger bubble. The total time of the process was found to be 21 milliseconds.

Figure 7.11 shows the process of coalescence of two bubbles (highlighted with white dashed line) into one bigger bubble at the vertical surface of industrial anode during electrolysis at a constant current density of 0.25 A cm^{-2}. Frame (1) is believed to be a frame where gas bubbles came in touch and "collision" of gas bubbles and drainage of the film occurred. Frames (8)-(12) show the film rupture and formation of one larger bubble which detached immediately (frame 13) from the anode surface. The total time of coalescence process was found to be 22 ms.

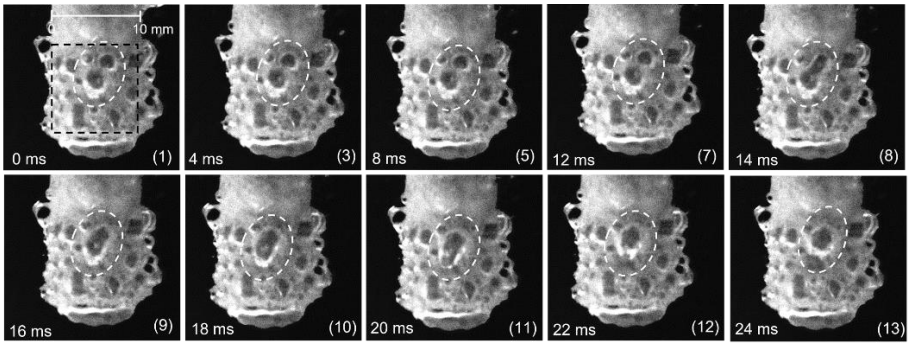

Figure 7.11. The process of coalescence of two bubbles (highlighted with white dashed line) into one bigger bubble at the vertical surface of industrial anode during electrolysis at a constant current density of 0.25 A cm^{-2}. Frame (1) represents the beginning of the coalescence process and is given a 0 ms timestamp, by that, other frames are relative to the first frame. The frame rate was 500 fps. The anode surface is highlighted with a black dashed line in frame (1) together with a scale bar.

The process of coalescence of two bubbles into one bigger bubble at the horizontal surface of the graphite anode during electrolysis at a constant current density of 0.1 A cm^{-2} is shown in Figure 7.12. Since observation is made from the side it is difficult to state when exactly the process of coalescence starts but it is believed that coalescence occurred in the interval 16-24 ms as was found for the bubbles on the vertical side. Two bubbles collided and film rupture happened at frames (1-3) and intermediate is formed, frames (4-6). A resulting big bubble was spread all over horizontal surface, frames (7-11). The bubble slid towards the anode edge, but did not detach, frame (16). As seen in frame (19), the bubble was centered at the horizontal surface and took nearly spherical shape. The bubble tended to be pulled into a spherical shape due to greater forces between the graphite and electrolyte. The bubble continued to grow covering majority of the anode surface and with thus removing electrolyte from the surface. After the bubble grew to a certain size it reached the edge and detached from the surface. The same bubble behavior was observed for the industrial carbon anode. Values for wetting angle of the bubble at the horizontal surface just before its detachment was measured to be in the interval 110°-125° for both anodes during electrolysis at 0.1 A cm^{-2}. The wetting angle was determined by drawing a tangent to the bubble profile at the point of the three-phase contact on an image.

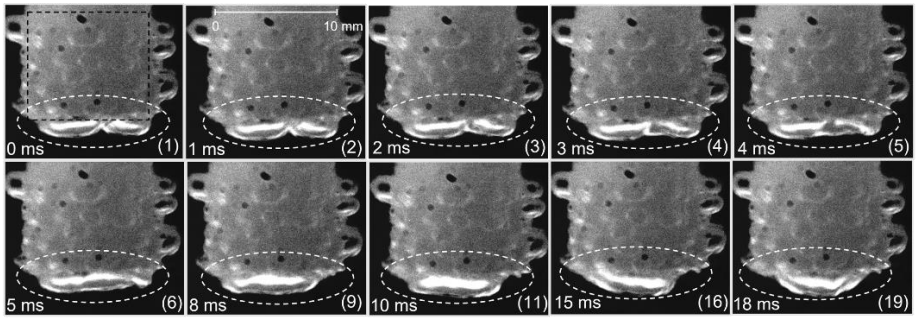

Figure 7.12. The process of coalescence of two bubbles (highlighted with white dashed line) into one bigger bubble at the horizontal surface of the graphite anode during electrolysis at a constant current density of 0.1 A cm^{-2}. Frame (1) represents the beginning of the coalescence process and is given a 0 ms timestamp, by that, other frames are relative to the first frame. The frame rate was 1000 fps. The anode surface is highlighted with a black dashed line in frame (1) together with a scale bar, frame (2).

Bubble size

The average bubble diameter after bubble detachment from the graphite and industrial anode as a function of current density is presented in Figure 7.13. Error bars represent a 95% confidence interval assuming a normal distribution. The bubble diameter was calculated as an average value of 10 bubbles detached from horizontal surface and an average value of 15 bubbles detached from vertical surface at each current density. The bubble diameter was measured using PFV4 software as explained by Stanic *et al.* [16]. The bubble diameter values in Figure 7.13 are from several different experiments. The bubble diameter decreases with increasing current density, but with a different rate for different materials. For the graphite anode, diameter of the bubbles from the horizontal part has an average value of 7.5 mm and is reduced to 6.7 mm at 0.5 A cm^{-2} wherefrom it stays nearly constant up to 2.0 A cm^{-2}. For the industrial carbon anode, diameter of the bubbles from the horizontal part has an average value of 7.5 mm and is reduced to 6.7 mm at 0.8 A cm^{-2} while from 1.0 A cm^{-2} decrease in average value is more pronounced (to 4.5 mm at 2.0 A cm^{-2}) and with a higher standard deviation. For the industrial carbon anode above 1 A cm^{-2}, a larger variance was observed in detached bubble diameter from horizontal surface. At the horizontal part of the anode close

to the anode edge, smaller bubbles that were formed there were detached without coalescing with the big bubble growing in the middle of the horizontal anode surface, *i.e.*, edge effect. Those bubbles grown to certain size, 2.5-3.5 mm, and are detached. Simultaneously in the middle of the anode a big bubble is growing and while reaching certain size (larger than bubbles from the edge), slides toward the edge and is detached. This edge effect was not observed for the graphite anode. Contrary at the graphite anode above 1 A cm^{-2} average bubble diameter is more or less constant.

Bubbles from the vertical surface are found to be similar in size for both anodes, Figure 7.13. It is believed that at lower currents bubble retention time is higher and bubbles have time to grow and coalesce more while at higher currents more bubbles are formed and their retention time is shorter, *i.e.* already existing bubbles are rapidly pushed by newly produced bubbles. Bubble induced convection also contributes bubble release and is larger with increasing current [30]. Results indicate that anode material also affects bubble size along with already discussed current density and convection. Industrial carbon has more variety in surface in comparison to graphite anode and greater number of nucleation sites. Due to larger variation in surface on the industrial carbon material, as discussed in section 7.3.1., one cannot conclude how some other anode made from the same industrial carbon material would behave. Bubble accumulation at the vertical side over time on the industrial carbon anode (discussed in 7.3.3.) is believed to be favored by lower current densities, while at higher current densities bubble accumulation is less pronounced. This is confirmed by obtaining the nearly constant value in bubble diameter above 1.0 A cm^{-2}.

As explained in our previous study [16], the increase in current density and thereby the corresponding increase in potential gives higher driving force for nucleation of relatively more bubbles. Cassayre *et al.* [31, 32] also found that the bubble diameter decreased with increasing current density. It was explained by less pronounced coalescence at higher current densities and that bubbles escape before covering the anode and grow to full size.

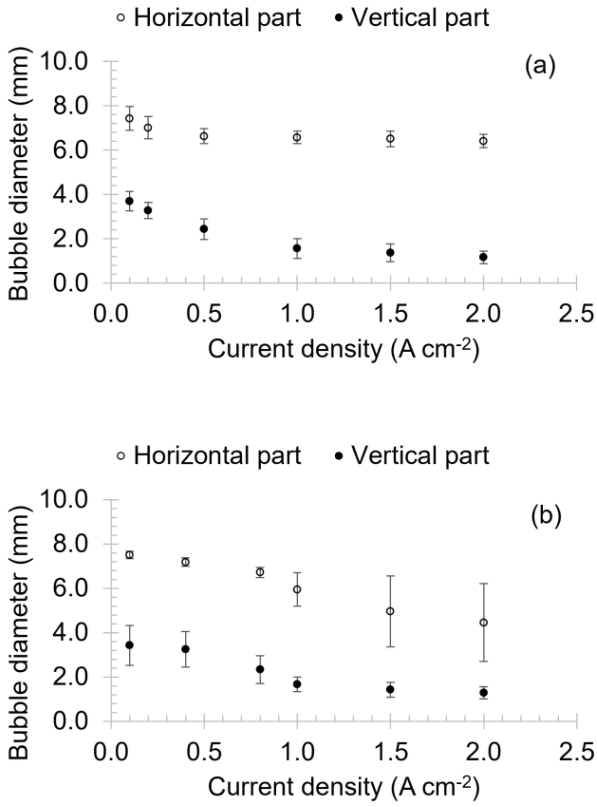

Figure 7.13. Bubble diameter from horizontal and vertical part of anode for the (a) graphite anode and (b) industrial anode as a function of the nominal current density.

Images of bubbles at the same graphite anode for different current densities can be seen in Figure 7.14. All images are taken at the same event in the bubble cycle, *i.e.*, the big bubble from the horizontal surface is sliding toward the anode edge, frame (a), the big bubble is detaching from the anode edge frame (b) and the big bubble is leaving the surface frame (c).

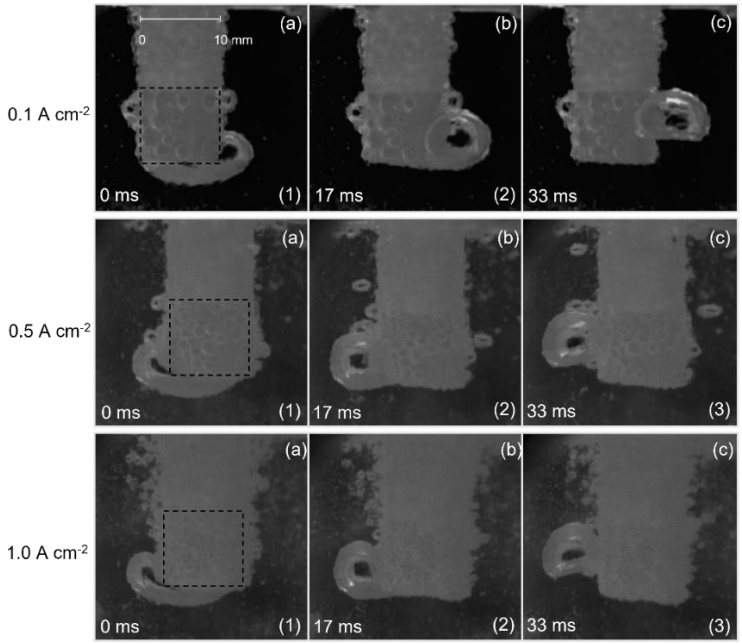

Figure 7.14. Shielded rod graphite anode during electrolysis at different current densities, 0.1, 0.5 and 1.0 A cm^{-2}, while a) big bubble from the horizontal surface is sliding toward the anode edge, b) big bubble is detaching from the anode edge and c) big bubble is leaving the anode surface. The frame rate was 60 fps. Frame numbers are given in brackets. Timestamp of 0 ms is added to frame (1), by that, other frames are relative to the first frame. The anode surface is highlighted with a black dashed line in frame (1) together with a scale bar.

7.3.4 Current density at the horizontal part of the anode

The volume of each bubble detached from the horizontal surface was calculated using the equation for the volume of a sphere since it was observed that after detachment bubbles in one moment had a spherical shape. Knowing the total number of detached bubbles and their diameter the total gas volume produced at the horizontal surface was calculated and results are shown in Figure 15(a). To get a volume fraction of gas produced at the horizontal surface, this value was divided with the total gas volume produced at the rod anode according to Faraday's law assuming even current distribution and CO_2 as the only gaseous product. In the current density interval 0.4-2.0 A cm^{-2} , the volume fraction was calculated to be ~ 10.4 % for the graphite anode and ~ 16.4 % for the industrial carbon anode. The fraction turned out to be more or less constant in the current

density interval. However, the percentage of the nominal area of the horizontal part is 20 % for both anodes (horizontal area/total area = 0.785/3.925). This implies that the current density on the horizontal part is ~ 50 % and ~ 80 % of the nominal current density for the graphite and industrial carbon anode, respectively. This difference is due to more active sites on the industrial carbon in comparison to the graphite which results in production of more bubbles. All results of gas fraction divided by nominal surface area for the different current densities are shown in Figure 7.15(b). Since the value is < 1 it means that less gas was produced from the horizontal surface of the anode than expected correlated to the surface area. This could be explained by a great number of smaller bubbles were produced and detached faster from the vertical surface while big bubbles were slowly building up at the horizontal surface blocking more and more of the surface. Figure shows that value did not change much with current density which was surprising as it could be expected that the bubble induced convection should help removing bubbles at higher current densities relatively more for the horizontal surface than the vertical surface.

Since the values in Figure 15(b) are less than 1 it means that the corresponding number for the vertical surface area are greater than 1, and the current density on the vertical surface for the graphite is higher than corresponding current density for the industrial carbon. An effort was done to count the bubble on the vertical part but due to great number of bubbles detached from the vertical surface and big bubbles taking with smaller bubbles when detaching, it was difficult to observe any difference between the graphite and industrial anode. Additionally, a stream of small bubbles on the industrial carbon anode can be seen that in theory should reduce the frequency of the detaching bubbles on the vertical part.

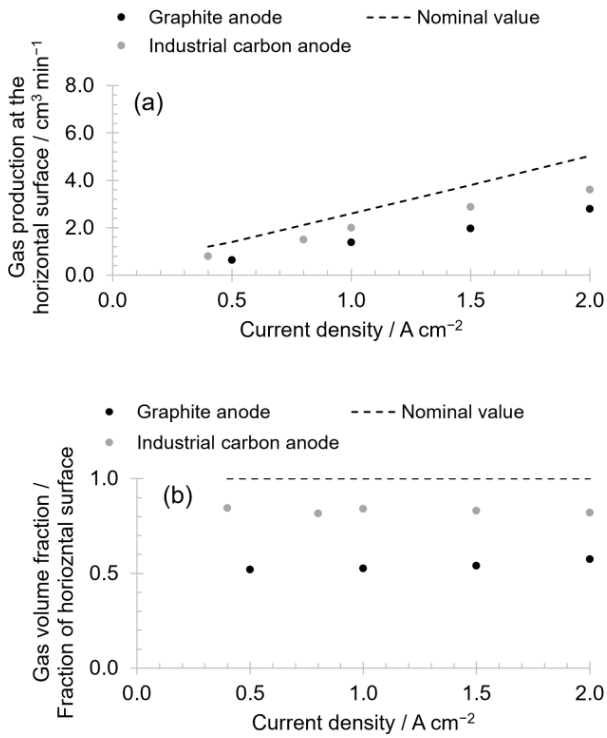

Figure 7.15. Gas production on the horizontal surface foe different current densities: (a) Gas volume rate, (b) Gas volume fraction.

7.3.5 Anode effect

In Figure 7.16 and Figure 7.18 linear sweep voltammograms for both anodes are presented. The videos are available in the Appendix. In both figures the voltammograms were recorded without IR-compensation. Afterwards the curves were IR-compensated using the value of the ohmic resistance at OCP for the cell. Frames from selected parts of the sweep are shown together with the current-voltage data.

As can be seen in Figure 7.16 starting from OCP, the first increase in current density is observed around 0.8 V. The current increase was due to CO_2/CO gas evolution. The current oscillations arise from growth, coalescence and detachment of bubbles as could be seen from the video recording using a high-speed camera. In frame (1) is shown production of bubbles and their detachment during reaction at around 1 A cm^{-2}. Frame

(2) represented the state of the anode just before the anode effect occurred. At cell voltage 5.9 V of the not-IR-compensated curve, the current suddenly decreased towards zero. The sudden decrease was attributed to the occurrence of the anode effect, forming a gas layer on the surface of the anode, frame (3) and (4). The bubble at the horizontal part of the anode was at its maximum size when the anode effect occurred. At the moment of anode effect bubble formation and bubble detachment stopped and the gas layer was formed at the surface completely covering the surface thus preventing contact between surface and electrolyte. The anode became completely non-wetted. The critical current density on the anode was exceeded, and the IR-compensated curve indicates that the potential of the anode is high enough to produce PFC according to reaction (7.1) and (2.8). Immediately after the decrease the current rose and decreased again whereupon it stayed unchanged with increasing voltage. The rise in current can be explained by the sudden increase in potential of the electrode when the current drops instantly to zero at anode affect, as seen from the IR-compensated curve. Some of the electrolyte that remained on the anode surface under the gas layer might have been oxidized during the abrupt potential increase of the anode. The layer was covering the whole anode surface, and gas produced after the initiation anode effect was trapped inside the gas layer and was ended up at C/BN boundary, frame (5) and (6).

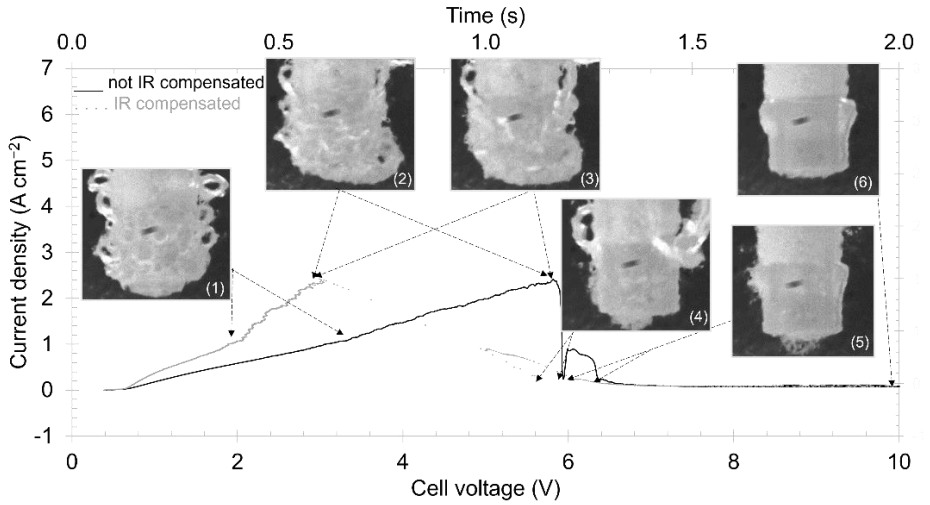

Figure 7.16. Linear sweep voltammetry (LSV) curves for graphite anode with sweep rate of 5 V s^{-1} with corresponding frames from video recordings. Frames are numbered in display order, not in true time frames. Not IR and IR-compensated data are shown. Sampling frequency was 500 Hz. Timeline is only valid for not IR-compensated data.

A principal sketch of the carbon anode before and after anode effect is shown in Figure 7.17(a) and b), respectively. During the production PFC gas, the surface has been teflonised. Åsheim *et al.* [33] studied wetting properties of the graphite using immersion/emersion technique and observed that anodes polarized to anode effect showed a consistent de-wetting which could confirm teflonisation of the anode surface. Haverkamp [34] studied fluorination of carbon anode using XPS and SEM and discovered fluorocarbon on the anode surface resulting from anode effect. The author concluded that a (C – F) film exist. It seemed that the interfacial tension at carbon-electrolyte interface (γ_{sl}) is sufficiently small so that that the electrolyte partly wets the carbon surface giving the bubbles a spherical shape, Figure 7.17(a). After anode effect the gas layer at the carbon surface is believed to be mixture of CO/CO_2/PFC gases, Figure 7.17(b). Since chemically similar media require less energy to form an interface between them, the interfacial tension between a teflonised carbon surface (C – F) and CO/CO_2/PFC gas layer (γ_{sg}) is low and the gas layer is covering all the anode surface, Figure 7.17(b). It appears that the (C – F) bond now have drastically increased the interfacial tension for the carbon-electrolyte interface (γ_{sl}). The gas layer contributed to de-wetting of the anode. As observed the gas layer does not extend into the BN surface. This could be due to good wetting between electrolyte and BN which was also found by Åsheim *et al.* [33].

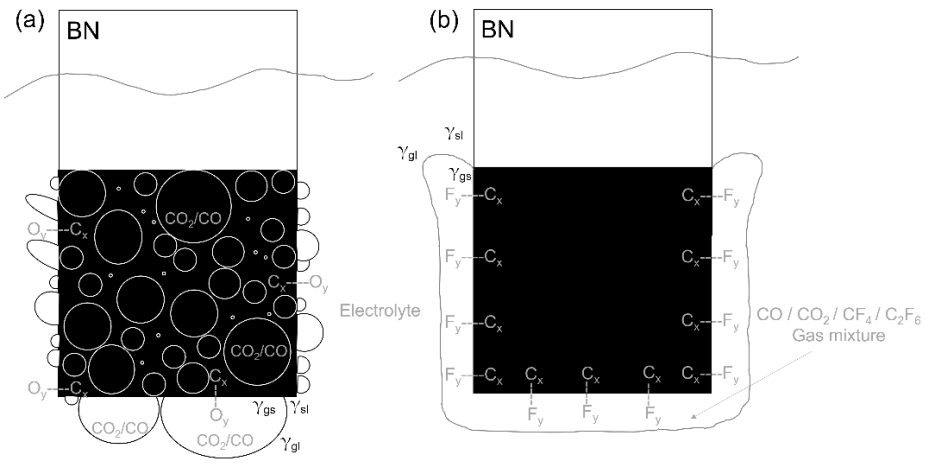

Figure 7.17. Principal sketch of a) CO_2/CO gas bubbles during the anode process for normal electrolysis and b) after initiation of anode effect. The thickness of the perfluorocarbon containing gas layer is exaggerated for reasons of clarity.

A similar discussion can be applied for the anode effect on the industrial carbon anode, shown in Figure 7.18. Starting from OCP the first increase in current density also occurred at 0.8 V. However, the current density increased faster. In frame (1) are shown production and detachment of bubbles during reaction at around 1.5 A cm^{-2}. In frame (2) is shown detachment of a big bubble from the horizontal surface prior to anode effect. The critical current density on the anode was exceeded, and the potential of the anode was high enough to produce PFC according to reactions (7.1) and (2.8), as can be seen from the IR-compensated curve. The decrease in current due to the onset anode effect is not abrupt as for the graphite, frame (3). From video recordings it can be observed that gas layer didn't spread as evenly and fast as for the graphite anode. Hence frame (4) still shows some gas bubble detachment. Similar phenomenon of rise in the current after initiation of the anode effect for the graphite was also observed here. The rise again can be explained by the sudden increase in potential of the electrode when the current drops towards zero at the onset of the anode affect and some of the electrolyte remaining under the gas layer might have been oxidized. Due to more porous surface of the industrial carbon anode, more electrolytes could be present beneath the gas layer on the anode surface leading to more gas production. The layer was covering the whole anode surface, and gas produced after the initiation anode effect was trapped inside the gas layer and was ended up at C/BN boundary but it does not stay trapped like in the case for graphite. The quantity of produced gas appears to be sufficient to overcome and break the layer to be detached, frame (5) and (6). The graphite anode has smoother, less porous and less complex surface than the industrial anode and the gas layer formed on the graphite anode appeared to be thicker, and more stable. The experiments were repeated five times for the same anode in the same crucible for a total six crucibles giving a total of approx. 30 sweeps. The anode effect always occurred on the graphite anode while on the industrial carbon, anode effect occurred only in approx. 60 % of the sweeps.

In the voltage range above 8.5 V, distortion of the curve occurred for both anodes, although more pronounced in the case of the industrial carbon anode. This could be due to instrument limitation. The voltage range limitation is 0-10 V. When current drops suddenly due to the onset on the anode effect, the voltage increases significantly from 3 V to 6 V in the case of the graphite anode and from 2.5 V to 8.5 V in the case of the

industrial carbon anode (this can be seen from IR-compensated curves), and probably due to short term overloading of the instrument curves gets distorted.

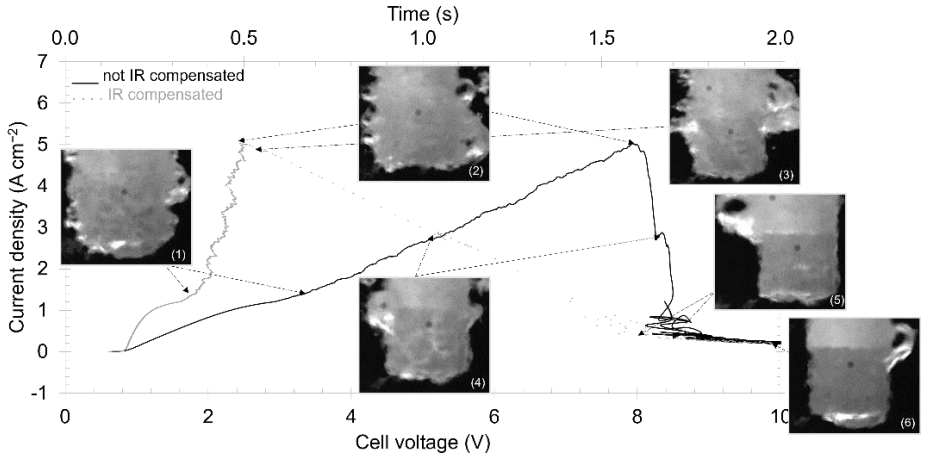

Figure 7.18. Linear sweep voltammetry (LSV) curves for the industrial carbon anode with sweep rate of 5 V s^{-1} with corresponding frames from video recordings. Frames are numbered in display order, not in true time frames. Not IR and IR-compensated data are shown. Sampling frequency was 500 Hz. Timeline is only valid for not IR-compensated data.

7.4 Conclusions

More bubbles were nucleated on the industrial carbon anode than on the graphite anode for the same current density. The higher number of bubbles was due to more active sites on the industrial carbon confirmed by CT analysis which showed that the industrial carbon has much larger aggregates with more pores, cracks and impurities in comparison to the graphite. On both horizontal and vertical surfaces, the smaller bubbles coalesced into bigger bubbles. The time related to the process of coalescence for both anodes was found to be in the interval 16 – 24 ms and independent of the current density. The bubbles on the vertical surface detached through a preceding coalescence process while the bubbles on the horizontal surface coalesced and went off as a one big bubble. However, on the industrial carbon more bubbles were produced. For both anode materials the diameter of detached bubbles decreased with increasing current density. Bubbles from the vertical surface are found to be similar in diameter for both anodes for the same current density. Big bubbles

detaching from the horizontal surface have also similar diameter for the same current density but the detachment frequency of big bubbles was higher for the industrial carbon. This was explained by the higher current density found on the horizontal surface of the industrial carbon anode compared to the graphite anode. For current densities > 1.0 A cm^{-2}, some smaller bubbles were produced alongside the big bubbles at the horizontal surface for the industrial carbon anode. On increased currents anode effect occurred on both anodes, the current being lower for the graphite anode at the onset. The video recordings and the electrochemical measurements showed more abrupt initiation of the anode effect on the graphite. A PFC-containing gas layer was formed around the anode and the layer appeared to be thicker and more stable on the graphite anode than on the industrial anode.

7.5 Appendix

The process of coalescence of two bubbles into one bigger bubble at the vertical surface of graphite anode during electrolysis at a constant current density of 0.1 A cm^{-2}, in relation to Figure 6.10. Video process with all frames (1-21): https://www.youtube.com/watch?v=0mUCRC6C21A . The video is captured with 1000 fps. The video is saved with playback frame equal to 10 fps, meaning the video is shown in 1 % of real speed.

The process of coalescence of two bubbles into one bigger bubble at the vertical surface of industrial anode during electrolysis at a constant current density of 0.25 A cm^{-2}, in relation to Figure 6. 11. Video process with all frames (1-13): https://youtu.be/3IClpm6WHCY . The video is captured with 500 fps. The video is saved with playback frame equal to 10 fps, meaning the video is shown in 2 % of real speed.

The process of coalescence of two bubbles into one bigger bubble at the horizontal surface of the graphite anode during electrolysis at a constant current density of 0.1 A cm^{-2}, in relation to Figure 6.12. Video process with frames (1-19) for coalescence process: https://youtu.be/zCHm19kzFgU . The video is captured with 1000 fps. The

video is saved with playback frame equal to 10 fps, meaning the video is shown in 1 % of real speed.

Video recording of the anode effect on the graphite anode https://www.youtube.com/watch?v=VkH5JFEPOoE , in relation to Figure 6.16. The video is captured with 1000 fps. The voltage was scanned at rate 5 V s^{-1} starting from OCP to 10 V making the recording time 2 s. The videos are saved with playback frame equal to 30 fps, meaning the videos are shown in 3 % of real speed.

Video recording of the anode effect on the industrial carbon anode https://youtu.be/9d-pg2wB4lU , in relation to Figure 6.18. The video is captured with 1000 fps. The voltage was scanned at rate 5 V s^{-1} starting from OCP to 10 V making the recording time 2 s. The videos are saved with playback frame equal to 30 fps, meaning the videos are shown in 3 % of real speed.

References

1. Stanic, N., A.M. Martinez, K.E. Einarsrud, and E. Sandnes, *A Study of Bubble Behavior and Anode Effect on the Graphite and Industrial Carbon Anode in a See-Through Furnace During Aluminium Electrolysis.* Metallurgical and Materials Transactions B, 2022. **53**(5): p. 3025–3043.
2. Zhao, Z., Z. Wang, B. Gao, Y. Feng, Z. Shi, and X. Hu, *Observation of Anodic Bubble Behavior Using Laboratory Scale Transparent Aluminium Electrolysis Cells*, in *Light Metals 2015*, M. Hyland, Editor. 2015, Springer: Cham. p. 801-806.
3. Huang, Y., Z. Wang, Y. Yang, B. Gao, Z. Shi, and X. Hu, *Anodic Bubble Behavior in a Laboratory Scale Transparent Electrolytic Cell for Aluminum Electrolysis.* Metals, 2018. **8**(10): p. 806.
4. Kasherman, D. and M. Skyllas-Kazacos, *Effect of anode material and bath composition on bubble layer resistivity and gaseous volume fraction in an aluminium electrolysis cell with sloping anode and cathode.* Journal of applied electrochemistry, 1991. **21**(8): p. 716-720.
5. Thorne, R.J., C. Sommerseth, A.P. Ratvik, S. Rorvik, E. Sandnes, L. Lossius, H. Linga, and A. Svensson, *Correlation between Coke Type, Microstructure and Anodic Reaction Overpotential in Aluminium Electrolysis.* J. Electrochem. Soc., 2015. **162**(12): p. E296-E306.
6. Thorne, R.J., C. Sommerseth, A.M. Svensson, E. Sandnes, L.P. Lossius, H. Linga, and A.P. Ratvik, *Understanding Anode Overpotential*, in *Light Metals 2014*, J. Grandfield, Editor. 2014, John Wiley & Sons, Inc.: Hoboken, NJ. p. 1213-1217.

7. Thorne, R.J., C. Sommerseth, E. Sandnes, O. Kjos, T.A. Aarhaug, L.P. Lossius, H. Linga, and A.P. Ratvik, *Electrochemical Characterization of Carbon Anode Perfomance*, in *Light Metals 2013*, B. Sadler, Editor. 2013, Springer. p. 1207-1211.
8. Tabereaux, A., *Anode Effects, PFCs, Global Warming, and the Aluminium Industry.* JOM, 1994. **46**: p. 30-34.
9. Thonstad, J., F. Nordmo, and K. Vee, *On the anode effect in cryolite-alumina melts—I.* Electrochimica Acta, 1973. **18**(1): p. 27-32.
10. Thonstad, J., F. Nordmo, and J.K. Rødseth, *On the anode effect in cryolite-alumina melts—II the initiation of the anode effect.* Electrochimica acta, 1974. **19**(11): p. 761-769.
11. Nordmo, F. and J. Thonstad, *On the anode effect in cryolite—alumina Melts—III. Current—voltage behaviour during anode effect.* Electrochimica acta, 1984. **29**(9): p. 1257-1262.
12. Thonstad, J., S. Rolseth, and R. Keller, *On the Mechanism Behind Low Voltage PFC Emissions*, in *Light Metals 2013*, B.A. Sadler, Editor. 2016, Springer International Publishing: Cham. p. 883-885.
13. Zhu, H. and D. Sadoway, *An electroanalytical study of electrode reactions on carbon anodes during electrolytic production of aluminum*, in *Light Metals: Proceedings of Sessions, TMS Annual Meeting (Warrendale, Pennsylvania)*. 2000. p. 257-263.
14. Zhu, H., *Towards Elimination of the Anode Effect and Perfluorocarbon Emissions from Hall-Héroult Cells.* ECS Proceedings Volumes, 2002. **2002-19**(1): p. 411-418.
15. Tabereaux, A.T., N.E. Richards, and C.E. Satchel, *Composition of reduction cell anode gas during normal conditions and anode effects*, in *Light Metals 1995*, J.W. Evans, Editor. 1995, TMS: Warrendale, Pennsylvania. p. 325-333.
16. Stanic, N., A.M. Martinez, K.E. Einarsrud, and E. Sandnes, *Bubble Phenomena and Bubble Properties for Horizontal and Vertical Carbon Anode Surfaces in Cryolite Melt Applying a See-Through Cell.* Metals, 2021. **11**(6): p. 24.
17. Stanic, N. and E. Sandnes, *Bubble Behavior on Horizontal and Vertical Carbon Anode Surfaces in Cryolite Melt Applying a See-Through Cell.* Materials Proceedings, 2021. **3**(1): p. 8.
18. SignalLab. *SigView Spectrum Analyzer*. 2021 [cited 2021; Available from: https://www.sigview.com/.
19. *ICDD PDF-4 Phase Identification & Quantitation*. 2021, International Centre Diffraction Data Newtown Square, PA. Accessed 27 Sept 2021
20. Villarraga-Gómez, H. and S. Smith, *Effect of the number of projections on dimensional measurements with X-ray computed tomography.* Precision Engineering, 2020. **66**: p. 445-456.
21. Picard, D., H. Alamdari, D. Ziegler, P.-O. St-Arnaud, and M. Fafard, *Characterization of a Full-Scale Prebaked Carbon Anode Using X-Ray Computerized Tomography*, in *Light Metals 2011*, S.J. Lindsay, Editor. 2011, Springer International Publishing: Cham. p. 973-978.
22. Vlahov, A., *XRD graphitization degrees: a review of the published data and new calculations, correlations, and applications.* Geologica Balcanica, 2021. **50**: p. 11-35.

23. Ouzilleau, P., A.E. Gheribi, and P. Chartrand, *Prediction of CO_2/CO formation from the (primary) anode process in aluminium electrolysis using an electrothermodynamic model (for coke crystallites).* Electrochimica Acta, 2018. **259**: p. 916-929.
24. Thonstad, J., *On the Anode Gas Reactions in Aluminum Electrolysis, II.* J. Electrochem. Soc., 1965. **111**(8): p. 959-965.
25. Droßbach, P., *Zur Elektrometallurgie des Aluminiums.* Zeitschrift für Elektrochemie und angewandte physikalische Chemie, 1936. **42**(2): p. 65-70.
26. Stanic, N., I. Jevremovic, A.M. Martinez, and E. Sandnes, *Bubble Evolution on Different Carbon Anode Designs in Cryolite Melt.* Metallurgical and Materials Transactions B, 2020. **51**(3): p. 1243-1253.
27. Thorne, R.J., C. Sommerseth, A.P. Ratvik, S. Rorvik, E. Sandnes, L.P. Lossius, H. Linga, and A. Svensson, *Bubble Evolution and Anode Surface Properties in Aluminium Electrolysis.* J. Electrochem. Soc., 2015. **162**(8): p. E104-E114.
28. Holbrough, J., J. Campbell, F. Meldrum, and H. Christenson, *Topographical Control of Crystal Nucleation.* Crystal Growth & Design, 2012. **12**: p. 750-755.
29. Westerheide, D.E. and J.W. Westwater, *Isothermal growth of hydrogen bubbles during electrolysis.* AIChE J, 1961. **7**(3): p. 357-362.
30. Obata, K. and F. Abdi, *Bubble-Induced Convection Stabilizes Local pH during Solar Water Splitting in Neutral pH Electrolytes.* Sustainable Energy & Fuels, 2021. **5**.
31. Cassayre, L., T. Utigard, and S. Bouvet, *Visualizing gas evolution on graphite and oxygen-evolving anodes.* JOM (USA), 2002. **54**(5): p. 41-45.
32. Cassayre, L., G. Plascencia, T. Marin, S. Fan, and T. Utigard, *Gas Evolution on Graphite and Oxygen-Evolving Anodes During Aluminium Electrolysis*, in *Light Metals 2006*, T.J. Galloway, Editor. 2006, TMS: Warrendale. p. 379-383.
33. Åsheim, H., I. Eidsvaag, A. Solheim, H. Gudbrandsen, G.M. Haarberg, and E. Sandnes, *The Influence of Polarisation on the Wetting of Graphite in Cryolite-Alumina Melts*, in *Light Metals 2020*, A. Tomsett, Editor. 2020, Springer International Publishing. p. 608-619.
34. Haverkamp, R.G., *An XPS study of the fluorination of carbon anodes in molten NaF–AlF3–CaF2.* Journal of Materials Science, 2012. **47**(3): p. 1262-1267.

Chapter 8

Bubble behavior on a downward-facing horizontal anode of different sizes

Nikolina Stanic[1] and Espen Sandnes[1]

[1] Department of Materials Science and Engineering, Norwegian University of Science and Technology NTNU, NO-7491 Trondheim, Norway

A draft for a future publication.

Abstract

The study aimed at investigating the effect of the size of the anode regarding bubble behavior. For this study cylindrical anodes with 10 mm and 20 mm diameter with a downward-facing horizontal surface were made. It was found that the bubble diameter was decreasing with increasing current density for both anodes. Bubbles detached from the 20 mm anode are larger in size than bubbles detached from the 10 mm anode for the same current density. The thickness of the bubble just before it starts to slide towards edge to be detached from the anode surface, was found to be around 4.6 mm for the 10 mm anode while for the 20 mm anode the thickness was 3.9 mm. At the moment of the anode effect initiation the bubble formation and bubble detachment stopped and the gas layer, a mixture of CO, CO_2 and PFC gases, was formed completely covering the surface thus preventing contact between the surface and the electrolyte.

8.1 Introduction

The lab scale anodes are typically used to study reaction kinetics and mass transport, anode effect phenomena, current efficiency, anode quality properties, *etc*. Increased knowledge of the bubble behavior is useful for further studies, especially in laboratory-scale studies applying similar anode designs.

To study the anode reaction in a lab scale cell a small anode is used, usually with 10 mm diameter[1-7], although in some works an anode with diameter < 10 mm [2] and > 10 mm diameter were used [2, 8, 9]. In this doctoral work a downward facing horizontal anode with diameter of 10 mm was used in [10] (Chapter 4), [11] Chapter 5 and [7] (Chapter 6). In the present chapter an anode with diameter 20 mm was applied to study the anode size dependency. 20 mm diameter is the practical maximum possible for the present furnace configuration.

The anode diameter affects the maximal bubble thickness/size, especially with the use of a very small horizontal anode. Thorne *et al.* [2] studied horizontal anode with different diameters: 6, 8, 10 and 14 mm. It was found that the potential oscillation magnitude and frequency were similar on 8, 10 and 14 mm horizontal anode for the same current density inferring a relatively similar limiting bubble volume and coverage despite changes in area. The surface of the anode of 6 mm was found to be completely blocked making it unusable. As this effect was not observed with the other anodes (8, 10 and 14 mm) Thorne *et al.* concluded that the bubble reached a maximum diameter of close to 6 mm. Horizontal anodes used by Thorne *et al.* [2] had ring of shielding material around anode of 2 mm thickness. Instead of BN, silicon nitride (Si_3N_4) material was used to shield the anode. Silicon nitride has a very low wettability to molten aluminium and a Si_3N_4-SiC composite is used for sidewall refractory in aluminum smelting pots [12] but wetting properties towards cryolite bath and possible impact on bubble behavior are not known.

Wang *et al.* [13] studied the effect of the current density and anode size on bubble size and bubble departure rate. Horizontal graphite anodes with 20, 30, and 40 mm diameter were studied. For smaller anodes the bubble size was smaller for the same current density. A larger number of bubbles and large bubbles give a higher probability for collision with other

bubbles leading to coalescence and bubble growth. Larger anodes are thought to sustain several bubbles simultaneously [14].

The aim of the present study was to compare bubble behavior and bubble size for facing-downwards horizontal anode with diameter 10 mm and 20 mm. The horizontal anode with 10 mm diameter was used earlier to study bubble phenomena and properties [1, 7, 10, 11]. A diameter of 20 mm is the diameter about the practical maximum possible for the furnace configurations used in previous studies. The bubble behavior was studied for both anodes for different current densities and discussed in detail. Another aim was to study the anode effect, and what happens on the anode surface at the initiation of the anode effect, during and after the anode effect.

8.2 Experimental part

8.2.1 Furnace and cell setup

The experiments were conducted in a see-through furnace and the experimental setup was the same as in [1, 7]. Video recording was performed from the side. Experiments were performed in a cryolite bath at a temperature of 890 ± 10 °C. A bath composition was 15 wt% AlF_3, 15 wt% LiF, 5 wt% CaF_2, 3 wt% Al_2O_3, rest synthetic cryolite. The high LiF concentration compared to that found in industry was used in order to maintain low liquidus and to improved visibility. The superheat was calculated to be ~ 50 °C and it was on purpose kept large in order to avoid bath freeze due to large heat losses and frequent opening of the furnace side lids.

8.2.2 Anode design

Two anode designs, one with a diameter of 10 mm and one with a diameter of 20 mm, were used, Figure 8.1. A purified graphite and an industrial carbon were used as the active electrode material. In the Chapter 7, the effect of the anode material on the bubble behavior was studied. In this chapter focus is not on the material properties but on the effect of the

anode size on the bubble behavior. Only the graphite anode was studied for bubbles size. The industrial anode was studied in detail for anode effect. Boron nitride (BN) was used for the anode shielding. The horizontal anode with 10 mm diameter was constructed as described in [10]. As illustrated in Figure 8.1(b), a BN ring is surrounding the anode. According to Åsheim *et al.* [15], BN is better wetted by the cryolite in comparison to graphite. Due to differences in wetting properties the BN ring causes prolongation of the bubble retention time by making it more difficult for bubble to be released. Hence, the horizontal anode with 20 mm diameter was constructed to avoid BN with 1 mm of graphite sticking out of the BN shielding, Figure 8.1(d). As a counter electrode, a stainless-steel (SS) rod with a diameter of 5 mm was used. The SS rod was immersed around 4 cm into the bath, which provided an area of approximately 6.5 cm^2.

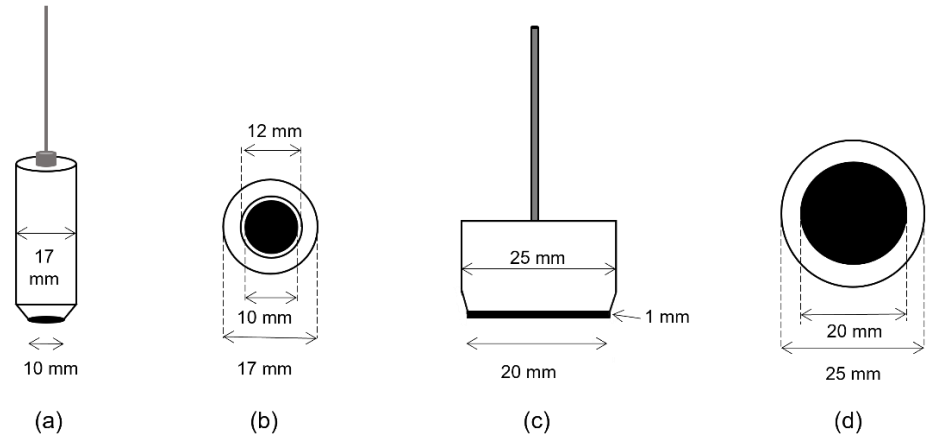

Figure 8.1. Horizontal anode designs with different diameter, (a) the horizontal anode with 10 mm diameter and surface area 0.79 cm^2, 45 degrees angle chamfered boron nitride edges, (b) the horizontal anode (Ø 10 mm) shown from below with small BN shielding around graphite surface, (c) the horizontal anode with 20 mm diameter and surface area 3.8 cm^2, 45 degrees angle chamfered boron nitride edges and 1 mm of graphite sticking out of the BN shielding, and (d) the horizontal anode (Ø 20 mm) shown from below.

8.2.3 Experimental methods

Electrochemical measurements were performed using a PARSTAT 4000+ (Princeton Applied Research) potentiostat and a 20 A booster (KEPCO). Due to smaller size of the quartz crucible and the reflections

inside the cell the reference electrode was not used and a two-electrode system was used. Electrolysis was performed at constant current density for both horizontal anodes (in the interval 0.25-1.0 A cm^{-2} for the 10 mm anode and 0.25-1.5 A cm^{-2} for the 20 mm anode). Linear Sweep Voltammetry (LSV) was performed sweeping from 0.3 V and up to 4.0 V at a sweep rate of 0.5 V s^{-1}. Electrochemical Impedance Spectroscopy (EIS) was used to determine the ohmic resistance at Open Circuit Potential (OCP). This value was used to post-IR compensate all electrochemical measurements. Voltage *vs.* time data from the constant current measurements for the both horizontal anodes were transformed into frequency spectra by using a Fast Fourier Transform (FFT) algorithm in "Sigview v4.3-spectrum and signal analysis" (SignalLab software) using spectral analysis default settings. The signals were transformed into the frequency domain to evaluate how the power of the signal is distributed over a range of frequencies to determine the dominant frequency. The sampling rate (Fs) was 10 Hz for 10 mm anode and 50 Hz for 20 mm anode. Consequently, the spectrum has a frequency range from zero to Fs/2, 0–5 Hz for 10 mm anode and 0-25 Hz for 20 mm anode respectively. Dominant frequency is considered the frequency where FFT peak with the maximum magnitude of the signal is observed.

All electrochemical measurements were simultaneously video recorded with a PhotronFastcam Mini AX camera. For this study a frame rate of 60 fps (frames per second) was used. Photron Fastcam Viewer 4 (PFV4) software was used for controlling the Photron high-speed camera, for data saving, and for image processing.

8.3 Results and discussion

8.3.1 Cell voltage fluctuation

Figure 8.2 shows cell voltage *vs.* time at 1.0 A cm^{-2} for the anode with 10 mm diameter (a) and 20 mm diameter (b). The characteristic saw-tooth shape of the potential oscillation appeared for both anodes but have different shape, potential oscillation magnitude, bubble time period and number of detached bubbles. Details of the characteristic saw-tooth curve for the horizontal anode with 10 mm diameter were interpreted earlier in

relation to Figure 4.5 in Chapter 4, [10]. Since the same graphite material was used to construct 10 mm and 20 mm diameter anodes, it is assumed that comparison of the anode performance in relation to anode diameter at similar potential/current density values is meaningful, although the anode design is not exactly the same due to existence of the BN ring at the 10 mm anode. The saw-tooth is sharper for the 10 mm diameter than for the 20 mm diameter anode. A voltage oscillation magnitude for the 10 mm and 20 mm anode is in the range 1.85 V-2.6 V and 1.8 V-2.3 V, respectively. As a bubble grows it covers more and more of the anode surface causing the potential to increase as the local current density increases. When the bubble detaches, the local current density decreases and consequently the voltage decreases quickly [16]. The smaller anode is shielded with the BN ring which makes it difficult for a bubble to detach and the bubble is forced to grow to maximum size, something that increases the bubble surface coverage. The large bubble is in contact with the BN ring surrounding the anode and due to differences in wetting the bubble cannot easily be detached. This is believed to be one reason for the larger potential oscillation for the 10 mm diameter anode.

For the 10 mm anode the average bubble time period is 2.10 s, which corresponds to the bubble release frequency of 0.48 Hz. Average bubble time period for the 20 mm anode is 3.83 s, which corresponds to the bubble release frequency of 0.26 Hz. During electrolysis for 30 seconds at 1.0 A cm^{-2}, 14 larger bubbles were released from the 10 mm anode and 8 larger bubbles from the 20 mm anode. This was confirmed from the video observations.

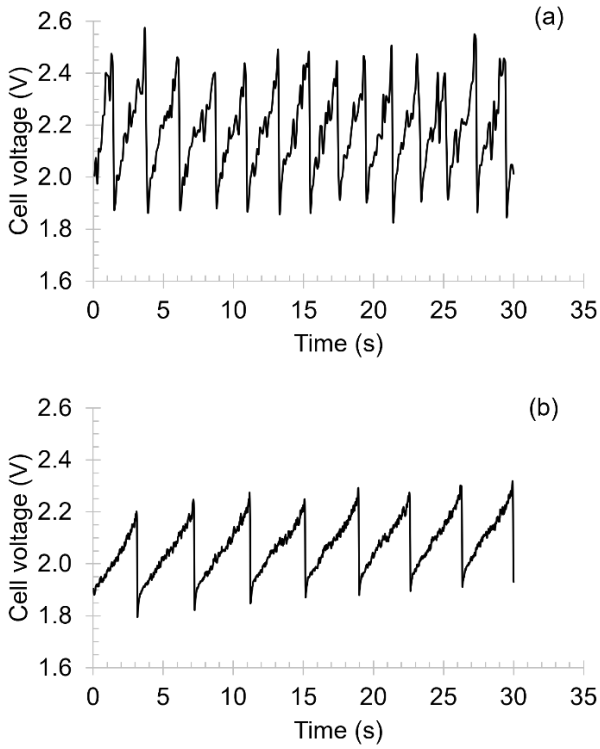

Figure 8.2. Cell voltage-time data at applied constant current density of 1.0 A cm^{-2} for the graphite anode (a) diameter 10 mm (b) diameter 20 mm. Cell voltage data are post-IR-compensated.

Fast Fourier transform analysis (FFT) of the voltage *vs.* time for both anode designs at 1.0 A cm^{-2} is shown in Figure 8.3. For 10 mm anode a major FFT peak is observed in range 0.38-0.68 Hz while for the 20 mm anode the range is 0.2-0.33 Hz. It was expected that the major FFT peak for the 10 mm anode would be higher than for the 20 mm. Due to the existence of the BN ring the frequency of the 10 mm anode is probably shifted towards a lower frequency. Dominant frequency extracted from Figure 8.3 is 0.5 Hz for 10 mm anode and 0.26 Hz for 20 mm anode. The bubble release frequency obtained from cell voltage *vs.* time data is in agreement with the dominant frequency obtained from FFT analysis.

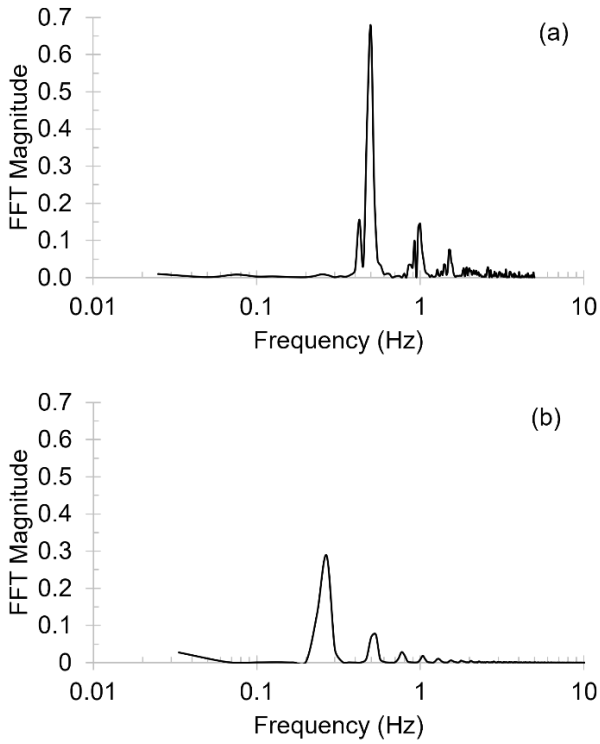

Figure 8.3. FFT spectra of voltage-time data for 1.0 A cm^{-2} for the graphite anode with (a) 10 mm diameter and (b) 20 mm diameter.

8.3.2 Bubble size

The average bubble diameter after bubble detachment from the horizontal surface as a function of current density is presented in Figure 8.4. Error bars represent a 95% confidence interval assuming a normal distribution. The bubble diameter from video recordings was calculated as an average value of 10 bubbles for the 10 mm anode and 15 bubbles for the 20 mm anode for both vertical and horizontal surfaces at each current density. The diameter was defined as the distance between two points of the spherical bubble and was measured as described in Chapter 6 in [7]. The bubble diameter was measured using PFV4 software. The target bubble was a bubble detached from the anodic surface that had a nearly spherical shape. As expected, the bubble diameter was decreasing with increasing current density for both anodes. Bubbles detached from the 20

mm anode are larger in size than bubbles detached from the 10 mm anode for the same current density. Since the anode surface is larger more bubbles can be formed and at lower current, bubbles have time to coalesce with each other and grow. For 0.25 A cm^{-2} and 0.5 A cm^{-2} the bubble diameter at the 20 mm anode is almost two times as large as the bubble diameter of the 10 mm anode. For higher current densities, newly formed bubbles are pushing already existing bubbles which then do not have time to coalesce with others and grow more in size.

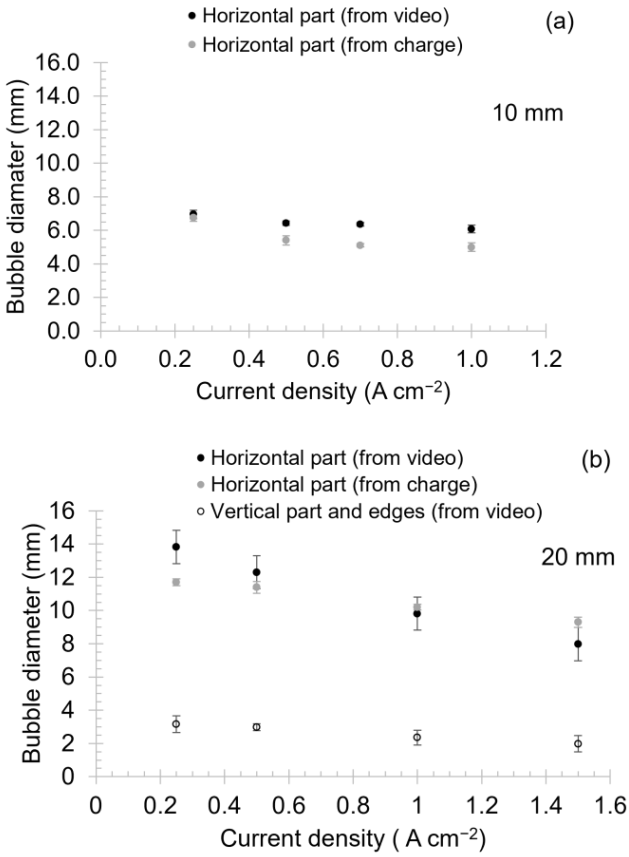

Figure 8.4. Bubble diameter as a function of the nominal current density, measured from the video recordings and calculated from the charge for the graphite anode with (a) 10 mm diameter and (b) 20 mm diameter.

The standard deviation is larger for the 20 mm than for the 10 mm anode for the same current density. As mentioned earlier bubbles at the 10

mm anode due to existing of the BN ring have difficulties to detach. Therefore, the bubble is forced to grow to artificially large size in order to detach. Hence these bubbles are more similar in size for the same current density than bubbles detached from the 20 mm anode. It seems that the bubbles from the 20 mm anode detached without great difficulties due to lack of BN ring. The diameter of bubbles detached from the vertical surface and the edge of the 20 mm anode does not change significantly with increasing current density, Figure 8.4(b).

Bubble diameter was also calculated using charge data assuming that only CO_2 gas is produced. A volume of each bubble detached from the horizontal surface was calculated from Faraday's law. Afterwards a diameter was calculated using the equation for the volume of a sphere. Results are also shown in Figure 8.4. Values are in correspondence with the diameter measured from video recording results.

8.3.3 Video recording

In Figure 8.5 are shown images of a bubble at the horizontal graphite anode surface in the growth stage just before it starts to slide towards the edge to be detached. Observing from the side it seems that at a certain point, *i.e.,* in the final growing stage before bubble detachment, one big bubble is covering majority of the anode surface, on the10 mm (a) and on the 20 mm (b) anode. It was observed that the bubble detachment for the 20 mm anode was faster. At 1.0 A cm^{-2} for the 10 mm anode bubble sliding and detachment occurred in the time range of 15.0-16.7 ms while for the 20 mm anode of 10.0-11.7 ms . Bubbles are detached from the 20 mm anode easier than from the 10 mm anode possibly due to BN ring surrounding 10 mm anode complicating and prolonging a bubble release. For the 10 mm anode at a current density of 1 A cm^{-2} the thickness of the bubble just before it start to slide toward edge to be detached from the anode surface, was found to be around 4.6 mm while for the 20 mm anode the bubble thickness was 3.9 mm.

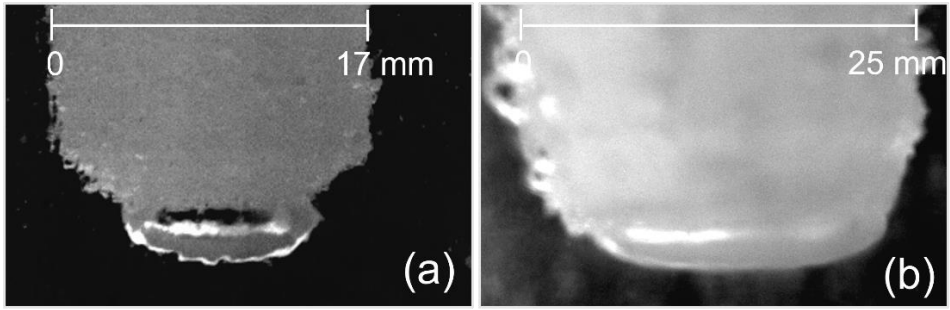

Figure 8.5. Images of the bubble at the graphite anode surface in the growth stage just before the bubble starts to slide towards the edge to be detached; (a) the 10 mm anode at 0.4 A cm^{-2}, (b) the 20 mm anode at 0.5 A cm^{-2}. A scale bar is shown.

Non-electrochemically formed bubbles which occurred at the anodic surface when the anode is immersed in bath were removed easily from the 20 mm diameter anode by gentle shaking of the anode and they did not cause the blockage of the anode surface and overloading of the potentiostat. During electrolysis, the voltage overloading of the potentiostat was not observed. It seems that the 10 mm anode is more easily blocked with bubbles than the 20 mm anode probably due to the existence of the BN ring shielding around graphite anode surface.

From the vertical carbon surface side of the 20 mm anode, there were always small bubbles formed and released quite fast without prolonged retention time, Figure 8.6. This phenomenon was observed for both graphite and industrial carbon anodes. The image in Figure 8.6 shows an industrial carbon anode and not of a graphite anode as this experiment gave particularly clear images. One small bubble that had already left the vertical side and was rising up can be seen in the right side in the image. While one big bubble was growing at the horizontal surface, smaller bubbles were detaching from the vertical surface.

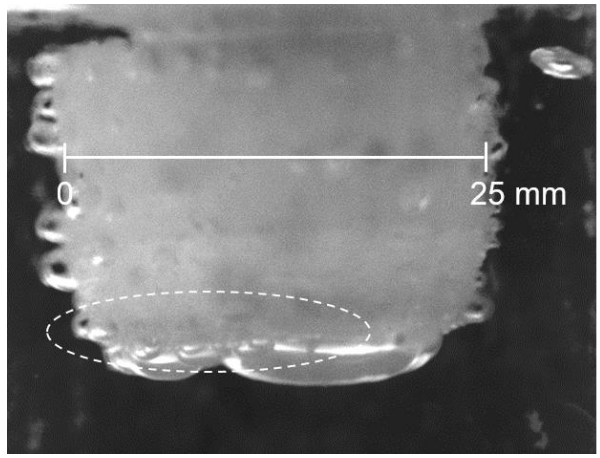

Figure 8.6. An image of the industrial carbon anode with 20 mm diameter showing smaller bubbles sticking to the vertical part and edge of the anode surface (highlighted) at current density 0.25 A cm^{-2}. A scale bar is shown.

8.3.4 Anode effect

Figure 8.7 shows linear sweep voltammograms with sweep rate 0.5 V s^{-1} for the horizontal graphite anodes with 10 mm and 20 mm diameter; (a) cell voltage not IR compensated, (b) cell voltage post-IR-compensated with the value of ohmic resistance at OCP. An increase in current density is observed around 0.7 V. The current increase was due to CO_2/CO gas evolution. After initiation of gas evolution, the current density for two different anodes started to differ. The current oscillations arise from growth, coalescence and detachment of bubbles [10]. At 3 V for the non-IR-compensated curve for the 10 mm anode, the current suddenly decreased towards zero, Figure 8.7 (a). The sudden decrease was attributed to the initiation of anode effect. Immediately after the decrease the current sudden increased and decreased again whereupon it stayed practically zero with increasing voltage. The small rise in current can be explained by the sudden increase in voltage of the electrode when the current drops instantly to zero at anode affect, from 2.6 V to 3.6 V. Some of the electrolyte that remained on the anode surface under the gas layer might have been oxidized during this increase of the anode potential. There is no video recording of this process. It was difficult to obtain successful linear sweep voltammograms for the graphite anode with 10 mm diameter due to frequent potential overloading of the potentiostat which was caused by

bubble blockage of the anodic surface. Further, as discussed in [7], the existence of non-electrochemically spontaneously formed bubbles block the anodic surface making it difficult to start the sweep. Anode effect did not take place on the voltammogram for the horizontal graphite anode with 20 mm diameter, Figure 8.7, but took place for higher sweep rates, 1 V s^{-1} and 5 V s^{-1}, but 0.5 V s^{-1} is presented for comparison with the 10 mm anode. Only 2-3 sweeps were performed.

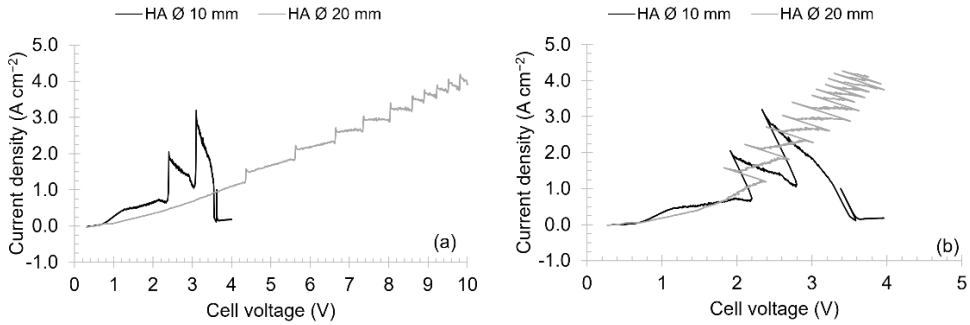

Figure 8.7. Linear sweep voltammetry for the graphite anode with 10 mm (black line) and 20 mm diameter (gray line) recorded with the sweep rate of 0.5 V s^{-1}, (a) non-IR compensated cell voltage, (b) post-IR-compensated cell voltage with the value of ohmic resistance at OCP.

Anode effect took place at the 20 mm industrial carbon anode, Figure 8.8. The link for the corresponding video of the process can be found in Appendix 8.5. In Figure 8.8(a) is shown a linear sweep voltammetry curve. Starting from 0 V, the first increase in current density is observed around 0.8 V. Figure 8.8(b) shows images from the video recording according to the numbers in 8.8(a). In frames (1-3) is shown evolution of bubbles and their detachment at around 0.8, 1.4 and 2.1 A cm^{-2}, respectively. Frame (4) represents the state of the anode just before the initiation of the anode effect.

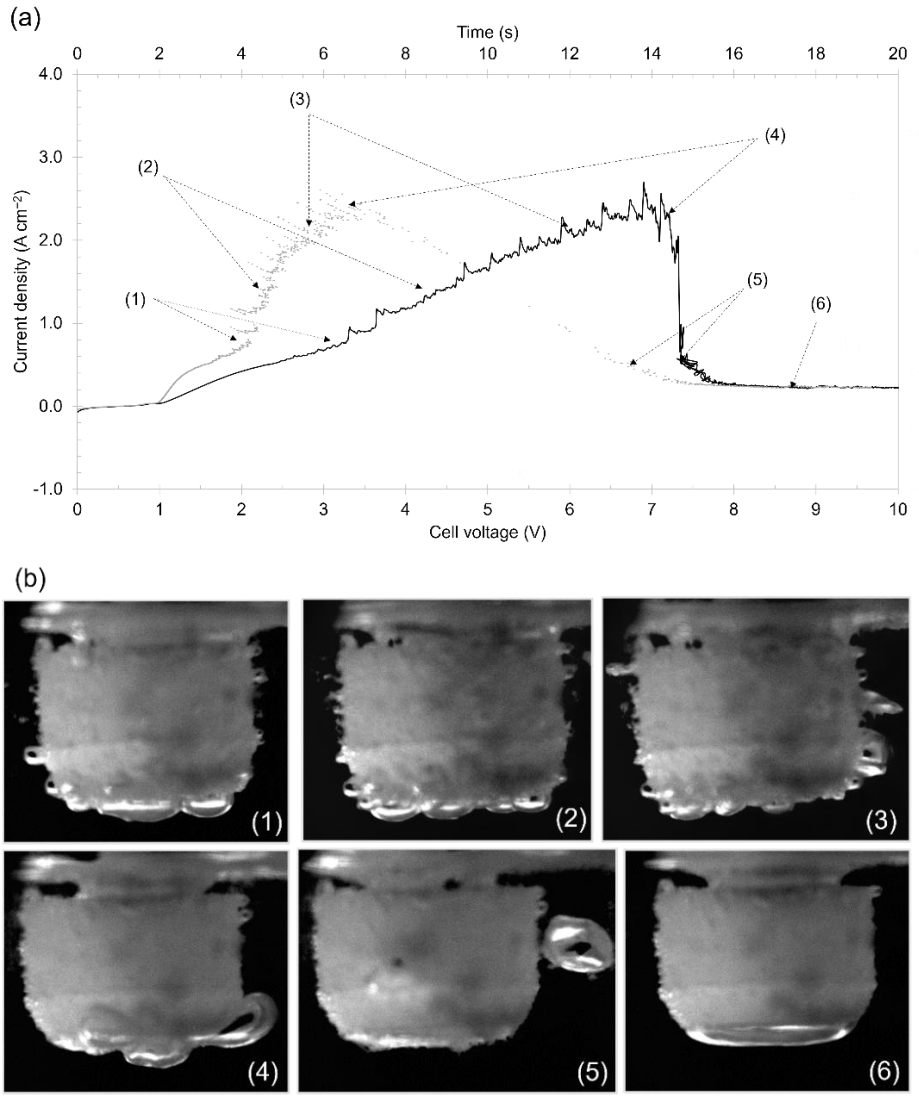

Figure 8.8. (a) Linear sweep voltammetry curve for the industrial carbon anode with sweep rate 0.5 V s^{-1}. Non IR and IR-compensated data are shown. Sampling frequency was 50 Hz. A timeline is only valid for non IR-compensated data. (b) Corresponding images from the video recordings.

At 7.5 V at the non-IR-compensated curve, the current suddenly decreased towards zero. The sudden decrease was attributed to the occurrence of the anode effect, forming a gas layer on the surface of the anode, frame (5). At the initiation of anode effect, the anode surface has been teflonised, *i.e.*, (C – F) film was formed [17]. The gas layer was

covering the whole anode surface and stayed stable for applied cell voltage up to 10 V, frame (6). The gas was trapped by the BN shielding due to better wetting of the BN by electrolyte as found by Åsheim *et al.* [15] and the faradaic current became approximately zero and the gas evolution therefore stopped. The anode became completely de-wetted. The critical current density on the anode was exceeded, and the IR-compensated curve indicates that the potential of the anode is high enough to produce PFC. The gas layer at the carbon surface is believed to be a mixture of CO, CO_2 and PFC gases [17].

8.4 Conclusion

The bubble diameter was decreasing with increasing current density for both, the 10 mm and the 20 mm anode. Bubbles detached from the 20 mm diameter anode are larger in size than bubbles detached from the 10 mm anode for the same current density. The thickness of the bubble just before it starts to slide towards the edge to be detached from the anode surface was found to be around 4.6 mm for the 10 mm anode and 3.9 mm for the 20 mm anode. The boron nitride shielding the 10 mm anode makes it difficult for bubbles to detach because of the good wetting of the boron nitride against the cryolite bath. Therefore, the bubble is forced to grow to artificially large size in order to detach. This also contributes to larger bubble surface coverage of the 10 mm anode. At the initiation of anode effect, the anode surface becomes teflonised and thereby completely de-wetting, and the existing CO/CO_2 bubbles are immediately detached from the anode surface. A gas layer, a mixture of CO, CO_2 and PFC gases, was formed at the surface completely covering the whole carbon surface thus preventing contact between the carbon surface and the cryolite bath.

8.5 Appendix

A video recording of linear sweep voltammetry on the horizontal industrial carbon anode with 20 mm diameter in relation to Figure 8.8, https://youtu.be/oN4iqx4kjWc . The video is captured with 60 fps. The video is saved with playback frame equal to 20 fps, meaning the video is shown in 33 % of the real speed.

References

1. Stanic, N. and E. Sandnes, *Bubble Behavior on Horizontal and Vertical Carbon Anode Surfaces in Cryolite Melt Applying a See-Through Cell.* Materials Proceedings, 2021. **3**(1): p. 8.
2. Thorne, R.J., C. Sommerseth, A.P. Ratvik, S. Rorvik, E. Sandnes, L.P. Lossius, H. Linga, and A. Svensson, *Bubble Evolution and Anode Surface Properties in Aluminium Electrolysis.* J. Electrochem. Soc., 2015. **162**(8): p. E104-E114.
3. Thorne, R.J., C. Sommerseth, A.M. Svensson, E. Sandnes, L.P. Lossius, H. Linga, and A.P. Ratvik, *Understanding Anode Overpotential*, in *Light Metals 2014*, J. Grandfield, Editor. 2014, John Wiley & Sons, Inc.: Hoboken, NJ. p. 1213-1217.
4. Thorne, R.J., C. Sommerseth, A.P. Ratvik, S. Rorvik, E. Sandnes, L. Lossius, H. Linga, and A. Svensson, *Correlation between Coke Type, Microstructure and Anodic Reaction Overpotential in Aluminium Electrolysis.* J. Electrochem. Soc., 2015. **162**(12): p. E296-E306.
5. Thorne, R.J., C. Sommerseth, E. Sandnes, O. Kjos, T.A. Aarhaug, L.P. Lossius, H. Linga, and A.P. Ratvik, *Electrochemical Characterization of Carbon Anode Perfomance*, in *Light Metals 2013*, B. Sadler, Editor. 2013, Springer. p. 1207-1211.
6. Xue, J. and H.A. Øye, *Bubble behaviour : cell voltage oscillation during aluminium electrolysis and the effects of sound and ultrasound*, in *Light Metals 1995*, J. Evans, Editor. 1995, TMS: Warrendale. p. 265-271.
7. Stanic, N., A.M. Martinez, K.E. Einarsrud, and E. Sandnes, *Bubble Phenomena and Bubble Properties for Horizontal and Vertical Carbon Anode Surfaces in Cryolite Melt Applying a See-Through Cell.* Metals, 2021. **11**(6): p. 24.
8. Zhao, Z., Z. Wang, B. Gao, Y. Feng, Z. Shi, and X. Hu, *Anodic Bubble Behavior and Voltage Drop in a Laboratory Transparent Aluminum Electrolytic Cell.* Metall. Mater. Trans. B, 2016. **47**(3): p. 1962-1975.
9. Gebarowski, W., A.P. Ratvik, S. Rørvik, L.P. Lossius, H. Linga, and A.M. Svensson. *Effect of Coke Properties on the Bubble Formation at the Anodes During Aluminium Electrolysis in Laboratory Scale*. 2017. Cham: Springer International Publishing.
10. Stanic, N., I. Jevremovic, A.M. Martinez, and E. Sandnes, *Bubble Evolution on Different Carbon Anode Designs in Cryolite Melt.* Metallurgical and Materials Transactions B, 2020. **51**(3): p. 1243-1253.
11. Stanic, N., E.T. Bø, and E. Sandnes, *CO and CO_2 Anode Gas Concentration at Lower Current Densities in Cryolite Melt.* Metals, 2020. **10**(12): p. 1694.
12. Jones, M.I., R. Etzion, J. Metson, Y. Zhou, H. Hyuga, Y.-I. Yoshizawa, and K. Hirao, *Corrosion behavior of reaction bonded Si3N4-SiC and SiAlON-SiC composites in simulated aluminum smelting conditions.* Nippon Seramikkusu Kyokai Gakujutsu Ronbunshi/Journal of the Ceramic Society of Japan, 2008. **116**: p. 712-716.
13. Wang, Z., B. Gao, H. Li, Z. Shi, X. Lu, and Z. Qiu. *Study on Bubble Behavior on Anode in Aluminum Electrolysis-Part I*. in *Technical Sessions, Minerals, Metals and Materials Society.; Light metals 2006*. 2006. Warrendale, Pa.:, San Antonio, Texas: TMS.

14. Cassayre, L., T. Utigard, and S. Bouvet, *Visualizing gas evolution on graphite and oxygen-evolving anodes.* JOM (USA), 2002. **54**(5): p. 41-45.
15. Åsheim, H., I. Eidsvaag, A. Solheim, H. Gudbrandsen, G.M. Haarberg, and E. Sandnes, *The Influence of Polarisation on the Wetting of Graphite in Cryolite-Alumina Melts*, in *Light Metals 2020*, A. Tomsett, Editor. 2020, Springer International Publishing. p. 608-619.
16. Einarsrud, K.E. and S.T. Johansen, *Modelling of bubble behavior in aluminium reduction cells.* Prog. Comput. Fluid Dyn., 2012. **12**(2-3): p. 119-130.
17. Tabereaux, A., *Anode Effects, PFCs, Global Warming, and the Aluminium Industry.* JOM, 1994. **46**: p. 30-34.

Chapter 9

Bubble evolution and anode effect on an upward-facing horizontal carbon surface

Nikolina Stanic[1], Ana Maria Martinez[2], Kristian Etienne Einarsrud[1] and Espen Sandnes[1]

[1] Department of Materials Science and Engineering, Norwegian University of Science and Technology NTNU, NO-7491 Trondheim, Norway
[2] SINTEF Industry, 7034 Trondheim, Norway

A draft for a future publication.

Abstract

Bubble behavior and dynamics on an upward-facing horizontal carbon anode was studied. This was done in order to get more detailed understanding of the regular electrolysis and anode effect in the Hall-Héroult process. The presence of weak saw-tooth features for this anode at low current densities was explained by bubble retention time large enough for coalescence into a larger bubble to take place. Different stages of bubble growth were observed and were in agreement with findings in the literature regarding aqueous solutions: hemispherical spreading, cylindrical spreading, cylindrical growth, and necking. Coalescence was observed only in the hemispherical spreading stage. A different necking was observed since the cryolite-carbon system in general shows poor

wetting and wetting affects the necking. The evolution of the anode effect depends on the possibility of the gas bubbles and gas layer to be detached from the anode surface. If the gas is trapped the gas layer is covering the anode surface, disabling contact between anode and electrolyte and further gas production is strongly hindered. The anode surface of the inverted horizontal anode after anode effect was found to be still electrochemical active with the increasing voltage. The gas was not trapped and the gas evolution could continue.

Keywords: gas bubble, carbon anode, cryolite, anode effect, see-through furnace

9.1 Introduction

A lab scale anode with upward-facing horizontal surface is termed as the inverted horizontal anode. It was constructed as shown in Figure 9.1(a), and studied in detailed in [1]. The inverted horizontal anode was designed to have a horizontal surface with more smaller bubbles and frequent bubble release in comparison to a downward-facing horizontal anode termed as horizontal anode. Bubbles from the horizontal anode cannot be detached easily and they have to grow to a certain size covering almost all of the anode surface. Resulting bubbles are large in size compared to bubbles from other anode designs: rod anode (studied in Chapter 4, Chapter 7) and vertical anode (studied in Chapter 4, Chapter 6).

This chapter presents a study of the bubble behavior on inverted anode using a see-through cell. Although this type of anode design is not applied in industry, it offered an opportunity to study bubble behavior on such a surface and this information could be used to better understand the bubble evolution on the horizontal surface. Topics studied, were among, others bubble growth and coalescence, bubble shape, bubble detachment as well as the anode effect process.

9.2 Experimental

9.2.1 Furnace and cell setup

The experiments were conducted in a see-through furnace and the experimental setup was the same as in Chapter 6 and Chapet 7 [2, 3]. Video recording was performed from the side. Experiments were performed in a cryolite bath with composition 15 wt% AlF_3, 15 wt% LiF, 5 wt% CaF_2, 3 wt% Al_2O_3, rest synthetic cryolite. The high LiF concentration compared to that found in industry was used in order to maintain low liquidus and because it was observed that LiF helped to reduce the fumes inside the furnace and, with that, improved visibility. The calculated liquidus temperature was 838 °C and the working temperature was 890 ± 10 °C. A superheat of ~ 50 °C was kept large in order to avoid bath freeze due to heat loss through furnace side lids.

9.2.2 Anode design

A purified graphite material (Schunk Tokai Scandinavia, AB, Sweden) was the active electrode material. Boron nitride (BN) (BN5000, Kennametal, UK) was used for anode shielding. As a counter electrode, a stainless-steel (SS) rod with a diameter of 5 mm was used. The SS rod was immersed around 4 cm into the bath, which provided an area of approximately 6.5 cm^2.

The inverted anode was previously studied in Chapter 4 and Chapter 5 [1, 4]. This design was not suitable for use in the see-through furnace. A few designs were made until a satisfying solution was obtained. Figure 9.1(a) shows the first design used in [1, 4]. Figure 9.1(b, c) show the anode design used in this work. As can be seen in (b, c) BN edges were 45 degrees angle chamfered and 2 mm of graphite was sticking out of the BN shielding. By using the first design inverted from Figure 9.1(a) two main problems occurred: reflections in the cell due to a relatively big size of the anode shielding (BN) in comparison to the size of the quartz crucible and a great amount of non-electrochemically formed bubbles resting at the BN. As was found in [2], bubbles were observed resting at the BN surfaces. The bubbles were formed spontaneously as soon as the anode was immersed in

the bath. These non-electrochemically formed bubbles rested at the BN surface did not take part in any electrochemical reaction. The bubbles were assumed to be either moisture or nitrogen arising from the bulk of the BN material. In Figure 9.2(a) is shown an illustration of non-electrochemically and electrochemically formed bubbles at the first inverted anode design. It can be seen that the anode surface is barely visible. Non-electrochemically formed bubbles resting at BN hindered the view of the anode surface. Therefore, it was necessary to introduce a new design which has more graphite and less BN in the construction. A few designs were tested before the properly working design in Figure 9.1(b, c) was found. In Figure 9.2(b) is given an illustration of the final anode design non-electrochemically and electrochemically formed bubbles on the final anode design. The graphite is sticking 2 mm out of the BN shielding with chamfered BN edges was not chamfered. Non-electrochemically formed bubbles resting on the BN surface were not hindering the anode surface Figure 9.2(b).

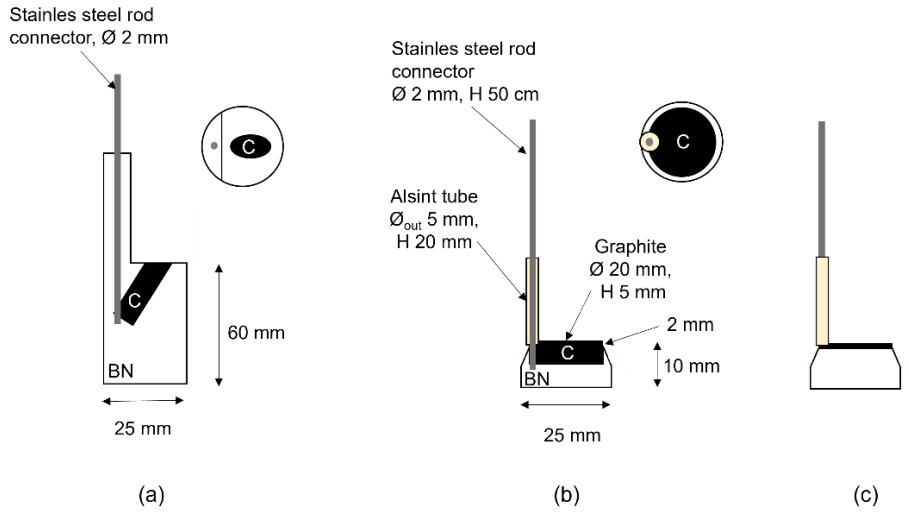

Figure 9.1 Anode with horizontal surface facing upwards, *i.e.*, inverted anode (a) cross-section of earlier constructed and studied design with a (surface area of 0.69 cm^2), (b) cross-section of a new improved design with a total surface area of 4.4 cm^2, of which the horizontal surface is 3.14 cm^2 and the vertical surface 1.26 cm^2, (c) the outer body of the new design. Insets in (a) and (b) shows the inverted anode seen from above.

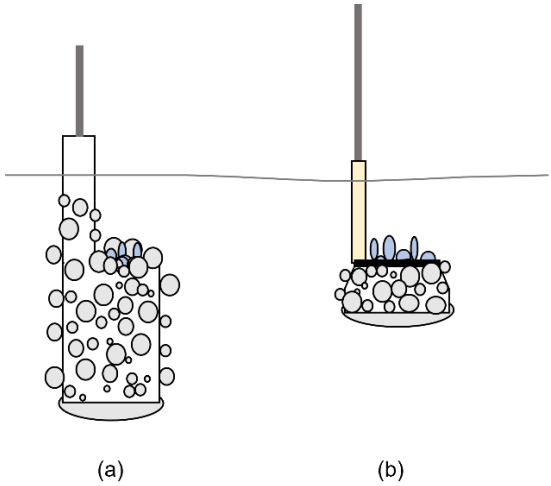

Figure 9.2. Illustration of the electrochemically and non-electrochemically formed bubbles on different types of the inverted anode (a) first constructed and studied inverted design, (b) new improved design with chamfered edges during electrolysis. In light gray color are shown non-electrochemical bubbles formed and resting at the BN surface, while light blue color shows electrochemically formed bubbles.

9.2.3 Experimental methods

Electrochemical measurements were performed using a PARSTAT 4000+ (Princeton Applied Research) potentiostat and a 20 A booster (KEPCO). Due to smaller size of the quartz crucible and the reflections in the quartz crucible the reference electrode was avoided and a two-electrode system was used. The SS rod functioned as the counter electrode. Electrolysis was performed at constant current in the interval 0.1-1.0 A cm^{-2}. At current densities above 0.5 A cm^{-2} turbulence in the cell is high due to bubble induced convection which reduces visibility in the cell. To be able to observe details about events happening at the electrode surface experiments at lower current densities were preferred. Linear Sweep Voltammetry (LSV) was performed sweeping cell voltage from 0 V and up to 9.0 V with a sweep rate of 1.0 V s^{-1}. Electrochemical Impedance Spectroscopy (EIS) was used to determine the ohmic resistance at Open Circuit Potential (OCP). This value was used to IR compensate some of electrochemical measurements.

All electrochemical measurements were simultaneously video recorded with a PhotronFastcam Mini AX camera (Photron, USA). For this

study a frame rate of 60 fps (frames per second) was used. Photron Fastcam Viewer 4 (PFV4) software was used for controlling the Photron high-speed camera, for data saving, and for image processing.

9.3 Results and discussion

9.3.1 Cell voltage-time data

Figure 9.3 shows cell voltage-time data at different current densities, 0.2, 0.5 and 1.0 A cm^{-2}. At 0.2 A cm^{-2} it can be observed saw-tooth features of the curve. At 0.5 A cm^{-2} saw-tooth features disappeared while at 1.0 A cm^{-2} random voltage oscillation were observed. A similar behavior was observed by studying voltage-time data of the first design of the inverted horizontal anode in Chapter 4 [1]. Direct voltage comparison between experiments using earlier and new anode design is difficult, since in the latter experiment no reference electrode was used but the shape of the voltage-time curves can be compared. The presence of weak saw-tooth features for this anode at low current densities was explained by bubble retention time large enough for a coalescence into larger bubble to take place. With increasing current, the convection is higher and bubbles detach at a smaller size and the extent of coalescence is thereby smaller resulting in disappearance of the saw-tooth features.

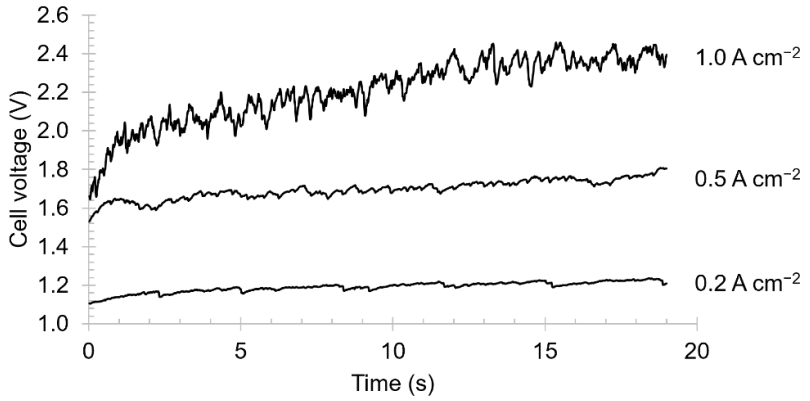

Figure 9.3. Cell voltage-time data for different current densities. The sampling rate was 50 Hz. Voltage data are post-IR-compensated.

9.3.2 Bubble size

Figure 9.4 shows bubble evolution at different current densities. All images are taken at the same event in the bubble cycle, the bubble detachment. The average bubble diameter after bubble detachment as a function of current density is presented in Figure 9.5. Error bars represent a 95% confidence interval assuming a normal distribution. The bubble diameter was calculated as an average value of 15 bubbles at each current density. Bubble diameter was measured using PFV4 software and calculated as described in Chapter 6 [2]. As expected, the bubble diameter was decreasing with increasing current density. The diameter of the bubbles at 0.1 A cm^{-2} has an average value of 5.1 mm and this is reduced to 3.2 mm at 1.0 A cm^{-2}.

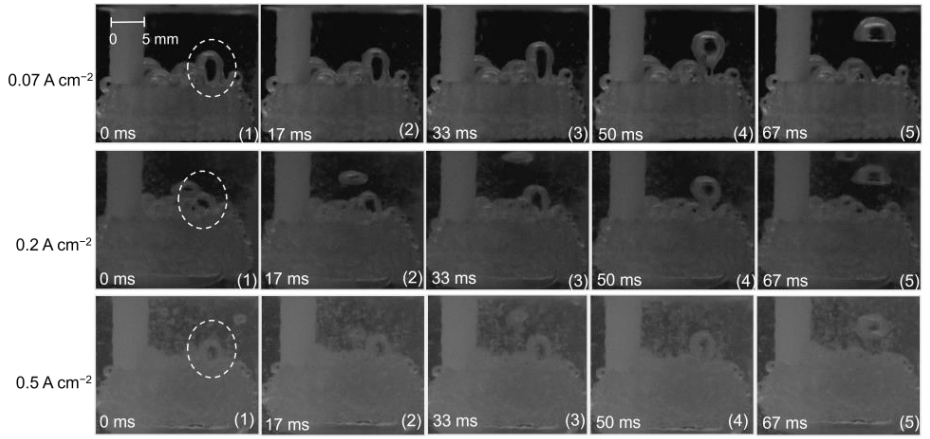

Figure 9.4. Bubble detachment from the inverted anode during electrolysis at constant current of 0.07 A cm^{-2}, 0.2 A cm^{-2} and 0.5 A cm^{-2}. The frame rate was 60 fps. Frame numbers are given in brackets. Timestamp of 0 ms is assigned to frame (1), by that, other frames are relative to the first frame. A scale bar is shown in frame (1).

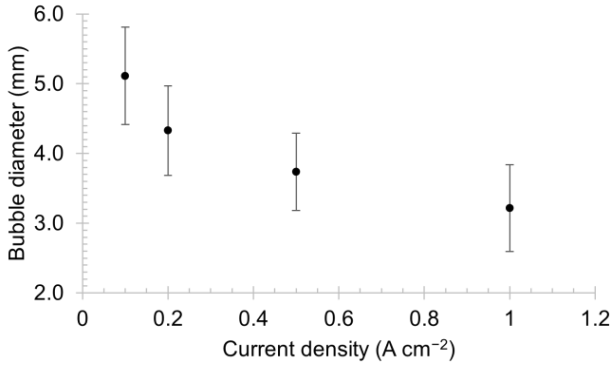

Figure 9.5. Bubble diameter detached from the inverted horizontal anode as a function of applied current density.

9.3.3 Video recording

Figure 9.6 shows voltage-time data for constant current electrolysis at 0.07 A cm^{-2}. The corresponding video of the process can be found in Appendix 9.5.

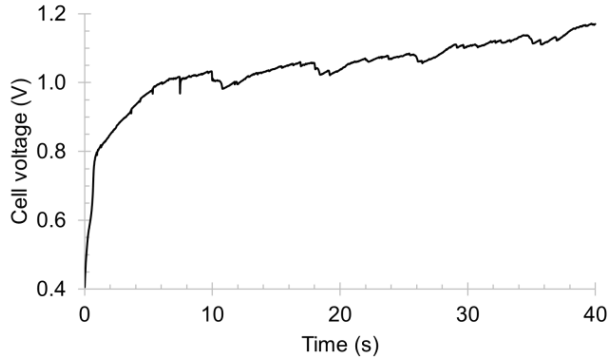

Figure 9.6. Cell voltage-time data under galvanostatic control for inverted anode at constant current density 0.07 A cm^{-2}. Data are post-IR-compensated. The sampling frequency was 50 Hz.

As mentioned above the saw-tooth features were observed and disappeared with increasing current density, Figure 9.3. From the video recordings in Appendix 9.5 in relation to Figure 9.6, the saw tooth features could be explained by mutual influence of both coalescence and simultaneous detachment of several bubbles in a periodic pattern. The

anode surface was never free of bubbles although the applied current density was rather low, 0.07 A cm^{-2}. The saw-tooth feature comes from coalescence of smaller bubbles into bigger bubbles which afterwards detached. In general, an increase in the cell voltage represents growth and coalescence of bubbles while a sudden decrease represents detachment of bubbles.

Zhang and Shoji [5] studied nonlinear behavior of bubbles formed from submerged orifice and reported that bubble formation has two stages, the expansion stage and the elongation stage. In the expansion stage, the bubble grows radially, but the base of the bubble is still attached to an orifice. This process continues as long as the opposing forces against bubble release (drag, surface tension, mass inertia) dominate the lifting forces (the gas momentum flux and buoyancy). The expansion stage will come to end when the opposing forces become equal to or larger than the lifting forces. In the elongation stage the bubble starts to lift off from the orifice but is still attached to it. The bubble forms a neck shape at the orifice. Eventually, the neck becomes very thin and pinches off from the orifice, *i.e.*, bubble detachment takes place.

Mirsandi *et al.* [6] studied the influence of wetting conditions on the dynamics of bubble formation from a submerged orifice. Among other things, the contact line and contact angle between three phases (gas, liquid, solid) was studied using a hydrophobic orifice plate and a series of ethanol–water solutions to vary the wettability. Mirsandi *et al.* observed that both, the contact line and contact angle, have influence on the detached bubble size in the case of poor wetting conditions. It was observed that contact diameter increases with increasing surface tension. With the increased surface tension, the contact angle increases (poor wetting). The surface tension restrains the bubble from detachment affecting the bubble size*, i.e.*, increases it. The authors also explained different stages of bubble growth: hemispherical spreading, cylindrical spreading, cylindrical growth, and necking. In the first stage, hemispherical spreading, the bubble attains the shape of an almost perfectly hemispherical shape. The bubble apex is nearly identical to the bubble height. The bubble spreads for some time while retaining a hemispherical shape. At the cylindrical spreading stage, the bubble spread further as its height keeps increasing. In the third cylindrical growth stage, the volume growth is captured in the height growth. The value of the contact angle increases as the bubble grows further. The third stage ends when the buoyancy force exceeds the surface

tension force. The last stage is the necking stage. A cylindrical shape changes into a spherical shape due to the formation of the bubble neck.

Figure 9.7 shows life cycle of one bubble during electrolysis at a constant current density of 0.07 A cm^{-2} and it is representing a saw-tooth event and is ending with the voltage drop observed at ~10 s in Figure 9.6. All mentioned stages of bubble growth by Mirsandi *et al*. [6] were observed although the necking was different. For bubbles of interest, highlighted with white dashed line, hemispherical spreading and coalescence occurred up to frame (326). It was observed that hemispherical-shaped bubbles were meeting at the base and coalescing forming bigger bubbles, frames (64-65), (152-154), (323-325). It was difficult to distinguish where cylindrical spreading ended and cylindrical growth started, but both cylindrical stages were observed after frame (326) up to frame (598). Afterwards, necking occurred and the big bubble is detached in frame (603). The video recording did not indicate that the process of coalescence occurs when bubbles were in the cylindrical stage. It seems that the driving force for coalescence is not present for elongated bubbles. Coalescence is preceded by collision. Since collision between elongated bubbles on the anode surface was not observed, this explains lack of coalescence. Bubbles in cylindrical stage were observed in video to be swinging at the anode surface. The same behavior was observed by Ying *et al.* [7]. The authors studied bubbles rising side by side experimentally in the system air-water and also by numerical calculation. The authors observed that when two bubbles rise side by side, bubbles repeatedly were attracted to and bounced against each other in cyclical process, and the bubbles swung up and down periodically.

Taqieddin *et al.* [8] provided a mathematical model for each phase of the life cycle of a bubble (nucleation, growth, detachment and transport) to contribute in bubble modeling in electrochemically gas-evolving systems. The detachment process begins with the necking stage. Bubble bulk move away from the surface producing so called neck that continues to shrink until it reaches zero thickness when the bubble detaches and rises up.

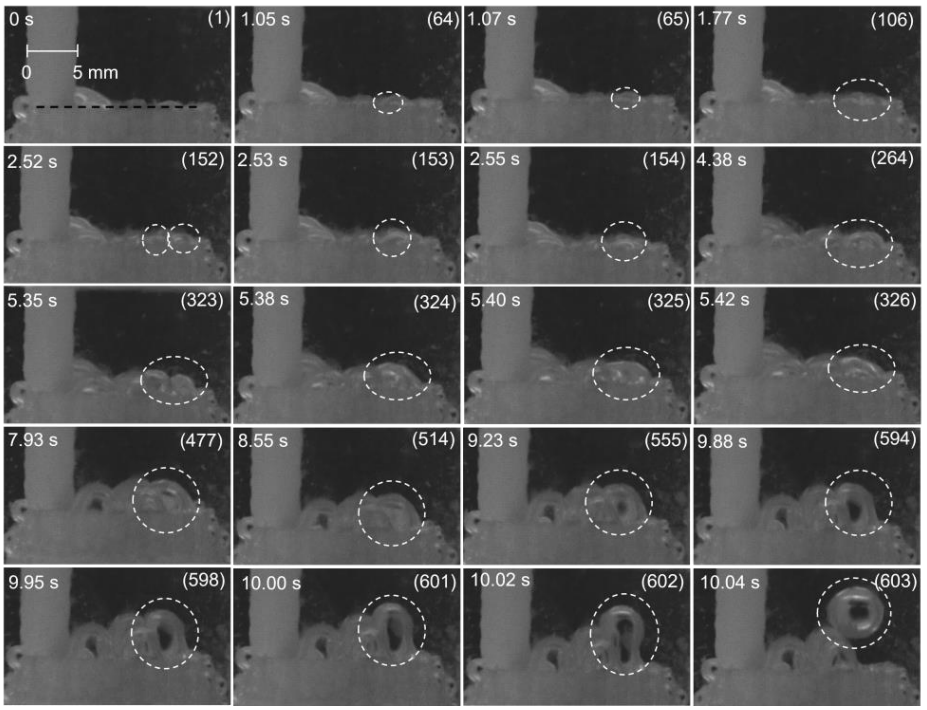

Figure 9.7. Life cycle of one bubble during electrolysis at a constant current density of 0.07 A cm^{-2}. The frame rate was 60 fps. Frame numbers are given in brackets. Frame (1) is defined as 0 s. The horizontal black dashed line in frame (1) represents the position of the carbon anode surface. Bubbles of interest are highlighted with white dashed line. A scale bar is shown in frame (1).

Figure 9.8 shows illustration and actual frames from video recordings of different necking. Among the already mentioned forces that affect bubble detachment, a wetting probably affects necking since the cryolite-carbon system in general shows poor wetting. When bubbles detach as shown in Figure 9.8 it is probably linked to poor wetting. Regarding necking shape shown in (c), it was observed that when the bubble detaches it is not leaving behind the bubble bulk bellow the neck. It appears that whole bubble is detached and nothing is left on the base. It was also observed that in some cases the necking transitioned between shapes shown in Figure 9.8 before detaching and again not leaving anything behind. In order to study this further in details, different camera position and higher frame rate is desirable.

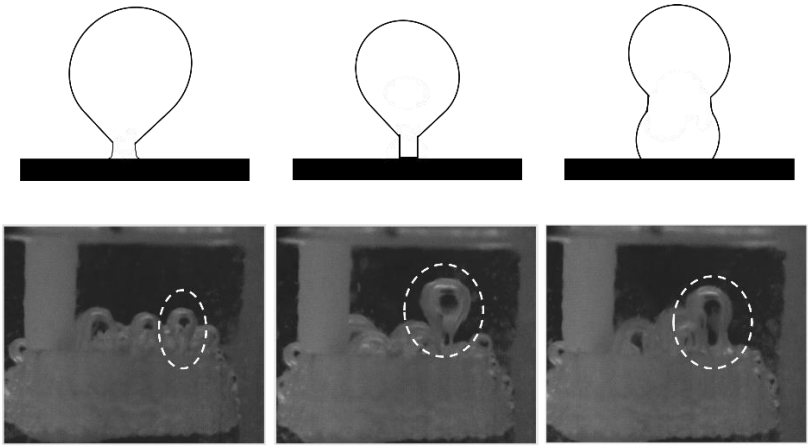

Figure 9.8. Illustration of different necking and pinning of the contact line in bubble detachment phase during electrolysis on the inverted anode.

9.3.4 Anode effect

In Figure 9.9(a) the linear sweep voltammogram with sweep rate of 1.0 V s^{-1} for inverted horizontal anode is presented. Starting from OCP, the first increase in current density is observed around 0.7 V. The current increase was due to CO_2/CO gas evolution. There is some noise on the curve which arises from growth, coalescence and detachment of bubbles. The link for the corresponding video of the process can be found in Appendix 9.5. A small stream of bubbles became more pronounced as the voltage increased. This bubble stream was hindering the visibility of the anode surface. Figure 9.9(b) shows selected frames of bubble detachment. In frame (1) is shown production of bubbles and their detachment at around 0.7 A cm^{-2}. Frame (2) shows the situation at the anode just before the anode effect occurred. At the cell voltage around 4.7 V the initiation of anode effect can be seen which is associated with the formation of (C – F) bond, *i.e.,* teflonisation of the surface, followed by a slight decrease in current, frame (3). The current increased slightly before suddenly decreasing towards zero, frame (4) and (5). The fact that the anode effect started at 4.7 V is based on the change in bubble detachment seen in frame (3). Before anode effect occurred, bubbles were formed and detached from all over the anode surface as small bubbles, big bubbles, and a stream of small gas bubbles. After anode effect,

all gas produced was detaching as one big bubble which is typically illustrated by the sequence represented by frames (6-8); frame (6) shows bubble growth at the anode surface, in frame (7) the bubble is detaching and in frame (8) the detached bubble is rising. From frame (5) and throughout the rest of the sweep the gas evolution follows what is illustrated by the sequence frames (6-8). After anode effect (frame 5) the current gradually increases again implying that the gas production continues. The existence of the (C – F) bond is probably the reason for the change in bubble evolution behavior as it causes non-wetting of the anode. The non-wetting can easily be seen in frame (8) and partly in frame (6). In frame (8) right after bubble detachment the new bubble on the anode surface has a small volume and the wetting angle is very close to 180°, meaning the bubble can hardly be seen. In frame (6) the bubble is bigger and the wetting angle is somewhat smaller. The bubble has to grow large to be able to escape the anode surface. The diameter of all bubbles detached after anode effect was in the interval 7.2-7.6 mm and it was independent of current density. The frequency of bubble release right after the first anode effect (at 5.2 s) was found to be approx. 1.8 Hz and the frequency increased up to approx. 3.3 Hz right before the second anode effect occurred (at 8.2 s). After the second anode effect the frequency dropped. The current after the first anode effect increased probably due to the continuously increasing voltage. From the video it is clear that the anode is on anode effect from the first anode effect occurred and throughout the rest of the sweep. The anode effect and formation of the PFC/CO/CO_2 gas layer was studied and discussed in detail for the rod anode (Chapter 7) and the facing-downwards horizontal anode (Chapter 8). It was observed that after anode effect a gas layer was formed covering completely the anode surface and the current dropped to zero and remained more or less zero. The behavior of the evolved gas after anode effect at the inverted anode was found to be different than for the rod anode and the facing-downwards horizontal anode. The produced gas was detached as one big bubble. As this bubble detached a new one started to grow at the anode surface. Due to the gas bubble covering the whole horizontal anode surface practically no faradaic current could pass through the horizontal surface. This is supported by the fact that no saw-tooth features or larger voltage drops were observed in the voltammogram although big bubbles were formed and detached. It is therefore believed that the active anode surface after anode effect was only the vertical sides of the anode. The bubbles formed on the vertical surface

are flat (meaning the wetting angle is close to 180°), since the vertical side of the anode is also on anode effect, and the bubbles can therefore not be seen from the video images. On the vertical surface the electrochemical reaction could proceed because the gas produced can easily escape upwards towards the horizontal surface, be accumulated there forming a larger bubble which will eventually detach as illustrated in Figure 9.10 and in the sequence frames (6-8) in Figure 9.9(b). However, it cannot be observed from the video images if the gas layer is covering the sharp corner of the carbon anode surface.

It appears that that the evolution of the anode effect depends on the possibility of the gas bubbles and gas layer to be detached from the anode surface. If the gas is trapped the gas layer is covering the anode surface, disabling contact between anode and electrolyte and further gas production is strongly hindered like observed for the rod anode (Chapter 7) and horizontal facing downwards anode (Chapter 8). In both of these cases the gas was trapped by the BN shielding due to better wetting of the BN by electrolyte as found by Åsheim *et al.* [9] and the faradaic current became approximately zero and the gas evolution therefore stopped. In the case of the inverted anode there was no BN shielding that could trap the gas and the gas evolution could continue.

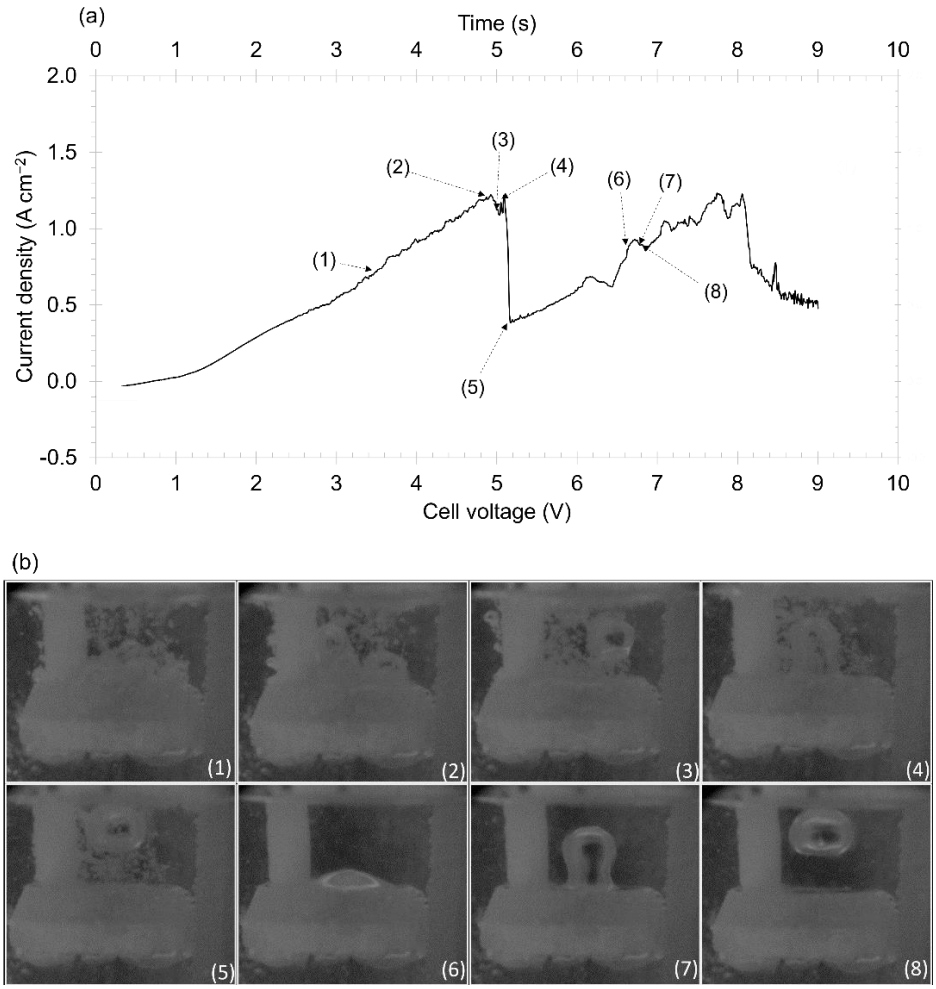

Figure 9.9. (a) Linear sweep voltammetry (LSV) curve for the inverted horizontal anode with sweep rate 1.0 V s^{-1}. The voltage is not IR-compensated. The sampling frequency was 500 Hz. (b) Corresponding frames from video recordings. The frame rate was 60 fps. Frame numbers are given in brackets. The large bubble in frame (4) is the next large bubble after the one in frame (3). The detached bubble in frame (5) is the same bubble in frame about to be detached (4). Frames (6-8) show different stages of the same bubble.

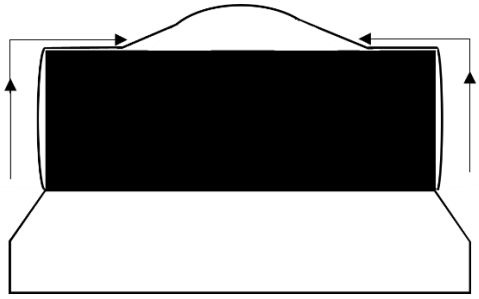

Figure 9.10. An illustration of the bubble behavior and bubble formation for the inverted anode during anode effect. Gas bubbles on the vertical surface appear to be almost flat due to absolute non-wetting of the anode. The arrows show the direction of bubble movement from the vertical surface towards the horizontal surface where the gas will be accumulated forming a larger bubble which will eventually be detached. The bubble thickness on the vertical surface and the height of the vertical surface are exaggerated for reasons of clarity.

Anode effect mechanisms in general

The mechanism of the initiation of the anode effect has not yet been clarified. A list of six possible mechanisms was proposed by Grjotheim *et al.* in 1982 in the book *Aluminium Electrolysis, Fundametals of the Hall-Héroult Process* [10]:

1. An insulating layer of solid material
2. Deterioration of the wetting of the anode by decreasing alumina content
3. Formation of surface compounds or gas which insulates the anode or renders it non-wettable
4. Electrostatic attraction of the anode by negatively charged gas bubbles
5. Fluid-dynamic effects creating a gas film at the anode
6. Evaporation of the electrolyte

Twenty years later, in 2001, the list was revised by Thonstad *et al.* in the new edition of the book [11]:

1. A surface compound of insulating (solid) material
2. An insulating layer of gas (gas film)

3. Partial gas coverage so that the actual current density exceeds critical current density (ccd)
4. Fluid-dynamic obstruction of gas release

Results from this doctoral work support the third mechanism of the first list and first and second of the revised list but the results do not exclude other mechanisms from the list. It was found that a gas layer only can cover the whole anode surface if the gas is not able to leave the anode. Even with the existence of a (C – F) surface compound on the anode surface, the anode seems to be electrochemically active towards both CO/CO_2 and PFC formation. Gao *et al.* [12] were observing anode effect occurring on carbon anode (100 × 50 × 70 mm, with the immersion depth of 5 mm) in a high-temperature see-through cell. The authors found that during anode effect the intermediate insulating film layer of CF_X was formed and did not observe bubble layer blanketing the horizontal anode surface. The anode effect first occurred at the opposite edges of the anode where the bubble disappeared, following that the bubble-free area expanded very quickly towards the center of the anode. After that ignition was observed at the anode center when all bubbles suddenly disappeared and with the quick rise of the cell voltage and a whole anode bottom surface was covered with small sparks. Considering this the authors stated that the gas layer mechanism for the anode effect is incorrect .

From the results of the inverted anode, it could be concluded that fluoride discharge forming (C – F) surface compounds at the anode surface changed wetting properties of the anode completely to de-wetting. Neither individual bubbles nor gas layer were observed at the horizontal surface after initiation of the anode effect. But the vertical surface after anode effect was still electrochemical active because of the contact between the surface and the electrolyte and gas evolution could proceed. As long as produced gas can escape there is no gas layer forming on the anode surface. This also supports the findings of Gao *et al*. that intermediate insulating film layer of CF_x surface compounds was formed on the surface without gas layer.

9.4 Conclusion

The saw-tooth features in voltage-time curve were observed and disappeared with increasing current density. The saw tooth features could

be explained by mutual influence of both coalescence and simultaneous detachment of several bubbles in a periodic pattern. The anode surface was never free of bubbles even at low current density. Different stages of bubble growth were observed and the growth mechanism is in agreement with findings in the literature regarding aqueous solutions: hemispherical spreading, cylindrical spreading, cylindrical growth, and necking. A different necking was observed than in aqueous solutions since the cryolite-carbon system in general shows poor wetting and wetting affects the necking. For all current densities it was observed that half spherical-shaped bubbles were meeting at the base and coalescing forming bigger bubbles. It was not observed that bubbles are coalescing when they are in the cylindrical growth stage. The anode process after initiation of the anode effect depends on the possibility of the PFC/CO/CO_2 gas containing bubbles and gas layer to be detached from the anode surface. If the gas is trapped the gas layer is covering the anode surface, disabling contact between anode and electrolyte and further gas production is strongly hindered. The anode surface of the inverted horizontal anode after anode effect is still electrochemically active with the increasing voltage as long as produced gas can escape and as the anode and electrolyte are in contact.

9.5 Appendix

Video recording of the electrolysis at constant current 0.07 A cm^{-2} in relation to Figure 9.6, https://youtu.be/HsZ4F5-QWKo. The video is captured with 60 fps. The video is saved with playback frame equal to 30 fps, meaning the video is shown in 50 % of the real speed.

Video recording of the anode effect on the inverted horizontal anode in relation to Figure 9.9, https://youtu.be/wyh-lDfr9yQ. The video is captured with 60 fps. The voltage was scanned at rate 1 V s^{-1} starting from 0 to 9 V making the recording time 9 s. The videos are saved with playback frame equal to 30 fps, meaning the videos are shown in 50 % of real speed.

References

1. Stanic, N., I. Jevremovic, A.M. Martinez, and E. Sandnes, *Bubble Evolution on Different Carbon Anode Designs in Cryolite Melt.* Metallurgical and Materials Transactions B, 2020. **51**(3): p. 1243-1253.

2. Stanic, N., A.M. Martinez, K.E. Einarsrud, and E. Sandnes, *Bubble Phenomena and Bubble Properties for Horizontal and Vertical Carbon Anode Surfaces in Cryolite Melt Applying a See-Through Cell.* Metals, 2021. **11**(6): p. 24.
3. Stanic, N. and E. Sandnes, *Bubble Behavior on Horizontal and Vertical Carbon Anode Surfaces in Cryolite Melt Applying a See-Through Cell.* Materials Proceedings, 2021. **3**(1): p. 8.
4. Stanic, N., E.T. Bø, and E. Sandnes, *CO and CO_2 Anode Gas Concentration at Lower Current Densities in Cryolite Melt.* Metals, 2020. **10**(12): p. 1694.
5. Zhang, L. and M. Shoji, *Aperiodic bubble formation from a submerged orifice.* Chemical Engineering Science, 2001. **56**(18): p. 5371-5381.
6. Mirsandi, H., W.J. Smit, G. Kong, M.W. Baltussen, E.A.J.F. Peters, and J.A.M. Kuipers, *Influence of wetting conditions on bubble formation from a submerged orifice.* Experiments in fluids, 2020. **61**(3).
7. Ying, H., G. Puzhen, and W. Chaoqun, *Experimental and Numerical Investigation of Bubble–Bubble Interactions during the Process of Free Ascension.* Energies, 2019. **12**(10): p. 1977.
8. Taqieddin, A., M. Allshouse, and A. Alshawabkeh, *Editors' Choice—Critical Review—Mathematical Formulations of Electrochemically Gas-Evolving Systems.* Journal of The Electrochemical Society, 2018. **165**: p. E694-E711.
9. Åsheim, H., I. Eidsvaag, A. Solheim, H. Gudbrandsen, G.M. Haarberg, and E. Sandnes, *The Influence of Polarisation on the Wetting of Graphite in Cryolite-Alumina Melts*, in *Light Metals 2020*, A. Tomsett, Editor. 2020, Springer International Publishing. p. 608-619.
10. Grjotheim, K., C. Krohn, M. Malinovsky, K. Matiašovsky, and J. Thonstad, *Aluminium electrolysis : Fundamentals of the Hall-Heroult process*. 1982, Dusseldorf: Aluminium-Verlag. 277-280.
11. Thonstad, J., P. Fellner, G.M. Haarberg, J. Híveš, H. Kvande, and Å. Sterten, *Aluminium Electrolysis, Fundamentals of the Hall–Héroult Process*. 3rd ed. 2001, Düsseldorf Aluminium-Verlag.
12. Gao, B., H. Niu, Y. Guan, Z. Wang, J. Liu, M.P. Taylor, and J.J.J. Chen, *Visualization of Anode Effect in Aluminum Electrolysis.* J. Electrochem. Soc, 2022. **169**(1).

Conclusion

The anode potential has been shown to be highly dependent on anode geometry and orientation in the Hall–Héroult process. From the polarization curves of the four anode designs (horizontal facing downwards, vertical, rod and horizontal facing upwards) the vertical anode and the horizontal facing downwards anode operated at lowest potentials. Above 1 A cm^{-2} the vertical anode showed the lowest potential, a result related to an easier bubble release from the vertical anode. As the current increases the transition towards smaller noise was found to be pronounced for the horizontal anode and to some degree for the vertical anode and inverted horizontal anode. This transition is caused by increased bubble induced convection effectively removing the bubbles.

The bubble life cycle which includes the bubble nucleation, bubble growth, coalescence, and detachment, at different carbon anodes was studied in detail in a see-through furnace. More bubbles were nucleated on the industrial carbon anode than on the graphite anode for the same current density. The higher number of bubbles was due to more active sites on the industrial carbon. For all anodes, the smaller bubbles coalesced into bigger bubbles. Results from this work indicated that the time related to the process of coalescence was in the interval 16-24 ms from initiation to the final bubble shape and independent of the anode material, anode orientation and the current density. After growing to a certain size, bubbles were detached from the anode surface and were rising. At the horizontal facing-downwards anode, it was found that one large bubble was formed by the growth and coalescence of smaller bubbles, and finally, the large bubble detached periodically. For the vertical anode surface, the detaching bubbles were smaller, and most of them had been going through a coalescence process prior to detachment. The bubbles detached randomly. The rod anode has mixed geometry, horizontal surface and vertical surface. On both horizontal and vertical surfaces, the smaller bubbles coalesced into bigger bubbles. As expected, the bubbles on the vertical surface were smaller and detached randomly while the bubbles on the horizontal surface coalesced and went off as a one big bubble. At the horizontal facing-upwards surface at the low current densities, < 0.5 A cm^{-2}, detachment of

several bubbles in a periodic pattern was observed while at higher current densities, > 0.5 A cm^{-2}, bubbles detached randomly.
Experimental findings gave values of diameter of detached bubbles for each carbon anode design. The bubble diameter decreased with the increasing current density for all carbon anodes. Explanations for these observations are the larger number of nuclei formed at higher potential and the more efficient bubble-induced convection. The increase in current density and thereby the corresponding increase in potential provide a higher driving force for nucleation of relatively more bubbles. These bubbles coalesce into larger bubbles, and the bubble cycle time is shorter within increasing current. Coalescence is less pronounced at higher current densities because bubbles are pushed by newly formed bubbles and bubbles detach before growing more in size.

Results of the off-gas analysis using graphite anodes during aluminium electrolysis showed that in the lower current density region, 0.015 A cm^{-2} to 0.07 A cm^{-2}, CO was found to be dominant anode gas product. Above 1.6 V and 0.12 A cm^{-2} the dominant gas became CO_2. Disintegration of the graphite anode forming carbon dust was observed to have taken place during the electrolysis. The carbon dust probably reacted through the Boudouard reaction with CO_2 and formed CO. Thus, the CO concentration was higher than the electrochemically formed CO should give, especially at higher current densities.

This doctoral work showed that the anode process after initiation of the anode effect depends on the possibility of the PFC/CO/CO_2 containing gas bubbles/gas layer to be detached from the anode surface. If the gas is trapped the gas layer is covering the anode surface, disabling contact between anode and electrolyte and further gas production is strongly hindered like was observed for the rod anode and horizontal facing downwards anode. In both cases the gas was trapped by the boron nitride shielding. Due to good wetting of the boron nitride by electrolyte, the evolved gas was trapped forming a gas layer and the gas evolution therefore stopped. For the horizontal facing upwards anode there was no boron nitride shielding that could trap the gas and the gas evolution could continue.

Increased knowledge of the bubble behavior from this work is useful for further improvement especially in laboratory scale experiments studying similar types of anode designs. In addition to the more technical findings commented above, the following could be stated:

- Graphite as an anode material is not a good choice to study CO/CO_2 gas concentration during aluminium electrolysis because it tends to disintegrate and the carbon particles react with the primary anodic gas product CO_2 producing considerable amount of CO.
- The current distribution across the working electrode (WE) is important. The counter electrode (CE) was placed on the side of the WE in all experiments, meaning the current distribution from a theoretical point of view would not be even, and the current path to the other side of the WE is longer. While studying bubble evolution in the see-through cell it was not observed more bubbles forming on the side of the WE facing the CE compared to the other side. It can then be assumed that the current distribution for this electrode setup is sufficiently good for all practical purposes.
- During all experiments in the see-through furnace, it was observed that as soon as the anode was immersed in the melt the gas bubbles were spontaneously formed on both carbon and BN surfaces. When electrolysis started bubbles at the carbon surface were removed but bubbles on the BN surface were resting at the surface during electrolysis. These bubbles did not take part in any electrochemical reaction. This information is relevant for the first time period when polarizing anodes in electrochemical measurements but also for wetting experiments where buoyancy is part of the equation.
- With the increasing current density more metal fog is produced which is efficiently spread due to increased convection. The presence of metal fog can influence bubble size, wetting, reaction products. Metal fog can be electrochemically oxidized on the anode and the CO/CO_2 ratio can be changed by the back reaction. To reduce complications caused by the metal fog the anode and cathode should be physically separated at least for longer duration experiments if no metal pad is present.

These findings could be helpful for better design of laboratory-scale studies investigating, *e.g.*, current distribution, anode bubble evolution and reaction kinetics, current efficiency, and wetting properties.

Further work

Many different adaptations to the laboratory setups and ideas for new experiments have been identified as the work has proceeded. Thus, further studies building on this doctoral work could look into:

- **Improvement of the gas measurements -** At low current densities it took long time for the produced gas to be transported to the gas analyzer. Therefore, the setup should be modified introducing a carrier gas for faster transport of produced gas.
  Due to the graphite anode disintegrating the Boudouard reaction occurs to a larger extent between produced CO_2 and carbon particles giving a higher CO concentration. It would be beneficial to replace graphite material with the industrial carbon material in order to reduce carbon disintegrating.
- **Optimization of the see-through cell -** Due to the small quartz crucible and the reflections in the quartz crucible the reference electrode (RE) was not used. The RE would be beneficial for having a more accurate measurements of the anode potential. This would require a larger crucible and possibly also a squared crucible to avoid reflections from the RE reducing the image quality of the bubbles.
- **See-through furnace with a bottom view –** The see-through furnace only had a side view to the cell. Building a see-through furnace with a bottom view to observe the anode from below would allow more information on the downward-facing horizontal anode and rod anode. The natural next step would be to make this functionality.
- **Anode effect mechanisms –** The anode effect was only investigated with potential control of the anode. Investigation of the anode effect mechanism on the same anode designs under galvanostatic control would give additional information which more would simulate conditions in the industrial cell.

Conferences and publications

Conferences

1st International Electronic Conference on Metallurgy and Metals (IECMM), 22 February-7 March 2021, presentation

7th Baltic Electrochemistry Conference: Finding New Inspiration (BEChem 2018), 4-7 November 2018, Tartu, Estonia, oral presentation

Publications

Stanic, Nikolina; Martinez, Ana Maria Cuellar; Einarsrud, Kristian Etienne; Sandnes, Espen. A study of bubble behavior and anode effect on graphite and industrial carbon anode in see-through furnace during aluminium electrolysis. *Metall Mater Trans B* 2022. 53(5): p. 3025–3043

Stanic, Nikolina; Martinez, Ana Maria Cuellar; Einarsrud, Kristian Etienne; Sandnes, Espen. Bubble Phenomena and Bubble Properties for Horizontal and Vertical Carbon Anode Surfaces in Cryolite Melt Applying a See-Through Cell. *Metals*. 2021, vol. 11 (6).

Stanic, Nikolina; Sandnes, Espen. Bubble Behavior on Horizontal and Vertical Carbon Anode Surfaces in Cryolite Melt Applying a See-Through Cell. *Mater. Proc.* 2021, vol 3. (8).

Stanic, Nikolina; Bø, Embla Knutsdotter Øi Tharaldse; Sandnes, Espen. CO and CO_2 Anode Gas Concentration at Lower Current Densities in Cryolite Melt. *Metals.* 2020, vol. 10 (12).

Stanic, Nikolina; Jevremovic, Ivana; Martinez, Ana Maria Cuellar; Sandnes, Espen. Bubble evolution on different carbon anode designs in cryolite melt. *Metallurgical and Materials Transactions B.* 2020, vol. 51 (3).

Manuscripts

Stanic, Nikolina; Martinez, Ana Maria Cuellar; Einarsrud, Kristian Etienne; Sandnes, Espen. Bubble evolution and anode effect on an upward-facing horizontal carbon surface. 2022 (Draft)

Stanic, Nikolina; Sandnes, Espen. Bubble behavior on a downward-facing horizontal anode of different sizes. 2022 (Draft)

Summer School

Electrochemistry Summer School: Instrumental Methods in Electrochemistry, University of Southampton, Southampton, June 2016

List of Figures

Figure 5.17. Relative amount of CO and CO_2 versus current density for the hollow gas anode.

Figure 5.18. Anode potential and CO and CO_2 amounts versus current density. (a) Data extracted from Thonstad [5], (b) Data extracted from Drossbach [6], (c) Data extracted from Silny and Utigard [7], (d) Data from this work (rod anode).

Figure 5.19. Drossbach's tabulated data plotted [6].

Figure 5.20. FFT spectrum of the current density - time data for the horizontal anode at different applied potentials. The current densities in the figure are the current densities measured in the moment the bubble has detached from the anode surface (i.e. the current obtained for the bubble-free surface).

Figure 6.1. Contact angle (θ) and surface tensions (γ) of gas bubble (g) in liquid (l) underneath the solid (s).

Figure 6.2. Advancing (θ_a) and receding (θ_r) contact angles for a gas bubble at the three-phase boundary where a liquid (l), gas (g), and solid (s) intersect.

Figure 6.3. (a) The see-through furnace, the potentiostat, and the high-speed camera, (b) principle sketch of the interior of the furnace.

Figure 6.4. Anode designs with the same dimensional length of 10 mm; (a) the horizontal anode with surface area 0.79 cm^2 45 degrees angle chamfered boron nitride edges (with small BN shielding around carbon surface, less than 1 mm), (b) the horizontal anode shown from below and (c) the vertical anode with surface area 3.14 cm^2.

Figure 6.5. The schematics of the two-electrode setup, the working (WE) and working sense (WSE) connected to the anode and the counter (CE) and reference electrode (RE) connected to SS rod.

Figure 6.6. The image (a) before and (b) after image processing in PFV4 (Photron Fastcam Viewer 4). The image shows an example of using the vertical anode design. The yellow dashed lines indicate the border between the carbon and boron nitride material. The stainless steel rod is shown on the right in the image. The image was taken during electrolysis at a constant current density of 0.25 A cm^{-2}.

Figure 6.7. Cycle of one bubble at the horizontal surface during electrolysis at a constant cell voltage of 1.5 V with an average current density of 0.4 A cm^{-2}. Each individual image represents one frame with the corresponding number. The frame rate was 60 fps. The frame number is given in the brackets. Frame (1) is defined as 0 s and shows the situation right after a large bubble from the previous bubble cycle is detached from the anode surface. The horizontal yellow line in frames (1) and (329) represents the position of the carbon anode surface. A scale bar is shown in frame (1).

Figure 6.8. The horizontal anode; (a) current *vs.* time at a constant cell voltage of 1.5 V and details of the saw-tooth shaped current density-time curve. Frame (318) corresponds to the smallest current measured, and frame (329) corresponds to the current peak. (b) FFT (Fast Fourier Transform) spectra of current density-time data.

Figure 6.9. A bubble rising after its detachment from the horizontal surface, bouncing and bursting at the bath surface during electrolysis at a constant cell voltage of 1.5 V with the average current density of 0.4 A cm^{-2}. The frame rate was 60 fps. Frame numbers are placed in brackets. Frame (1) is defined as 0 s right after the bubble was detached from the anode surface. A scale bar is shown in frame (1).

Figure 6.10. One small bubble detaching from the surface (yellow arrow pointing) while one large bubble growing at the surface during electrolysis at a constant cell voltage of 2.0 V. Average current density was 0.7 A cm^{-2}. A scale bar is shown.

Figure 6.11. Bubble diameter after detachment from the horizontal surface and bubble release frequency as a function of the nominal current density.

Figure 6.12. The change of contact angle of the bubble at the horizontal anode during electrolysis at different current densities.

Figure 6.13. Process of coalescence of two bubbles (marked in yellow dashed line) into one bigger bubble and its immediate detachment from the vertical surface during electrolysis at a constant current density of 0.1 A cm^{-2}. The frame rate was 125 fps. The frame number is given in the brackets. Frame (1) is defined as 0 s. A scale bar is shown in frame (1).

Figure 6.14. Process of coalescence of three bubbles (marked in yellow dashed line) into one larger bubble and its prolonged resting at the upper part of the anode at the boundary between BN and C during electrolysis at a constant current density of 0.1 A cm^{-2}. The frame rate was 125 fps. The frame number is given in the brackets. Frame (1) is defined as 0 s, indicating the start of the coalescence process. A scale bar is shown in frame (1). The yellow arrows in frame (1) indicate the C-BN borders.

Figure 6.15. Bubble bouncing and bursting at the bath surface after detachment from the vertical anode at 0.1 A cm^{-2}. Upper BN part of the anode is shown. The frame number is given in the brackets. Frame (1) is defined as 0 s, indicating bubble detachment from the carbon surface and rise. A scale bar is shown in frame (1).

Figure 6.16. One small bubble (yellow arrow pointing) is detaching from the vertical surface (at the left) at a constant current density of 0.1 A cm^{-2}. A scale bar is shown in the figure.

Figure 6.17. Bubble diameter after detachment from the vertical surface as a function of nominal current density.

Figure 6.18 Images of bubble evolution at the vertical anode during electrolysis at different current densities: (a) 0.1, (b) 0.5, (c) 1.0, and (d) 1.5 A cm^{-2}. The yellow line indicates the border between the carbon and boron nitride material. The frame rate was 125 fps. A scale bar is shown in (a).

Figure 6.19. Lower and upper contact angle and the bubble diameter as a function of applied current density for the vertical anode, (a) for the bubble resting at the surface in the growth stage just before coalescence (b) for the bubble after coalescence just before detachment.

electrolysis at a constant current density of 0.1 A cm^{-2}. Frame (1) represents the beginning of the coalescence process and is given a 0 ms timestamp, by that, other frames are relative to the first frame. The frame rate was 1000 fps. The anode surface is highlighted with a black dashed line in frame (1) together with a scale bar.

Figure 7.11. The process of coalescence of two bubbles (highlighted with white dashed line) into one bigger bubble at the vertical surface of industrial anode during electrolysis at a constant current density of 0.25 A cm^{-2}. Frame (1) represents the beginning of the coalescence process and is given a 0 ms timestamp, by that, other frames are relative to the first frame. The frame rate was 500 fps. The anode surface is highlighted with a black dashed line in frame (1) together with a scale bar.

Figure 7.12. The process of coalescence of two bubbles (highlighted with white dashed line) into one bigger bubble at the horizontal surface of the graphite anode during electrolysis at a constant current density of 0.1 A cm^{-2}. Frame (1) represents the beginning of the coalescence process and is given a 0 ms timestamp, by that, other frames are relative to the first frame. The frame rate was 1000 fps. The anode surface is highlighted with a black dashed line in frame (1) together with a scale bar, frame (2).

Figure 7.13. Bubble diameter from horizontal and vertical part of anode for the (a) graphite anode and (b) industrial anode as a function of the nominal current density.

Figure 7.14. Shielded rod graphite anode during electrolysis at different current densities, 0.1, 0.5 and 1.0 A cm^{-2}, while a) big bubble from the horizontal surface is sliding toward the anode edge, b) big bubble is detaching from the anode edge and c) big bubble is leaving the anode surface. The frame rate was 60 fps. Frame numbers are given in brackets. Timestamp of 0 ms is added to frame (1), by that, other frames are relative to the first frame. The anode surface is highlighted with a black dashed line in frame (1) together with a scale bar.

Figure 7.15. Gas production on the horizontal surface for different current densities: (a) Gas volume rate, (b) Gas volume fraction.

Figure 7.16. Linear sweep voltammetry (LSV) curves for graphite anode with sweep rate of 5 V s^{-1} with corresponding frames from video recordings. Frames are numbered in display order, not in true time frames. Not IR and IR-compensated data are shown. Sampling frequency was 500 Hz. Timeline is only valid for not IR-compensated data.

Figure 7.17. Principal sketch of a) CO_2/CO gas bubbles during the anode process for normal electrolysis and b) after initiation of anode effect. The thickness of the perfluorocarbon containing gas layer is exaggerated for reasons of clarity.

Figure 7.18. Linear sweep voltammetry (LSV) curves for the industrial carbon anode with sweep rate of 5 V s^{-1} with corresponding frames from video recordings. Frames are numbered in display order, not in true time frames. Not IR and IR-compensated data are shown. Sampling frequency was 500 Hz. Timeline is only valid for not IR-compensated data.

Figure 8.1. Horizontal anode designs with different diameter, (a) the horizontal anode with 10 mm diameter and surface area 0.79 cm^2, 45 degrees angle chamfered boron nitride edges, (b) the horizontal anode (Ø 10 mm) shown from below with small BN shielding around graphite surface, (c) the horizontal anode with 20 mm diameter and surface area 3.8 cm^2, 45 degrees angle chamfered boron nitride edges and 1 mm of graphite sticking out of the BN shielding, and (d) the horizontal anode (Ø 20 mm) shown from below.

Figure 8.2. Cell voltage-time data at applied constant current density of 1.0 A cm^{-2} for the graphite anode (a) diameter 10 mm (b) diameter 20 mm. Cell voltage data are post-IR-compensated.

Figure 8.3. FFT spectra of voltage-time data for 1.0 A cm^{-2} for the graphite anode with (a) 10 mm diameter and (b) 20 mm diameter.

Figure 8.4. Bubble diameter as a function of the nominal current density, measured from the video recordings and calculated from the charge for the graphite anode with (a) 10 mm diameter and (b) 20 mm diameter.

Figure 8.5. Images of the bubble at the graphite anode surface in a growth stage before the bubble starts to slide towards edge to be detached; (a) the 10 mm anode at 0.4 A cm^{-2}, (b) the 20 mm anode at 0.5 A cm^{-2}. A scale bar is shown.

Figure 8.6. An image of the industrial carbon anode with 20 mm diameter showing smaller bubbles sticking to the vertical part and edge of the anode (highlighted) at current density 0.25 A cm^{-2}. A scale bar is shown.

Figure 8.7. Linear sweep voltammetry for the graphite anode with 10 mm (black line) and 20 mm diameter (gray line) recorded with the sweep rate of 0.5 V s^{-1}, (a) not IR compensated cell voltage, (b) post-IR-compensated cell voltage with the value of ohmic resistance at OCP.

Figure 8.8. (a) Linear sweep voltammetry curve for the industrial carbon anode with sweep rate 0.5 V s^{-1}. Not IR and IR-compensated data are shown. Sampling frequency was 50 Hz. Timeline is only valid for not IR-compensated data. (b) Corresponding images from video recordings.

Figure 9.1. Anode with horizontal surface facing upwards, *i.e.*, inverted anode (a) cross-section of earlier constructed and studied design with a (surface area of 0.69 cm^2), (b) cross-section of a new improved design with a total surface area of 4.4 cm^2, of which the horizontal surface is 3.14 cm^2 and the vertical surface 1.26 cm^2, (c) the outer body of the new design. Insets in (a) and (b) shows the inverted anode seen from above.

Figure 9.2. Illustration of the electrochemically and non-electrochemically formed bubbles on different types of the inverted anode (a) first constructed and studied inverted design, (b) new improved design with chamfered edges during electrolysis. In light gray color are shown non-electrochemical bubbles formed and resting at the BN surface, while light blue color shows electrochemically formed bubbles.

Figure 9.3. Cell voltage-time data for different current densities. The sampling rate was 50 Hz. Voltage data are post-IR-compensated.

Figure 9.4. Bubble detachment from the inverted anode during electrolysis at constant current of 0.07 A cm^{-2}, 0.2 A cm^{-2} and 0.5 A cm^{-2}. The frame rate was 60 fps. Frame numbers are given in brackets. Timestamp of 0 ms is assigned to frame (1), by that, other frames are relative to the first frame. A scale bar is shown in frame (1).

Figure 9.5. Bubble diameter detached from the inverted horizontal anode as a function of applied current density.

Figure 9.6. Cell voltage-time data under galvanostatic control for inverted anode at constant current density 0.07 A cm^{-2}. Data are post-IR-compensated. The sampling frequency was 50 Hz.

Figure 9.7. Life cycle of one bubble during electrolysis at a constant current density of 0.07 A cm^{-2}. The frame rate was 60 fps. Frame numbers are given in brackets. Frame (1) is defined as 0 s. The horizontal black dashed line in frame (1) represents the position of the carbon anode surface. Bubbles of interest are highlighted with white dashed line. A scale bar is shown in frame (1).

Figure 9.8. Illustration of different necking and pinning of the contact line in bubble detachment phase during electrolysis on the inverted anode.

Figure 9.9. (a) Linear sweep voltammetry (LSV) curve for the inverted horizontal anode with sweep rate 1.0 V s^{-1}. The voltage is not IR-compensated. The sampling frequency was 500 Hz. (b) Corresponding frames from video recordings. The frame rate was 60 fps. Frame numbers are given in brackets. The large bubble in frame (4) is the next large bubble after the one in frame (3). The detached bubble in frame (5) is the same bubble in frame about to be detached (4). Frames (6-8) show different stages of the same bubble.

Figure 9.10. An illustration of the bubble behavior and bubble formation for the inverted anode during anode effect. Gas bubbles on the vertical surface appear to be almost flat due to absolute non-wetting of the anode. The arrows show the direction of bubble movement from the vertical surface towards the horizontal surface where the gas will be accumulated forming a larger bubble which will eventually be detached. The bubble thickness on the vertical surface and the height of the vertical surface are exaggerated for reasons of clarity.

References

1. Grjotheim, K. and H. Kvande, *Introduction to aluminium electrolysis : understanding the Hall-Héroult process*. 2nd ed. 1993, Düsseldorf: Aluminium-Verlag.
2. Prasad, S., *Studies on the Hall-Heroult aluminum electrowinning process.* Journal of the Brazilian Chemical Society, 2000. **11**(3): p. 245-251.
3. Photron. *Photron - Ultra High-Speed Cameras*. Available from: https://photron.com/fastcam-mini-ax/.

4. Stanic, N., I. Jevremovic, A.M. Martinez, and E. Sandnes, *Bubble Evolution on Different Carbon Anode Designs in Cryolite Melt.* Metallurgical and Materials Transactions B, 2020. **51**(3): p. 1243-1253.
5. Thonstad, J., *On the Anode Gas Reactions in Aluminum Electrolysis, II.* J. Electrochem. Soc., 1965. **111**(8): p. 959-965.
6. Droßbach, P., *Zur Elektrometallurgie des Aluminiums.* Zeitschrift für Elektrochemie und angewandte physikalische Chemie, 1936. **42**(2): p. 65-70.
7. Silny, A. and T.A. Utigard, *Determination of the factors which control the CO/CO_2 ratio of the anode gas.*, in *Light metals 1995* J.W. Evans, et al., Editors. 1995, Minerals, Metals & Materials Society: Warrendale, Pa. p. 205–211.

List of Tables

ISBN 978-82-326-5921-0 (printed ver.)
ISBN 978-82-326-6148-0 (electronic ver.)
ISSN 1503-8181 (printed ver.)
ISSN 2703-8084 (online ver.)

NTNU
Norwegian University of
Science and Technology